CHARACTERIZATION AND MODELING OF SOLUBLE MANGANESE REMOVAL FROM DRINKING WATER BY OXIDE-COATED FILTER MEDIA

by

Peter B. Merkle

Dissertation submitted to the Faculty of the
Virginia Polytechnic Institute and State University
in partial fulfillment of the requirements for the degree of
DOCTOR OF PHILOSOPHY
in
Civil Engineering

APPROVED:

William R. Knocke, Co-Chair
W. Curtis English Professor
of Civil Engineering

Daniel L. Gallagher, Co-Chair
Associate Professor
Civil Engineering

Michael F. Hochella, Jr.
Associate Professor
Geological Sciences

J. Donald Rimstidt
Professor
Geological Sciences

John C. Little
Assistant Professor
Civil Engineering

February, 1995
Blacksburg, Virginia

CHARACTERIZATION AND MODELING OF SOLUBLE MANGANESE REMOVAL FROM DRINKING WATER BY OXIDE-COATED FILTER MEDIA

by

Peter B. Merkle

Committee Chair: William R. Knocke, Ph.D., P.E.
Environmental Engineering Division
Department of Civil Engineering

(ABSTRACT)

Where $Mn^{2+}_{(aq)}$ is found in water supplies, filter media may naturally develop surface coatings bearing $MnO_{x(s)}$. These may absorb $Mn^{2+}_{(aq)}$, and in the presence of oxidant, sorbed Mn^{2+} is oxidized to $MnO_{x(s)}$, regenerating sorption capacity. The filter accomplishes $Mn^{2+}_{(aq)}$ removal, a process called the "natural greensand effect".

Characterization of naturally coated media showed variation in coating composition and structure. With thicknesses from 1 - 125 μm, primary coating constituents were Al and Mn, with incorporation of minor amounts of Fe, Cu, and Si and trace elements. "Growth ring" features in coating cross-section corresponding to compositional variation were characterized by SEM, electron microprobe, and energy-dispersive x-ray analysis (EDS). Media surface areas of 2 - 135 $m^2\ g^{-1}$ and microporosity of 15 - 533 $cm^3\ kg^{-1}$ were linearly related to extractable Mn content. Diatom remains found in coatings suggest a key role for coating deposition in filtration phenomena. Atomic force microscopy found surface self-similarity over 10 nm - 10 μm. X-ray photoelectron spectroscopy (XPS) confirmed heterogeneous surface composition including C, Al, Si, and Fe.

A method to rapidly deposit up to 4 mg g^{-1} Mn on media was developed, employing sequential batch and recycle reactors. Mn(IV) was the surface species found by XPS analysis. The Freundlich isotherm described Mn^{2+} sorption on this and the naturally coated media; sorption capacity increased between pH 6.0 and 7.5, and was reduced by $[Ca^{2+}]$ = 60 mg L^{-1}. The global Mn^{2+} oxidation rates for all coated media at pH 7.5 were 0.008 - 0.11 mg Mn^{2+} g^{-1} hr^{-1}; rates increased with flow and decreased with pH.

A numerical process model for sorption and oxidation of $Mn^{2+}_{(aq)}$ was calibrated with short bed absorber and differential reactor columns. The Freundlich isotherm, film transport, internal diffusion, and hydrodynamic dispersion were included, with sorption capacity apportioned into kinetically available and unavailable sites. The model performed well in calibration, predicting dynamic system response across a range of flow, pH, $[Ca^{2+}]$, and reactant levels. Model performance in validation was less satisfactory, probably due to experimental difficulties and the sensitivity of process performance on recent coating history and media regeneration status.

ACKNOWLEDGMENTS

This research was made possible by the patient instruction and support provided by each member of the examining committee. I thank them for their encouragement and tolerance. I thank Dr. Knocke for his diligence, and for allowing me to pursue analytical methods somewhat unfamiliar to the field of water treatment; thanks to Dr. Gallagher for accommodation of my idiosyncratic computer programming techniques. Special thanks go to Don Rimstidt, whose purchase of a surface area analyzer provided critical information about media coatings which helped me formulate the process model. I thank Mike Hochella for allowing an engineer to use very expensive and fragile scientific instrumentation, and also for the phenomenal teaching he provided in his surface science course. John Little provided important reviews and key suggestions for formulation of the mass transfer aspects of the process model. I also thank Dr. Andrea Dietrich and Dr. John Dillard serving for as interim committee members.

I would like to single out for special recognition the tireless and enthusiastic assistance of Todd Solberg, Staff Analyst, Geological Sciences Department. I am indebted to him for his selfless dedication to teaching and passion for scientific discovery that built a bridge between the disciplines of water treatment and geological analysis which many should cross in the future. The expert assistance of Dr. Jodi Junta in conducting and interpreting spectroscopic and microscopic analyses was crucial in development of a coherent picture of surface phenomena. I thank her for enthusiastic support and enlightening discussions which helped me consider many aspects of the

problem from a fundamental perspective. I would also like to thank a few of the many who provided assistance and support: Dr. John Novak, Dr. Bob Hoehn, Dr. Lucien Zelazny, Marylin Grender, Matt Higgins, Ken Carlson, Herb Evans, Chris Tadanier, Mike Robinson (for help in computer programming), Wes Geertsema, Holly Shorney, Scott Dewhirst, Andrea Crowe, Bridget Kolda, Steve Via, Amit Pramanik, Amy Eagan (for help with the validation studies), Rebecca Cuming, John Lawrence, and Jennifer Herbst.

The field studies were made possible by the valuable time and resources donated by Gerry Higgins and the staff of the Blacksburg-Christiansburg-VPI Water Treatment Facility, and by Terry Rolan, George Carter, and the accomplished staff of the City of Durham, NC Department of Water Resources. The generous hospitality (and use of the kitchen oven for baking media) of Professor Andrew Krystal of Duke University are gratefully acknowledged.

I would also like to thank Dr. Larry Swanson of the SUNY Stony Brook Waste Management Institute for wise counsel and mentorship. I acknowledge three remarkable teachers that I have been privileged to know as a student: Dr. Akira Okubo of the SUNY Marine Sciences Research Center, a true *sensei*, and Brother Romuald, C.F.X. and Steve Heibel of St. Mary's Ryken High School, Leonardtown, MD. Brother Rom has expertly taught mathematics, chemistry, computer science and physics to thousands of students, as well as coached sports for over 30 years. His dedication and vocation are responsible for guiding countless alumni. I thank Mr. Heibel for his commitment to his students.

I above all wish to acknowledge the tremendous contribution made by my wife Pamela. Her support made everything in this document possible, and I wish to apologize to her for too many long hours, late nights, and weekends in the

lab. She brought our two wonderful children into the world, Tobias Gregory Akira in February, 1993, and Bridget Eleanor in December, 1994. She endured many real hardships in order to make this dissertation a reality, and I dedicate this to her and our children, with love. The assistance and support from my family was invaluable: sincere thanks are due to Greg and Chips Merkle, George and Mary Ann Parks, Drs. Drew and Lucy Dossett, Maggie, Sarah, Katharine, Clare, and Cushie Merkle, who all gave freely of their hearts and homes.

I also wish to acknowledge the generous financial support of the late Mrs. Marion Via, whose endowment provided the opportunity to study at Virginia Tech. Additional financial support was provided by the Virginia Section of the American Water Works Association, and by the National Science Foundation through a grant awarded to Dr. Knocke and Dr. Gallagher.

To the many others who gave cultivation and friendship, my sincere thanks: Bill and Maria Dawson, Jon Wade, Teri Calleja, John Kirsch, Paul Hajian, Andy Krystal, Doug Bell, Pat Foley, Rich Potash, Peter Russo, Dale Zimmerman, Sydney and Kate Rubin, J. R. Tracy, Jeff Lobo, Dan Penney, and the great ones, Mark McQuain and Larry Wagner.

TABLE OF CONTENTS

ABSTRACT	ii
ACKNOWLEDGMENTS	iv
TABLE OF CONTENTS	vii
LIST OF TABLES	viii
LIST OF FIGURES	ix
INTRODUCTION	xv
DISSERTATION	1 - 259
VITA	260

DISSERTATION

CHAPTER 1.	CHARACTERIZATION OF FILTER MEDIA MINERAL COATINGS: IMPLICATIONS FOR FILTRATION THEORY AND PRACTICE	1
CHAPTER 2.	DEVELOPMENT OF A METHOD FOR COATING FILTER MEDIA WITH SYNTHETIC MANGANESE OXIDE	85
CHAPTER 3.	DYNAMIC PROCESS MODEL OF SOLUBLE MANGANESE REMOVAL BY OXIDE-COATED FILTER MEDIA	123
CHAPTER 4.	PRACTICAL GUIDE FOR IMPLEMENTATION OF THE NATURAL GREENSAND EFFECT	230
CHAPTER 5.	SUMMARY	245
APPENDIX I.	EFFECT OF OXYGEN ON Mn^{2+} UPTAKE BY OXIDE-COATED MEDIA	247
APPENDIX II.	MODEL CALIBRATION RESULTS	250

LIST OF TABLES

Chapter 1

1	Isoelectric points of minerals (pH_{IEP})	32
2	Treatment processes of media sample sources	33
3	Media properties	34
4	X-ray photoelectron spectroscopy Mn3s peak splitting analysis	35

Chapter 2

1	Summary of coated media analyses	109
2	Reaction conditions for samples 8 and 9	110
3	Media coating levels and surface areas	112
4	Regression analysis, Mn^{2+} oxidation studies	113

Chapter 3

1	Protocol for recycle absorber isotherm determination	165
2	Test conditions for global Mn^{2+} oxidation rate study	166
3	Protocol for short bed sorption - desorption test	167
4	Freundlich isotherm parameters for oxide-coated media	168
5	Global Mn^{2+} oxidation rate study results	169
6	Model fitting results: sorption - desorption synthetic media #2	170
7	Model fitting results: special cases, sorption - desorption	171
8	Model fitting results: continuous regeneration, steady state conditions	172
9	Model sensitivity analysis and parameter estimation	173
10	Summary of energy dispersive x-ray analyses	174

Chapter 4

1	Likely qualitative effects of dynamic conditions on filter effluent [Mn^{2+}]	242
2	Filter core analyses, Ft. Collins, CO NGE process study	243

LIST OF FIGURES

Chapter 1

1	Reflected light cross-section, Durham, NC media	36
2	Reflected light cross-section, extracted Durham, NC media	37
3	Mineral deposits on uncoated anthracite, SEM	38
4	Mineral deposits on uncoated anthracite, SEM	39
5	Ft. Collins, CO media, showing coating initiation, SEM	40
6	Blacksburg, VA media cross sections, SEM	41
7	Blacksburg, VA media surface, SEM	42
8	Lorton, VA media, SEM	43
9	Lorton, VA media surface detail, SEM	44
10	Lorton, VA media surface and cross section, SEM	45
11	Norfolk, NE media, SEM	46
12	Norfolk, NE media cross-section, SEM	47
13	Norfolk, NE authigenic media particles	48
14	Ft. Collins, CO media, SEM	49
15	Durham, NC Brown facility media (archived sample), SEM	50
16	Durham, NC Brown media (archived),surface detail, SEM	51
17	Durham, NC Brown media (archived), surface and section, SEM	52
18	Durham, NC Brown 1993 sample, pre-backwash, SEM	53
19	Durham, NC Brown 1993 sample, post-backwash, SEM	54
20	Durham, NC Brown 1993 sample, post-backwash, biological inclusions in coating	55
21	Durham, NC Brown 1993 sample, post-backwash, biological inclusions in coating	56
22	Electron microprobe transect, Durham, NC Brown coating	57
23	Electron microprobe map of Al, Mn, Fe in Durham, NC Brown coating	58
24	Water quality reported by the Durham Brown facility, 1990-93	59
25	Electron microprobe transect, Ft. Collins, CO coating	60
26	Electron microprobe map of Mn, Ft. Collins CO coating	61
27	Electron microprobe map of Cu, Lorton, VA coating	62
28	Powder x-ray diffractogram, Norfolk, NE coating	63
29	Powder x-ray diffractogram, Durham Brown coating (archive)	64
30	Powder x-ray diffractogram, synthetic $MnO_{x(s)}$ coating	65
31	X-ray photoelectron spectrum of uncoated anthracite surface	66
32	X-ray photoelectron spectrum of $MnO_{x(s)}$-coated anthracite	67
32B	Mn3s multiplet splitting, $MnO_{x(s)}$-coated anthracite	68
33	Surface area vs. extractable Mn, oxide-coated media	69
34	Micropore volume vs. extractable Mn, oxide-coated media	70
35	Surface area - pore size distributions of $MnO_{x(s)}$-bearing media	71

LIST OF FIGURES
(continued)

Chapter 1 (continued)

36	Atomic force microscopy, "shiny" anthracite surface	72
37	Atomic force microscopy, detail of "shiny" surface features	73
38	Atomic force microscopy, detail of Figure 37 surface feature	74
39	Atomic force microscopy, "dark" anthracite surface	75
40	Atomic force microscopy, detail of center region, Figure 39	76
41	Atomic force microscopy, $MnO_{x(s)}$ surface on anthracite	77
42	Atomic force microscopy, detail of "smooth" region, Figure 41	78
43	Atomic force microscopy, $MnO_{x(s)}$ surface on pebble	79
44	Atomic force microscopy, detail of Figure 43 surface features	80
45	Atomic force microscopy, Durham, NC Brown coating (archive)	81
46	Turbidity removal profile for uncoated and oxide-coated anthracite, at 1.5 hours	82
47	Turbidity removal profile for uncoated and oxide-coated anthracite, at 2.5 hours	83
48	Kaolinite particles on synthetic $MnO_{x(s)}$ coating	84

Chapter 2

1	Mineral deposits on uncoated anthracite, SEM	114
2	Synthetic $MnO_{x(s)}$ coating on anthracite, SEM	115
3	Synthetic $MnO_{x(s)}$ coating on anthracite, SEM	116
4	Blacksburg, VA media coating, SEM	117
5	Synthetic $MnO_{x(s)}$ coating on anthracite, SEM	118
6	X-ray photoelectron spectrum of uncoated anthracite surface	119
7	C1s peak region of uncoated anthracite surface	120
8	Effluent $[Mn^{2+}]$ vs. pH, sorption of Mn^{2+} by synthetically coated anthracite	121
9	Effluent $[Mn^{2+}]$ vs. pH, oxidation of Mn^{2+} by synthetically coated anthracite	122

Chapter 3

1	Recycle absorber apparatus for isotherm determination	175
2A	Reservoir $[Mn^{2+}]$ during recycle absorber tests (n=4)	176
2B	Reservoir $[Mn^{2+}]$ during recycle absorber tests for pH 6.00, pH 6.75, pH 7.50	177

LIST OF FIGURES
(continued)

Chapter 3 (continued)

3	Diagram of hypothetical mass transfer and surface interactions of $Mn^{2+}_{(aq)}$ with oxide coating	178
4	Media size distributions by sieve analysis	179
5	Column apparatus for model validation studies	180
6	Isotherm data for Mn^{2+} - synthetically coated media at pH 6.00, 6.75, 7.50	181
7	Effluent [Mn^{2+}] vs. pH, oxidation of Mn^{2+} by synthetically coated anthracite	182
8	Global Mn^{2+} oxidation rates vs. extractable Mn, coated media	183
9	Global Mn^{2+} oxidation rates vs. surface area, coated media	184
10	Global Mn^{2+} oxidation rates vs. micropore volume, coated media	185
11	Global Mn^{2+} oxidation rates vs. flow rate, showing predicted mass transfer coefficient k_f	186
12	Global Mn^{2+} oxidation rates vs. pH, showing predicted media sorption capacity	187
13	Global Mn^{2+} oxidation rates vs. [Mn^{2+}], showing predicted media sorption capacity	188
14A	Intermittent regeneration model calibration, variation of AFR (available fraction for sorption) with estimated sorption capacity	189
14B	Intermittent regeneration model calibration, RMS error vs. pH	190
14C	Intermittent regeneration model calibration, RMS error vs. flow	191
15	Intermittent regeneration model calibration, model fit for pH 7.50, 2.5 gpm ft^{-2}	192
16	Intermittent regeneration model calibration, model fit for pH 7.50, 5 gpm ft^{-2}	193
17	Intermittent regeneration model calibration, model fit for pH 7.50, 10 gpm ft^{-2}	194
18	Intermittent regeneration model calibration, model fit for pH 7.50, 5 gpm ft^{-2}, [Ca^{2+}] = 60 mg L^{-1}	195
19	Intermittent regeneration model calibration, model fit for pH 6.75, 10 gpm ft^{-2}	196
20	Intermittent regeneration model calibration, model fit for pH 6.75, 2.5 gpm ft^{-2}	197
21	Intermittent regeneration model calibration, model fit for pH 6.00, 2.5 gpm ft^{-2}	198
22	Intermittent regeneration model calibration, model fit for pH 6.00, 10 gpm ft^{-2}	199

LIST OF FIGURES
(continued)

Chapter 3 (continued)

23	Intermittent regeneration model calibration, model fit for pH 6.00, 10 gpm ft^{-2} by varying external and internal mass transfer and AFR	200
24	Intermittent regeneration model calibration, Blacksburg media, model fit for pH 7.50, 5 gpm ft^{-2}	201
25	Continuous regeneration model calibration, optimized two-parameter fit at pH 7.50, 5 gpm ft^{-2}	202
26	Continuous regeneration model calibration, predicted replicate #1 at pH 7.50, 5 gpm ft^{-2}	203
27	Continuous regeneration model calibration, predicted replicate #2 at pH 7.50, 5 gpm ft^{-2}	204
28	Continuous regeneration model calibration at pH 7.50, 2.5 gpm ft^{-2}	205
29	Continuous regeneration model calibration at pH 7.50, 10 gpm ft^{-2}	206
30	Continuous regeneration model calibration at pH 7.50, 5 gpm ft^{-2}, $[Ca^{2+}]$ = 60 mg L^{-1}	207
31	Continuous regeneration model calibration, Blacksburg media, at pH 7.50, 5 gpm ft^{-2}	208
32	Continuous regeneration model calibration, Swift Run media, at pH 7.50, 5 gpm ft^{-2}	209
33	Intermittent regeneration model sensitivity analysis for AFR	210
34	Continuous regeneration model sensitivity analysis for AFR	211
35	Continuous regeneration model sensitivity analysis for k_3	212
36	Parameter elasticities for continuous regeneration model	213
37	Validation study: Blacksburg steady state intermittent regeneration, pH 7.4, 5 gpm ft^{-2} (predicted)	214
38	Validation study: Blacksburg steady state intermittent regeneration, pH 7.4, 5 gpm ft^{-2} (best-fit)	215
39	Validation study: Blacksburg steady state intermittent regeneration, pH 7.4, 5 gpm ft^{-2}, with 0.1 mg L^{-1} free chlorine	216
40	Validation study: Blacksburg steady state continuous regeneration, pH 7.4, 9 gpm ft^{-2} (predicted)	217
41	Validation study: Blacksburg steady state continuous regeneration, pH 6.6, 9.35 gpm ft^{-2} (predicted)	218
42	Validation study: Blacksburg steady state continuous regeneration, pH 6.6, 9.35 gpm ft^{-2} (AFR = 1)	219

LIST OF FIGURES
(continued)

Chapter 3 (continued)

43	Validation study: Durham steady state intermittent regeneration, pH 6.0, 5 gpm ft^{-2} (predicted)	220
44	Validation study: Durham steady state intermittent regeneration, pH 6.0, 5 gpm ft^{-2}, 25% media regenerated initially	221
45	Validation study: Durham steady state intermittent regeneration, pH 6.0, 5 gpm ft^{-2}, 12.5% media regenerated initially	222
46	Validation study: Durham dynamic continuous regeneration, pH 6.0, 3.9 gpm ft^{-2} (predicted)	223
47	Blacksburg, VA #1 calibration media oxide coating, SEM	224
48	Blacksburg, VA #2 validation media oxide coating, SEM	225
49	Blacksburg, VA oxide coatings #1 and #2 cross section, SEM	226
50	Durham, NC validation media, SEM	227
51	Durham, NC validation media cross section, SEM	228
52	Blacksburg backwash study media cross section, SEM	229

Chapter 4

1	Filter core profiles of extractable Mn, Ft. Collins, CO study	244

Appendix I

I - A	Effluent $[Mn^{2+}]$, oxygenated and deoxygenated short-bed absorber studies at pH 7.00	249

Appendix II

II - A	Intermittent regeneration model calibration, pH 6.00, 5 gpm ft^{-2}	251
II - B	Intermittent regeneration model calibration, pH 6.75, 5 gpm ft^{-2}	252
II - C	Intermittent regeneration model calibration, pH 6.75, 5 gpm ft^{-2}, influent $[Mn^{2+}]$ = 0.33 mg L^{-1}	253
II - D	Intermittent regeneration model calibration, pH 7.50, 5 gpm ft^{-2}, influent $[Mn^{2+}]$ = 0.33 mg L^{-1}	254

LIST OF FIGURES
(continued)

Appendix II (continued)

II - E Intermittent regeneration model calibration, pH 6.75, 5 gpm ft^{-2}, $[Ca^{2+}]$ = 60 mg L^{-1} 255

II - F Intermittent regeneration model calibration, pH 6.75, 5 gpm ft^{-2}, $[Ca^{2+}]$ = 60 mg L^{-1}, influent $[Mn^{2+}]$ = 0.33 mg L^{-1} 256

II - G Intermittent regeneration model calibration, pH 7.50, 5 gpm ft^{-2}, $[Ca^{2+}]$ = 60 mg L^{-1} 257

II - H Continuous regeneration model calibration, pH 6.00, 5 gpm ft^{-2} 258

II - I Continuous regeneration model calibration, pH 6.75, 5 gpm ft^{-2} 259

INTRODUCTION

The presence of dissolved Mn^{2+} in drinking water is undesirable for several reasons: it causes bad taste, stains on laundry and plumbing fixtures, and pipe-fouling deposits. In the U.S., the initial stages of the conventional process for treating most surface waters involves chlorination of the raw water, addition of aluminum sulfate or ferric chloride as coagulant, flocculation and settling of coagulated solids, and filtration. A common filter design, the dual-media filter, is a stratified bed of graded gravel and sand overlain with a layer of anthracite coal, for a total bed depth typically less than 1 meter. If dissolved Mn^{2+} is present in the raw water, Mn-bearing mineral deposits or coatings may grow on the surface of the filter media. These deposits are known to absorb Mn^{2+}, and in the presence of free chlorine as oxidant, the coatings catalyze oxidation of sorbed Mn^{2+}, and the filters act as the treatment process for Mn removal. This phenomenon is known as the "natural greensand effect" (NGE) process. Greensand is a glauconite mineral treated with $KMnO_4$ typically used in a fixed-bed contactor to remove soluble Mn^{2+}. Process options for Mn removal include addition of strong oxidants such potassium permanganate, ozone, or chlorine dioxide to produce $MnO_{x(s)}$, followed by solid-liquid separation processes such as coagulation, settling, and filtration. However, these methods may produce undesirable colloidal $MnO_{x(s)}$ particulates which may not be efficiently removed by settling or filtration.

Oxide-coated media (OCM) perform a dual function in the NGE process, permitting two modes of operation for soluble Mn^{2+} removal. In the intermittent

regeneration mode, the OCM filter bed absorbs Mn^{2+} in the absence of a strong oxidant, with sorption capacity periodically regenerated by application of an oxidant such as free chlorine or potassium permanganate. In the continuous regeneration mode, free chlorine is continuously supplied to oxidize the sorbed Mn^{2+} to insoluble $MnO_{x(s)}$ on the coated media surface, continuously regenerating sorption capacity and maintaining catalytic function. While the NGE process is gaining acceptance for use in water treatment plants, a predictive design model is needed for engineering control and process specification. In particular, a numerical process model which can account for dynamic changes in process variables of flow rate, pH, and reactants is needed. The primary objective of this study was to formulate, calibrate, and validate in field studies such a model, based on fundamental process phenomena of mass transport, sorption, and surface-catalyzed Mn^{2+} oxidation. A secondary objective was the development of a rapid method for deposition of $MnO_{x(s)}$ on filter media, which could aid in treatment operations for soluble Mn^{2+} removal.

Three studies comprised the effort: the first study is the characterization of filter media coatings, summarized in Chapter 2, in which analytical techniques from the geological sciences were applied to fundamentally characterize the natural coating deposits on media samples from several filtration plants. The coating chemical composition and physical structure were studied to inform the modeling effort regarding relevant mass transport and surface chemical phenomena. The evident complexity of the coatings led to consideration of the role that oxide-coated media in removal of colloidal particulates (including human pathogens) in filtration, an unexpected finding of the investigation.

The second study is the method development and characterization of synthetically coated media, summarized in Chapter 3. The $MnO_{x(s)}$ deposition method was applied to anthracite and gravel media, and shows promise for ready application in filter operations, either for preparation of media at the treatment plant or as a commercial commodity. The third study is summarized in Chapter 4, which describes the model development, laboratory calibration, and field validation work. Chapter 5 is a brief practical guide for implementation and troubleshooting of the NGE process, intended for the audience of filtration process engineers. This dissertation is written as separate chapters which may be submitted for publication after minor editing; any duplication of material between Chapters is for purposes of clarity.

CHAPTER 1

CHARACTERIZATION OF FILTER MEDIA MINERAL COATINGS: IMPLICATIONS FOR FILTRATION THEORY AND PRACTICE

INTRODUCTION

This work began as an effort to fundamentally characterize filter media bearing manganese-rich deposits, commonly known as oxide-coated media (OCM). In the presence of free chlorine, OCM catalyze soluble Mn^{2+} removal from aqueous solution by the abiotic sorption and oxidation process known as the "natural greensand effect" (NGE).[1] The process is "natural" in that the coatings develop in-situ within weeks to months on new, uncoated "raw" filter media during normal filter operation; the OCM mimic the Mn^{2+} removal ability of Mn "greensand", a glauconite mineral treated with permanganate.[2] The NGE process may thus initiate and sustain itself under suitable conditions without deliberate intervention by the filtration process engineer. Since Mn^{2+} removal by oxide-coated media filtration can offer substantial economic and product quality benefits,[3] a process design model would be useful for engineered application and maintenance of the NGE. Analytical techniques from the geological sciences were applied to OCM to assist in the continued development of such a dynamic numerical process model based on fundamental chemical reactions on the media surfaces.[4]

Initial results of microscopic studies on OCM from different filter plants indicated that the coatings had physical and chemical characteristics likely to affect removal of both particulate and dissolved inorganic species. Viewed in cross section, the coatings had what appeared to be growth ring features,

possibly corresponding to compositional variation, as well as internal porosity and pronounced surface roughness. These features suggested a greater potential for improving the quality of filtered water through a better understanding of the fundamental characteristics of filter media mineral coatings. This led us to a broader consideration of the role that OCM play in the filtration process in addition to Mn^{2+} removal, as well as additional studies of uncoated anthracite and OCM from a wide variety of filter plants.

BACKGROUND

Fundamental models of filtration in natural and engineered porous media consider the interaction of ideal particles and collector surfaces as a function of surface characteristics that may vary with solution pH and ionic strength. Historical reviews of theoretical and experimental developments in this field of study are beyond the scope of this work, and excellent summaries are available from Amirtharajah[5] and O'Melia.[6] A central problem is that filtration models of colloidal particles employing classical electrical double-layer theory (EDL) often grossly under predict filtration performance under surface charge conditions unfavorable for particle-surface interaction, even in idealized systems of spherical glass beads filtering spherical latex particles.[7] The assumptions of applied EDL theory (homogeneous surface potential, spherical particles, and flat collector surfaces) have been reexamined in light of real physical and chemical surface characteristics. Recent efforts in filtration modeling have focused on more accurate representations of real surfaces and investigations of surface alteration on filtration performance.[8,9] However, these efforts have focused on

initial clean-bed filtration, before retained particles become significant in function as collector surfaces.

The modeling approach developed by Song, Johnson and Elimelech[10] involved explicit consideration of surface charge heterogeneity in EDL interaction by incorporating patchwise or random distributions of favorable particle-collector interaction sites. Their models could be fit to colloid deposition rate data over a range of ionic strength for removal of latex spheres (sulfate surface functionality) on soda-lime glass beads with trace amounts (< 1%) of chemical impurities Al_2O_3 and Fe_2O_3. At the experimental pH of 6, these impurities were considered to provide favorable deposition sites (positively charged) for removal of the latex spheres (negatively charged) relative to the bulk glass surface sites. The model could also account for changes in colloid deposition rates measured on glass beads whose surfaces were cleaned with either HCl or HCl/chromic acid solutions. The latter treatment greatly reduced deposition rates relative to the HCl wash, which was attributed to the removal of surface heterogeneity derived from organic contaminants. They concluded that surface charge heterogeneity, even on glass beads with trace impurities, was the controlling factor in colloid removal in unfavorable electrostatic conditions.

Stenkamp and Benjamin[9] examined the effects of iron oxide coatings on silica sand filter media in filtration of latex spheres and ferrihydrite particles. While the sand and latex were negatively charged near neutral pH, the coated sand and ferrihydrite were positively charged. They concluded that simple electrostatic interactions (favorable vs. unfavorable) were sufficient to generally account for differences in observed filtration efficiencies over a range of pH and ionic strength conditions for the individual media. However, the differences in

performance of the media at the same pH and ionic strength were "not as large as expected". The surfaces of both media used were microscopically rough under SEM, and the authors noted that surface roughness and chemical heterogeneity may have figured in determining relative media filtration efficiencies. The potential full-scale application of such synthetically coated filter media raises several performance-related questions that illustrate the need for information about filter media coatings in general.

Given that the positive surface charge of an iron-oxide coated media is favorable for interaction with negatively charged particles, what are the effects of sorbed organics and accumulated particles on collector efficiency? To what extent can this favorable surface be maintained over backwash cycles which could dislodge the coating? In a filter where an alum coagulant floc (near its isoelectric point) is being removed, are media surface electrostatic considerations relevant? By analogy, how important to filtration performance are natural or synthetic Mn-rich oxide media coatings which are typically negatively charged at operational pH? Since naturally-deposited oxide coatings are common in filter plants (if not ubiquitous), it would seem that some understanding of the surface heterogeneity of real media in operating filters is in order if filtration modeling is to proceed from laboratory to practice. The isoelectric pH points of some turbidity constituents and likely filter media surfaces (original or deposited) are summarized in Table 1.

Filters are subject to process conditions that may not optimize collector efficiencies. For example, the pH of filter-applied waters may be decreased below the neutral range (pH 6-8) to control the formation of disinfection byproducts, or increased well into the alkaline range to reduce the potential for

corrosion of lead and copper pipes in the distribution system. Filtration is relied upon for removal of colloidal-sized pathogens such as *Giardia lamblia* and *Cryptosporidium*, and the possibility exists that their removal may be substantially affected by process modifications designed to control inorganic and organic chemical contaminants that do not cause acute mortality in sensitive populations.

The results presented here are intended as an initial survey of the physical and surface chemical heterogeneity of filter media in actual service. They are intended to assist others in development of fundamental filtration theory on issues related to the nature and complexity of particle collector surfaces in practice, and the processes involved in the formation and behavior of oxide-coated media.

METHODS AND MATERIALS

Chemical extraction and microscopy: Filter media samples were obtained from a variety of water treatment facilities. Two types of samples were analyzed, new and stored. New samples were obtained from operating filters, placed in finished process water in headspace-free containers, and shipped to Virginia Tech for immediate analysis. Stored samples were media that had been collected and archived dry in sealed containers prior to this work. Descriptions of the sample types and process conditions at the various plants are given in Table 2.

For determination of extractable Mn content, replicate media samples were extracted in acidified hydroxyl amine sulfate solution, and 0.2 μm-filtered extracts were analyzed for Mn by flame atomic absorption. Results were

expressed on the basis of total surface extractable Mn content per unit weight of filter media. For scanning electron microscope (SEM) analysis of the media surfaces, samples were dried in air, glue mounted and carbon-coated by vacuum electric arc to a thickness of at least 250 Å. Cross-section samples for SEM and reflected light microscopy were embedded in epoxy, ground, polished, and carbon-coated.[11] Standardless qualitative elemental analysis was performed with an hnu™ energy dispersive x-ray spectrometer system (EDS) attached to a Cameca Series 2 SEM.[12]

Electron microprobe analysis (EPMA): Cross-section maps of elemental abundances in Durham, NC, Lorton, VA and Ft. Collins, CO media coatings were obtained with a Cameca SX-50 scanning electron microprobe using internal mineral standards.[13] Cross section samples of Durham and Ft. Collins coatings were analyzed in transect for Mn, Al, and Fe at 1 μm^2 resolution with accelerating voltage of 15 KeV at 20 nÅ beam current.

Powder x-ray diffraction: Diffraction patterns were obtained for four oxide-coated anthracite media, three with "natural" coatings (Norfolk NE, Durham NC, and Lorton VA) and one with a synthetic coating. The synthetically coated media was prepared by a rapid MnO_X deposition method, described elsewhere in detail.[14] Oxide coatings were detached from 5 g samples of coated media by sonication for 15 seconds in ethanol. Powder residues were rinsed in distilled water, air dried and mounted on glass slides. All x-ray diffractograms were taken with a Scintag Powder X-ray Diffractometer using the Scintag Diffraction Management System computer software.[15] Due to low signal intensities, five scans of the synthetic sample were added together to obtain a pattern for analysis. Pattern identification by automated search of the

JCPDS database[16] was unsuccessful; candidate patterns were found by a manual search of likely minerals, based on the EDS identifications of primary coating constituents Mn and Al, and the media substrate materials sand and anthracite.

X-ray photoelectron spectroscopy (XPS): A detailed description of this analytical technique is not possible here; an excellent review of XPS theory and application is available from Hochella.[17] In simplest terms, a sample is irradiated with x-rays of a narrow energy distribution, ejecting electrons from the sample surface. The kinetic energy spectrum of the electrons is recorded and converted to a binding energy scale. The energies and shapes of spectral peaks are characteristic of electron orbital states and interatomic bonding environments in the outer atomic layers of the sample. Analyses were conducted with a Perkin Elmer Model 5400 XPS instrument, using 400 W MgKα or AlKα x-rays. Single grains of raw and synthetically-coated anthracite were mounted with conductive graphite paste (DAG) on solvent-cleaned steel mounts. The samples were briefly outgassed in the sample introduction vacuum lock until the vacuum became stable. Five-minute survey scans of electron binding energies from 0 to 1200 eV were taken, and automatic peak identification was used where possible. Spectra recorded were unshifted relative to absolute binding energies. The C1s peak of raw anthracite was found at 285.04 eV, slightly higher than the reference value for adventitious carbon of 284.9 eV. Narrow scans of Mn3s peak multiplet splitting were used to determine the Mn oxidation state of the outer atomic layers by automated curve fitting.[18,19]

Surface area and internal porosity: Surface areas of selected samples were obtained by automated cryogenic N_2 adsorption using Quantasorb NOVA

1000 instruments at Virginia Tech and the Quantachrome Corporation. This microprocessor controlled instrument performs automated surface area, pore size and pore size distribution measurements according to user-specified protocol.[20] Prior to analyses, coated media samples were outgassed under vacuum at 80 °C for at least 45 minutes. Single point and five-point BET surface area were measured by the following protocol: from calculated atmospheric pressure P_0, N_2 adsorption was measured in 0.05 relative pressure increments from P = 0.10 to 0.30 P_0, with the single point BET measurement taken at 0.30 P_0. Pressure was then increased to 0.90 P_0, and pore size distribution calculated by the Barrett, Joyner, and Halenda (BJH) method from the desorption isotherm at 11 points spanning the range from 0.875 to 0.10 P_0.[21]

Atomic force microscopy: Media were examined by atomic force microscopy (Digital Instruments Nanoscope III AFM), and the images analyzed by the accompanying image processing software to obtain surface topographic maps and estimates of surface roughness.[22] This technique detects features of surfaces from the microcrystalline to near-atomic scale, and may operate on a surface undergoing alteration in solution.[19] Since AFM is a relatively new technique, its application and the interpretation of results is not routine; to our knowledge, these were the first such analyses of filter media. This technique works by scanning a microscopic Si_3N_4 tip across a surface. The tip is mounted upon or integral with a cantilever which is moved by a piezoelectric crystal stage capable of motion increments of angstrom precision. A laser reflects from the cantilever to a photodiode array, and cantilever deflections from a complete raster scan are combined to produce a topographic relief image. The samples

were scanned in deflection mode, with the tip touching with a force of 10^{-7} to 10^{-8} N, using a 200 μm, wide-legged cantilever.

Particle identification in filtration performance: A method development study was done of turbidity removal by raw and synthetically coated (1 mg g^{-1} Mn) anthracite media. Columns (4 cm inner diameter) were packed to a depth of 10" and washed with distilled water until effluent and mid-column turbidities were below 0.05 NTU. A stirred reservoir solution of 1.25 mg L^{-1} kaolinite, 10^{-3} M HCO_3^-, and 10 mg L^{-1} Ca^{2+} at pH 7.0 was applied at 2 gpm ft^{-2}; influent turbidity was approximately 1 NTU. Turbidity vs. media depth samples were taken at 1.5 hours and measured immediately by nephelometer. Kaolinite particles were located and identified on the coated media using the SEM in backscattered electron mode (BSE), and by EDS analysis. In BSE images, the kaolinite particles appeared dark on the bright background of $MnO_{x(s)}$, and the Al:Si ratio 1:1 was confirmed by EDS, consistent with the kaolinite composition of $Al_2Si_2O_5(OH)_4$.

RESULTS AND DISCUSSION

Chemical extraction and microscopy: The effect of the chemical extraction process is illustrated in Figures 1 and 2, respectively the pre- and post-extraction reflected light images of the Durham, NC Brown plant media in cross section. In Fig. 1, the white rectangular areas are anthracite, and the dark encapsulating rings are mineral coating, approximately 75 - 125 μm thick. After extraction, the media surface is thoroughly cleaned of deposits. The chemical extraction results of selected media are summarized in Table 3. Only a trace amount of extractable Mn^{2+} is found on the raw anthracite media originally

placed in the Blacksburg, VA filters. The Mn content of synthetically-coated media is similar to that of a commercial greensand. The naturally-coated media show a wide range of coating levels, from 0.8 to 95 mg g^{-1}, consistent with the prior survey of Knocke *et al.*[1]

Electron microscopy of raw anthracite found a variety of surficial mineral deposits, as well as fine layered bands in the grain interiors. In the BSE imaging mode, mineral deposits associated with anthracite show up as bright features, corresponding to higher relative nuclear density, from which x-ray spectra (EDS) may be obtained for elemental identification. In the following discussion, the elements indicated as being associated with specific mineral deposits were detected by EDS. Since the standardless EDS technique analyzes a volume extending several microns below the surface, the atomic ratios of surface coatings are only estimated, since subsurface signal effects may be present.

The uncoated anthracite surface is shown in Figures 3 and 4. The surface appears uniform under low magnification (Fig. 3a), but higher magnification shows numerous embedded particles below 10 μm diameter (Fig 3b). The EDS spectra of these particles indicated that Al and Si were the primary constituents, natural components of the mined coal deposit. Other surface features contained Fe and S (Fig. 4a), possibly a microcrystalline pyrite. Patches of Fe-rich deposits are also common (Fig. 4b), occasionally visible to the naked eye as iron rust flecks on the grains.

The SEM analysis also provides evidence for a mechanism for initiation of the natural coatings on new anthracite filter media. The cross section BSE images of the Ft. Collins media show the fine, layered internal heterogeneous mineral deposits commonly present in all anthracite samples studied. These are

most apparent at the upper left and center of Fig. 5a. A typical layer consists primarily of Al and Si, with Fe, S, and Mn sometimes found. This sample has a sparse coating (Mn, 0.8 mg g^{-1}); it was obtained from the filter after only a few weeks after the seasonal Mn^{2+} problem began, in August 1994. The Mn-rich coating is visible as a thin bright line on the grain at the center of Fig. 5a. To its right, a very thick deposit can be seen, predominantly Ca and Al. A media grain from a sample taken in November 1994 shows a linear arrangement of individual mineral deposits on the surface (Fig. 5b), suggesting that exposed mineral layers provide nucleation sites for growth of coating by Mn^{2+} sorption and subsequent oxidation.

The Blacksburg media (Fig. 6 a,b) show internal mineral deposits as well as a layered external coating (25 - 40 μm) consisting of Al, Mn and Si. The typical grain is nearly uniformly encapsulated. The "broken pavement" appearance of Fig. 7a is probably an artifact of sample preparation induced by rapid drying and heating during carbon coating. The recessed area at the lower right of Fig. 7a shows interesting detail at higher magnification (Fig. 7b). To the left is a mineral deposit with a bactroidal structure indicating diffusion-limited growth in this surface depression. At right is a region of sparse growth on exposed anthracite where the fine, banded mineral layers intersect the surface.

The Lorton, VA media also have internal mineral deposits and a layered coating (Fig. 8), but this coating has a porous structure, unlike the Blacksburg media, and the surface coverage is not as uniform. The surface is very rough at the scale of 30 - 100 μm (Fig. 9), with irregular, columnar growths. At high magnification (Fig. 10a), the porosity appears to result from agglomerated or actively growing particle clusters. The Lorton cross section BSE (Fig 10b)

shows compositional variation as well. The Mn:Al atomic ratio in the central bright band is 1.45, but only 0.43 in the outermost solid band at bottom right, as determined by EDS.

Coated media from the Norfolk, NE facility have a Mn-rich phase covering both anthracite (Fig. 11a) and sand (Fig. 11b and 12a), with trace amounts of Fe and Si. The BSE cross section of the 1 mm diameter sand coating (Fig. 12b) shows a banded brightness variation within the Mn-rich phase; EDS analysis indicated that Al, Ca, Fe and Si are enriched relative to Mn in the dark bands. This variation may result from the Norfolk treatment plant practice of switching between well field sources of different chemistry, or some other regular fluctuation in process conditions. On the top layer of these filters, an unusual layer of authigenic particles was found (Fig. 13). These have a yellow-white exterior shell rich in Ca surrounding a dark brown to black internal deposit of fine Mn-rich particulates, and apparently formed in place without a media core.

The Ft. Collins, CO samples show a typical surface oxide deposit (Fig. 14a). Some grains are completely coated, while others appear to be in the process of being encapsulated as individual growths merge into a complete coating. A thin coating is visible on a sample taken in early October (extractable Mn, 1.5 mg g^{-1}), two months after elevated Mn^{2+} levels began to appear in the raw water source, with Mn:Al of 3.3 (Fig. 14b).

The most abundant oxide coatings found were on the Durham, NC anthracite media from the Brown plant (Figs. 15 to 17), where the NGE process is an integral part of filter operations.[23] The anthracite surface is completely buried under the oxide deposit (Fig. 15a), and internal mineral deposits are present as well (Fig 15b). The cracks visible may result from the sample

preparation process, as previously discussed. The exposed, outer surface and internal coating structures are shown in Fig. 16, with some layering visible in the exposed cracks. In cross section (Fig. 17a), the coating has alternating layers of solid phase interspersed with porous layers, with a varying composition across the 120 μm thickness. The outermost surface is comparatively smooth; a media sample taken immediately before filter backwash has a porous microstructure at the outer surface (Fig. 17b).

Samples of Durham Brown treatment plant media taken before and after filter backwash show markedly different surface features. The "before backwash" media ("BBW", Fig. 18 a, b) is uniformly coated with a layer of particles a few microns in diameter, apparently cemented or growing on an underlying base coating. The Mn:Al ratio of BBW particles by EDS was 1:1. The "after backwash" media ("ABW", Fig. 19 a, b) show a surface with detached coating sections, and largely cleaned of the surface attached particles. The underlying base coating has a Mn:Al ratio of 1.8:1, and is slightly enriched in Fe. Surface area analysis and HAS extraction confirmed physical and chemical alteration by backwash, with Mn content decreasing by 35%, and surface area by 38% (Table 3). This set of media samples were taken in 1993 from filter beds that had been in place for less than five years, in contrast to the archived sample (75 mg g^{-1}) analyzed from an older filter installation at the Brown plant, which had been in use since at least 1979.

Diatom casts were found associated with the mineral coating of the post-backwash Durham Brown filter media (Fig. 20 and 21). Some of the casts appear embedded and cemented to the surface across fractures, indicating that they are securely attached. Bacterially-generated Mn oxide formations were not

obvious in several coated media examined by SEM, although Mn-oxidizing bacteria are common in surface waters.[24] If they reached the filter, the free chlorine residual may have killed them, or insufficient nutrients prevented sustained bacterial growth. If they were present in any capacity, it is possible that the inorganic Mn oxidation process may be catalyzed on the bacterial shell, encasing the structure and making it unrecognizable as a biogenic-based oxide.

Electron microprobe analysis (EPMA): The EPMA transect analysis of the Durham coating (Fig. 22) shows cyclic variation in elemental abundance. Areal maps of the coating section (Fig. 23) show variation in Al, Mn and Fe as changes in brightness, (brighter areas corresponding to higher elemental abundance). Process and water quality data reported by the Durham plant over a three year period (Fig. 24) also show cyclic changes in raw water turbidity, Mn^{2+} and residual aluminum in finished water. The time period for this data (1990 - 1992) is not the period during which the coating analyzed was deposited, but the dynamics are representative of typical annual variations in process conditions. Plant personnel reported that they usually increase coagulant dose in response to turbidity increases, and that elevated Mn^{2+} typically occurs during low turbidity conditions. This process management information is reported here as received by the author: the accuracy of the plant personnel observations and their correspondence with the true dynamics of source water quality are not known. It should be noted that this facility recycles filter backwash water, and the reader is directed to the study of Cornwell *et al.*[25] for additional information regarding the impacts of filter backwash recycling on water quality. Both plant personnel and process records provide evidence for a seasonal variation in influent Mn^{2+}, turbidity, and alum coagulant dose.

Whether or not these variations cause the observed compositional variation in the media coating is not known. Fundamental principles of mineral surface geochemistry are not inconsistent with variations in solution chemistry causing (by unknown mechanisms) a variation in a coexisting solid phase. The archived sample analyzed was not placed into the filter under conditions controlled for experimental determination of coating origin. Its date of installation and subsequent sampling are unknown, and detailed information is lacking regarding its chemical (pH, $[Mn^{2+}]$, etc.) and physical history (depth in filter, number of backwash cycles). Therefore, the analysis presented is for descriptive purposes only, not as experimental evidence supporting any hypothesis. All comments made here regarding this and similar analyses are conjecture when referring to any causal relation between coating variation, process conditions, and deposition mechanism.

The EPMA transect of the late November 1994 Ft. Collins sample shows a progressive enrichment in Mn from the media surface (Fig. 25), with trace amounts of Fe throughout. The map of the transect region for Mn shows this enrichment (Fig. 26, media surface at left). The Lorton media contain Cu (0.1 mg g^{-1}) in addition to Al and Mn.[14] The Lorton EPMA map (Fig. 27) shows Cu disseminated throughout the coating, probably derived from copper-containing algicides used for reservoir management.

The variations in the three samples may be caused by any of several processes, but without knowing exactly how long it took to deposit the coatings, it is difficult to single out one mechanism. Physical incorporation of particulates (natural turbidity and alum flocs) which vary in composition is one possible process, and simultaneous chemical incorporation of several inorganic species

by sorption or precipitation is also likely. Since filter backwashing dislodges portions of the coating from the media, the patterns preserved are the likely a net result of deposition and removal processes, further complicating interpretation of transect analyses. Whatever the mechanisms responsible, intra-coating compositional variation appears to be a common feature of oxide-coated media, as evidenced by the SEM/BSE and EPMA analyses.

Powder x-ray diffraction: Considering the chemical environment of filter media in service, the most likely mineral forms in natural media coatings are hydrous Mn and Al oxides. Again, both of these mineral forms may accumulate through capture of alum coagulant flocs and Al and Mn-bearing particulates such as clay minerals, or they may form through Mn^{2+} sorption and oxidation with incorporation of soluble and/or particulate Al. Precipitation of $Al(OH)_{3(s)}$ is possible due to the passage of water supersaturated with respect to this phase through the filter. The coating powder samples were also visibly contaminated with media particles (sand and anthracite) dislodged during sonication.

The x-ray diffractograms of the naturally-coated media do not definitively identify a coating mineral phase. The extremely poor peak resolution (peak broadening) is most probably caused by small particle size and lack of crystallinity. Hydrous Mn oxyhydroxides are typically x-ray amorphous, with mixed Mn oxidation states common.[26] However, similarities between the Durham and Norfolk samples suggest that aluminum manganese oxide hydrate ($Al_5Mn_{13}O_{28}\cdot 8H_2O$) may be present in their coatings. In the Norfolk pattern, four broad peaks (A, B, C, and D in Fig. 28) match this phase. A strong peak (E) matches manganese oxide hydrate ($Mn_7O_{13}\cdot 5H_2O$, see Fig. 30 for its pattern), and two other characteristic peaks of this phase (if present) would be obscured

in the broad C peak region, but no other peaks definitely confirm this phase. The Durham pattern (Fig. 29) has three broad peaks of the aluminum manganese oxide hydrate pattern (B, C, and D) but the 100% peak at 9 Å is missing. The synthetic coating pattern is also indeterminate for any specific phase (Fig. 30), but one feature is consistent with the presence of poorly crystalline and hydrous Mn oxides. The two small, broad peaks between 35 and 38 Å are in the region where strong peaks from synthetic and natural MnO_2 and MnOOH are found.

X-ray photoelectron spectroscopy (XPS): The XPS scan of raw anthracite (Fig. 31) shows minor quantities of Al, Si, and Fe in addition to the expected bulk C and O composition; this finding is consistent with SEM/EDX studies finding submicron aluminosilicate particles, Fe oxide and sulfides. This confirms that the anthracite media present a notably heterogeneous surface chemical environment. The scan of a synthetically-coated anthracite (Fig. 32A) shows Mn and O signatures predominating, consistent with near-complete coverage of the underlying carbon-rich anthracite surface by manganese oxides. The patchwise model of electrostatic surface potential[10] is supported by these analyses, although spatial resolution is not achieved by this XPS instrument. Another analysis technique may be applicable, Auger electron spectroscopy (AES), which can achieve lateral resolution of 0.05 μm for mapping of surface heterogeneity.[17] The Mn3s multiplet peak splitting is shown in Figure 32B, and Table 4 summarizes the analysis. The peak splitting of 4.75 eV and peak area ratio of 1.74 determined for this sample indicate that Mn(IV) is present in the outer atomic layers of this sample, based on analyses reported by Oku,[27] Murray *et al.*[18], and Junta and Hochella[19].

Surface area and internal porosity: Specific surface areas of anthracite-based media are considerably higher than the estimated nominal geometric area of 0.0038 $m^2\ g^{-1}$, calculated by assuming a density of 1.59 g cm^{-3} and particle diameter of 1 mm (Table 3). The surface areas of synthetically-coated and plant media increase with the amount of Mn-oxide coating (Fig. 33), as does the specific micropore volume (Fig. 34). The surface area characteristics of the coatings seem to be similar, despite the wide variety in origins. The pore size distributions (Fig 35) of coated media show that the majority of surface area is associated with micropores less than 70 Å in diameter. The mean surface areas of before- and after-backwash samples (BBW and ABW, respectively) from the Durham Brown plant 1993 sampling were significantly different by two sample t-test ($p=0.039$), assuming equal sample variances.

The surface area properties of filter media are important in several respects. Sorption of Mn^{2+} (and other solutes) at surface sites is the most likely removal mechanism, so any change in sorptive surface area will affect process performance. However, the availability of sites in the entire coating will determine how rapidly the coating approaches sorptive equilibrium. If the majority of surface area is associated with micropores, the internal mass transport mechanism (pore and/or surface diffusion) would be significant in sorption kinetics. External mass transport would then be driven by the concentration difference between the pool of outermost, kinetically available surface sites and the bulk fluid.[28] Also, the micropore solution chemistry pH may differ substantially from that of the external fluid if Mn^{2+} sorption is coupled with proton release, further complicating the development of a fundamental

mechanistic model of Mn^{2+} uptake. In the presence of free chlorine, the sorption of Mn^{2+} is coupled with oxidation at a surface site. If the oxidation reaction is rapid compared to both external and internal transport kinetics, only the outermost, available sites on the coating will be active in sorption and site regeneration by oxidation catalysis. Laboratory column studies of both the sorption and oxidation modes of the NGE process suggest that a portion of sorption sites are kinetically unavailable, depending on chemical and physical system conditions.[14]

In the interception and retention of particulates, surface roughness enhances the transport of non-Brownian particles to interceptor surfaces by disrupting the laminar sublayer. Since some pathogenic organisms fall into this category, a physical understanding of the surfaces with which they associate is of interest. The physical processes involved in particle interception and retention by media with increased surface area are of interest, even if roughness-enhanced bulk fluid to surface mass transport is ignored. For all particles, greater exterior surface area increases the effective collector area for attachment at the media surface. The physical interactions of both Brownian and non-Brownian particles with surface features of similar physical scale may be significant, especially if the surface is undergoing active mineral deposition.

The encapsulation of otherwise reversibly-attached particulates in a coating is evident at the scale of a few microns. For Brownian particles such as viruses, encapsulation on exterior surfaces is probably very significant, even if the viruses are primarily associated with larger particulates. Brownian particles that have diffused into micropores would be trapped by any closure of micropores due to coating overgrowth. Surface roughness also provides

crevices and pits of the same size range as intermediate-sized particles which are inefficiently removed by either sedimentation or diffusion. In this case, enhanced transport due to roughness may bring such a particle into the neighborhood of a physical structure that may entrap it into a more secure attachment by a surface "straining" mechanism.

The impact of backwashing on surface physical characteristics (and related chemical properties) may contribute to differences in filter performance. The samples studied showed marked changes in surface topography and surface area as a result of backwashing. This suggests that external and internal mass transport processes and total sorption capacity for Mn^{2+} and other solutes are affected by changes in the coating caused by backwash. The degree to which backwash is effective in removing mineral deposits and how these deposits contributed to pre-backwash filtration efficiency is likely of primary interest in modeling filtration performance from first principles. The EDS analyses also suggest that the newly exposed coating surface may often be different in chemical composition from the shed surfaces, bringing into question how media surface chemistry (and particle removal) may change as a result of a physical filter operation such as backwash. The effects of these changes in comparison to process efficiency effects caused by retained flocs and particulates acting as collector surfaces is a valid question. However, since the Mn^{2+} removal process can remain viable throughout the entire backwash and filter cycle (if backwash does not entirely remove the coating), the surface activity of persistent mineral deposits appears to be continuous.

Atomic force microscopy: Atomic force microscopy was conducted on uncoated and synthetically-coated anthracite, coated gravel, and the Durham coated anthracite. Artifacts caused by irregular tip shape may be present in AFM images, especially on surfaces as microscopically rough as those examined here. Potential artifacts can be identified by scanning the same area twice, with a 90° change in scanning direction. This orthogonal scanning "quality control" technique was used to screen the images presented here for gross tip artifacts, which were not readily identifiable.

The results presented here should be evaluated in the context of methodological development, as initial attempts to apply this new technology to filter media surfaces, and not as definitive AFM characterizations. Although the technique merely provides an approximate physical map of a surface, this physical data, especially at the submicron scale, can inform the conceptual framework of surfaces as particle collectors in filters. The rationale for using AFM to characterize microtopography of media surfaces proceeds from the need to better understand the nature of such surfaces on the physical level. The classical Gouy-Chapman and Stern models of the electrically-charged interface in solution assume infinite, flat homogenous surfaces.[29] The limitations imposed by these assumptions are obvious, since heterogeneous composition and surface irregularity are the norm for most real environmental surfaces. For modeling of sorption, one question which AFM can address is how irregular these surfaces are at the length scale of hydrated ions and the electrical double layer (1 - 10 nm), and how this irregularity can be parameterized in fundamental theory.[29] Also, if characteristic crystal morphologies are present, these might be identifiable, delineating specific surface chemical reactions.

On visual inspection, raw anthracite grains typically present two different types of surface. One is a smooth region which is shiny and lustrous, resembling a cleavage plane. The other type of surface is a rough, irregular area which appears dark. The AFM image of the shiny region (Fig. 36) shows that over a 25 μm^2 area, most of the surface is generally flat, with vertical relief of about 1% (50 nm), with indications of transverse striations. These striations may correspond to the typical mineral banding seen in the cross section BSE image of Fig. 6. Comparatively large and prominent surface inclusions are present (resembling the aluminosilicate particles seen by SEM). A 0.36 μm^2 scan of the flat region shows the striations in detail (Fig. 37), which resemble narrow grooves (about 20 nm wide) in a rough surface, with general relief of at least 4% (32 nm) across the 600 nm traverse. Over a 250 nm traverse (Fig. 38), a single depression less than 75 nm wide has a depth of at least 25 nm. This feature and others like it may be pore openings, but the AFM tip cannot penetrate to map the internal structure. The irregular, dark region of the raw anthracite has more surface relief than the shiny region at the micron scale, about 2% over a 1.25 μm traverse (Fig. 39). The central region of this image is shown in Fig. 40 over a 500 nm scan, and the relief at this smaller scale is comparable.

The surface of the synthetically-coated anthracite also features two types of regions, smooth and rough. A 100 μm^2 scan (Fig. 41) shows these, a relatively planar region bounded by cracks and surface clumps of $MnO_{x(s)}$. Over a smaller region (Fig. 42), the details of the coating surface emerge as rounded bumps and ridges on the scale of 50 - 100 nm. The coated pebble surface was more uniform than the anthracite, with submicron particles forming

an encapsulating layer, with relief of more than 12% (750 nm) over a 6.25 μm scan (Fig. 43). At a very small scale (Fig. 44), 10 nm diameter features can be seen in a formation at center. The image of a "smooth" region of a Durham coated media surface (Fig. 45) shows relief of about 20 nm, or about 125 - 250 ionic radii for Mn(II-IV) across the 186 nm scan width.

Same-scale AFM images of the raw anthracite grain and the synthetically coated pebble were analyzed for surface roughness parameters by two techniques included in the Nanoscope III software: scaled fractal dimension (f_d), and root-mean-square roughness (rms) by ASTM method E 42.14 for STM/AFM.[22] The raw anthracite region studied had a scaled f_d value of 2.02 (for an ideal planar surface, f_d = 2.0) and rms of 12.4 nm, while the coated pebble f_d was 2.16, with rms of 41.8 nm. The latter two AFM images would correspond to areas about 1 millionth of the entire grain surface, which poses some difficulty in determining what constitutes a "representative sample" by AFM, but the surfaces shown here appeared representative, based on evaluation of several dozen samples by AFM and SEM. These roughness parameters are subject to the influence of the tip artifacts mentioned previously, but by using the same tip, similar sample areas, and the aforementioned "quality control" of the images, these errors may be minimized.

The features identified by AFM indicate that filter media surfaces exhibit significant topographical relief over length scales of 10 nm to 10 μm. Some features are similar to cracks, pits, and trenches. At the smallest size range, the microtopography is on the same order as the estimated thickness of the Gouy-Chapman electrical double layer, or 2.8 to 11.2 nm for solution ionic strengths of 0.01 and 0.001 M, respectively. The solute mass transport enhancement (bulk

fluid to surface) provided by roughened surfaces is well documented,[30] and these coated media qualify in that respect. Although AFM is typically applied to near atomically-flat crystalline cleavage planes, it appears from this initial study that it could be applied to these rougher natural surfaces, possibly in reactive solutions to observe surface alterations.[19]

Particle identification in filtration performance: The turbidity profiles (ratio of influent to sample, C/C_0) at both 1.5 and 2.5 hours show enhanced turbidity removal for the coated media column (Fig. 46 and 47). While the absolute removal difference in nephelometric turbidity units (NTU) was slight over this depth (0.1 NTU), the beneficial effect of the coating is apparent, consistent with previous studies of enhanced particle removal by rough media.[5] The profiles grow closer together with time, also consistent with the retained kaolinite obscuring the original particle surfaces, and becoming the effective filtration surface. The kaolinite particles could be identified on the media by combined SEM/BSE/EDS analysis. Typically, these particles were lodged or attached in the roughest coated areas of the filter grains. Similar in size and shape to adjacent Mn oxide particles, the kaolinite is indistinguishable by SEM (Fig 48a). The simultaneous BSE image (Fig 50b) shows the lighter atomic weight aluminosilicate particles as darker spots on the brighter background of Mn oxide (Mn:Al, 16:1) The Al:Si ratio of the dark particles was 1:1, consistent with kaolinite composition, $Al_2Si_2O_5(OH)_4$. This technique of discriminating retained "natural" particles from background mineral deposits could be adapted to characterize particle collection efficiencies in systems of filter media and turbidity components of heterogeneous composition.

CONCLUSIONS

Oxide-coated media from a variety of sources were studied as part of an effort to develop a process engineering model of the natural greensand effect process. These descriptive studies indicate that the physical and chemical characteristics of $MnO_{x(s)}$-bearing coatings and other surface mineral deposits may be of central importance for a variety of filtration phenomena, and thus have direct implications for several aspects of drinking water quality. The analytical techniques originally developed for study of geologic materials may be useful tools for development and evaluation of fundamental filtration theory and filter surface chemistry models. The studies suggest that a filter grain, considered as a particle collector, presents surface characteristics that may be physically, electrically, and chemically heterogeneous and variable in time, and the extent of variability challenges current understanding and capability in predictive modeling of filtration processes. It should be emphasized that the specific chemical conditions of water treatment processes employing filtration are almost invariably site-specific and unique, and coated filter media surfaces are very likely as variable in certain important respects. However, common characteristics are apparent in the coated media studied here which support the idea that similar descriptive studies may prove useful in understanding filtration phenomena of importance under real treatment plant conditions.

The results of these studies indicate the following:

1) Microscopic imaging of filter media surfaces is informative and useful, especially when coupled with energy dispersive x-ray analysis (EDS). The surface roughness features and retained particulates observed suggest a key role for coating formation in particle interception, attachment, and retention over

backwash cycles. With further development, an analytical technique used here (employing SEM coupled with EDS) may prove useful for direct observation of particle attachment under different solution and surface chemistry conditions. Particle interception and retention in a filter actively depositing a mineral coating may involve processes such as surface "straining" and encapsulation by cementation, in addition to enhanced near-surface hydrodynamic turbulence. Filter backwashing may alter both the physical and surface chemical properties of coated media.

2) The new technique of atomic force microscopy (AFM) may prove especially useful for imaging oxide coating surfaces at submicron length scales characteristic of viral and microbial contaminants. AFM also provides the capability to image surfaces in solution, which could be applied to describe submicron surface alteration in the reactive aqueous solutions which are apparently characteristic of filter-applied water.

3) The heterogeneous mineral deposits appear to be archival records, preserving the dynamics of coating growth and filtered water composition over extended time periods. The outermost, growing surfaces of coated media studied have apparently undergone nearly continuous chemical and physical alteration, incorporating inorganic species such as Al, Fe, Ca, and Cu. The technique of electron probe microanalysis (EPMA) is especially well-suited to describing cross-sectional variation in the coatings, which may provide new information on process phenomena and historical inorganic contaminants.

4) X-ray photoelectron spectroscopy may be used to describe the surface atomic structure and chemical bonding of filter media coatings. This technique

may be useful in fundamental studies of the surface complexation phenomena, reactivity, and heterogeneity of coated media in practice.

5) Physical characterization of coating surface area and pore structure by N_2 adsorption indicates that the interactions of coated media and inorganic solutes may parallel those of granular activated carbon and organic solutes in certain respects. Process phenomena common to both systems may include isotherm behavior, external and internal transport phenomena, background solute interference, and the importance of the chemical and physical "history" of the media. This suggests that modeling of inorganic solute interactions with oxide coatings may be analogous in some fashion to modeling of GAC performance.

Filter media mineral coatings (natural and synthetic) show the potential for removal of a variety of soluble inorganic species of regulatory concern through control of both solution and media surface chemistry. A broad range of unintended and possibly unknown improvements in filtered water quality may result from application of the natural greensand effect. These benefits may be provided in the absence of engineering control in filter plants where the NGE occurs. Compliance with currently anticipated U.S. Federal drinking water regulations may require significant re-design of many water treatment facilities. This work suggests that it may be prudent to understand the existing role which OCM play in determining finished water quality at a given installation, and the degree to which process changes may impair any beneficial functions of the surface mineral deposits.

ACKNOWLEDGMENTS

The authors thank the students, staff and faculty of the Department of Geological Sciences at Virginia Tech for their invaluable assistance: Dr. Jodi Junta, Mr. Udo Becker, Dr. Mike Hochella, Dr. J. Donald Rimstidt. Special thanks to Todd Solberg for patient instruction and assistance, and for conducting the microprobe and x-ray diffraction analyses.

LITERATURE CITED

1 - Knocke, W. R.; Occiano, S.; Hungate, R. Removal of Soluble Manganese from Water by Oxide-Coated Filter Media **1990**, AWWA Research Foundation, Denver, Colorado.

2 - McGhee, T. J. Water Supply and Sewerage **1991**, McGraw-Hill, New York.

3 - Byerly, G. P. "Oxide-coated media aids in manganese control", *AWWA MainStream* **1994** (May), American Water Works Association, Denver, Colorado.

4 - Coffey, B. M.; Gallagher, D. L.; Knocke, W. R. "Modeling Soluble Manganese Removal by Oxide-Coated Filter Media", Journal of the Environmental Engineering Division - ASCE **1993** (119:4), 679.

5 - Amirtharajah, Appiah. "Some Theoretical and Conceptual Views of Filtration", J. AWWA **1988** (80:12), 36-46.

6 - O'Melia, C. R. "Kinetics of Colloid Chemical Processes in Aquatic Systems", in Aquatic Chemical Kinetics, W. Stumm, Ed. **1990**, John Wiley & Sons, U.S.A.

7 - Tobiason, J. E., O'Melia, C. R. "Physicochemical Aspects of Particle Removal in Depth Filtration", J. AWWA **1988** (80:12), 54-64.

8 - Tien, C.; Gimbel, R. "On the Development of a comprehensive Model of Deep Bed Filtration", in Proceedings of the Symposium on Water Filtration, **1982** European Federation of Chem. Eng., Antwerp, Belgium.

9 - Stenkamp, V. S., Benjamin, M. M. "Effect of Iron Oxide Coating on Sand Filtration", J. AWWA **1994** (86:8), 37-50.

10 - Song, L.; Johnson, P. R.; Elimelech, M. "Kinetics of Colloid Deposition onto Heterogeneously Charged Surfaces in Porous Media", Environ. Sci. Technol. **1994** (28:6), 1164-1171.

11 - Buehler Limited. "Petrographic Sample Preparation", Metal Digest® **1973** (12/13:1), Evanston, IL.

12 - Chalker, C. P. "Characterization of coatings and interfaces" in Advanced Surface Coatings: a Handbook of Surface Engineering **1991**, A. Matthews and D. Rickerby, Eds., Blackie & Son, Ltd, London.

13 - Solberg, T. N.; Abrecht, J.; Hewitt, D. A. "Graphical Procedures for the Refinement of Electron Microprobe Analysis of Fine-grained Particles" in Microbeam Analysis, R. Geiss, Ed. **1981**, San Francisco Press, San Francisco.

14 - Merkle, P. B. Ph.D. Dissertation, Virginia Polytechnic Institute and State University, **1995**.

15 - DMS 2000 Powder X-ray Diffractometer, Scintag Corp., Sunnyvale, CA, U.S.A.

16 - Joint Committee on Powder Diffraction Standards. Powder Diffraction Files - Inorganic Phases, JCPDS, **1990**.

17 - Hochella, M. F., Jr. "Auger electron and x-ray photoelectron spectroscopies", in: Reviews in Mineralogy: Spectrosopic Methods in Mineralogy and Geology, **1988**, F. C. Hawthorne, Ed., Mineralogical Society of America, Washington, D.C.

18 - Murray, J.; Dillard, J.; Giovanoli, R.; Moers, H.; Stumm, W. "Oxidation of Mn(II): Initial mineralogy, oxidation state and aging", Geochim. Cosmochim. Acta **1985** (49), 463-470.

19 - Junta, J. L., Hochella, M. F., Jr. "Manganese (II) oxidation at mineral surfaces: A Microscopic and spectroscopic study", Geochim. Cosmochim. Acta **1994** (58), 4985-4999.

20 - Smith, J. M. Chemical Engineering Kinetics, Ch. 8, **1981**, 3rd ed., McGraw-Hill, New York.

21 - Krupa, N. E., Cannon, F. S. "Characterization of the Pore Structure of Thermally Regenerated Activated Carbon Using Adsorbates of Varying Molecular Dimensions", Proceedings of the Annual Conference of the American Water Works Association **1994** (June), New York.

22 - ASTM E-42.14 STM/AFM Subcommittee Recommendation for Analyzing and Reporting Surface Roughness.

23 - Bailey, T. A. "Procedures for Conditioning Filters for Manganese Removal" (Appendix A), in: Knocke, W. R.; Occiano, S.; Hungate, R. Removal of Soluble Manganese from Water by Oxide-Coated Filter Media **1990**, AWWA Research Foundation.

24 - Nealson, K. H., C. R. Myers. "Microbial Reduction of Manganese and Iron: New Approaches to Carbon Cycling", Applied and Environmental Microbiology, **1992** (Feb.), 439-443.

25 - Cornwell, D. A., Lee, R. G. "Waste Stream Recycling: Its Effect on Water Quality", J. AWWA **1994**, (86:11), 50 -63.

26 - Davis, J. A.; Kent, D. B. "Surface Complexation Modeling in Aqueous Geochemistry", in: Reviews in Mineralogy: Mineral-Water Interface Geochemistry, **1990**, M. F. Hochella, Jr. and Art F. White, Eds.

27 - Oku, M.; Hirokawa, K.; Ikeda, S. "X-ray photoelectron Spectroscopy of Manganese-Oxygen Systems", J. Electron Spectrosc. Rel. Phenom. **1975**, (7), 465-473.

28 - Suzuki, M. Adsorption Engineering, Chemical Engineering Monographs No. 25, **1990**, Kodansha Ltd., Tokyo, and Elsevier Science Publishers, Amsterdam.

29 - Morel, F. M. M. Principles of Aquatic Chemistry, Ch. 8, **1983**, John Wiley & Sons, New York.

30 - Van Vliet, B. M.; Weber, W. J. "Particle Surface Roughness Effects on the Interfacial Mass transfer Dynamics of Microporous Adsorbents", Chem. Eng. Commun. **1988**, (68), 165-176.

TABLE 1

ISOELECTRIC POINTS OF MINERALS, pH_{IEP}*

Mineral	$pH_{(IEP)}$
Birnessite, δ - MnO_2	2.2
Goethite, α- FeOOH	7.3
Calcite, $CaCO_3$	9.5
Quartz, α - SiO_2	2.9
γ - Al_2O_3	8.5

* - Values from Davis and Kent, Reference 26.

TABLE 2

TREATMENT PROCESSES OF MEDIA SAMPLE SOURCES

Media	**Sample type**	**Source and Treatment Process**
Blacksburg, VA	coated anthracite	New River, alum coagulation, dual-media filtration
Lorton, VA	coated anthracite	Occoquan reservoir, alum coagulation, dual-media filtration
Ft. Collins, CO: #1	coated anthracite	Snow melt reservoir, $KMnO_4$ preoxidation, alum coagulation, sludge-blanket clarification, NGE process implemented
Swift Run, VA	coated anthracite	Swift Run reservoir, $KMnO_4$ preoxidation, alum coagulation and dual-media filtration
Durham, NC:	coated anthracite	Surface waters pumped to terminal reservoirs, conventional alum coagulation, dual-media filtration
Brown #7	archive sample	
before backwash	1993 sample	
after backwash	1993 sample	
Brown #1	coated sand	
Williams	coated anthracite	
Norfolk, NE:		
coal	coated anthracite	Groundwater: Fe, Mn removal only
sand	coated sand	
authigenic	formed in place	
Portsmouth, VA	coated anthracite	Surface water, conventional treatment

TABLE 3

MEDIA PROPERTIES

Media	Surface area $m^2\ g^{-1}$	Extractable Mn, $mg\ g^{-1}$	Micropore vol., $cm^3\ kg^{-1}$
raw anthracite	0.17	0.01	1.6
raw gravel	1.6	-	7.3
Mn greensand	46	3.4	177
synthetic coatings:			
anthracite	0.56	2	4.8
gravel	1.3	1.4	6.6
Blacksburg, VA	11.3	5	31
Lorton, VA	-	11.5	-
Ft. Collins, CO: #1	-	0.83	-
#3	-	2.0	-
Swift Run, VA	3.7	20	18.8
Durham, NC:			
Brown archive #7	95	75	335
before backwash	7.6	9.5	47.4
after backwash	4.7	6.1	32.3
Brown sand #1	135	-	533
Williams	21	95	89
Norfolk, NE: coal	2.5	13.8	14.6
sand	1.6	-	-
authigenic	186	160	513
Portsmouth, VA	28	31.5	107

TABLE 4

X-RAY PHOTOELECTRON SPECTROSCOPY

Mn3s PEAK SPLITTING ANALYSIS

Study	**Specimen analyzed**	**Mn3s peak splitting, eV**	**Peak area ratio**
This study	Synthetically coated anthracite	4.75	1.74
Oku *et al.*[27]	MnO_2	4.7	
Murray *et al.*[18]	MnO_2	4.6	1.8 (± 1)
	MnO	5.8	1.9
	γ - MnOOH	5.3	1.8
Junta and Hochella[19]	MnO_2	4.5	
	γ - MnOOH	5.4	

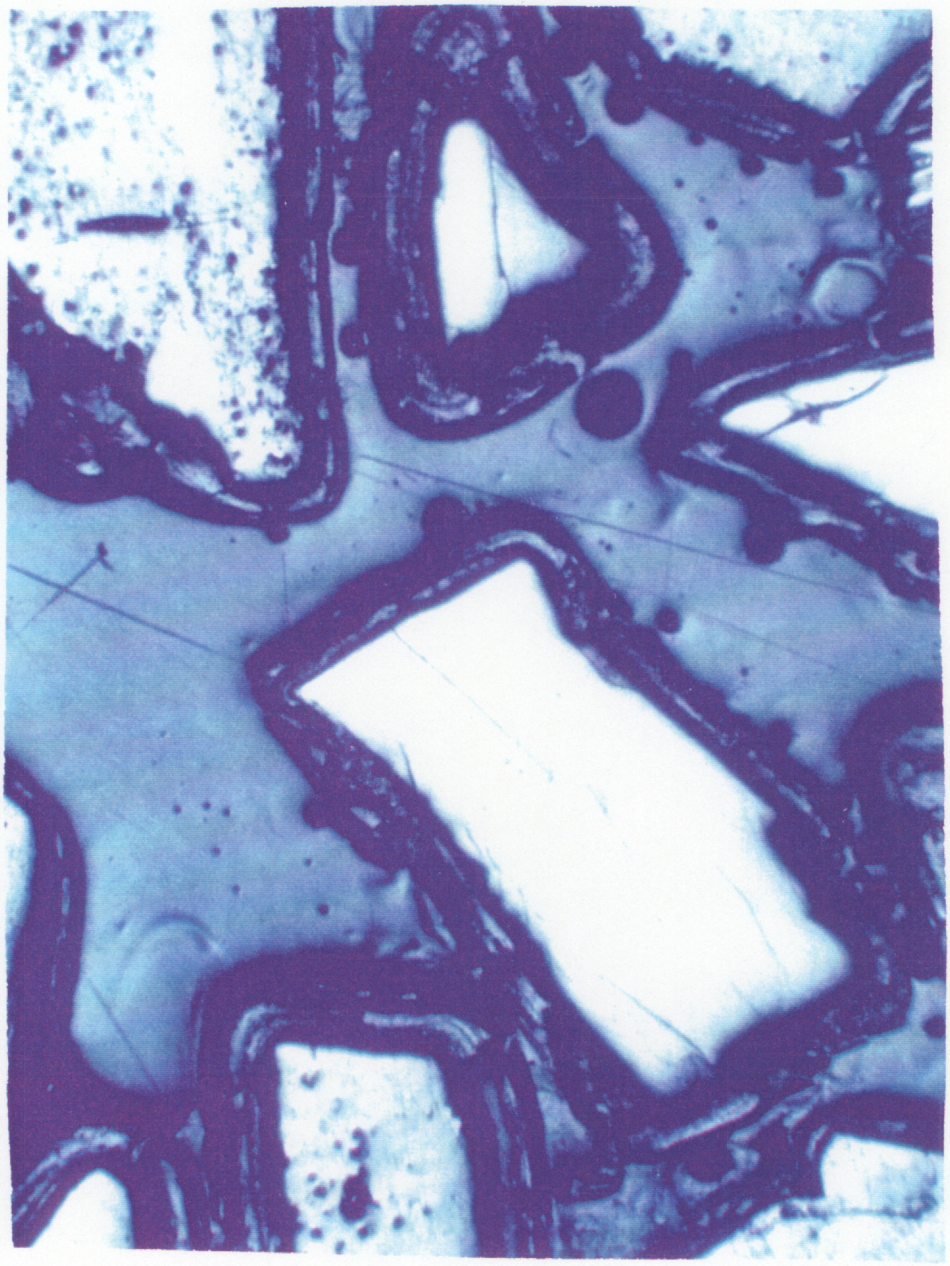

FIGURE 1: Durham, NC Brown facility, oxide-coated anthracite media (archived sample), reflected light image of polished cross section. Anthracite appears white, surrounded by dark rings of encapsulating coating. Dark circular features are air bubbles in the epoxy embedment.

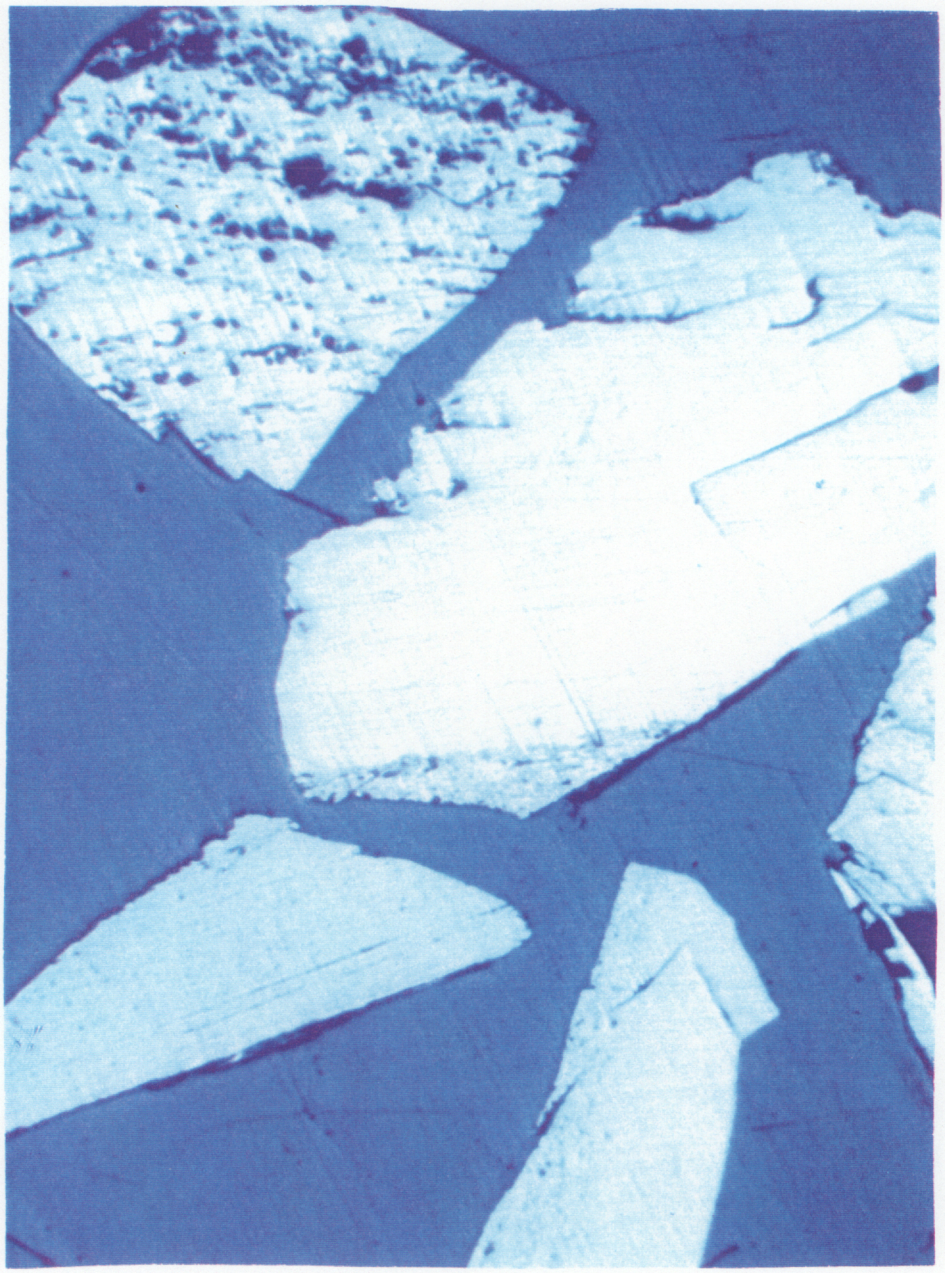

FIGURE 2: Durham, NC Brown facility, oxide-coated anthracite media (archived sample), reflected light image of polished cross section after chemical extraction to remove surface oxide deposits.

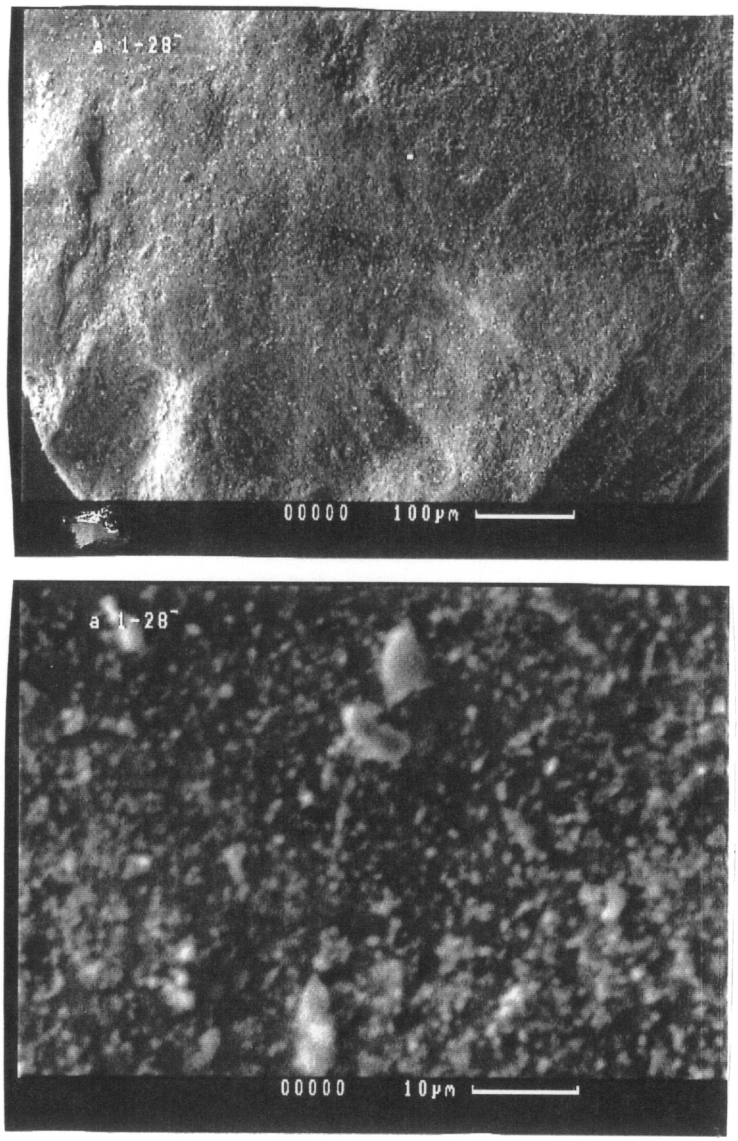

FIGURE 3: A) Scanning electron microscope (SEM) image of uncoated anthracite surface.

B) Particles embedded in uncoated anthracite surface (SEM). Qualitative energy dispersive x-ray spectral analysis (EDS) identified Al and Si as the primary cation constituents (excluding H^+).

A

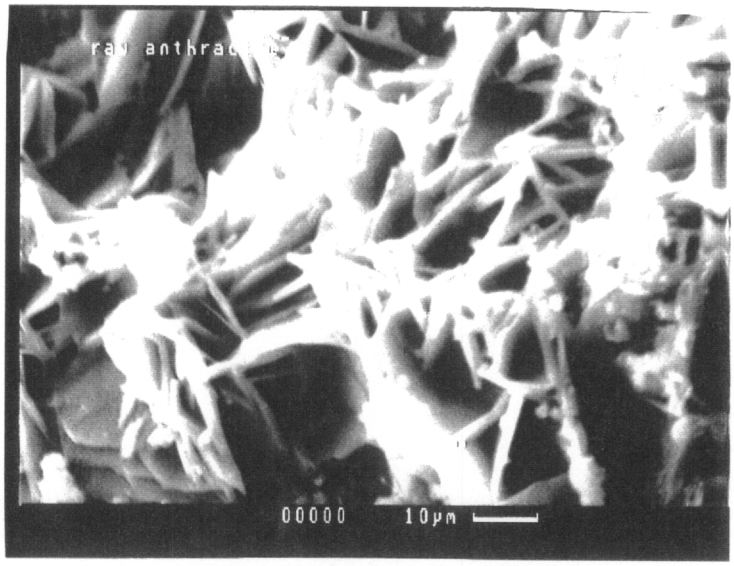

B

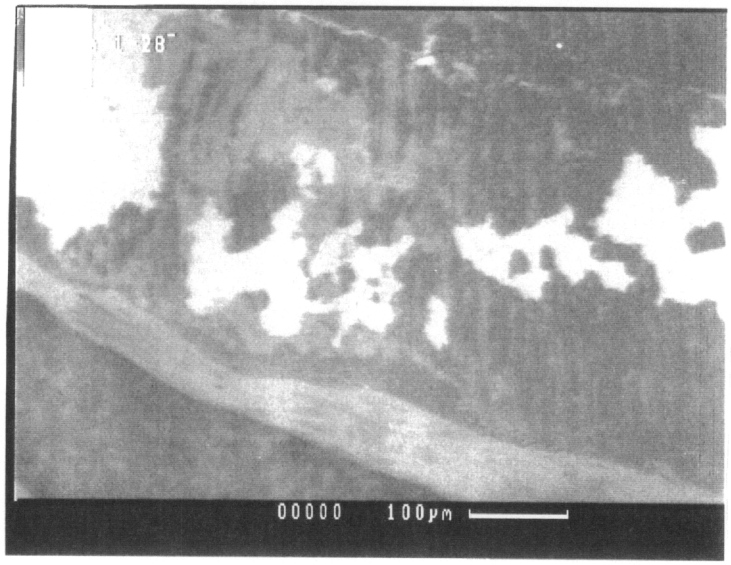

FIGURE 4: A) Native mineral deposit on uncoated anthracite (SEM). Fe and S identified by EDS as primary elemental constituents.

B) Native mineral deposit on uncoated anthracite, backscattered electron image (BSE) in which relative brightness corresponds to higher relative nuclear density. Fe identified by EDS as primary cation constituent.

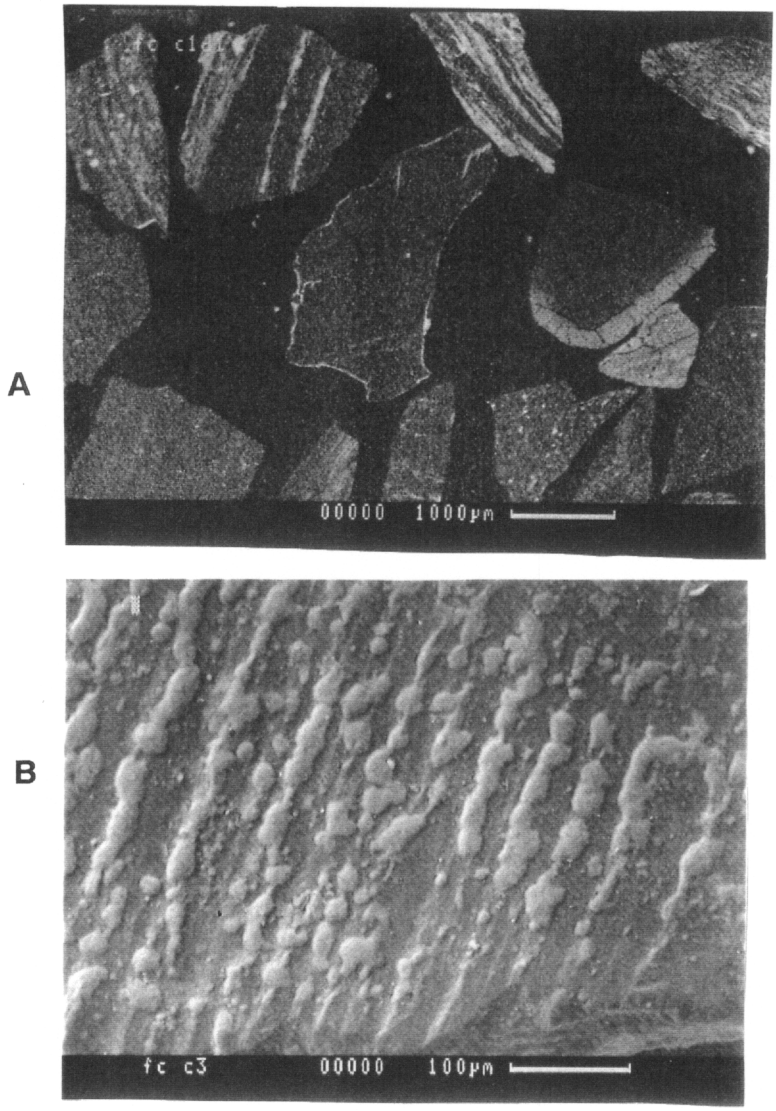

FIGURE 5: A) Ft. Collins, CO oxide-coated anthracite media, BSE image of polished cross section. Primary cation constituents of the native, banded mineral deposits inside the grains are Al and Si, with Fe, S, and Mn detected.

B) Ft. Collins, CO oxide-coated anthracite media, SEM image of linearly-arranged oxide growths in grain surface, with Mn identified by EDS as primary cation constituent. Native internal banded mineral deposits intersect the grain surface, possibly serving as nucleation sites for initiation of oxide coating growth.

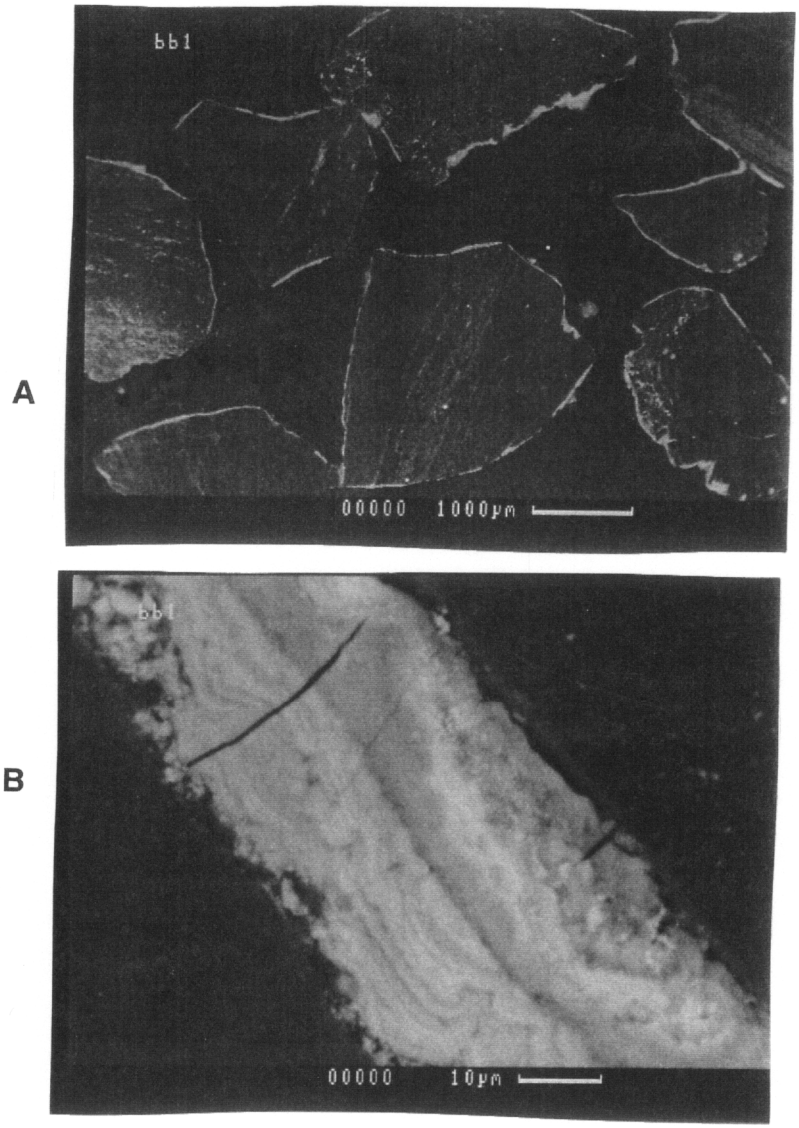

FIGURE 6: A) Blacksburg, VA oxide-coated anthracite media, BSE image of polished cross section, showing native, banded mineral deposits inside the grains.

B) Blacksburg, VA oxide-coated anthracite media, BSE image of polished cross section, detail of exterior coating, with media surface at top right. Al, Mn, and Si identified by EDS as primary cation constituents.

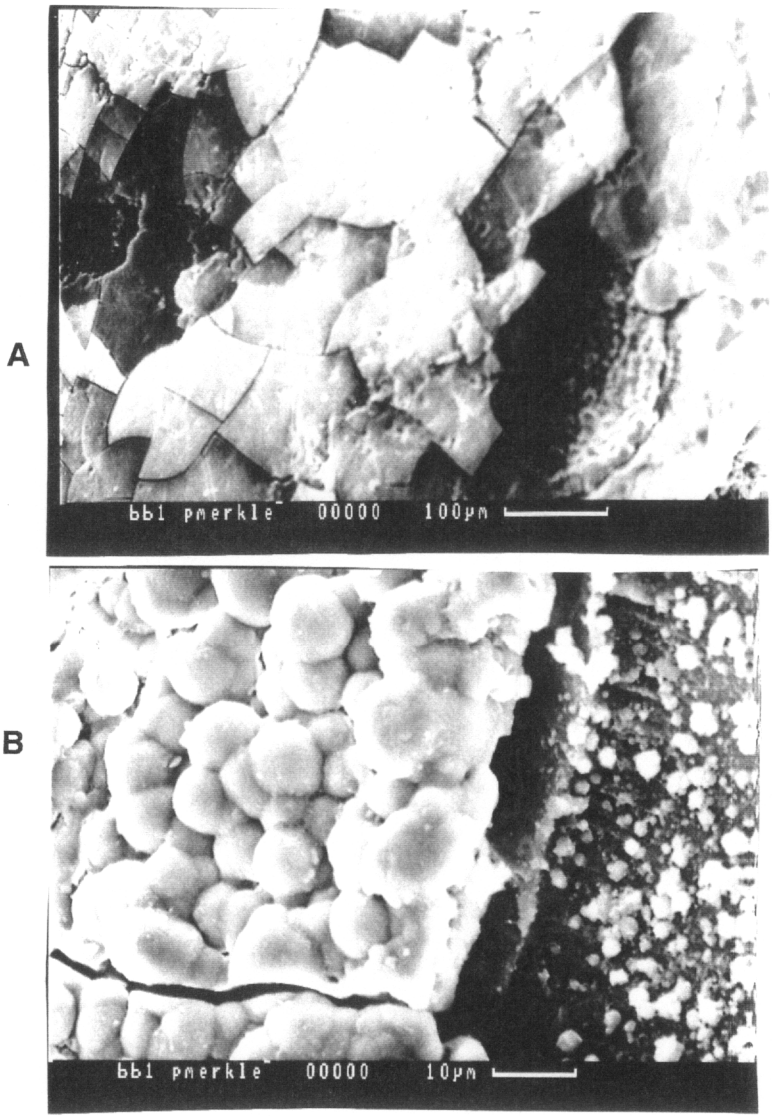

FIGURE 7: A) Blacksburg, VA oxide-coated anthracite media, SEM image of surface coating. Broken pavement appearance is probable artifact of sample preparation.

B) Detail of pit at lower right of Figure 7A, SEM image. Native, banded mineral deposits intersect surface at right.

A

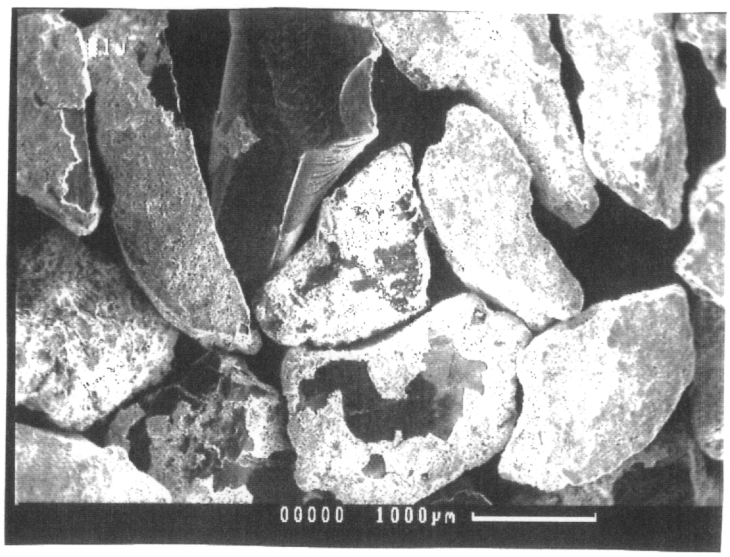

B

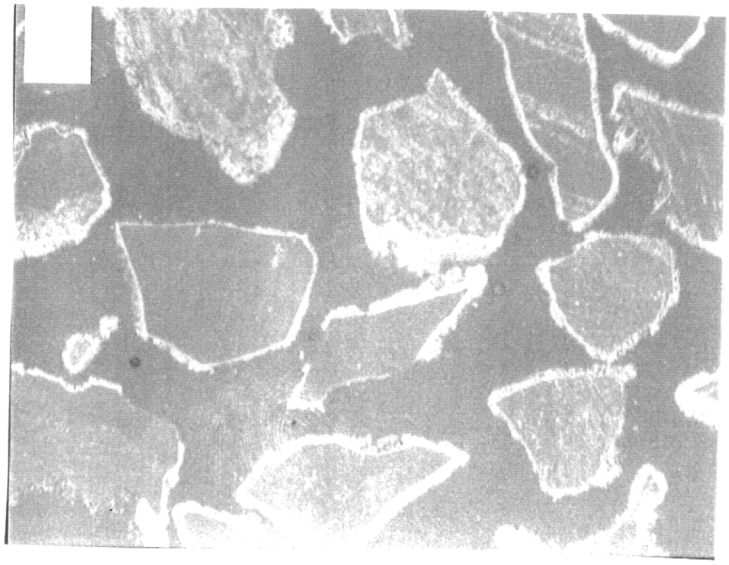

FIGURE 8: A) Lorton, VA oxide-coated anthracite media, BSE image of grain surfaces. Anthracite appears dark, oxide coating appears bright.
B) Lorton, VA oxide-coated anthracite media, BSE image of polished cross section showing native, banded mineral deposits inside the grains, with encapsulating oxide coating.

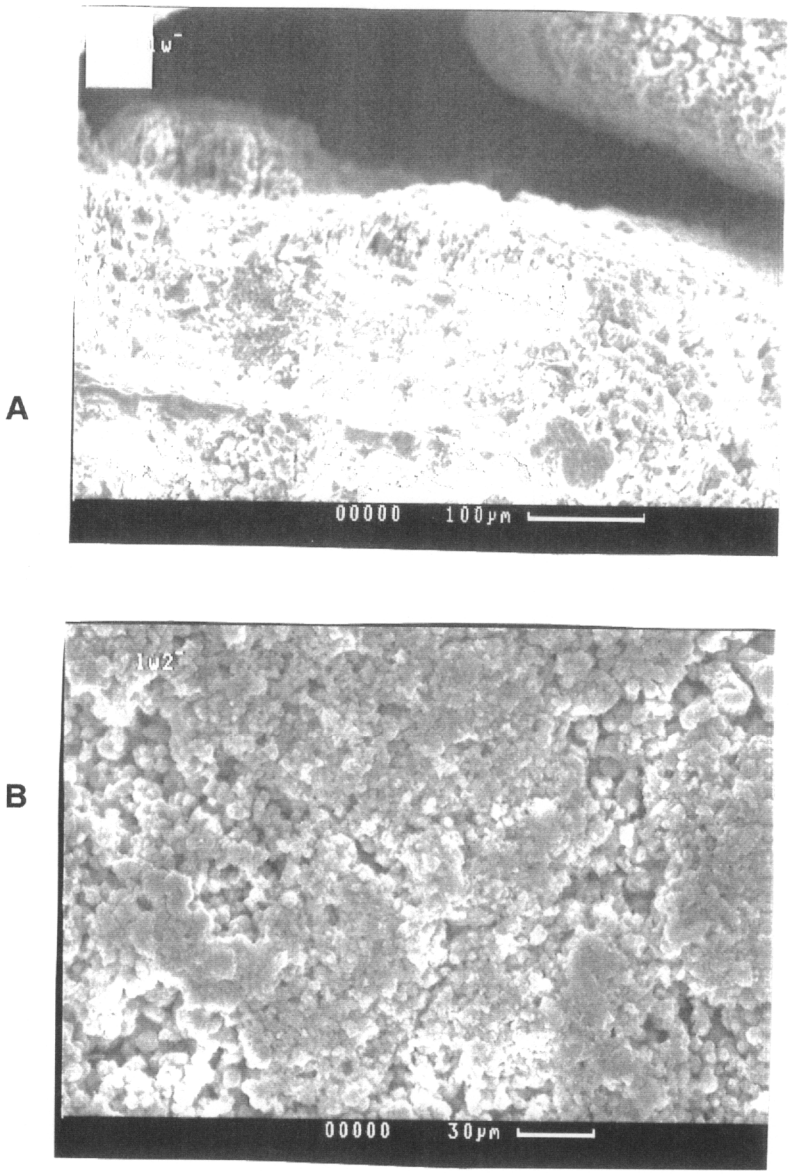

FIGURE 9: A) Lorton, VA oxide-coated anthracite media, SEM image of coating surface, showing columnar growth features
B) Lorton, VA oxide-coated anthracite media, SEM image of coating surface, showing roughness features and particle clusters.

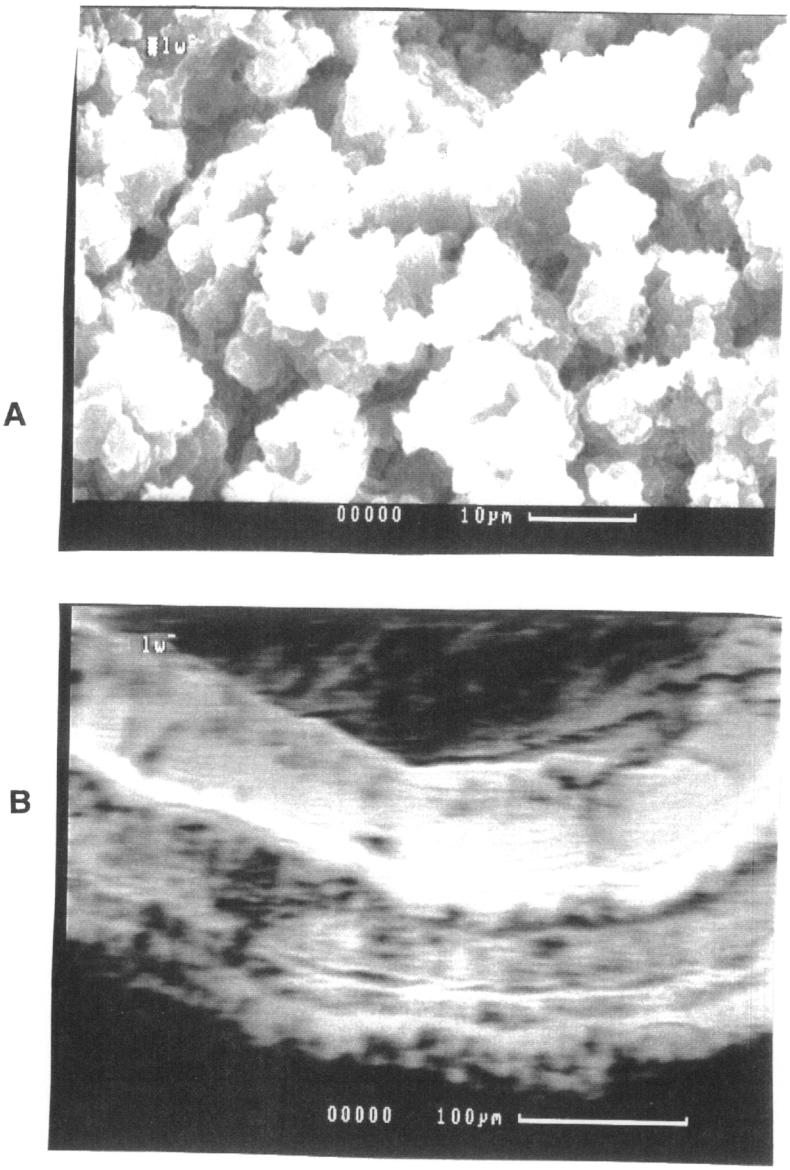

FIGURE 10: A) Lorton, VA oxide-coated anthracite media, SEM image of coating surface, showing the fine structure of particle clusters.

B) Lorton, VA oxide-coated anthracite media, BSE image of polished cross section, single encapsulated media grain at top of photo. "Ring" features in coating indicate variation in composition, confirmed by EDS (see text for details).

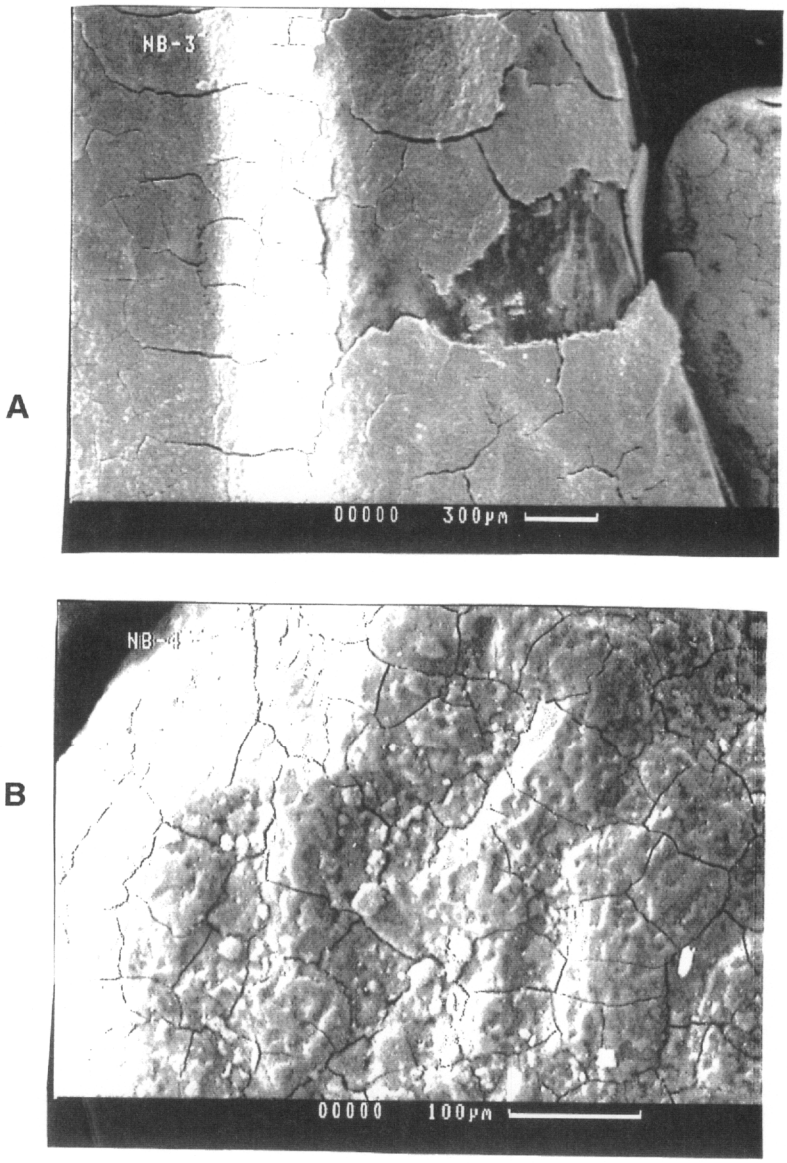

FIGURE 11 A) Norfolk, NE oxide-coated anthracite media, SEM image of coating surface.

B) Norfolk, NE oxide-coated sand media, SEM image of coating surface.

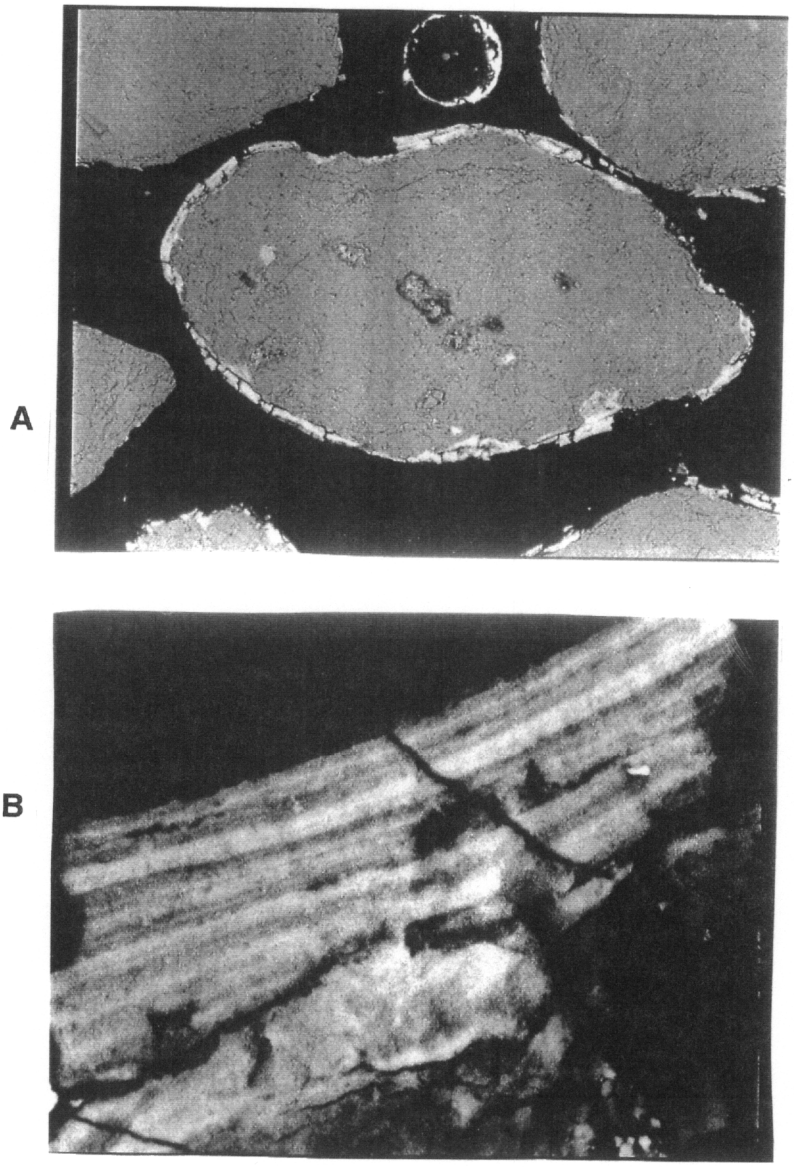

FIGURE 12 A) Norfolk, NE oxide-coated sand media, BSE image of polished cross section.

B) Detail of Figure 12A coating, BSE image of banding features in coating. Mn identified as primary cation constituent by EDS throughout the coating, with Al, Ca, Fe, and Si enriched in dark bands.

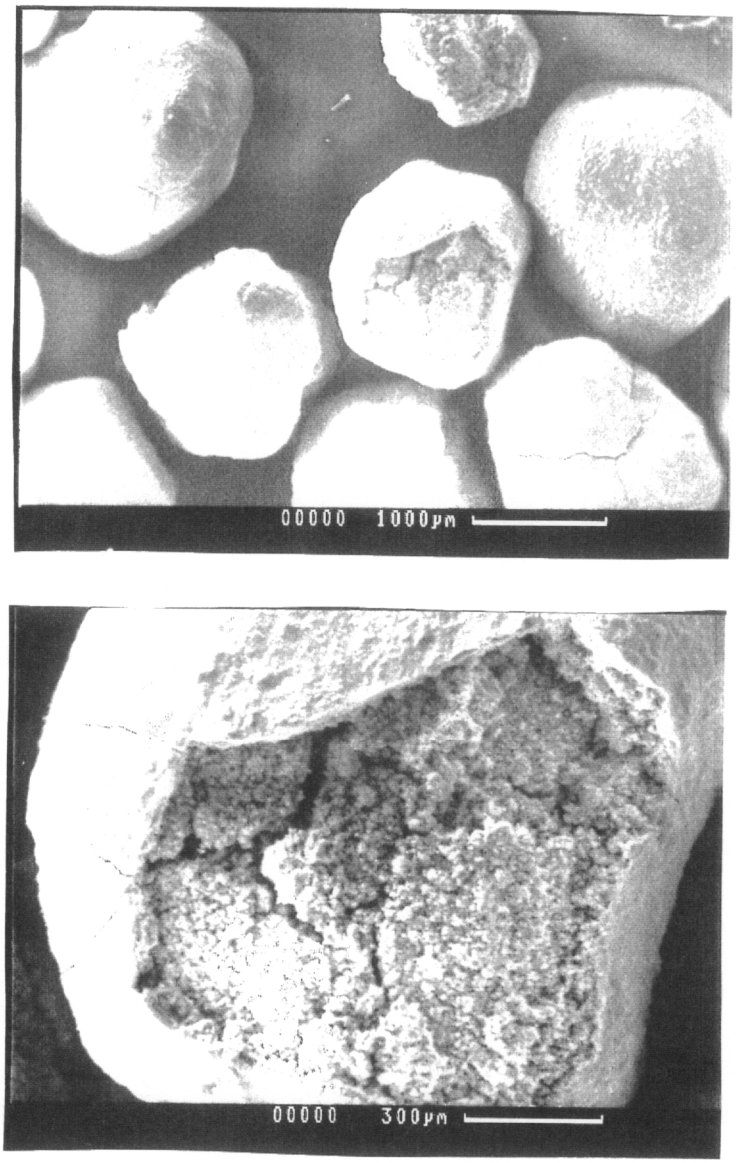

FIGURE 13 A) Norfolk, NE authigenic particles composing a thin top layer on a dual-media filter, SEM image.

B) Detail of particle at center of Figure 13A, SEM image. Ca and Mn identified by EDS as primary cation constituents in the exterior shell, and Mn as primary constituent of the interior deposit.

A

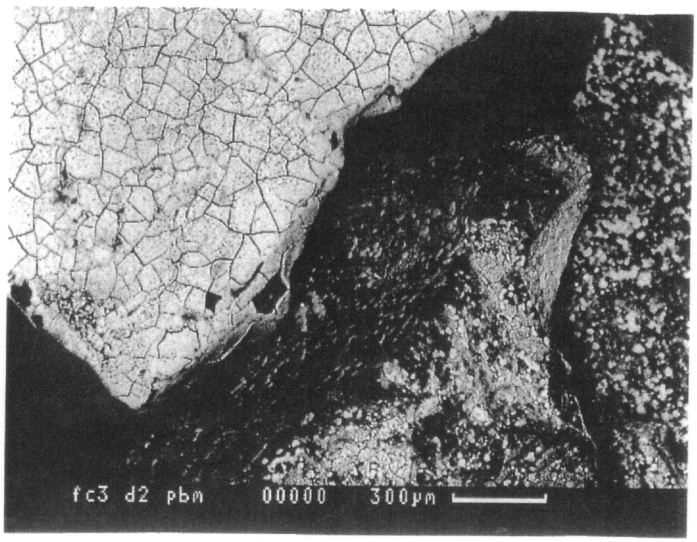

B

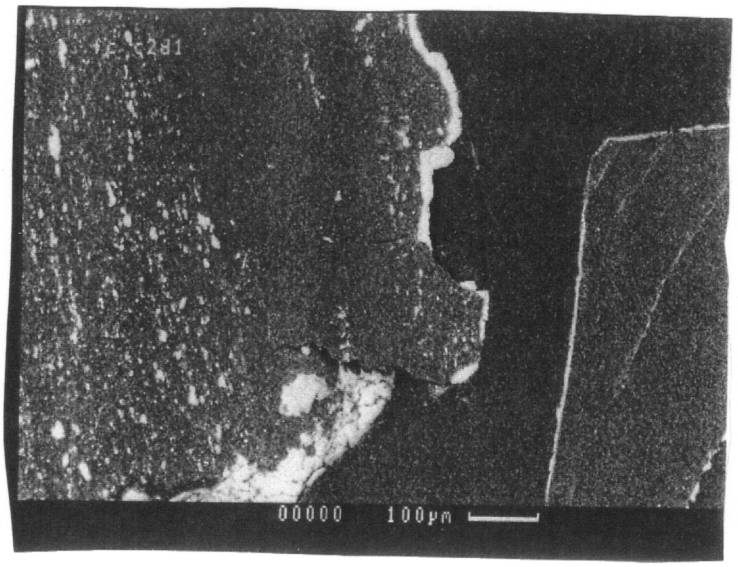

FIGURE 14 A) Ft. Collins, CO oxide-coated anthracite media, BSE image, with variation in coating apparent between grains.
B) Ft. Collins CO oxide-coated anthracite media, BSE image of polished cross section.

A

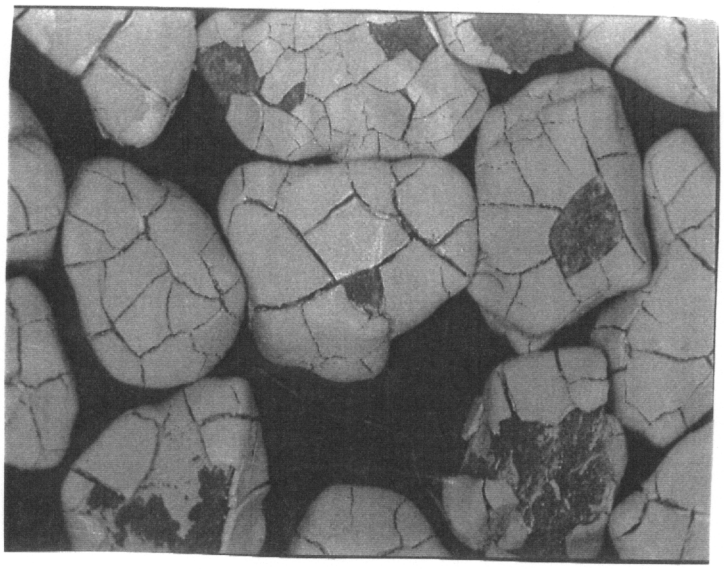

B

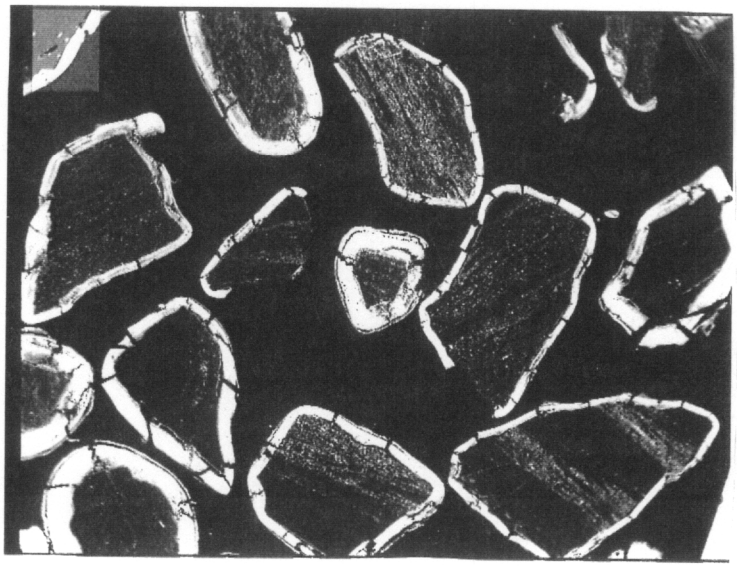

FIGURE 15 A) Durham, NC Brown facility, oxide-coated anthracite media (archived sample), BSE image of whole media.
B) Durham, NC Brown facility, oxide-coated anthracite media (archived sample), BSE of polished cross section.

A

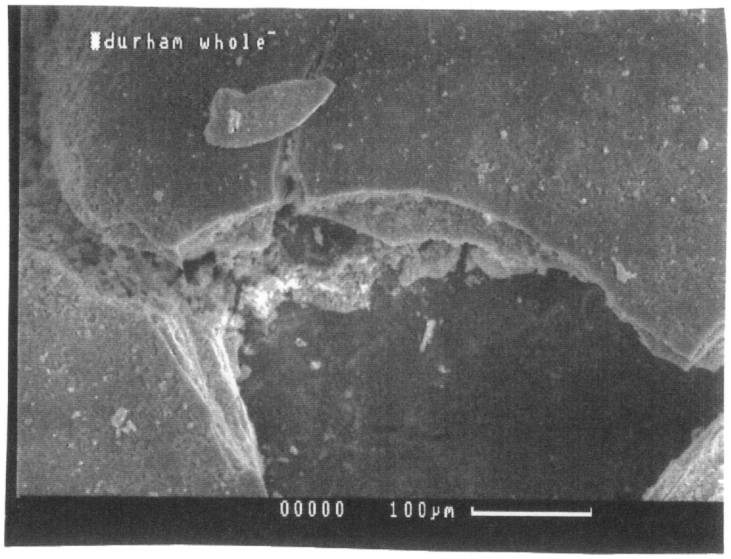

B

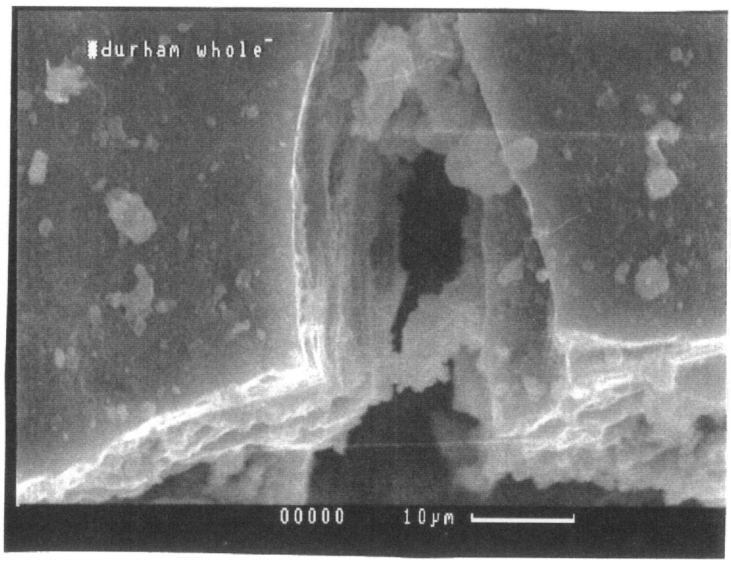

FIGURE 16 A) Durham, NC Brown facility, oxide-coated anthracite media (archived sample), SEM image of surface coating.

B) Detail of Figure 16A, SEM image of fine layering in coating exposed by media cracking (cracks are probable artifacts of sample preparation).

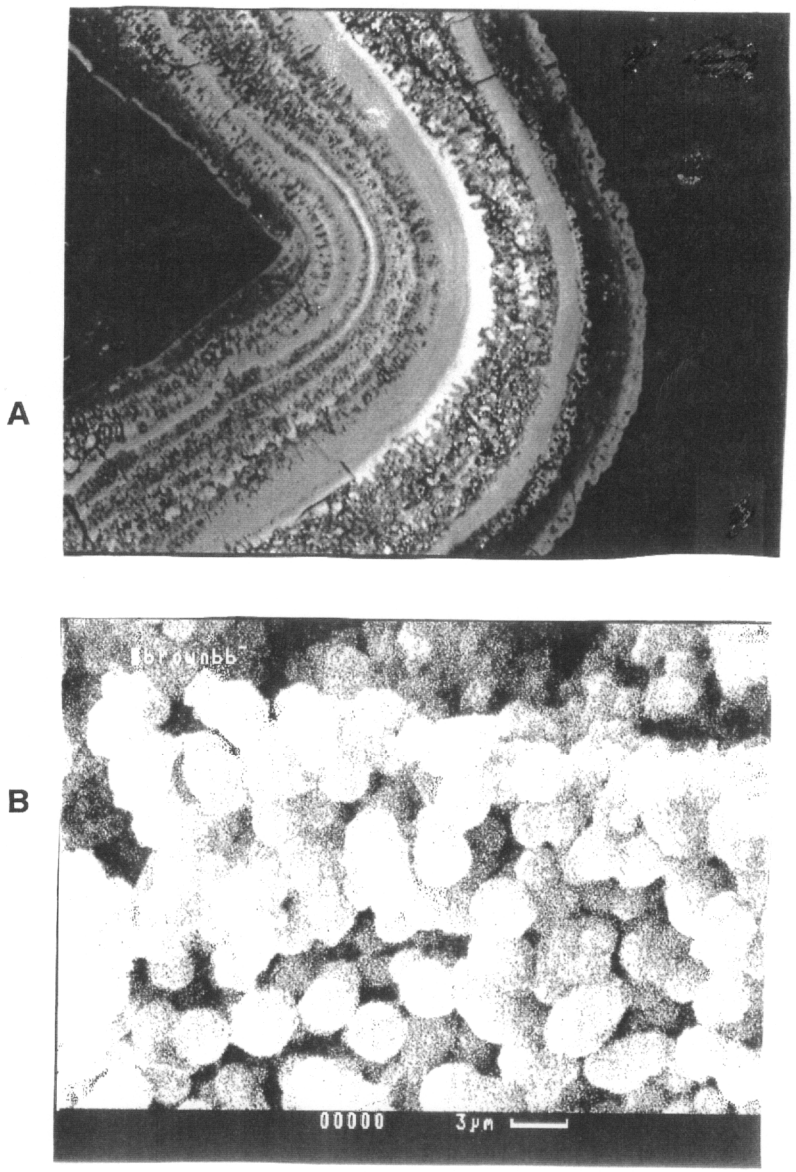

FIGURE 17 A) Durham, NC Brown facility, oxide-coated anthracite media (archived sample), BSE of polished cross section, single media grain at left, showing alternating layers of porous and solid coating.

B) Durham, NC Brown facility, oxide-coated anthracite media 1993 sample taken immediately prior to filter backwash, BSE image of surface structure.

A

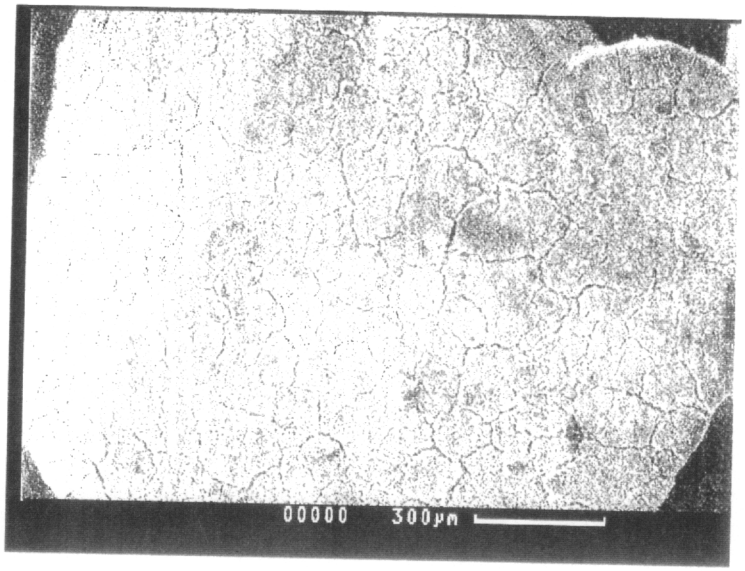

B

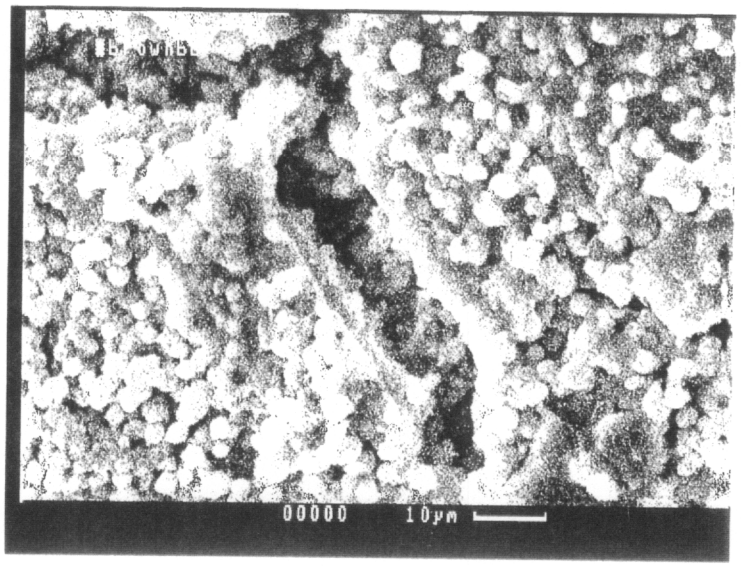

FIGURE 18 A) Durham, NC Brown facility, oxide-coated anthracite media 1993 sample taken immediately prior to filter backwash, BSE image of a single grain completely encapsulated with coating.

B) Detail of Figure 18A surface, BSE image.

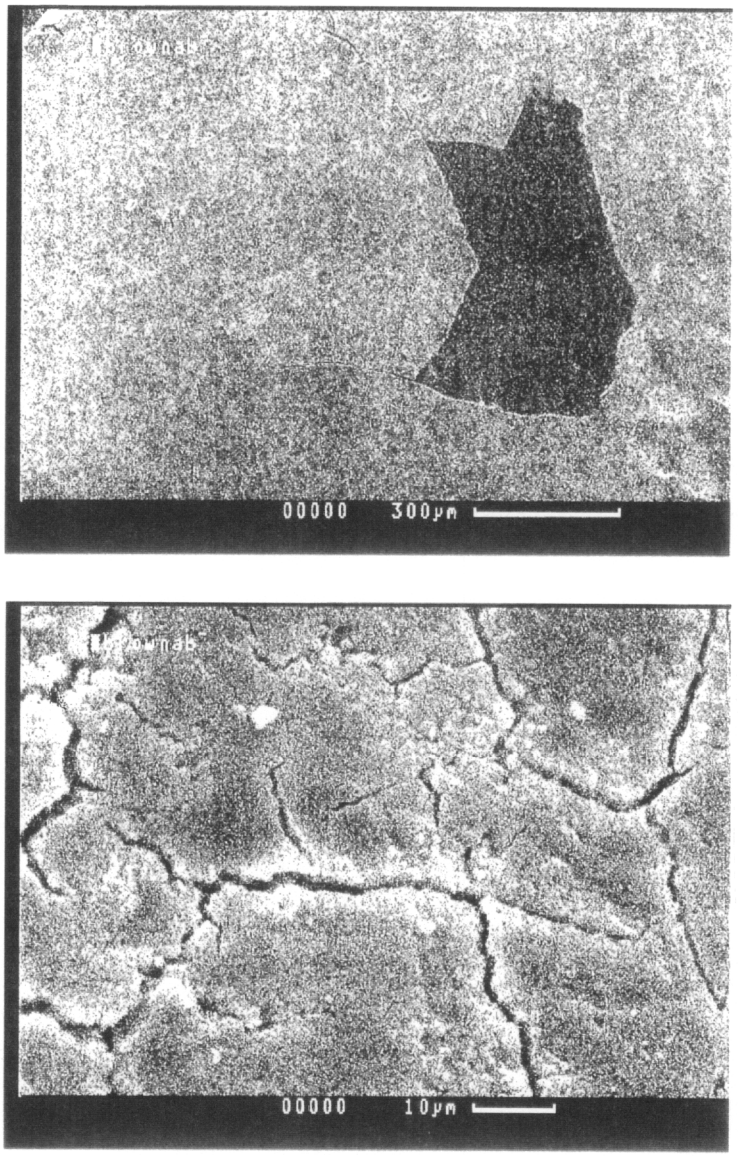

FIGURE 19 A) Durham, NC Brown facility, oxide-coated anthracite media 1993 sample taken immediately after filter backwash, BE image of a single grain with underlying anthracite surface showing in broken coating.

B) Detail of coated region of Figure 19A, BSE image. This surface lacks the particles seen in pre-backwash Figure 18A.

A

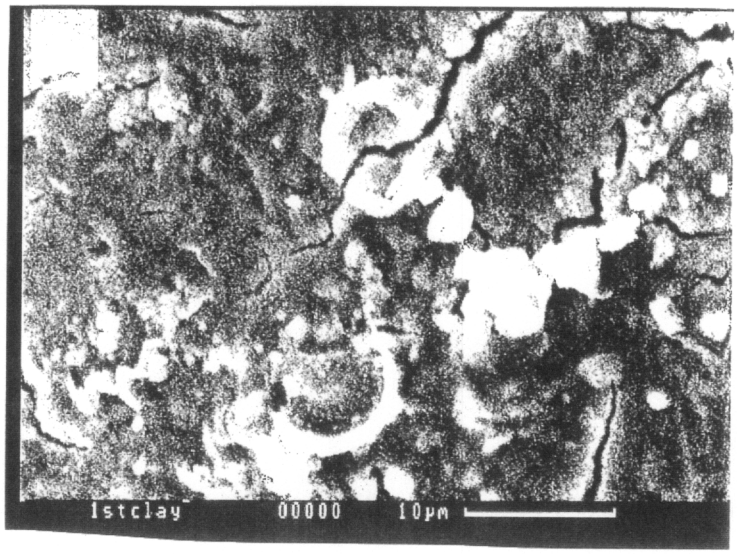

B

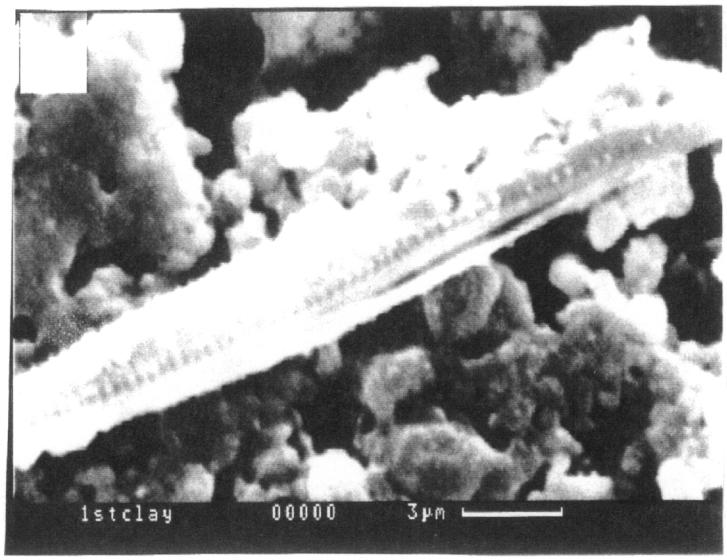

FIGURE 20 A) Durham, NC Brown facility, oxide-coated anthracite media 1993 sample taken immediately after filter backwash, SEM of diatom casts cemented in exterior coating.

B) Durham, NC Brown facility, oxide-coated anthracite media 1993 sample taken immediately after filter backwash, detail of diatom cast attached to media coating surface.

A

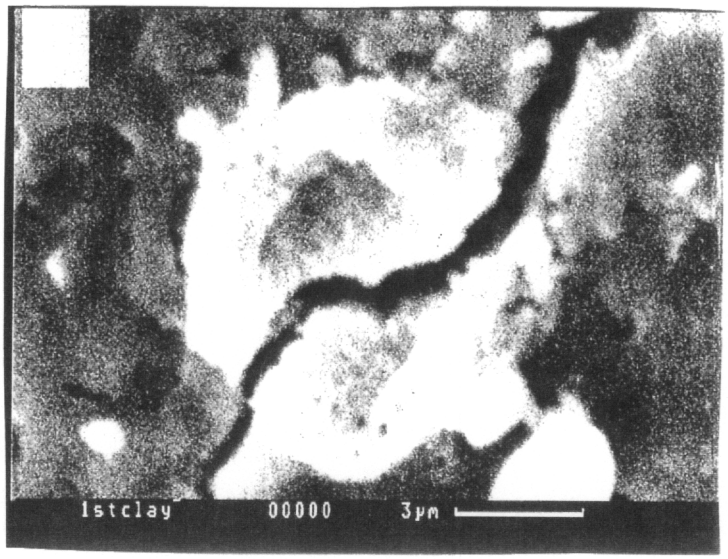

B

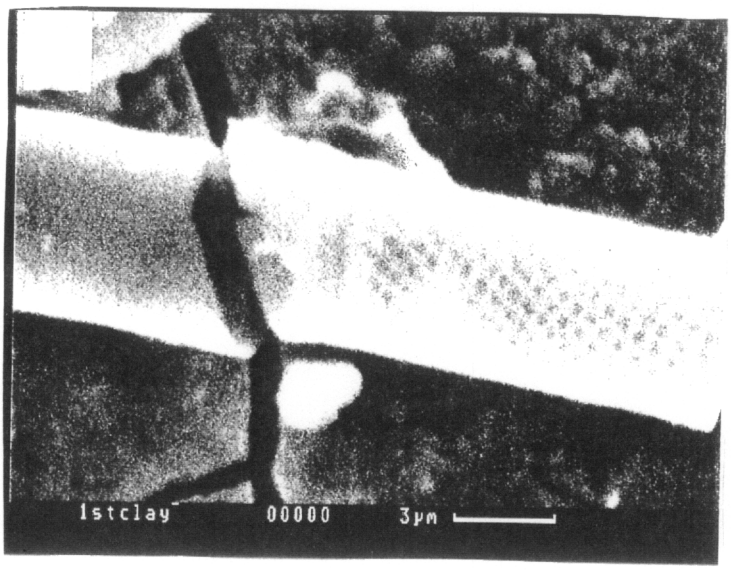

FIGURE 21) A) and B) Durham, NC Brown facility, oxide-coated anthracite media 1993 sample taken immediately after filter backwash, SEM images of diatom casts fractured along with coating.

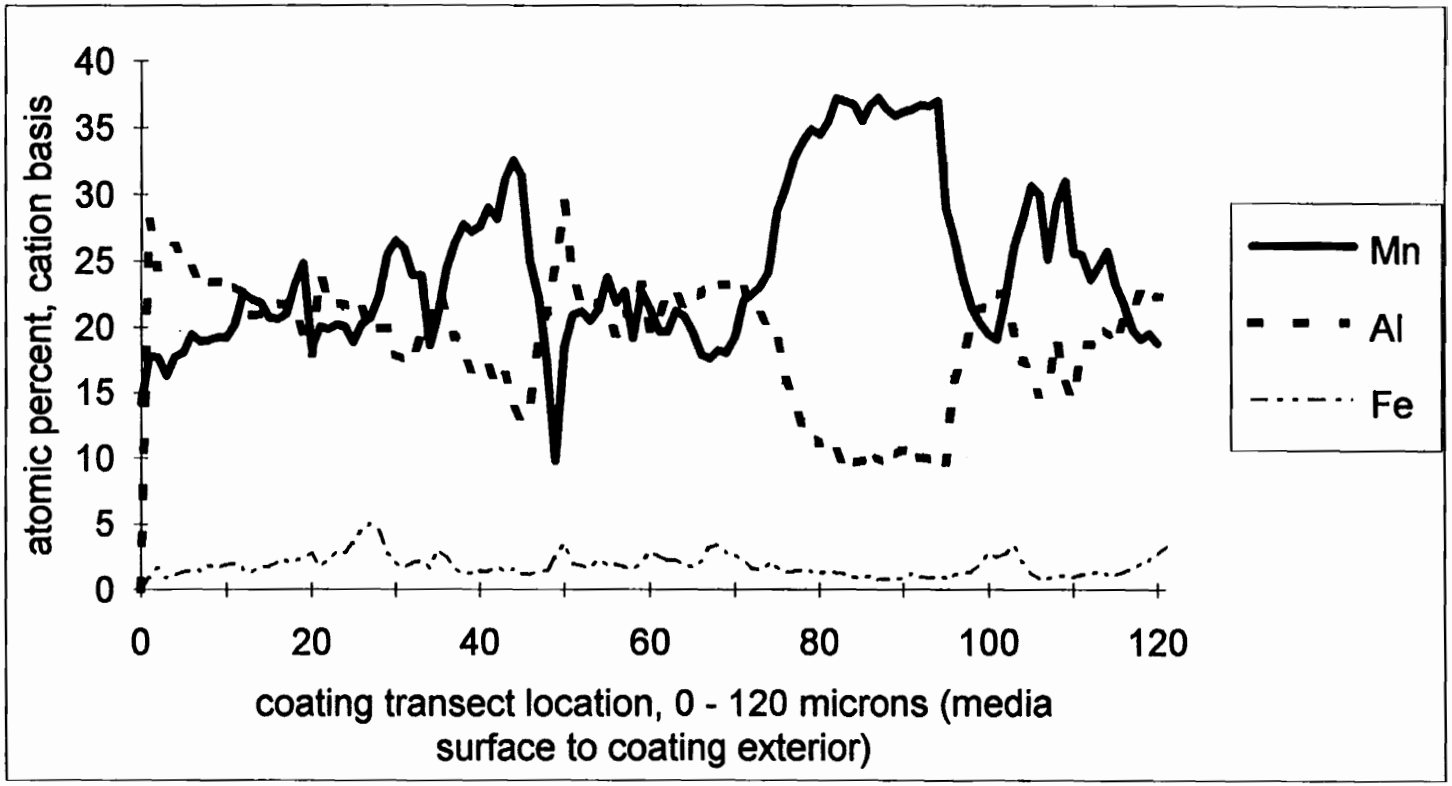

FIGURE 22 Electron microprobe transect analysis of the Durham Brown facility oxide coating on anthracite (archive sample, polished cross section). Oxide immediately adjacent to the media surface corresponds to the 0 micron position, and the outermost coating corresponds to the 120 micron position. Analyses were conducted in 1 micron step increments.

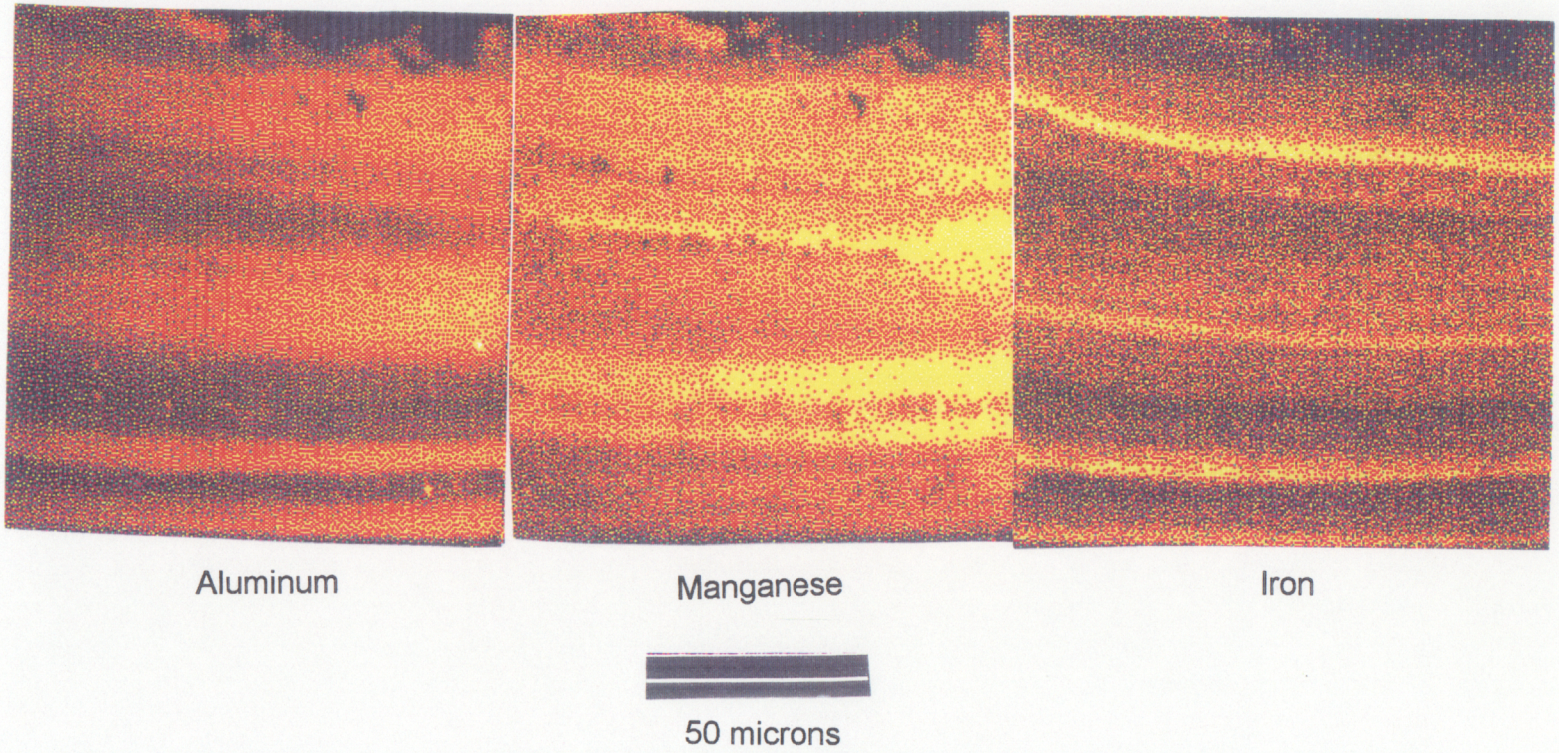

FIGURE 23 Areal maps of Al, Mn, and Fe by electron microprobe analysis, Durham Brown facility oxide coating on anthracite (archive sample, polished cross section). Media grain is at the top of each map, exterior coating surface at bottom. Brightness corresponds to greater elemental abundance.

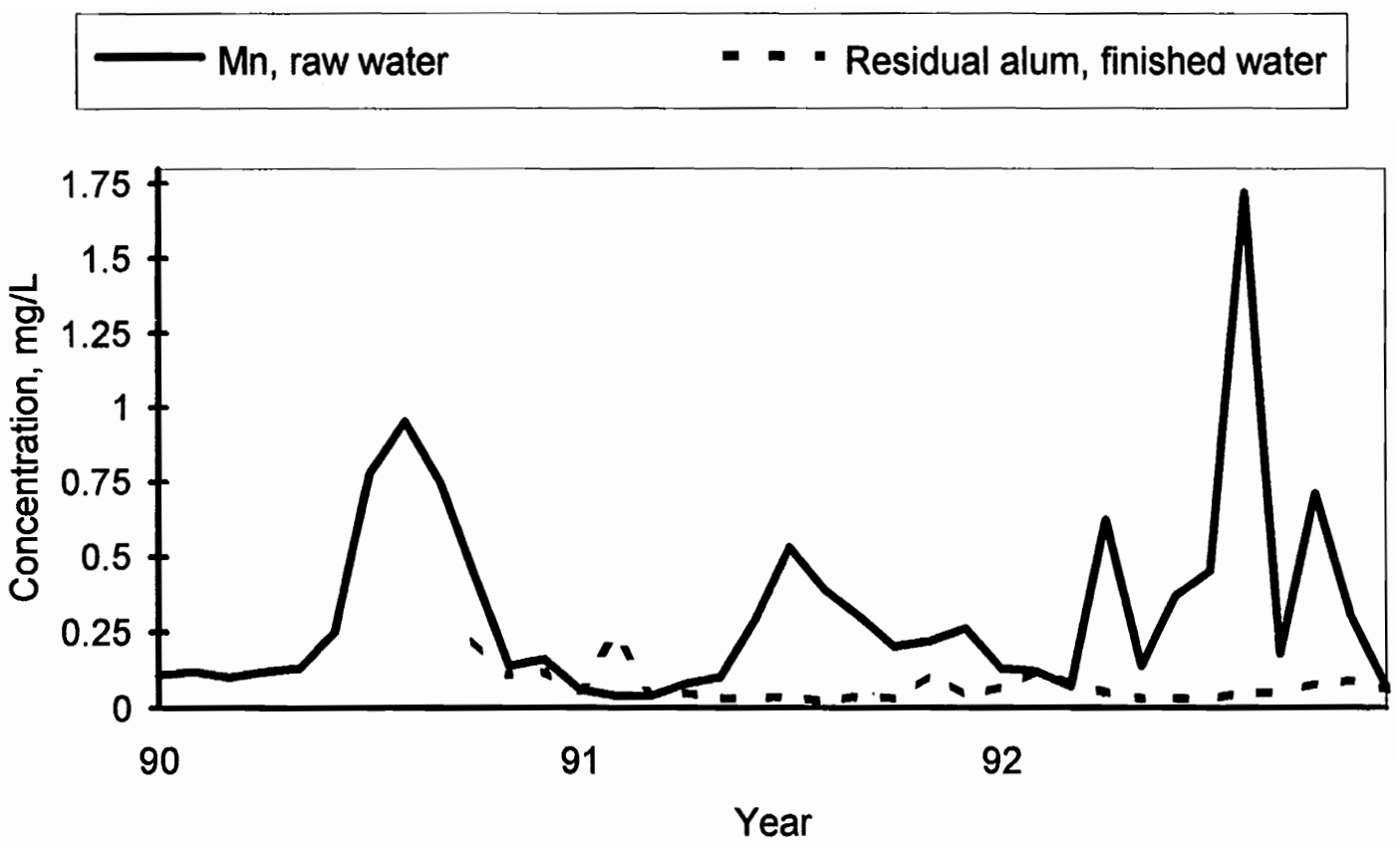

FIGURE 24 Water quality as reported by the Durham Brown facility for 1990 through 1992.

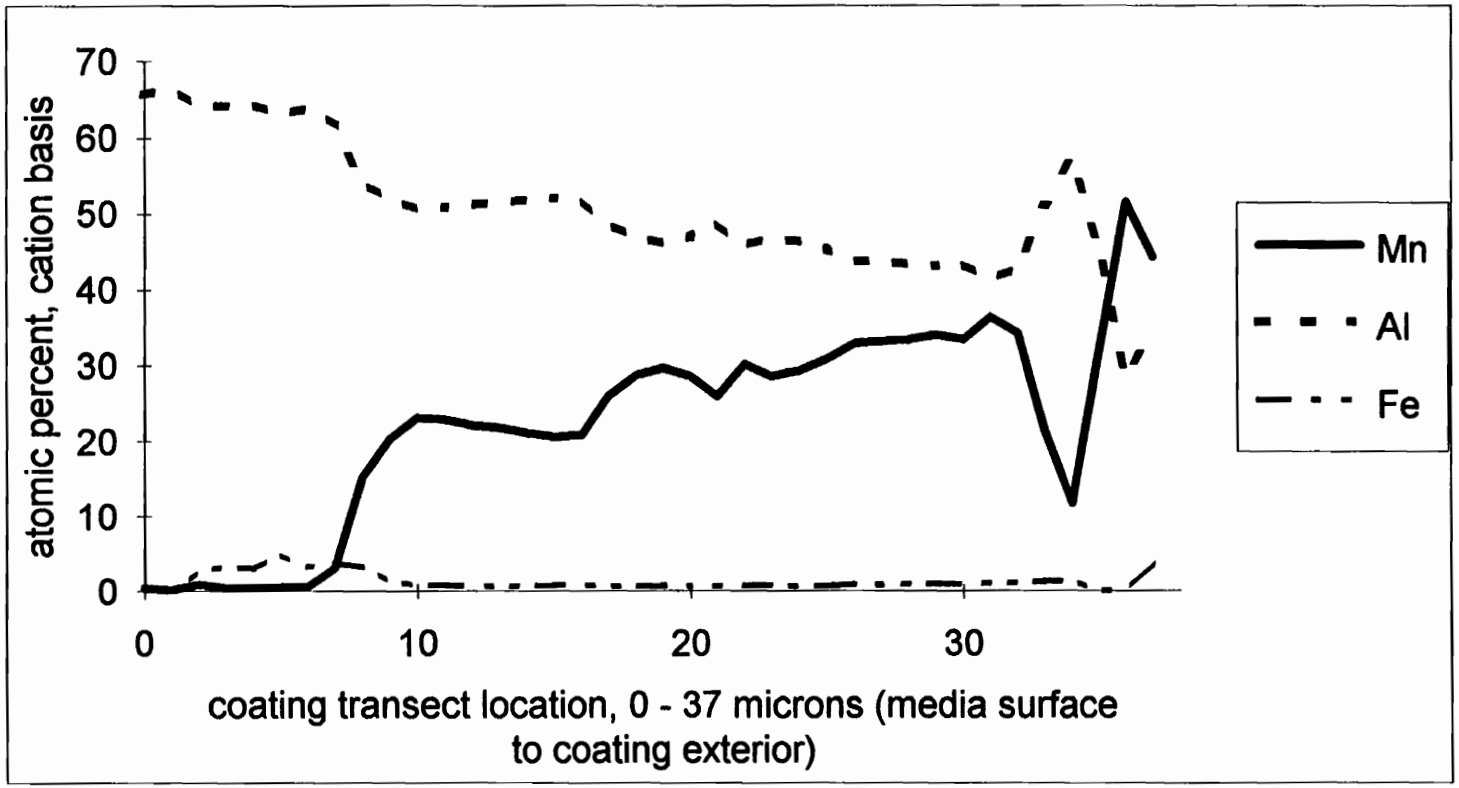

FIGURE 25 Electron microprobe transect analysis of the Ft. Collins, CO facility oxide coating on anthracite (Nov. 1994 sample, polished cross section). Oxide immediately adjacent to the media surface corresponds to the 0 micron position, and the outermost coating corresponds to the 37 micron position. Analyses were conducted in 1 micron step increments.

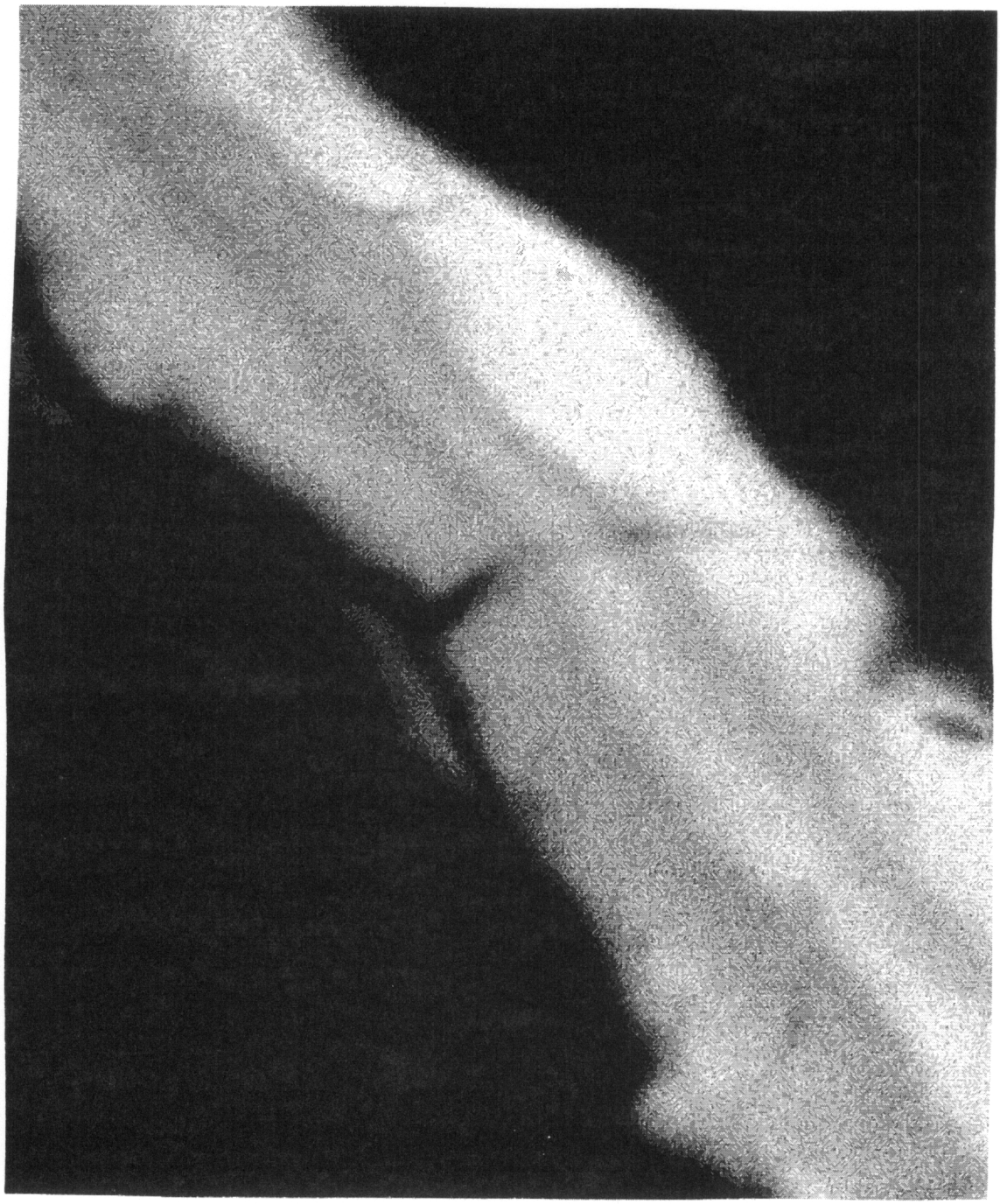

FIGURE 26 Areal map of Mn by electron microprobe analysis, Ft. Collins, CO facility oxide coating on anthracite (Nov. 1994 sample, polished cross section). Media grain is at left, coating outer surface at right. Vertical dimension of figure is 37.5 microns.

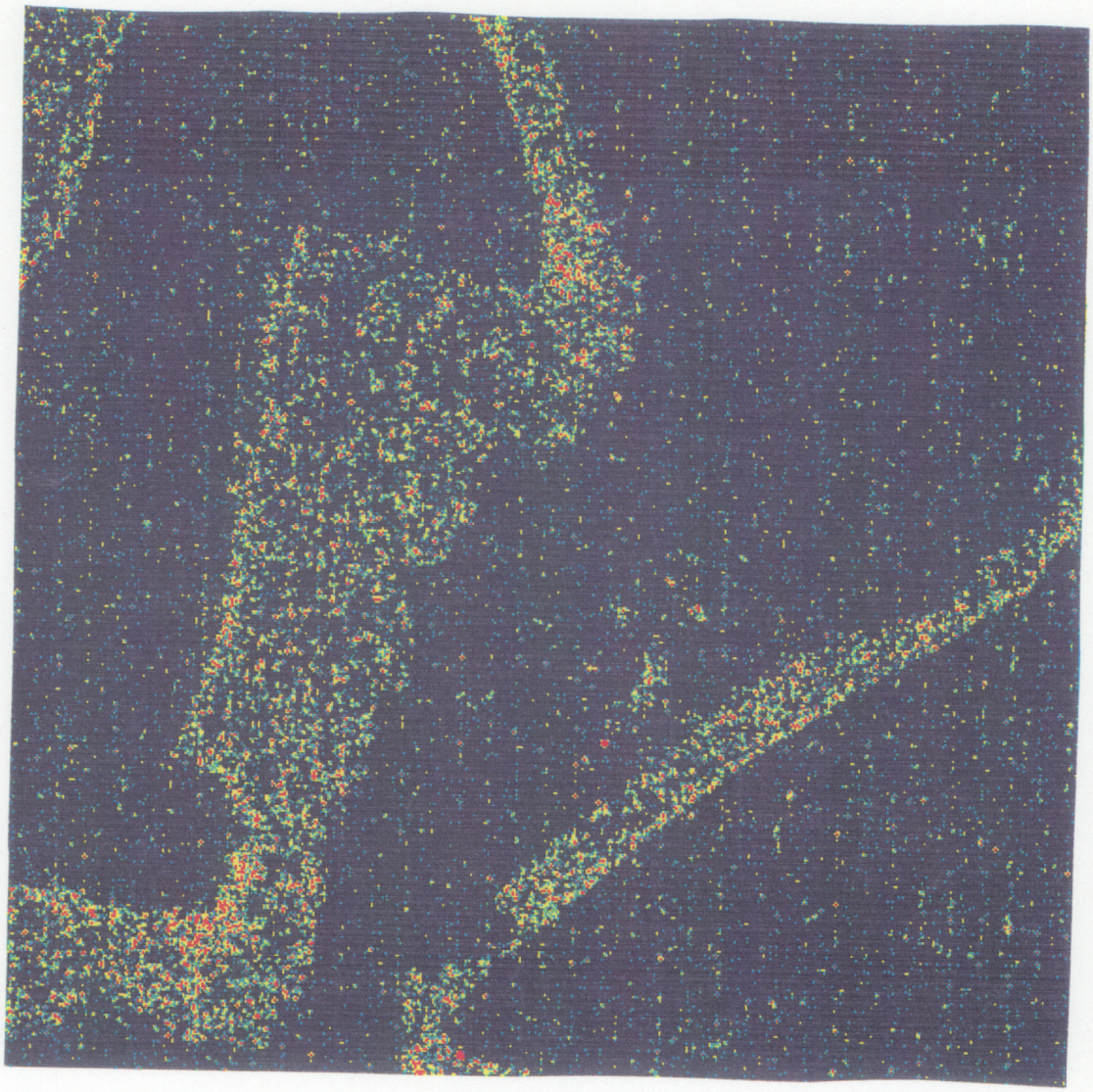

FIGURE 27 Areal map of Cu by electron microprobe analysis, Lorton, VA facility oxide coating on anthracite (archive sample, polished cross section). Two media grains are visible, one in sagittal cross section at lower right, and one in a more tangential cross section at upper left.

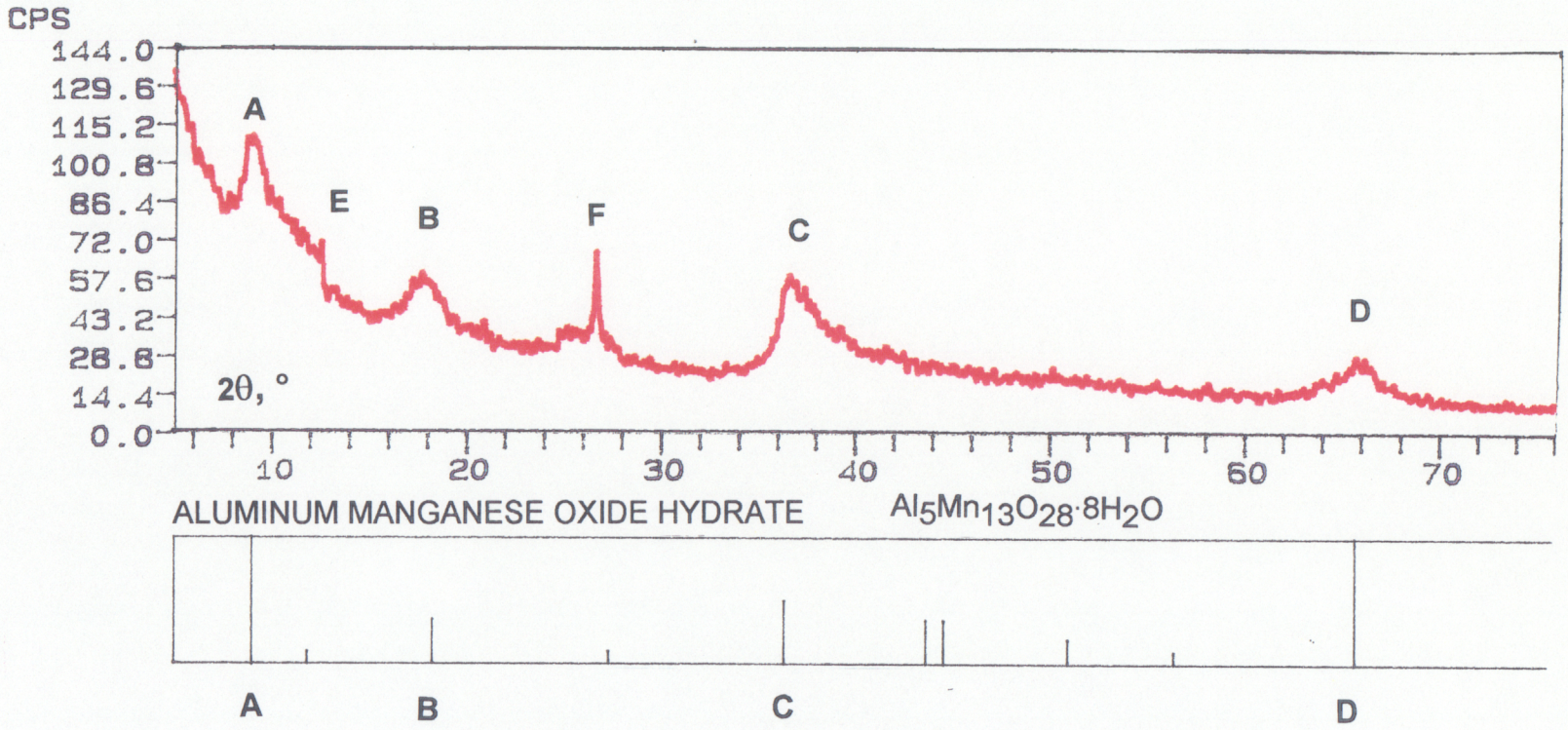

FIGURE 28 Powder x-ray diffractogram of material sonically dislodged from the Norfolk, NE oxide-coated anthracite filter media. Peaks A - D identified with corresponding peaks from Joint Committee on Powder Diffraction Standards reference pattern # 04 - 0098 for aluminum manganese oxide hydrate. Peak E possible match for $Mn_7O_{13}·5H_2O$ (see Figure 30 reference pattern), Peak F from SiO_2 (see Figure 29).

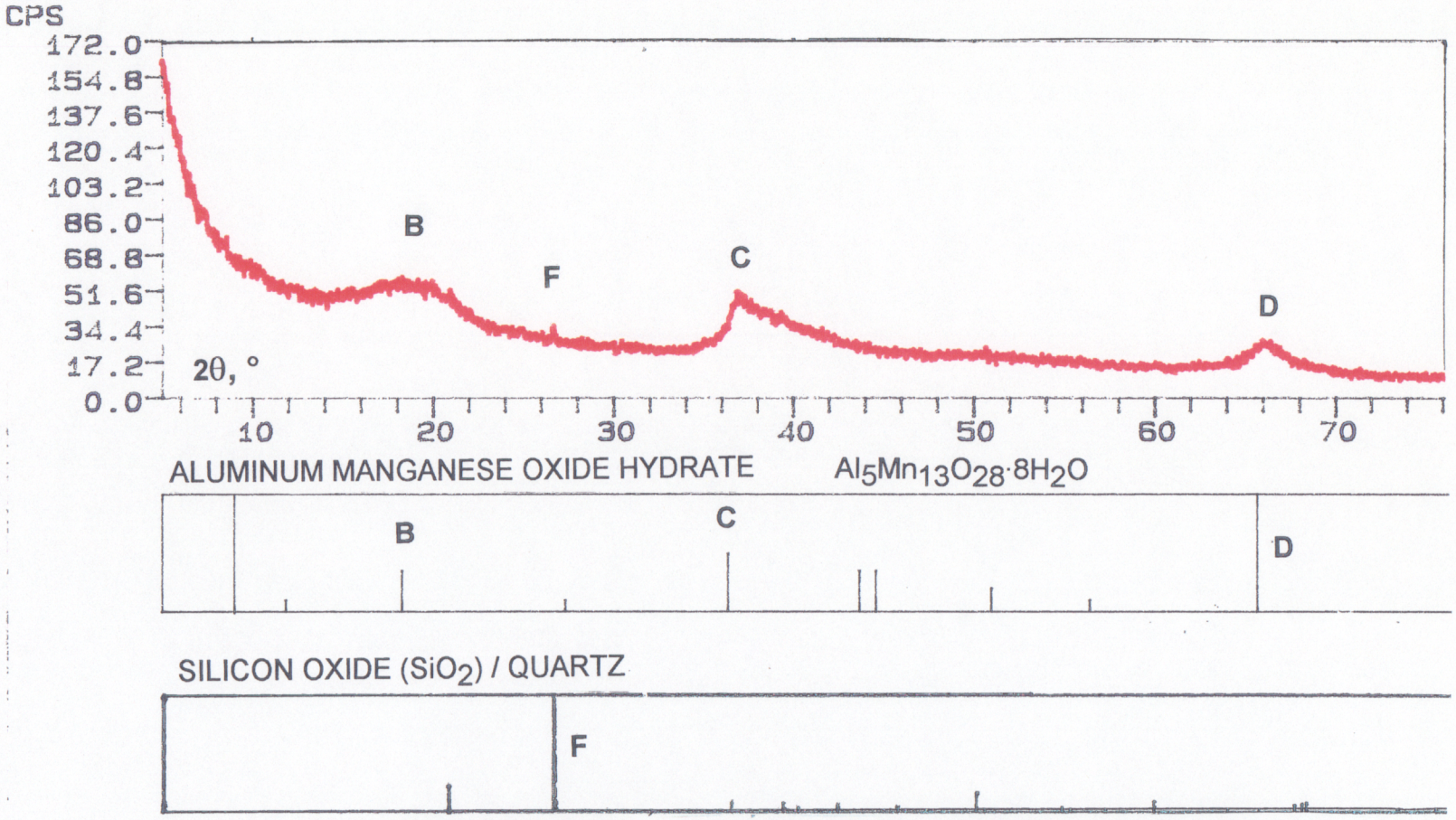

FIGURE 29 Powder x-ray diffractogram of material sonically dislodged from the Durham, NC Brown facility (archive sample) oxide-coated anthracite filter media. Peaks B - D identified with corresponding peaks from Joint Committee on Powder Diffraction Standards reference pattern # 04 - 0098 for aluminum manganese oxide hydrate. Peak F from SiO_2.

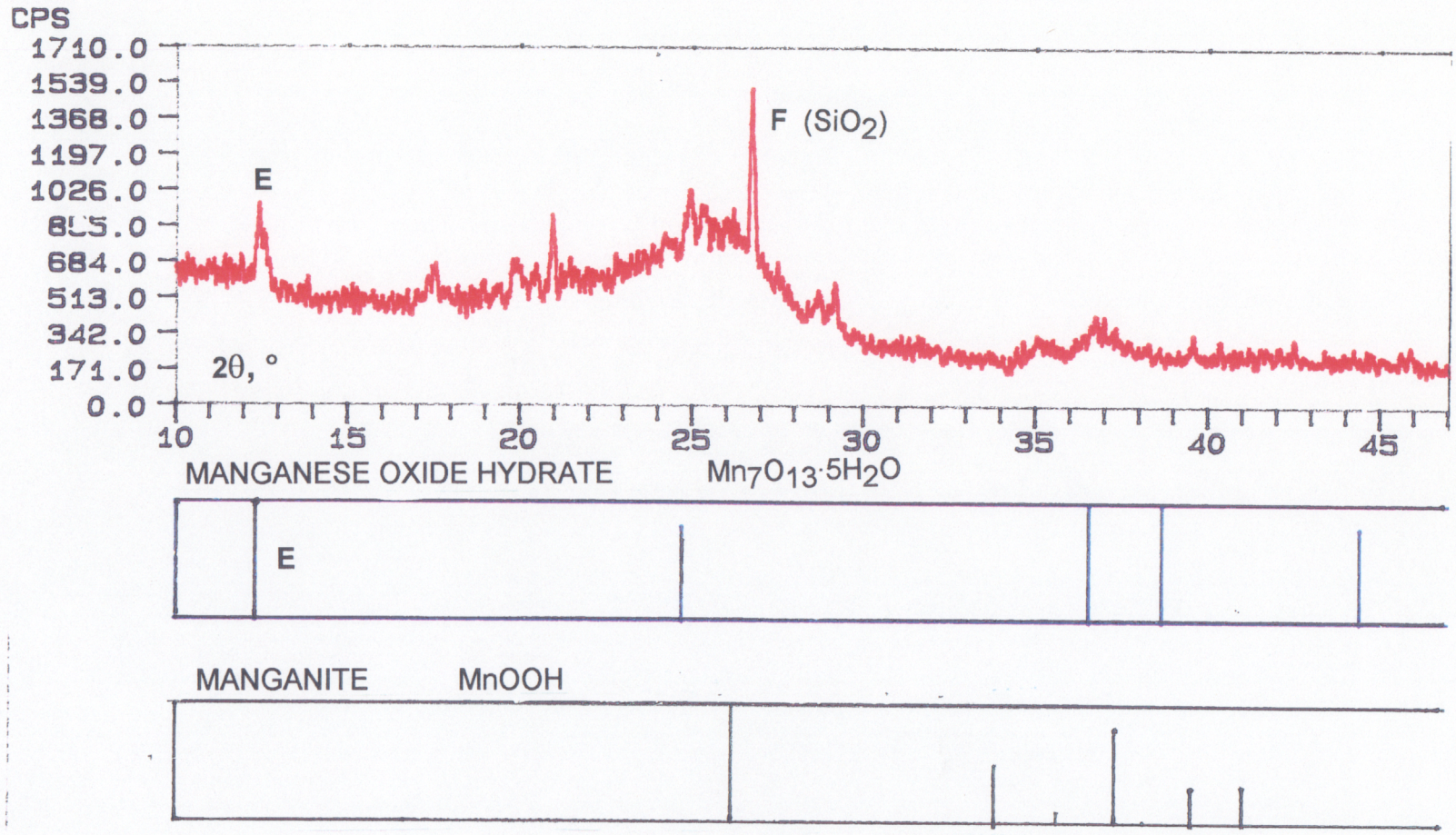

FIGURE 30 Powder x-ray diffractogram of material sonically dislodged from anthracite filter media synthetically coated with $MnO_{x(s)}$. Peak E corresponding to manganese oxide hydrate, $Mn_7O_{13}\cdot 5H_2O$.

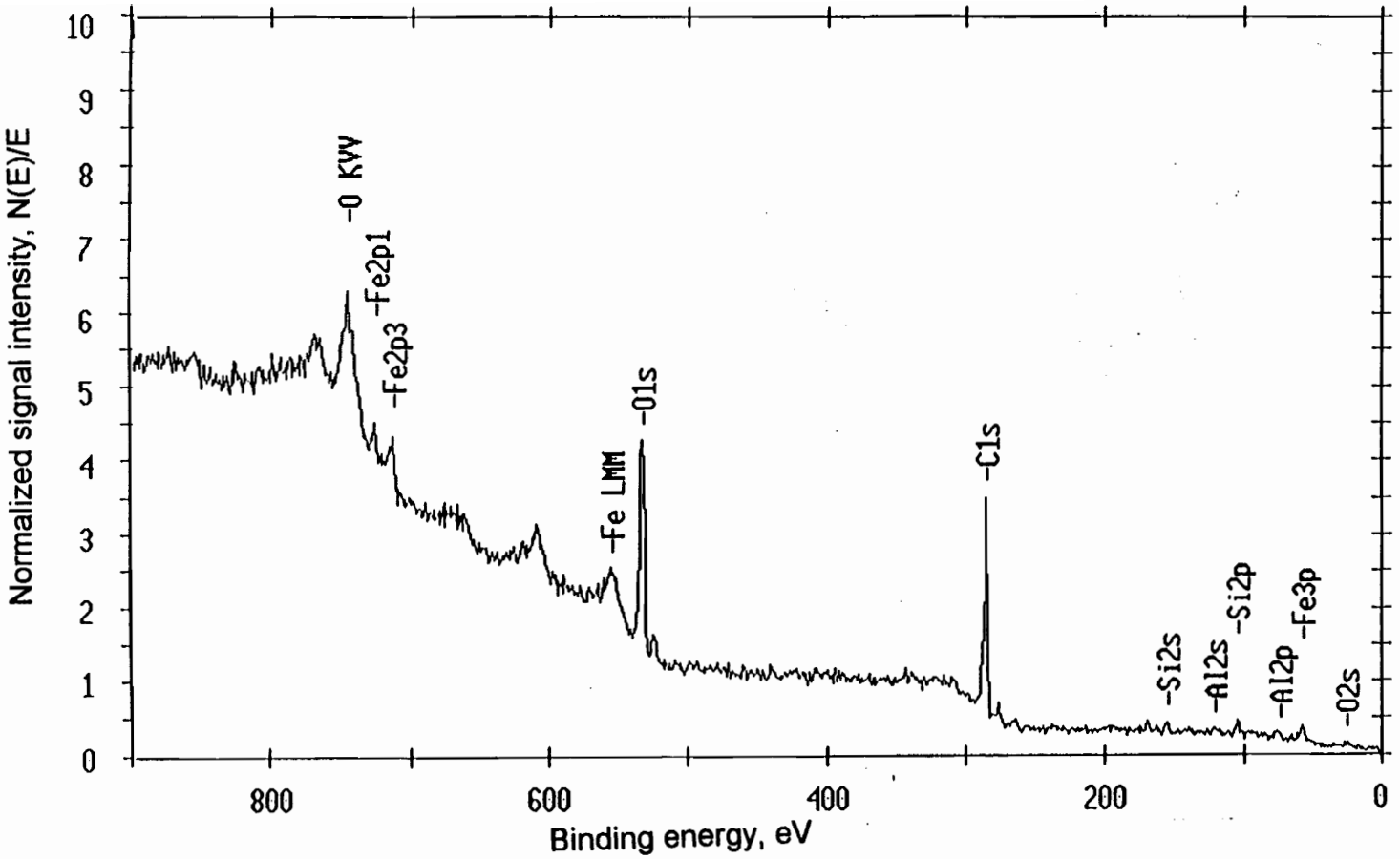

FIGURE 31 X-ray photoelectron spectrum of uncoated anthracite surface. Individual photoelectron peaks are labeled with the appropriate source orbital designation (e.g. C1s or Al2p). Characteristic Auger electron peaks are labeled by orbital transition (e.g. Fe LMM).

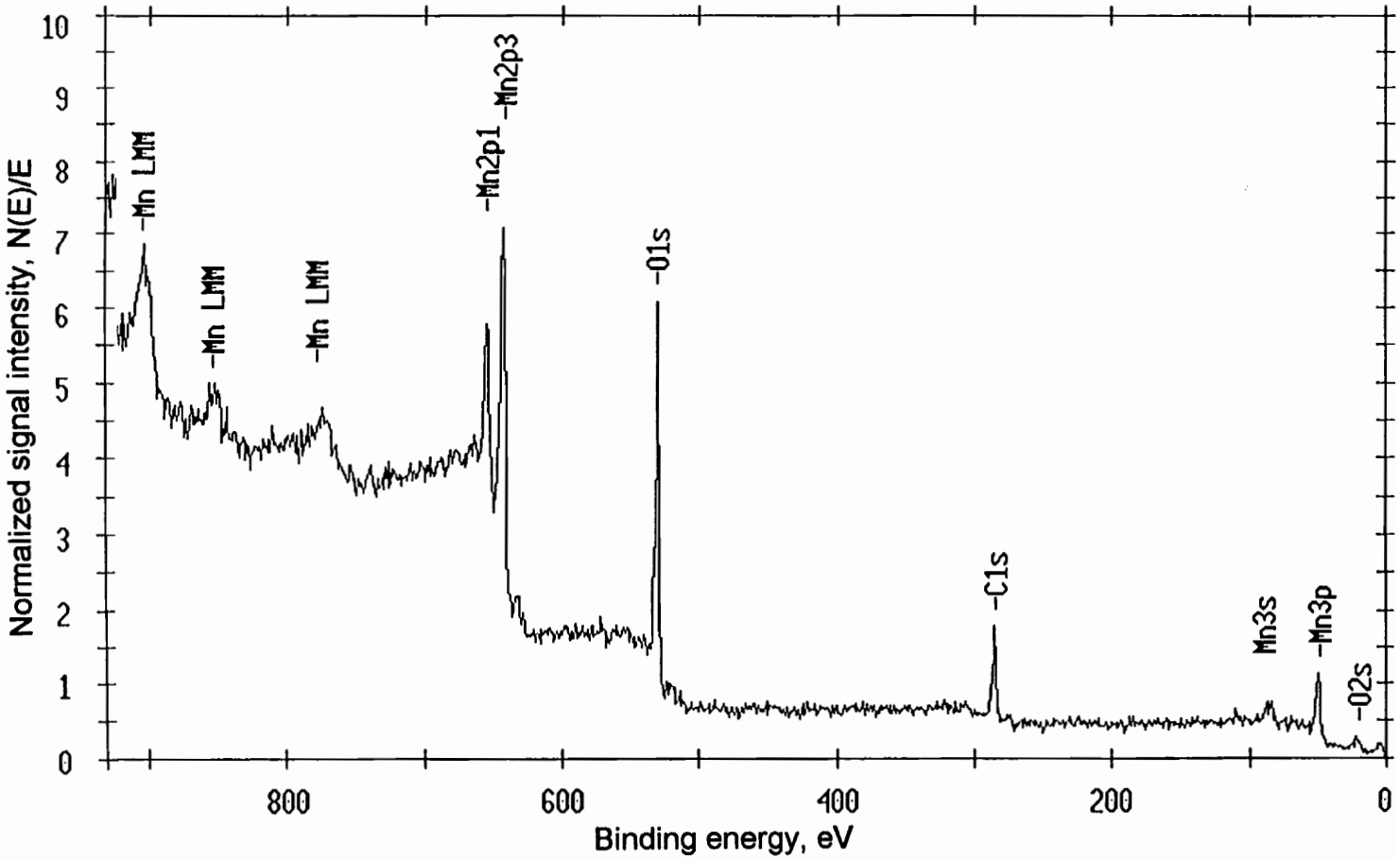

FIGURE 32A X-ray photoelectron spectrum of anthracite coated with synthetic $MnO_{x(s)}$. Individual photoelectron peaks are labeled with the appropriate source orbital designation (e.g. C1s or Mn3s). Characteristic Auger electron peaks are labeled by orbital transition (e.g. Mn LMM).

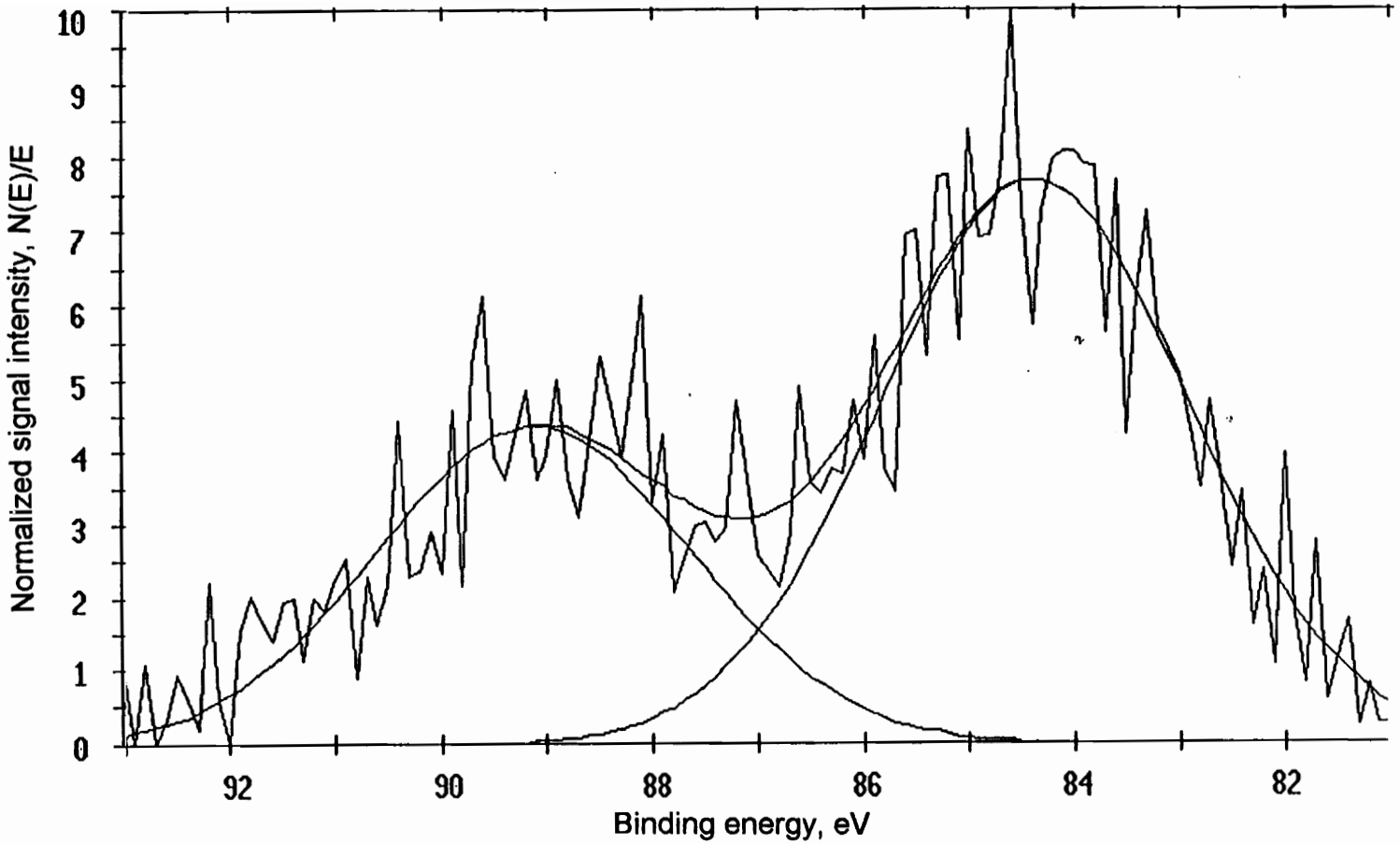

FIGURE 32B Scan of Mn3s peak multiplet region from X-ray photoelectron spectrum of anthracite coated with synthetic $MnO_{X(s)}$. Smooth curves are fitted to the data (jagged line). Fitted peak splitting is 4.75 eV, with peak area ratio of 1.74, consistent with Mn(IV) oxidation state in the outermost atomic layers.

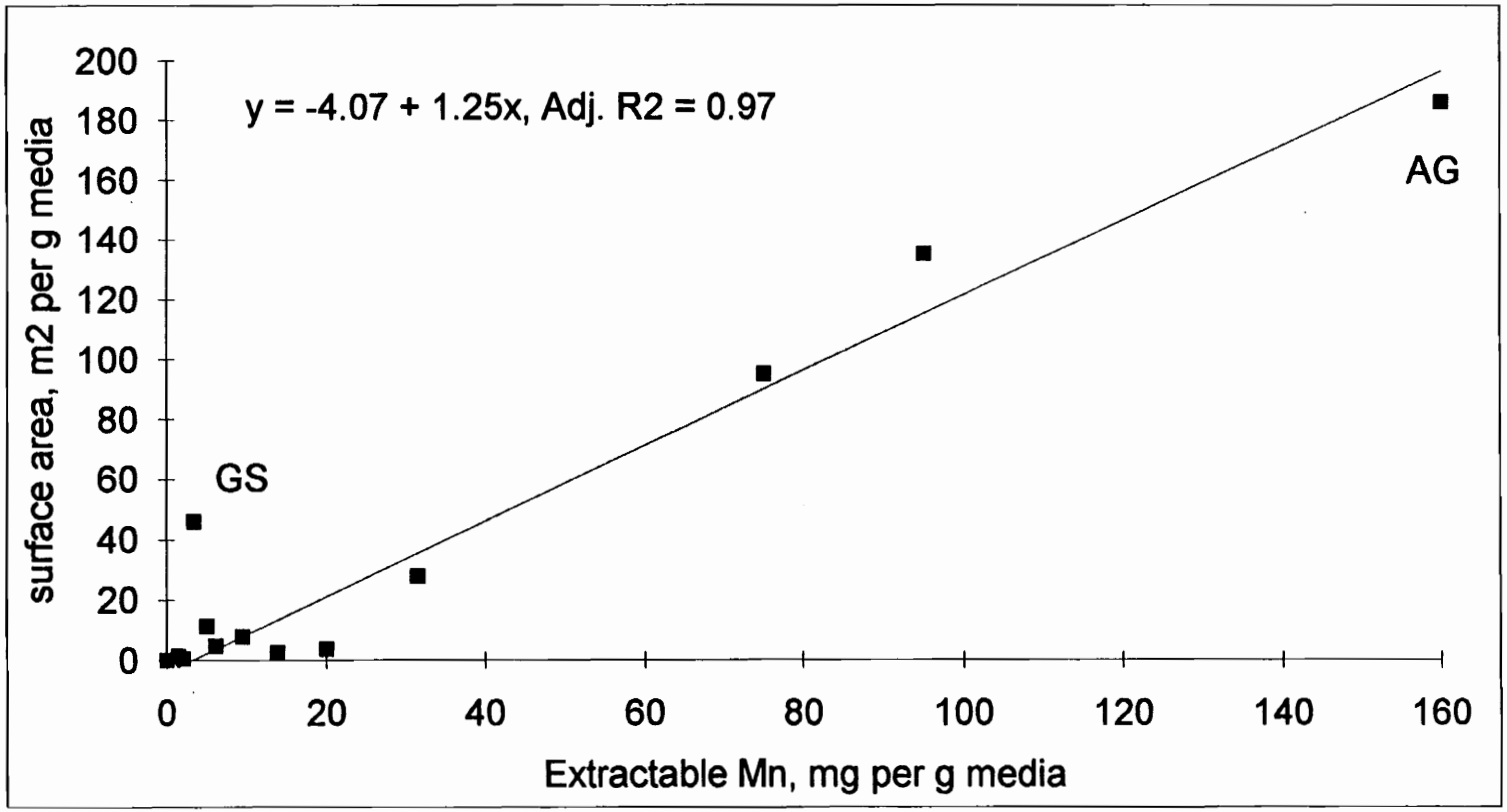

FIGURE 33 Surface area of oxide-coated filter media (natural and synthetic) vs. extractable Mn. Samples below 4 mg g^{-1} extractable Mn are synthetically coated anthracites. "AG" is the authigenic media from Norfolk, NE; GS is commercial Mn greensand, which was excluded from the regression.

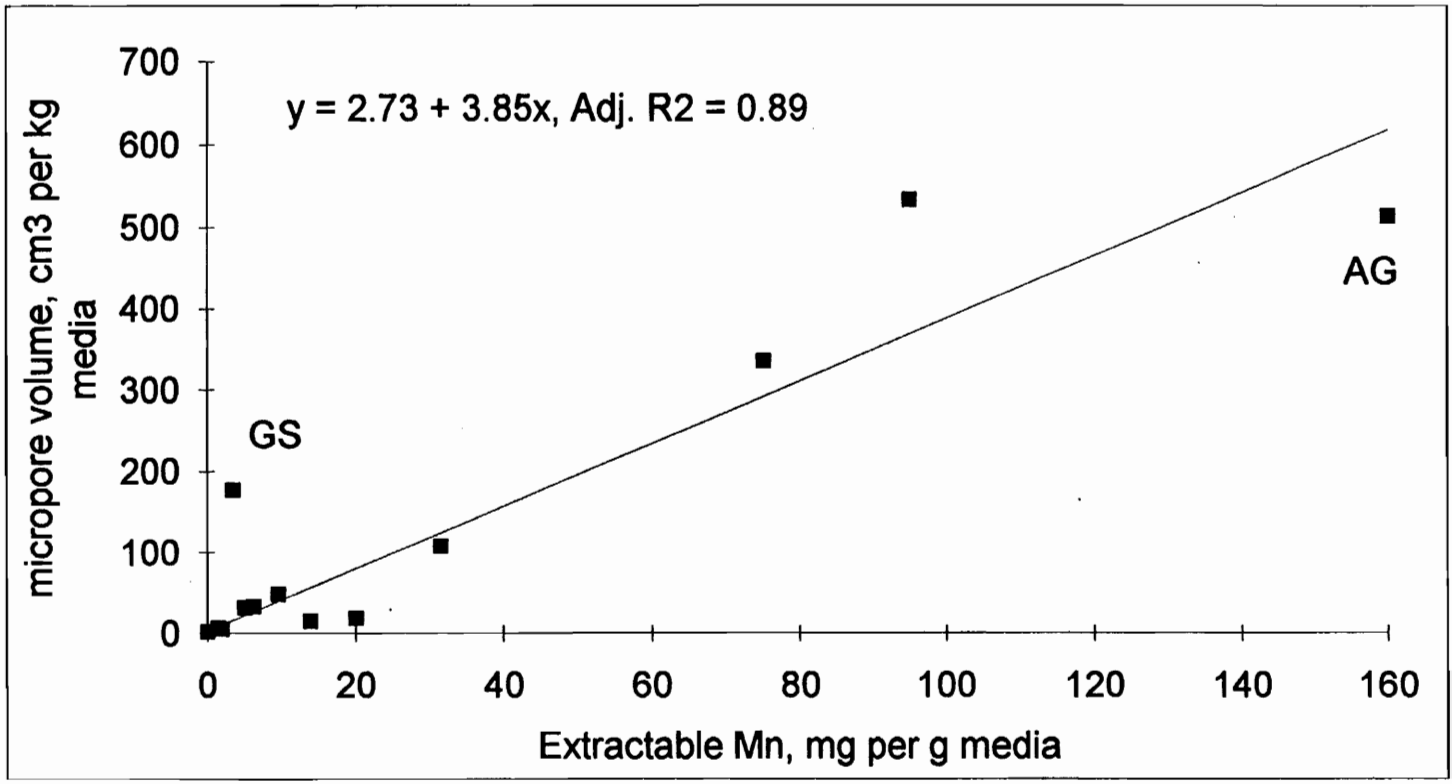

FIGURE 34 Micropore volume of oxide-coated filter media (natural and synthetic) vs. extractable Mn. Samples below 4 mg g^{-1} extractable Mn are synthetically coated anthracites. "AG" is the authigenic media from Norfolk, NE; GS is commercial Mn greensand, which was excluded from the regression.

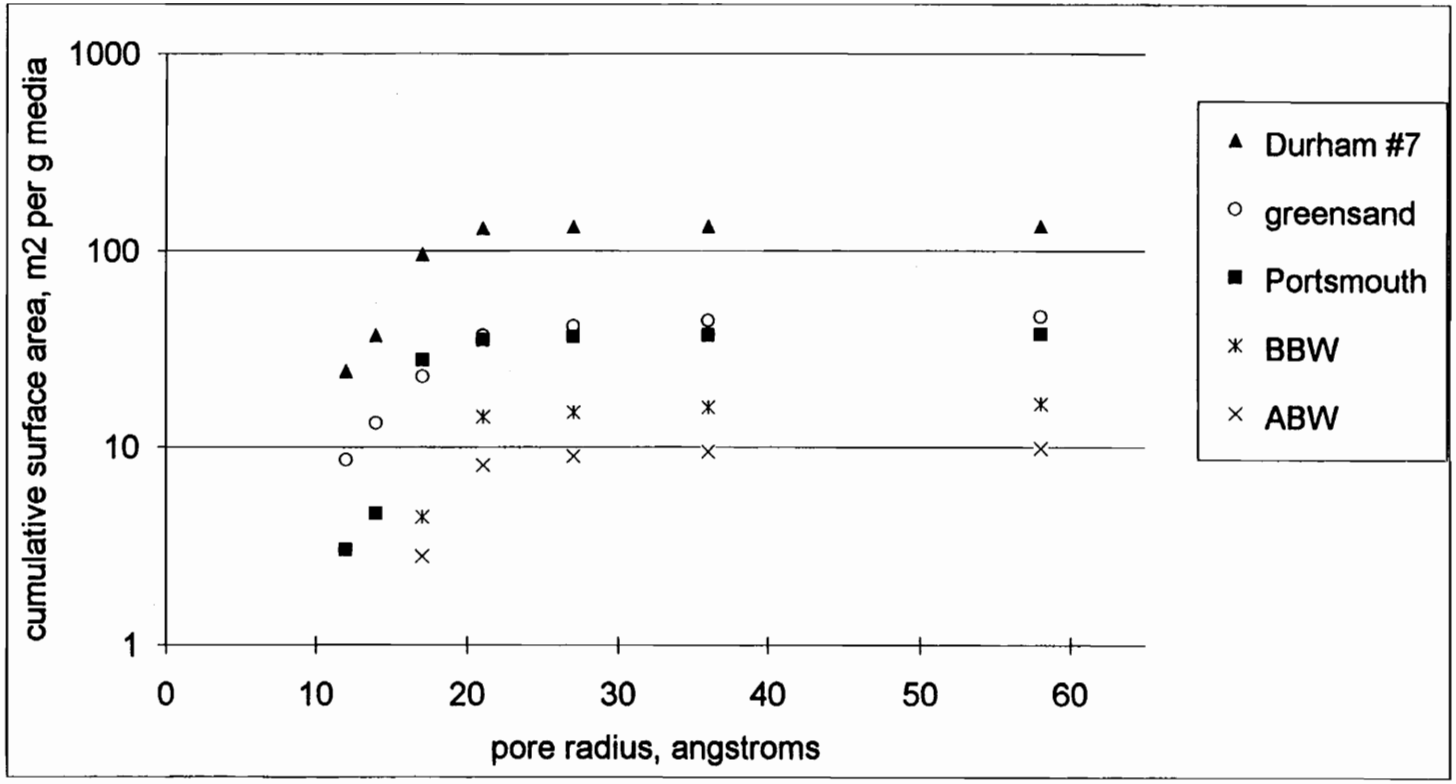

FIGURE 35 Cumulative surface area - pore size distribution for naturally coated anthracite media and commercial Mn greensand. "BBW" = Durham, NC Brown facility 1992 sample before backwash, "ABW" = after backwash. See Table 3 for media descriptions.

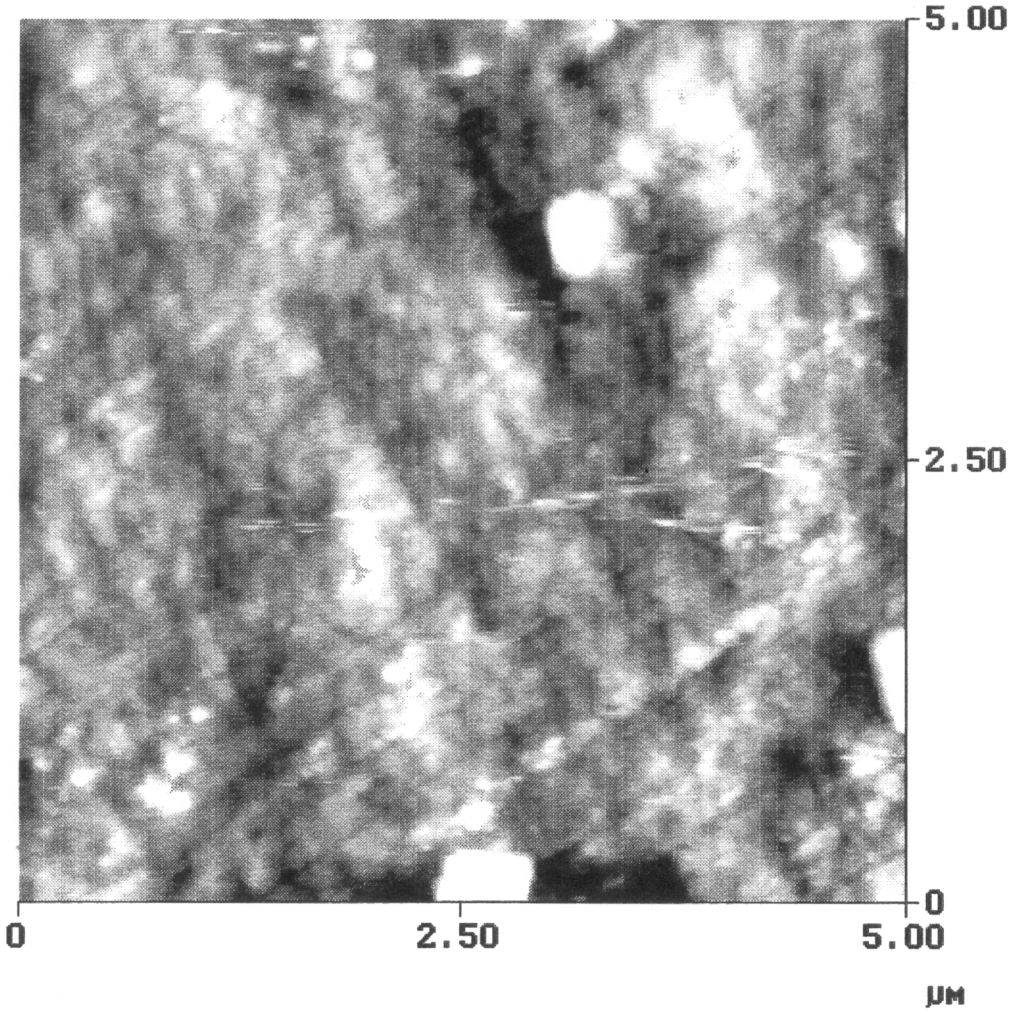

FIGURE 36 Atomic force microscopy image of visually "shiny", flat region of uncoated anthracite, showing surface inclusions (top and bottom center), and transverse striations.

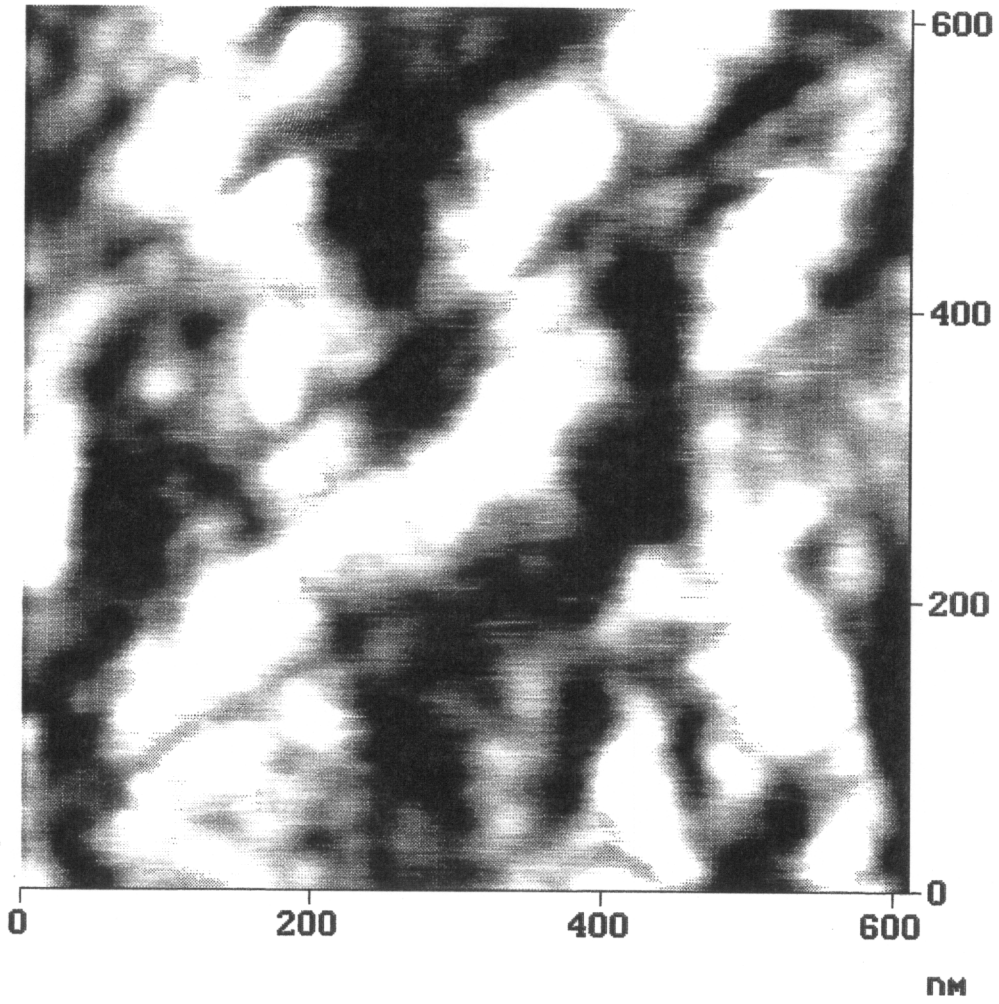

FIGURE 37 Atomic force microscopy image of visually "shiny" flat region of uncoated anthracite, detail of striations and grooves about 20 nm wide.

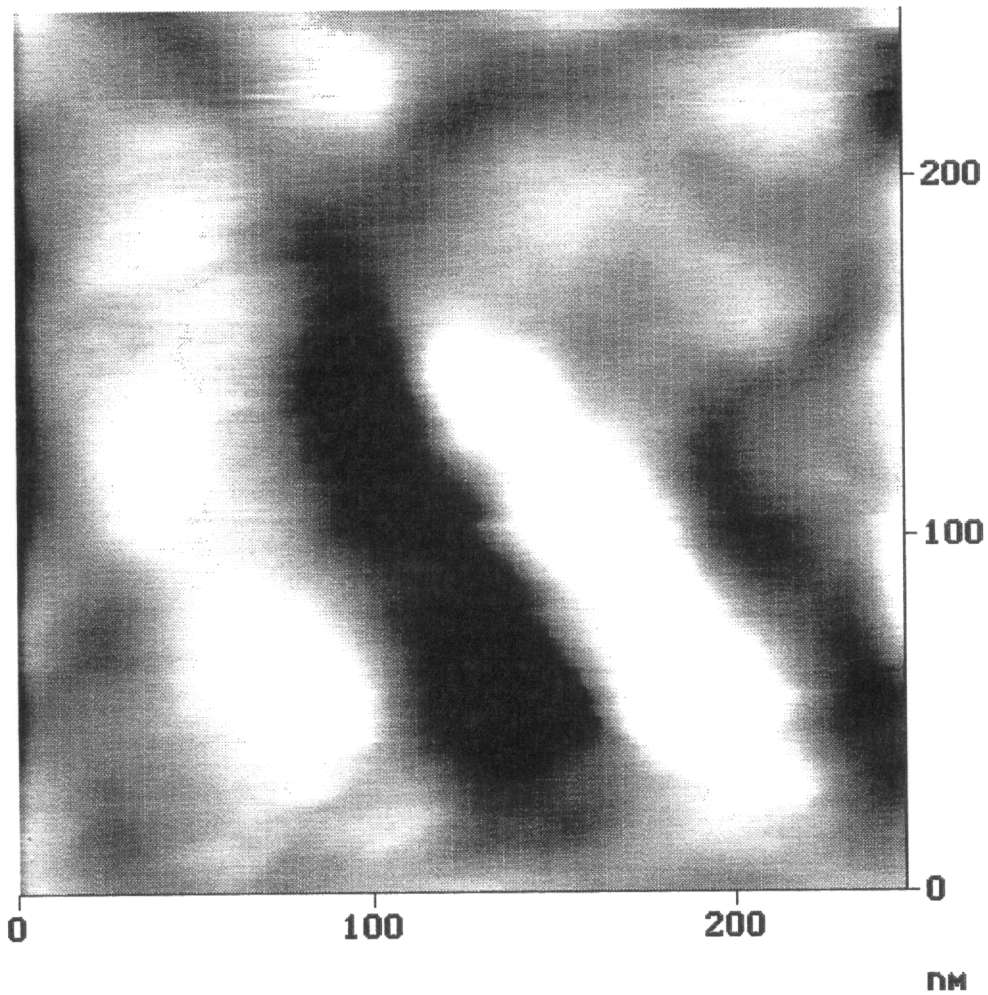

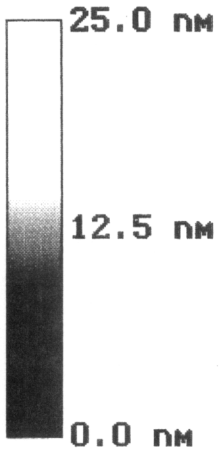

FIGURE 38 Atomic force microscopy image of visually "shiny" flat region of uncoated anthracite, showing single depression feature.

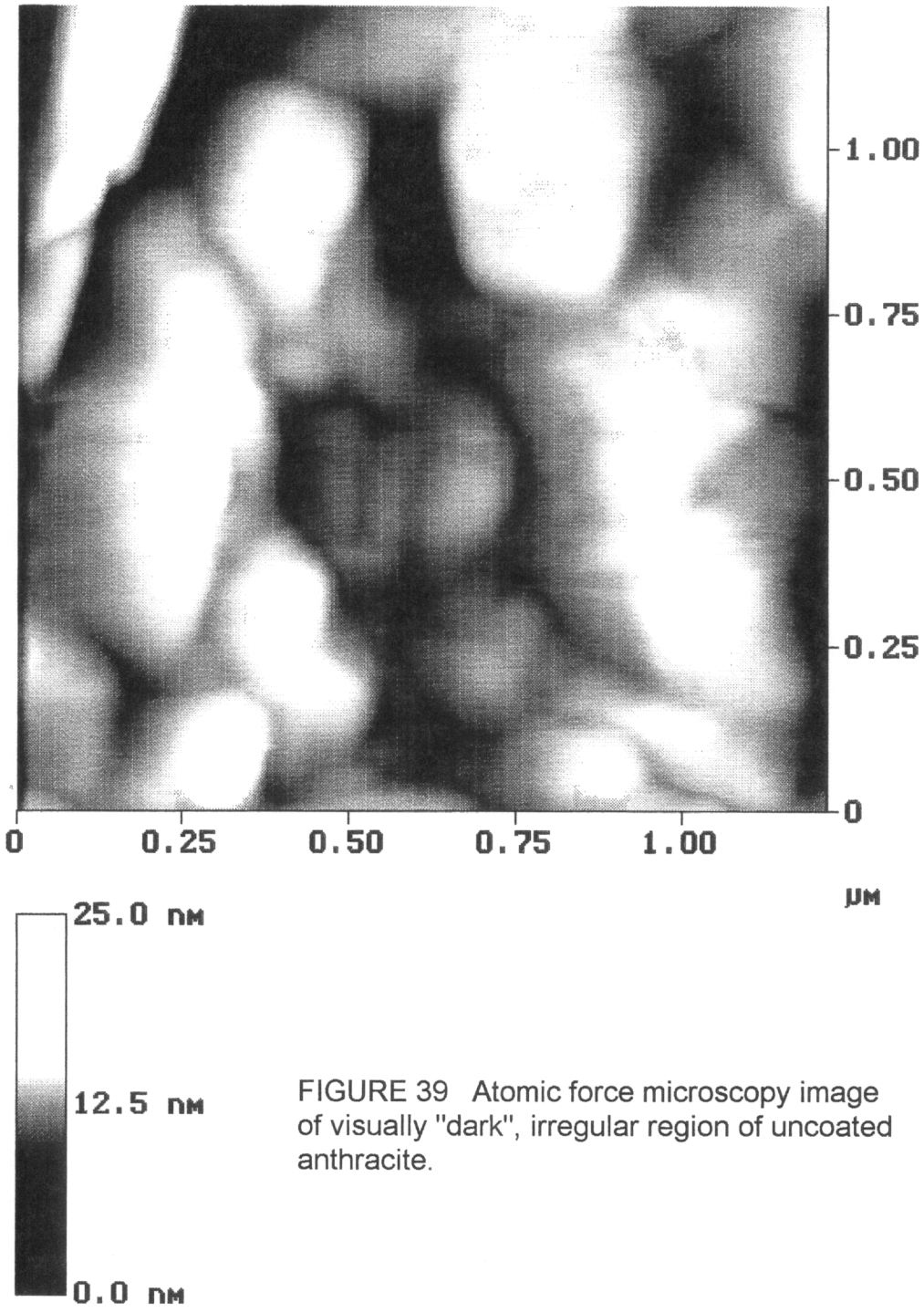

FIGURE 39 Atomic force microscopy image of visually "dark", irregular region of uncoated anthracite.

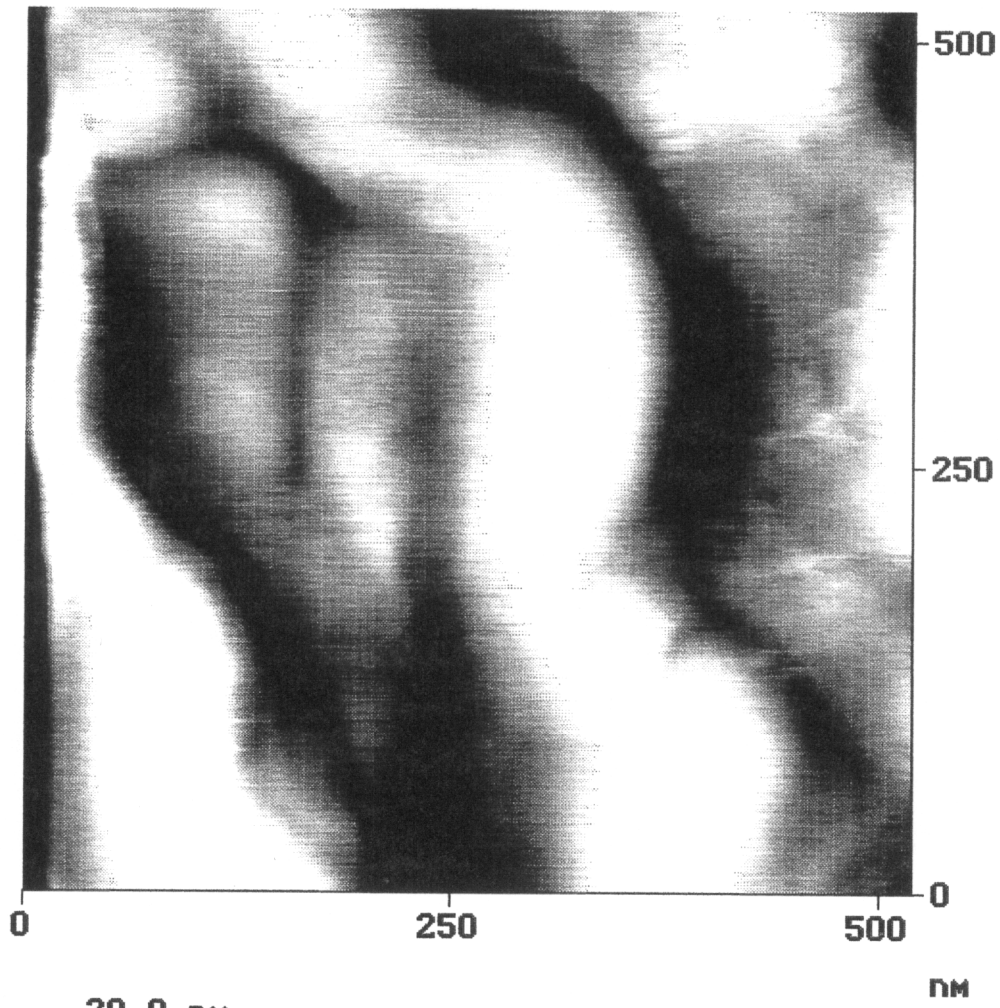

FIGURE 40 Atomic force microscopy image of visually "dark", irregular region of uncoated anthracite, detail of center of Figure 39.

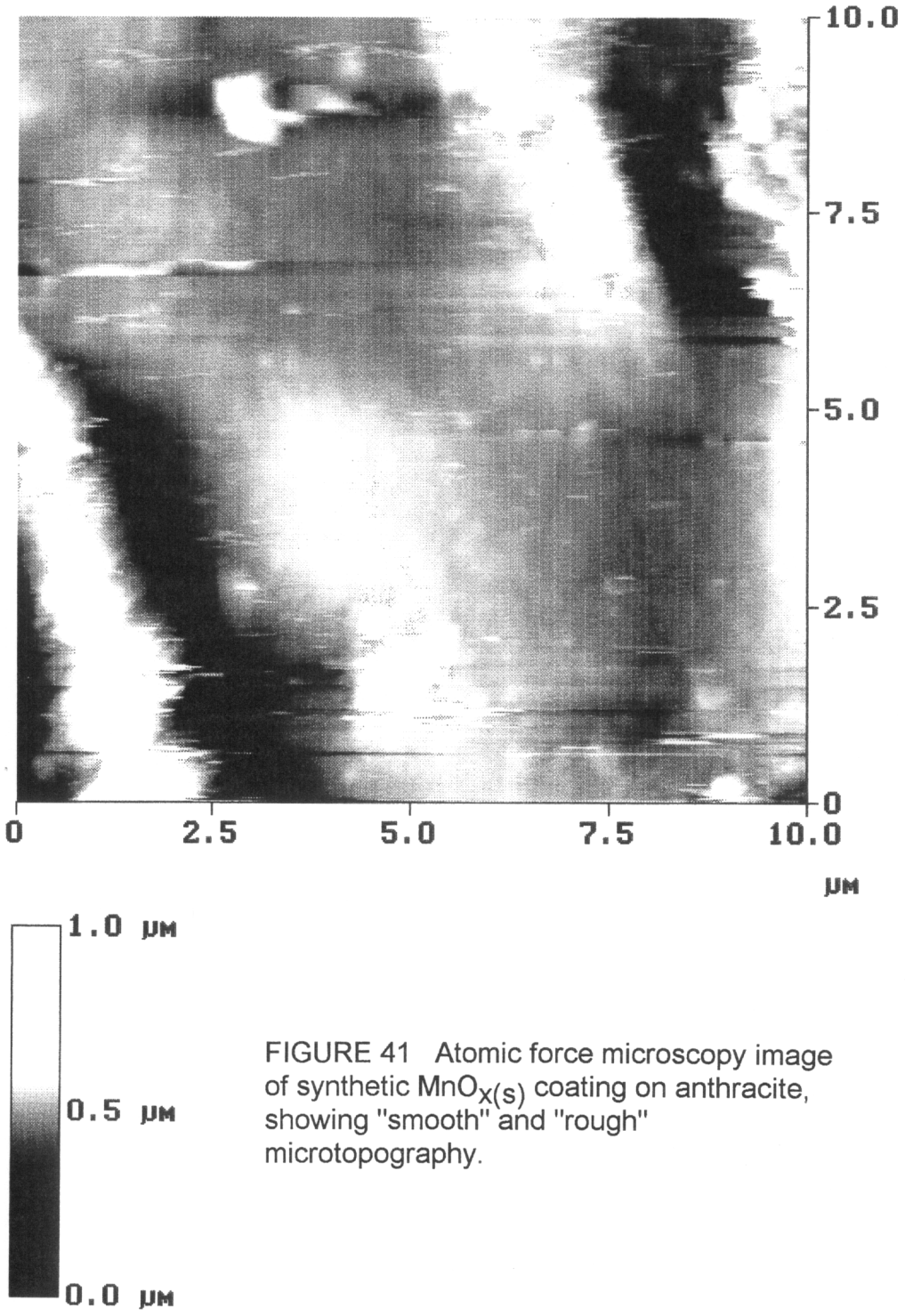

FIGURE 41 Atomic force microscopy image of synthetic $MnO_{X(s)}$ coating on anthracite, showing "smooth" and "rough" microtopography.

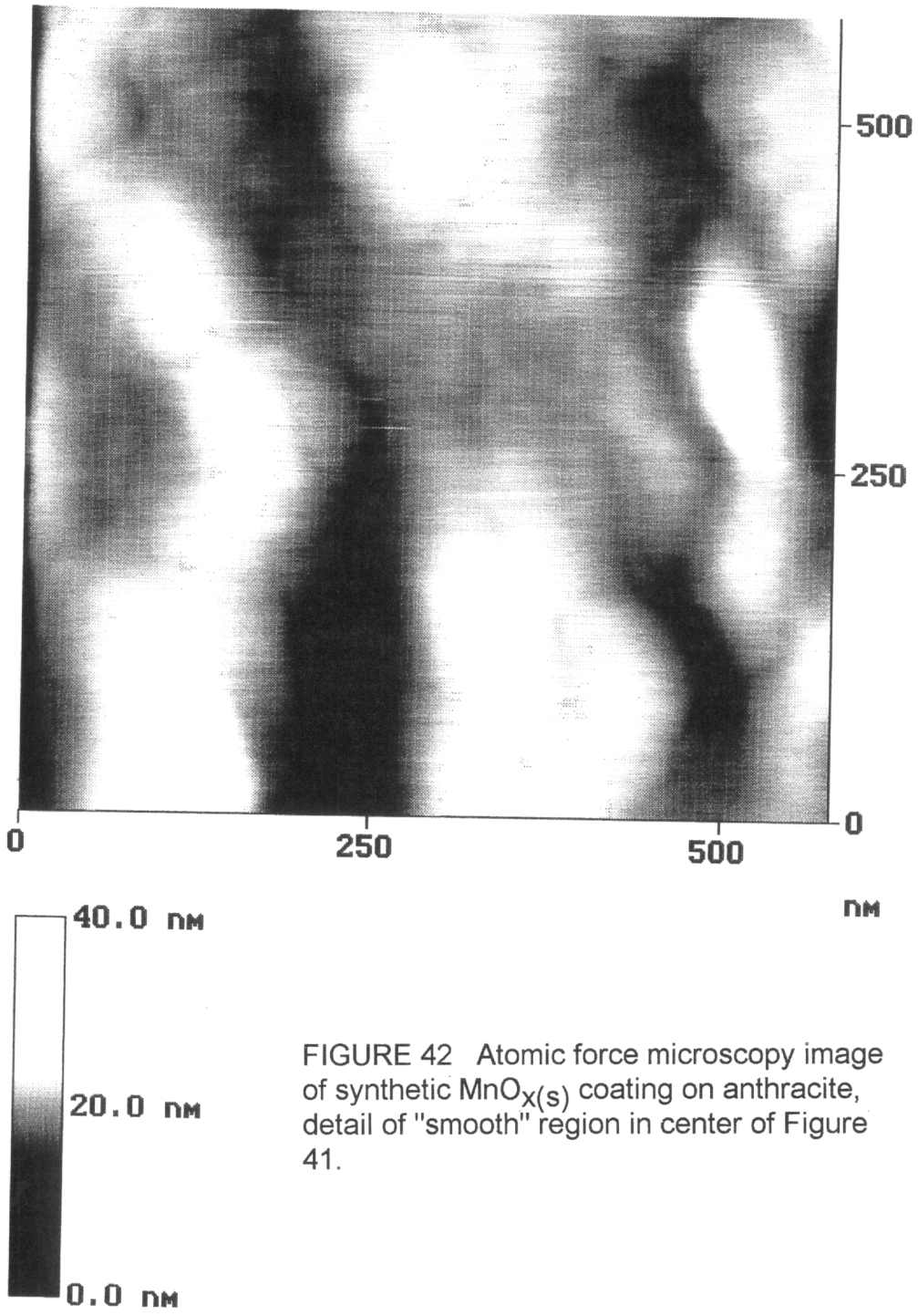

FIGURE 42 Atomic force microscopy image of synthetic $MnO_{X(s)}$ coating on anthracite, detail of "smooth" region in center of Figure 41.

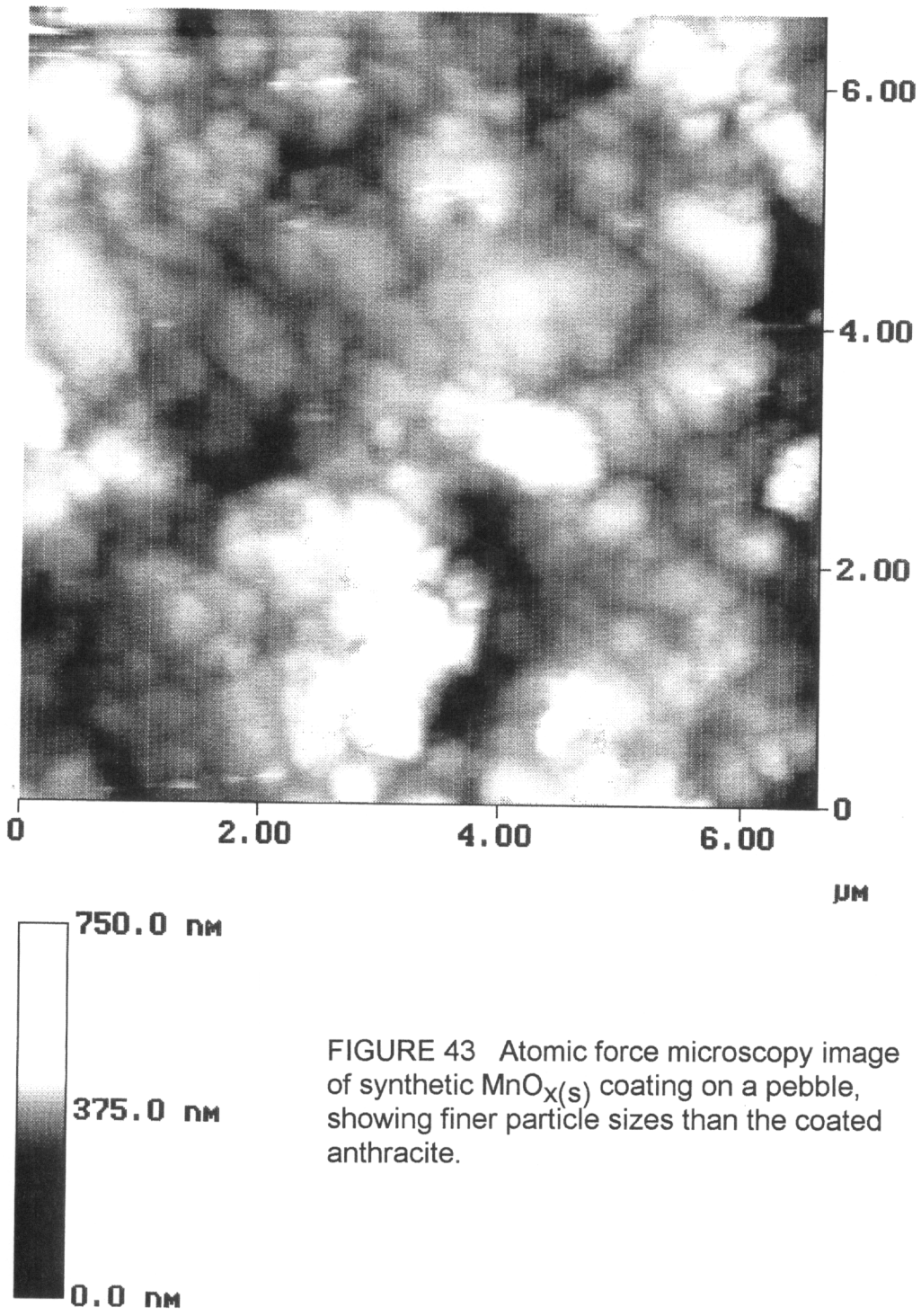

FIGURE 43 Atomic force microscopy image of synthetic $MnO_{x(s)}$ coating on a pebble, showing finer particle sizes than the coated anthracite.

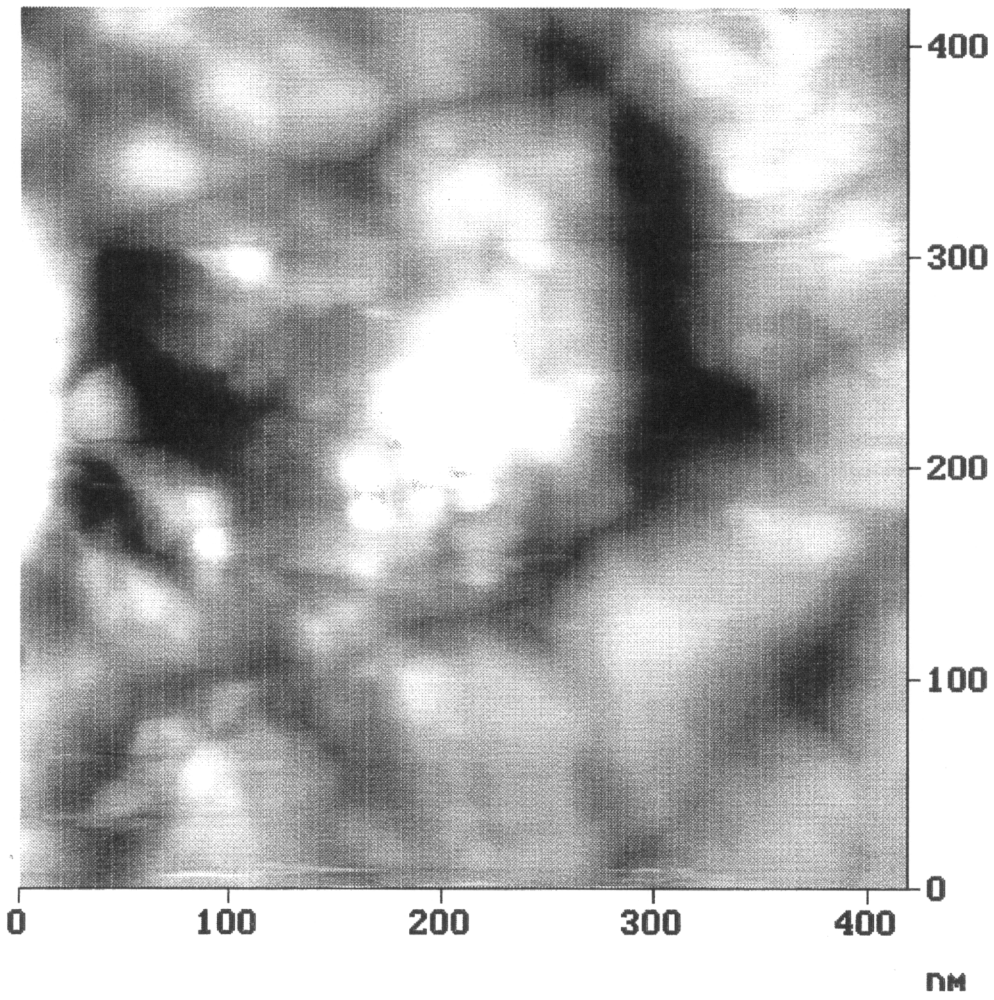

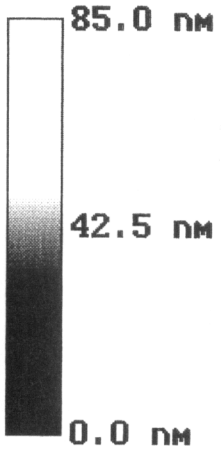

FIGURE 44 Atomic force microscopy image of synthetic $MnO_{X(S)}$ coating on a pebble, detail of fine surface structure, a cluster of 10 nm diameter features at center.

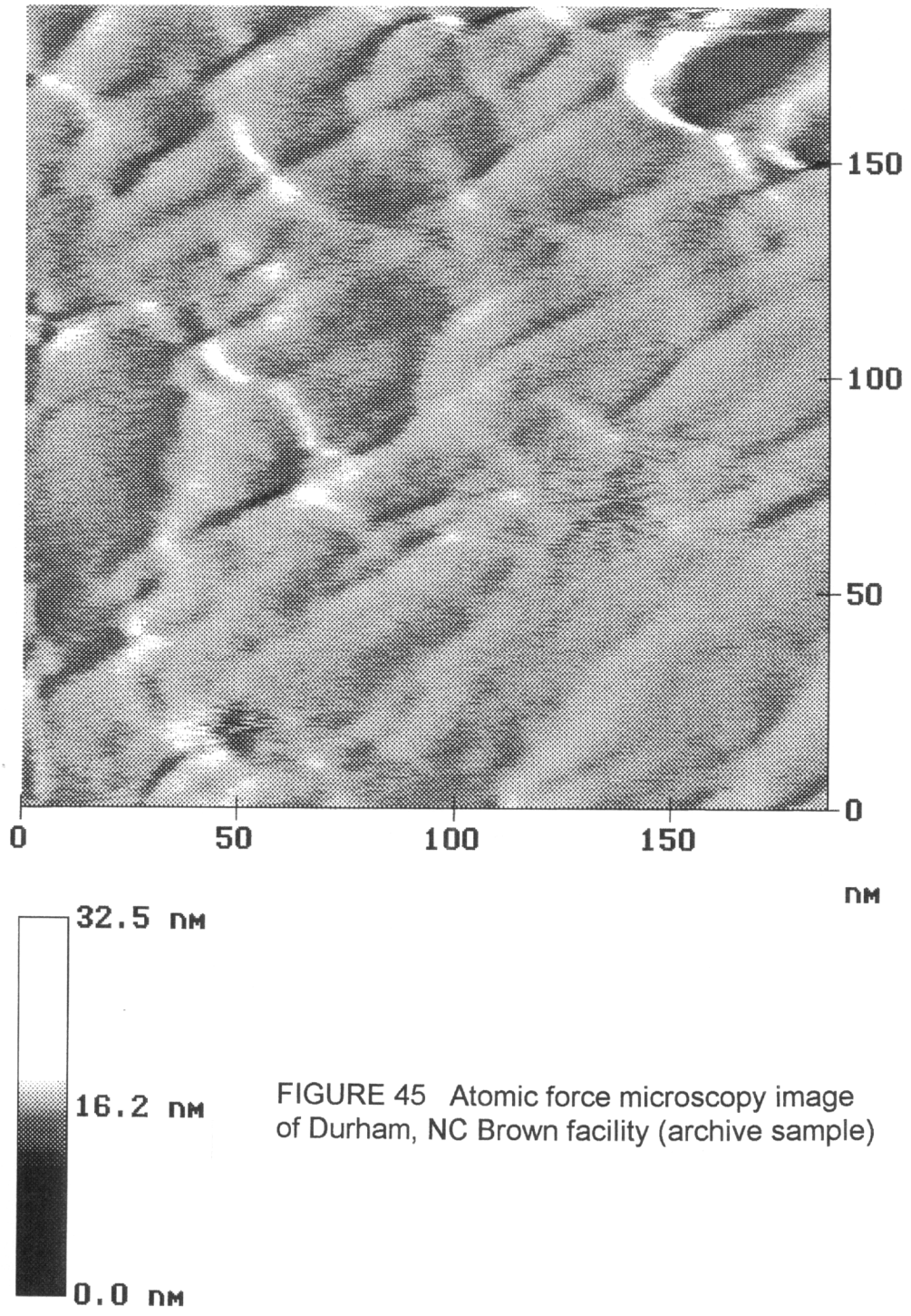

FIGURE 45 Atomic force microscopy image of Durham, NC Brown facility (archive sample)

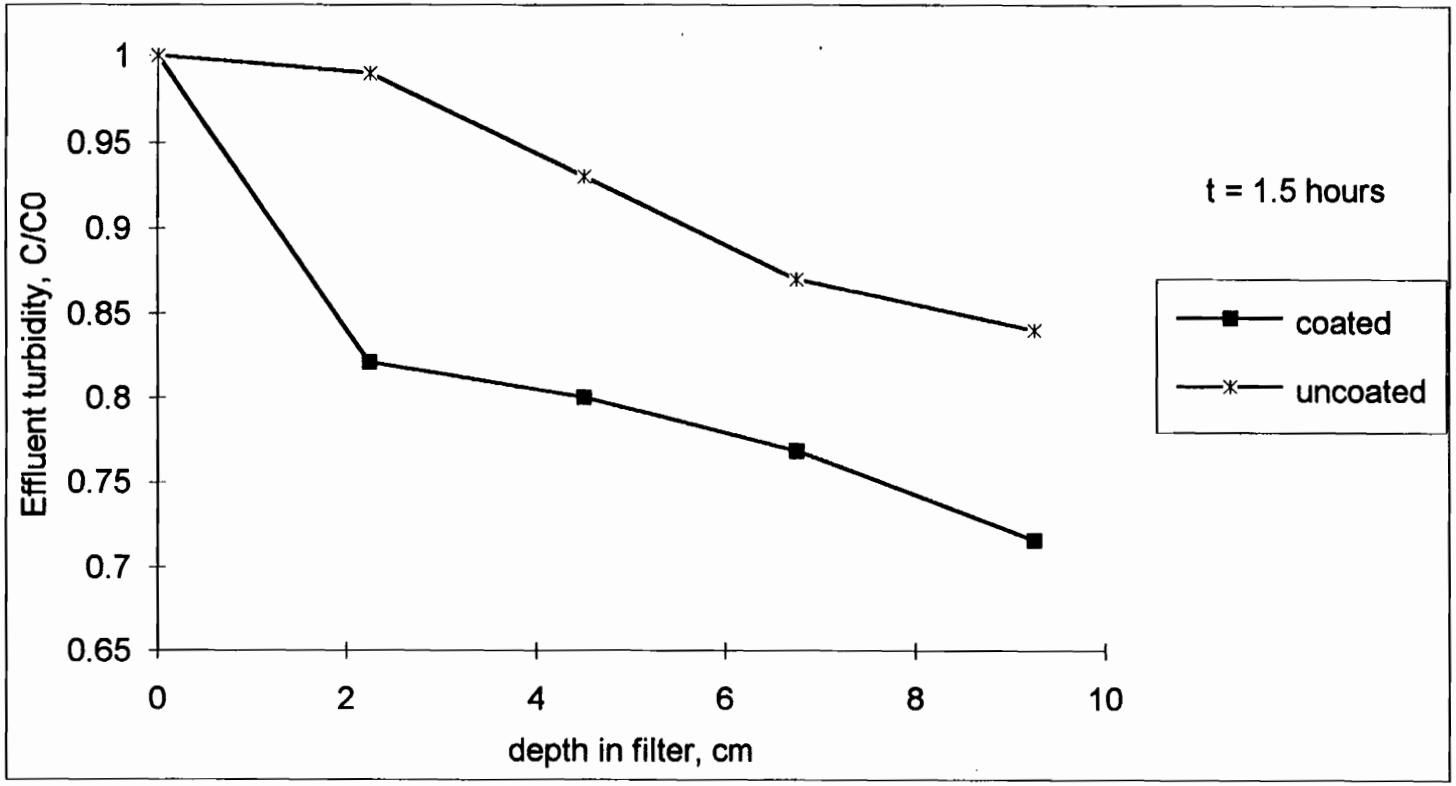

FIGURE 46 Turbidity removal 1.5 hours after start of filtration by anthracite media, uncoated and synthetically coated with $MnO_{x(s)}$, with 1.25 mg L^{-1} kaolinite in deionized water applied at 2.5 gpm ft^{-2}, pH 7.0, $[Ca^{2+}]$ = 10 mg L^{-1}, influent turbidity approximately 1 NTU.

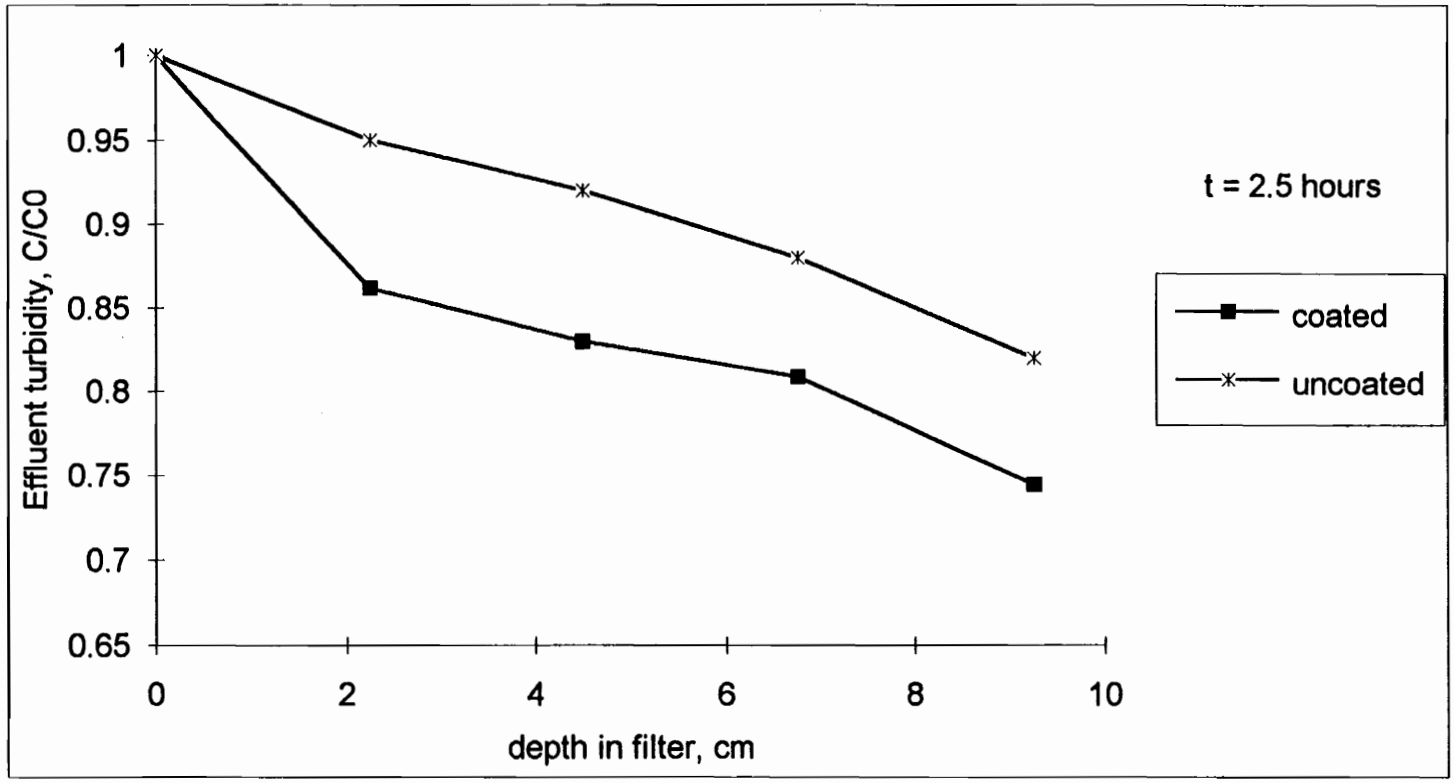

FIGURE 47 Turbidity removal 2.5 hours after start of filtration by anthracite media, uncoated and synthetically coated with $MnO_{x(s)}$, with 1.25 mg L^{-1} kaolinite in deionized water applied at 2.5 gpm ft^{-2}, pH 7.0, $[Ca^{2+}]$ = 10 mg L^{-1}, influent turbidity approximately 1 NTU.

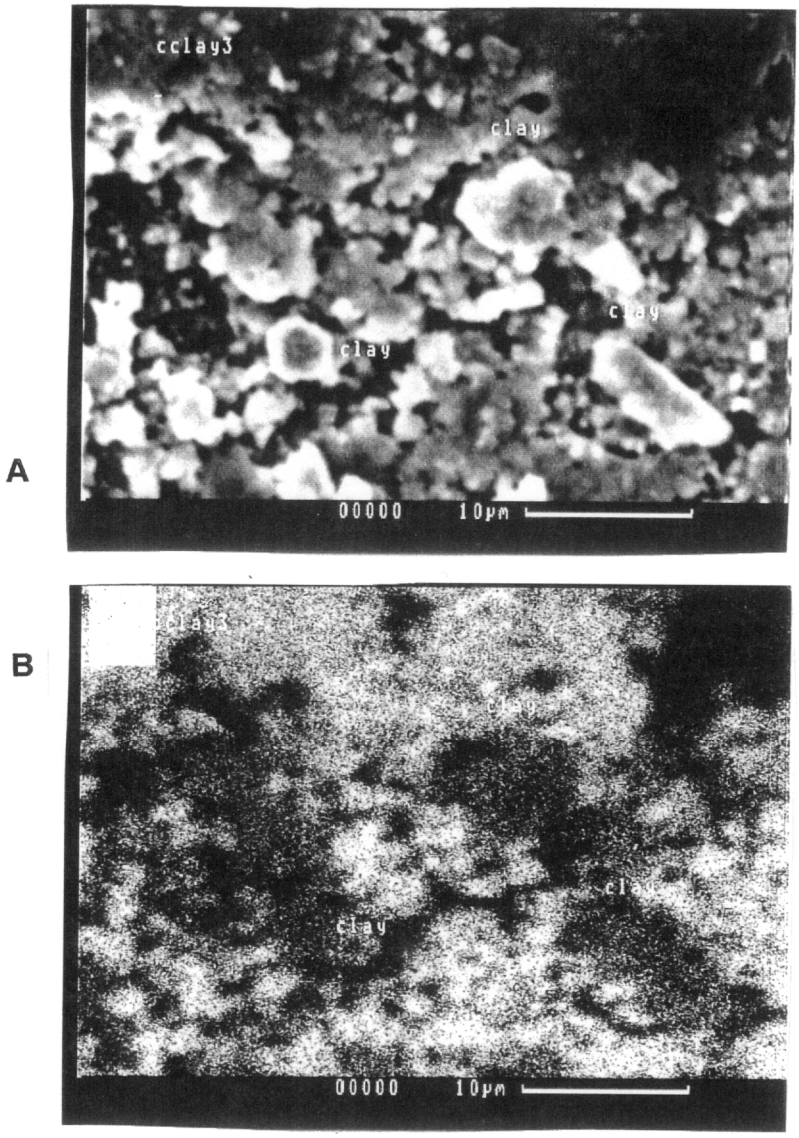

FIGURE 48 A) SEM image of three kaolinite particles retained on the $MnO_{x(s)}$ surface of synthetically coated anthracite, difficult to distinguish from background.

B) BSE image of same region as A), showing kaolinite particles appearing as dark patches due to lower nuclear density. Atomic ratio of 1:1 confirmed by EDS for the particles, consistent with kaolinite composition of $Al_2Si_2O_5(OH)_4$.

CHAPTER 2

DEVELOPMENT OF A METHOD FOR COATING FILTER MEDIA WITH SYNTHETIC MANGANESE OXIDE

ABSTRACT

A method was developed to coat anthracite and sand filter media with synthetic manganese oxides. The two-stage method used a stirred tank reactor followed by a recirculating flow fixed-bed reactor. Treated anthracite developed encapsulating coatings of manganese oxides up to 30 microns thick, at loadings over 4 mg g^{-1} extractable Mn^{2+}. Media were characterized by B.E.T. surface area analysis, electron microscopy with energy-dispersive x-ray spectroscopy, and x-ray photoelectron spectroscopy. Lab-scale column tests confirmed Mn-removal capability of the synthetically coated media in adsorption and oxidation modes. This method may help improve the removal of Mn^{2+} from drinking water and hazardous effluents by the oxide-coated media process.

INTRODUCTION

Anthracite and sand filter media used in conventional drinking water filters may routinely develop exterior coatings or "stains" of Mn-bearing oxides. The ability of these oxide-coated media (OCM) to remove Mn^{2+} from solution has been extensively studied.[1-4] In the presence of a regenerative oxidant such as hypochlorite, OCM remove soluble Mn^{2+} through an abiotic adsorption and oxidation process known as the "natural greensand effect" (NGE). The NGE

process is "natural" in that the mineral deposits develop in-situ within weeks to months on new, uncoated filter media during normal filter operation. The OCM mimic the Mn^{2+} removal ability of Mn greensand media, the aluminosilicate mineral glauconite treated with permanganate.[5] Due to its size (dia. $\leq$ 0.5 mm), using greensand for Mn^{2+} removal may require pressurized filtration to compensate for increased hydraulic head loss, and periodic regeneration of the bed with permanganate to restore adsorption capacity is needed.[1] Both of these requirements entail added costs compared with the NGE process as typically employed in filtration of surface or groundwater supplies high in dissolved Mn^{2+}.

The U.S. EPA has proposed a primary, enforceable maximum contaminant level (MCL) of 0.2 mg L^{-1} for Mn in drinking water, and the existing secondary MCL guideline is 0.05 mg L^{-1}.[6] Since elevated Mn^{2+} concentrations in surface raw water supplies may be seasonal, having a means to quickly implement the NGE process in existing filters is desirable for a plant where other Mn^{2+} removal processes such as greensand filters are not maintained. In concert with development of a design model for the NGE process, a synthetic coating technology for use in generating OCM was developed. A rapid coating method could be applicable in practice for NGE process implementation and maintenance so that utilities could respond to a sudden increase in raw water Mn^{2+} levels. An alternative existing method relies upon addition of potassium permanganate to filters,[7] but in some instances the effectiveness of this method may involve regeneration of an existing coating's adsorption capacity rather than deposition of new oxide onto uncoated media. One facility reported that treatment of filters with 100 mg L^{-1} $KMnO_4$ increased the oxide coating from an initial 0.26 mg g^{-1} extractable Mn^{2+} to 0.34 mg g^{-1} after two days of treatment.[8]

The primary objectives of this study were the laboratory-scale production and physical and chemical characterization of kilogram quantities of homogeneously coated media. This synthetic media was used for laboratory column studies of the NGE process. The goal of the work presented here was not to rigorously delineate the fundamental chemical reactions and kinetics of the coating process to a degree suitable for scale-up to industrial production. Consideration of likely mechanistic pathways for surface chemical reactions led to development of a method based on the reaction of free chlorine and Mn^{2+} at the media surface. The laboratory protocol for method development began with "trial and error" experiments, guided by the working hypothesis that there should be a way to accelerate the slow "natural" mechanism of OCM formation. The NGE process has been considered as reactions between a sorptive mineral surface of manganese oxide (or $MnO_{x(s)}$, where x varies from 1 to 2), dissolved Mn^{2+}, and an oxidant such as hypochlorite. Coffey *et al.*[4] modeled Mn oxidation in the presence of free chlorine and oxide surface after Nakanishi:[9,10]

$$Mn^{2+} + MnO(OH)_{2(s)} \Leftrightarrow MnO_2MnO_{(s)} + 2H^+ \quad (1)$$

$$MnO_2MnO_{(s)} + HOCl \Rightarrow 2MnO_{2(s)} + H^+ \quad (2)$$

An implicit assumption here is the regeneration of one surface site as $MnO(OH)_{2(s)}$ and incorporation of one MnO_2 into the oxide phase. Keeping the regenerated sites in the accounting, the overall reaction is:

$$Mn^{2+} + MnO(OH)_{2(s)} + HOCl + H_2O \Rightarrow MnO_{2(s)} + MnO(OH)_{2(s)} + 3H^+ + Cl^- \quad (3)$$

The above sequence of reactions requires two hydroxyl groups per adsorption site, or bidentate complexation. Following the convention of Luther[11] to describe aqueous phase oxidation by O_2, reactions (1) and (2) may be written in terms of a bidentate complex 2[S-OH], where S is Mn(IV):

$$[Mn^{II}(H_2O)_6]^{2+} + 2[S^{IV}\text{-}OH] \Leftrightarrow [S^{IV}\text{-}O]_2[Mn^{II}(H_2O)_4]^0_{(s)} + 2H_3O^+ \quad (4)$$

$$[S^{IV}\text{-}O]_2[Mn^{II}(H_2O)_4]^0_{(s)} + HOCl \Leftrightarrow \text{activated complex} \quad (5)$$

$$\text{activated complex} \Leftrightarrow 2[S^{IV}\text{-}OH] + Mn^{IV}O_2 + 3H_2O + H_3O^+ + Cl^- \quad (6)$$

Reactions (4) to (6) simplify to:

$$Mn^{2+} + 2[S\text{-}OH] + HOCl + H_2O \Rightarrow MnO_{2(s)} + 2[S\text{-}OH] + 3H^+ + Cl^- \quad (7)$$

Reaction (7) is equivalent to (3). If the adsorption site is considered to be monodentate [S-OH], reaction (7) is also obtained, with S-OH as the reacting site that is regenerated; the change in solution pH upon adsorption is not definitive for the site structure. Reactions (3) and (7) simplify further to the stoichiometric reaction:

$$Mn^{2+} + HOCl + H_2O \Rightarrow MnO_{2(s)} + Cl^- + 3H^+ \quad (8)$$

While the complete reduction of HOCl requires two electrons, these are probably transferred sequentially in two or more rapid elementary reactions upon formation of the activated complex.[12] For surface catalyzed reactions,

confusion of stoichiometry with mechanistic pathway is a concern. As an alternative to the bidentate reaction series, both Wilson[13] and Davies[14] have suggested that the reaction with oxygen can proceed as:

$$[S\text{-}O^{+}] + MnOH^{+} + O_2 \Rightarrow MnOOH_{(s)} + H_2O \quad (9)$$

Following the initial one electron transfer, disproportionation may proceed slowly:[15]

$$2MnOOH_{(s)} + 2H^{+} \Rightarrow MnO_{2(s)} + Mn^{2+} + 2H_2O \quad (10)$$

Formation of some stable Mn(III) species in the oxide surface is not unexpected in either reaction (9) or (10), and by analogy, mixed oxidation states may be expected in the case of oxidation with hypochlorite. This departure from MnO_2 stoichiometry may depend on the availability of an alternative oxidant species, the presence of a reductants such as natural organic matter,[16] the surface coordination of the adsorbed manganese, and the oxide surface composition.[17] For conditions prevailing in the NGE process, Knocke *et al.*[1] found the stoichiometry of oxide coatings varied between filter media from different treatment plants ($MnO_{1.4\text{-}2.0}$). Incorporation of other inorganic species such as Fe, Cu, and Al has been noted in media from a wide variety of sources.[18]

The "natural" reaction sequence which eventually produces adequate surface coverage of oxide coating requires an oxidant (oxygen or hypochlorite), dissolved Mn^{2+}, and surface adsorption sites. Several qualitative aspects of the NGE process were noted:

1) Some potential surface adsorption sites must already be present on raw media (or filter-retained particulates) for the NGE to initiate. These sites could be surface silanol groups (Si-OH) on filter sand or retained clay particulates, or surface carboxyl groups on anthracite. These sites would correspond to the Mn-centered surface coordination site (S-OH) of equation 4.

2) Since the NGE reaction is autocatalytic, once an oxidized Mn surface site forms (either on the anthracite or on a colloidal $MnO_{x(s)}$), it will sorb another Mn^{2+} and catalyze its oxidation. In light of this, one approach to developing a synthetic coating technique would be to promote and establish autocatalysis on the media surface.

3) Homogeneous (solution phase) Mn^{2+} oxidation must be minimized so the media surface is not deprived of reactants by competition with the high surface area, colloidal particulates formed by any autocatalytic solution phase oxidation. As an example, consider the production of a 2 kilogram batch of media coated to 2 mg g^{-1} in a 10 L laboratory batch reactor, requiring a high initial concentration of Mn^{2+} (400 mg L^{-1}). Assuming equation 11 (or a similar scheme) as the reaction mechanism, this high concentration will promote homogeneous oxidation in the presence of free chlorine, by the law of mass action.

4) Adsorption capacity of $MnO_{x(s)}$ for Mn^{2+} increases with pH, but homogeneous oxidation of Mn^{2+} by both hypochlorite and oxygen is significant above pH 9.0, producing colloidal precipitates undesirable in this system.[17] (The stoichiometric oxidant requirement for conversion of Mn(II) to Mn(IV) is 1.30 mg HOCl per mg Mn^{2+}.) Thus, some provision for pH control is indicated in

order to avoid the low pH generated by oxidation (equation 12), or high pH resulting from free chlorine (e.g. hypochlorite) addition.

Initial trials of a coating method were conducted by placing the required stoichiometric concentrations of reactants in 250 mL flasks to simulate a 10 L reactor containing 2 kg of raw media (50 g media, $[Mn^{2+}]$ = 400 mg L^{-1}, and [HOCl] = 520 mg L^{-1}). As expected, this approach proved unworkable due to excess reactant concentrations: precipitation of colloidal $MnO_{x(s)}$ in solution was nearly immediate, and the media remained uncoated. This result suggested the strategy pursued, which was to minimize excess oxidant concentrations and maximize the concentration of adsorption sites by reducing the solution to media volume ratio. The method eventually developed is based on a gradual addition of oxidant in less than stoichiometric increments.

METHODS AND MATERIALS

Media preparation and wet chemical analysis: Uncoated or "raw" anthracite media was obtained from the Blacksburg, VA water treatment plant. On visual inspection, the majority of the flat grain surfaces appeared shiny and smooth. Filter gravel (diameter = 10 mm) was supplied by the Northern Gravel Company; this appeared to consist of a variety of minerals typical of a riverine gravel deposit. For determination of Mn content, replicate samples of air-dried raw and synthetically-coated media were extracted in acidified hydroxyl amine sulfate solution, and 0.45 μm-filtered extracts were analyzed for Mn by flame atomic absorption.[20] Before and after the coating method treatments, media were rinsed thoroughly of fine particulates in tap water containing approximately 1 mg L^{-1} free chlorine. Free chlorine concentrations were determined by DPD

tablet method for media synthesis and regeneration, and by PAO titration for the column studies.[20]

Determination of pH: During method development, pH was monitored with an Ag/AgCl reference pH probe (Fisher Scientific, model 13-620-97). However, this probe gave erratic and fluctuating readings in solutions containing free chlorine and [Mn^{2+}], and the pH buffer standards were not reproducible. For the batch syntheses of samples 2 through 9 described below, test paper was used to estimate solution pH (Microessential Laboratories, "pHydrion Vivid", range pH 6 to 8). The initial pH of each stirred batch solution was adjusted to between 7.2 and 8.0 with dropwise addition of 0.5 M NaOH or 0.5 M HCl as needed, and pH was periodically checked and adjusted to above pH 7.0 during the synthesis. For sample 10, solution pH was monitored with a Pt - KCl internal reference probe with a free-flowing ceramic junction (Orion Research, model 80-03 "Ross Sure-Flow^{TM}") which performed satisfactorily.

Media coating methods: *Sample 1:* To 500 mL Milli-Q water was added 20 mg $MnSO_4 \cdot H_2O$, 2.5 g raw anthracite, and a Teflon-coated magnetic stirring bar. An oxidant solution of 1 mL 5.5% NaOCl in MilliQ water to 50 mL volume (1100 mg L^{-1} HOCl) was added to the gently stirred solution at 5 mL min^{-1}. Stirring continued for 1 minute after all oxidant was added, then the supernatant was drained and the media rinsed.

Conditions for additional media syntheses are summarized in Table 1. The initial stirred tank batch syntheses for amounts greater than a few grams of anthracite were as follows:

Sample 2: 3.6 g $MnCl_2 \cdot 4H_2O$ ([Mn^{2+} = 100 mg L^{-1}) and 84 mg $NaHCO_3$ (10^{-4} M HCO_3^- added in addition to atmospheric CO_2 buffering capacity) were

added to an open-top Pyrex reaction vessel holding 10 L of tap water (approx. 1 mg L^{-1} HOCl), to which was added 50 g dry weight of rinsed anthracite. Addition of bicarbonate was minimized to try to avoid formation of $MnCO_{3(s)}$ (rhodochrosite). The reactants were stirred with a paddle mixer at approximately 60 rpm, gently enough to suspend the media in solution, in an attempt to avoid excessive media abrasion and solution turbulence. Oxidant solution was prepared by adding 10 mL of 5.5% NaOCl to 500 mL tap water (1100 mg L^{-1} HOCl). The entire oxidant solution was added to the stirred reactor at 50 mL min^{-1} for a final solution volume of 10.5 L. The maximum possible oxidant concentration was 52 mg L^{-1} HOCl, or 0.52 mg HOCl mg^{-1} Mn^{2+}, or 42% of stoichiometric demand for the complete oxidation of Mn(II) to Mn(IV). Stirring continued for 30 minutes, then the reactor was drained and the media rinsed and placed on a tray to air dry. A dark brown haze was visible in solution by the end of stirring, likely colloidal Mn oxides ($MnO_{x(s)}$). The reactor walls were coated with a translucent brown deposit which could be removed by rinsing with acidified hydroxyl amine sulfate solution used for media extractions.

Sample 3: The same reactor configuration and stirring for sample 2 was used for this sample and for samples 4, 5 and 6 below. For sample 3, reactants were increased to obtain a usable quantity of coated media for column experiments: 500 g anthracite, initial [Mn^{2+}] = 1000 mg L^{-1}, and 10^{-3} M HCO_3^- added (over atmospheric buffering) were used, with an oxidant solution of 50 mL of 5.5% NaOCl in 1500 mL tap water (1830 mg L^{-1} HOCl) added at 25 mL min^{-1}. The maximum possible oxidant concentration was higher than for sample 2 (240 mg L^{-1} HOCl), but the stoichiometric ratio was lower (0.24 mg HOCl mg^{-1} Mn^{2+}). The reactor was stirred for 30 additional minutes, drained, and media

was rinsed as for sample 2. The procedure was repeated to recoat the media. A similar brown haze and wall coating was seen at the end of the synthesis, as in sample 2, typical of colloidal $MnO_{x(s)}$.

Samples 4 through 7: Samples 4, 5 and 6 were taken during a single batch synthesis, in an attempt to discover if longer batch reaction time could increase coating deposition. The sample 7 batch was conducted to see how additional coating could be deposited on a previously-coated media. Reactants for samples 4, 5 and 6: 10 L tap water, 50 g of 2-4-B, $[Mn^{2+}]$ = 1000 mg L^{-1}, and 10^{-4} M HCO_3^- added, with an oxidant solution of 10 mL of 5.5% NaOCl in 500 mL tap water ([HOCl] = 1100 mg L^{-1}). Besides minimizing the potential for $MnCO_3$ formation, the lower added alkalinity was used since the small amount of media relative to sample 3 was anticipated to not catalyze as much alkalinity-consuming Mn^{2+} oxidation. The maximum possible oxidant concentration in the reactor was [HOCl] = 53 mg L^{-1} or 4% of stoichiometric requirement for complete oxidation to Mn(IV). Gradual addition of oxidant solution (50 mL min^{-1}) was followed by stirring for 30 minutes, and a 10 g sample was taken (sample 4). At 60 minutes, another 10 g sample was taken (sample 5), and at 90 minutes, the reactor was drained and media rinsed to obtain sample 6. The brown haze was observed in solution and the reactor walls were coated as for previous batches. Sample 7 was generated by one batch coating of 250 g of sample 3 by the protocol of the original sample 3 synthesis.

Additional method development trials were conducted, with the objective to conserve reactants, shorten reaction time, increase media quantity, and maximize precipitation of Mn^{2+} on the media rather than in solution. Again, these studies proceeded according to an informed trial-and-error approach, with

the primary goal of rapidly depositing $MnO_{x(s)}$, rather than elucidating reaction kinetics or mechanism. For example, coated anthracite samples 8 and 9 were produced using variations of the stirred tank batch method, summarized in Table 2. After these studies, the following procedure was used to prepare 2.9 kg of coated anthracite with 2 mg g^{-1} MnO_x. This procedure is very likely not optimized with respect to reactant conversion or reaction time, but it is useful for the stated purpose of further work on the NGE process. The procedure consists of two stages, the first stage using the stirred tank to deposit the initial base coating on raw media. The second stage is a recirculating bed reactor to deposit additional coating. The fixed bed was adopted to minimize coating abrasion and reduce solution volume. Unless noted, distilled deionized water was used for the two-stage method. The solution pH changes observed during one synthesis are noted. These pH changes were typical of those observed in all prior batch reactions.

Stage 1: 500 g of anthracite rinsed in tap water was added to 10 L of gently stirred water containing 13.25 g $MnCl_2 \cdot 4H_2O$ ($[Mn^{2+}]$ = 370 mg L^{-1}) and 36 mg $SnCl_2 \cdot 2H_2O$. The reactants were chosen so that the Mn^{2+} present would deposit about 3.7 mg g^{-1} extractable Mn^{2+} on the media if 50% conversion to Mn(IV) were accomplished. The $SnCl_2$ was used to promote the initial sorption of Mn^{2+} on uncoated media; Sn(II) species are used in industry as surface sensitizers in the deposition of coatings.[21] Separate oxidant and bicarbonate solutions were prepared by adding to 500 mL water 3.36 g $NaHCO_3$ and 10 mL of 5.5% NaOCl. Then, 250 mL of bicarbonate solution and 50 mL oxidant solution were added to the stirred reactor (pH changed from 4.2 to 7.3). At 20 minutes, 150 mL bicarbonate solution and 50 mL oxidant solution were added

(pH changed from 6.8 to 7.3). At 40 minutes, 100 mL bicarbonate solution and 100 mL oxidant solution were added (pH changed from 6.7 to 6.9). At 50 minutes, 50 mL oxidant solution was added. At 60 minutes, 250 mL oxidant solution was added, the vessel stirred for 1 more hour and then drained. The media was rinsed in tap water, and air dried.

Six batches of 500 g were prepared by this method. These were combined, placed in a column, and regenerated by passing a 400 mg L^{-1} NaOCl solution through the column until influent and effluent chlorine concentrations were equal. The regenerated media was rinsed in the column with tap water, and dried in air, producing sample 10, having 0.64 mg g^{-1} MnO_x.

Stage 2: 2.9 kg of sample 10 from stage 1 was placed in the reaction vessel containing 6 L of water with 10^{-3} M HCO_3^- added, and $[Mn^{2+}]$ = 1.9 g L^{-1} (initial solution pH = 6.7). The high $[Mn^{2+}]$ was used to facilitate any diffusion-limited transport processes from solution to the catalytic media surfaces. Oxidant solution was prepared by adding 250 mL of 5.5% NaOCl up to 1 L of distilled deionized water ([HOCl] = 13.75 g L^{-1}). A recirculating pump was used to continuously withdraw solution overlying the media bed, reintroducing it at the base of the bed at a rate of 250 mL min^{-1}. To initiate coating deposition, 50 mL of oxidant solution were added to the top of the reactor initially (pH increased to 7.3), and 50 mL additional oxidant solution was added every 15 minutes for 1 hour (5 additions total). The pH was adjusted to 7.0 between oxidant additions with dropwise addition of 0.5 M NaOH. The solution was recirculated for two hours, then drained out and replaced with water to cover the media bed. The remaining 250 mL oxidant solution was added in one step, and the solution recirculated 15 minutes. (Some slight solution precipitation was noted during this

stage). The reactor was drained, the media rinsed and regenerated as in Stage 1 to obtain sample 11, having 2 mg g^{-1} MnO_x).

Sequential Batching Method: Another variation of the coating method was developed for coating both anthracite and gravel. For the gravel coating, solution 1 was 250 mL tap water with $[Mn^{2+}]$ = 1000 mg L^{-1}, solution 2 was 1 mL of 5.5% NaOCl in 400 mL tap water ([HOCl] = 138 mg L^{-1}). Step 1: In a 1 L beaker, 25 g of raw gravel (rinsed in tap water) and solution 1 were combined and gently agitated by swirling for two minutes, then solution 1 was drained off and saved. Step 2: Solution 2 was added to the gravel and gently agitated, then poured off and saved. Steps 1 and 2 were repeated for 15 minutes total reaction time. Solutions were replaced during the procedure if they became cloudy with colloidal MnO_x precipitation. The gravel was rinsed in tap water and air dried.

Sample 12: 500 g of raw anthracite were rinsed in tap water, and the batching procedure described as Step 1 and Step 2 above was followed as for the gravel sample. However, fresh solution 2 (oxidant) was used for each application. The sample was rinsed in tap water and air dried.

Short bed absorber and reactor columns: Column tests were performed on sample 11 to assess Mn^{2+} adsorption and catalytic removal with hypochlorite as oxidant. A 4 cm diameter glass column fitted with a perforated Teflon media support disk was used with a hydraulic loading of 5 gpm ft^{-2}. Feed solutions were prepared from distilled deionized water with 10^{-3} M HCO_3^- and background salt added ([NaCl] = 0.26 g L^{-1}). Effluent samples were filtered through 0.45 μm syringe filters and analyzed for Mn by flame atomic absorption, and effluent chlorine was determined by PAO titration method. The adsorption tests used 100 g (10 cm bed depth) of media at pH 6.00, 6.75, and 7.50 with

influent $[Mn^{2+}]$ = 1 mg L^{-1}. The pH levels were chosen to span the range of filter-applied waters typically found in treatment practice. Triplicate catalytic removal tests at pH 7.50 used 40 g of synthetic media sample 11 (bed depth 4 cm), with approximate influent reactant concentrations as follows: $[Mn^{2+}]$ = 0.34 mg L^{-1}, [HOCl] = 1 mg L^{-1}, or 220% of stoichiometric requirement for complete oxidation to Mn(IV).

Electron microscopy: For scanning electron microscope (SEM) analysis of the media surfaces, samples were dried in air, glue mounted and carbon-coated by vacuum electric arc to a thickness of at least 250 angstroms. Cross-section samples were embedded in epoxy, ground, polished, and carbon-coated.[22] Standardless qualitative elemental analysis of the coatings was done with an hnu™ energy dispersive x-ray spectrometer system (EDS) attached to the Cameca Series 2 SEM.[22]

Surface area: Surface areas of selected samples were obtained by automated cryogenic N_2 adsorption using Quantasorb NOVA 1000 instruments at Virginia Tech and the Quantachrome Corporation. This microprocessor controlled instrument performs automated surface area, pore size and pore size distribution measurements according to user-specified protocol. Prior to analyses, coated media were outgassed under vacuum at 80 °C for at least 45 minutes. Single point and five-point B.E.T. surface areas[23] were measured by the following protocol: from calculated atmospheric pressure P_0, N_2 adsorption was measured in 0.05 relative pressure increments from P = 0.10 to 0.30 P_0, with the single point measurement taken at 0.30 P_0.

X-ray photoelectron spectroscopy (XPS): This method was used to analyze the chemical composition and bonding of the top few atomic layers of

the raw anthracite surface. An excellent review of XPS theory and application is available from Hochella.[24] In simplest terms, a sample is irradiated with x-rays of a narrow energy distribution, ejecting electrons from the sample surface. The kinetic energy spectrum of the electrons is recorded and converted to a binding energy scale. The energies and shapes of spectral peaks are characteristic of electron orbital states and interatomic bonding environments in the sample. Analyses were conducted with a Perkin Elmer Model 5400 XPS instrument, using 400 W MgKα or AlKα x-rays. A single grain of raw anthracite was mounted with conductive graphite paste on a solvent-cleaned steel mount. The sample was briefly outgassed in the sample introduction vacuum lock until the vacuum became stable. Five-minute survey scans of electron binding energies from 0 to 1200 eV were taken, and automatic peak identification was used where possible. Spectra recorded were unshifted relative to absolute binding energies. The C1s peak of raw anthracite was found at 285.04 eV, slightly higher than the reference value for adventitious carbon of 284.9 eV.

RESULTS AND DISCUSSION

Media coating methods and surface area: Results of media extractions and surface area determinations are given in Table 3. The uncoated media showed trace levels of Mn initially. The coating methods succeeded in depositing appreciable quantities of Mn, ultimately over 4 mg g^{-1} after repeated stirred tank treatments. For samples 4 through 6, longer reaction times did not increase $MnO_{x(s)}$ deposition, perhaps because coating abrasion and deposition reached a steady state, or homogenous precipitation eventually predominated in the concentrated reactant conditions. For the large-scale stirred tank syntheses,

reactant conversion from Mn^{2+} to $MnO_{x(s)}$ were 16% conversion for sample 3, and 8.6% for sample 10. Although conversion was lower for sample 10, undesirable homogeneous precipitation was minimal compared to sample 3, probably due to the lower reactant concentrations.

If solution pH had been maintained above pH 7.5 for the sample 10 synthesis, the $MnO_{x(s)}$ sorption capacity would have been greater, possibly resulting in a higher overall conversion. Slightly acidic conditions developed between oxidant additions as the Mn^{2+} oxidation proceeded. Better pH control could be accomplished with a continuous, gradual addition of oxidant solution to the stirred reactor. A longer reaction time may have also increased coating amounts, since the reactants Mn^{2+} and free chlorine were not exhausted. However, the effect of media abrasion from continued stirring time might have negatively impacted the total amount of media coating achieved.

The fixed bed stage for sample 11 accomplished a 35% conversion. In principle, conversion for this stage can be essentially complete given adequate oxidant supply, pH control and prolonged recirculation time. The sequential batch technique deposited coating on both media, and the reduced reaction time indicates that this type of method might be economical in process scale-up to production quantities of 100 kg in a fixed-bed configuration.

The specific surface areas of coated anthracite media were in the range of 0.5 to 0.9 $m^2\ g^{-1}$, roughly three to five times higher than the uncoated. Assuming all surface area measured is from the coating, these correspond to very high specific surface areas for the oxide material itself, 272 $m^2\ g^{-1}$ of $MnO_{x(s)}$ (sample 2-94) to 496 $m^2\ g^{-1}$ (sample 5-21). In a typical dual-media filter (porosity = 0.5, media density = 1.59 g cm^{-3}), these correspond to surface

area concentrations of 400,000 to 716,000 m^2 m^{-3} in a synthetically-coated media bed. The Blacksburg media surface area was about ten times higher at 11.3 m^2 g^{-1}, but the coating also contained aluminum. The coated gravel surface area was slightly less than the uncoated. Without knowing if the underlying pebble surface contributed to the measured surface area, the contribution of the coating itself to the surface area cannot be determined from this analysis.

Electron microscopy: In conjunction with the electron microscopy, elemental identifications of surface features were performed by qualitative EDS analysis. Samples were also viewed in backscattered electron mode (BSE), in which image brightness corresponds with higher relative nuclear density and atomic weight. The SEM analysis of raw anthracite found a patchy distribution of surface mineral deposits and inclusions. A deposit rich in Fe and S on uncoated coal is seen in Figure 1a. Occasional iron oxide stains were visible as well. Microscopic particulate inclusions rich in Si and Al are shown in Figure 1b; these are probably clay minerals native to the anthracite. The small-scale synthesis sample 1 shows Mn-rich growths distributed sparsely over the anthracite surface (Figure 2a). The BSE image of sample 2 (Figure 2b) shows a near-complete surface coverage of Mn oxide deposits. The underlying anthracite (black in this BSE image) shows through what appear to be abrasion marks, possibly resulting from agitation in the stirred tank reactor. At the micron scale, the synthetic coating is composed of small particles on top of a more consolidated coating (Figure 3a, b). Based on a comprehensive survey of the synthetic coatings, there appear to be two physically distinct topographic regions. In some regions, individual particles (dia. = 1 - 3 μm) appear to be growing in clumps in surface

depressions and coating cracks. In other, adjacent regions, the coating appears relatively more smooth and uniform, with a finer particle structure and cementation. This surface morphology is consistent with transport-limited reaction kinetics: in recessed sites, the laminar sublayer persists, and particle growth occurs most rapidly at the outermost particle edge. In a separate study (described in detail in Chapter 1), atomic force microscopy characterized surface relief of up to 10%.[25]

The synthetically-coated media can resemble "naturally" coated media in both surface coverage and coating thickness. A sample of coated anthracite from the Blacksburg, VA filter plant was studied for comparison. The naturally-produced media coating appears to encapsulate the anthracite (Figure 4a, b). The EDS spectrum of the Blacksburg coating indicates Al and Mn in the deposit. In cross-section BSE view, the natural coating appears 30 to 50 μm thick, and shows indications of compositional variation, with banding features. The synthetic sample 2 appears quite similar in both respects; the surface oxide coverage is fairly complete (Figure 5a, b), with a coating thickness of 10 - 30 μm.

XPS: A survey scan of the raw anthracite is shown in Figure 6. In addition to the major O1s and C1s photopeaks, minor Fe, Mn, Si, and Al peaks and are detected, consistent with the SEM/EDS studies. The narrow scan of the C1s peak (Figure 7) shows a broad shoulder toward higher binding energies, consistent with the indicated curve fits for carbon ligands, based on position relative to the C1s maximum: A = hydroxyl, B = carbonyl, C = carboxyl. Using the Mn3s peak splitting method[26] (discussed in detail in Chapter 1), Mn(IV) was determined to be the predominant surface oxidation state in the synthetic coating of sample 7.

The raw anthracite spectrum provides evidence for potential surface adsorption sites on Fe, Mn and Al oxide inclusions in raw anthracite. At these sites, dissolved Mn^{2+} could sorb to initiate the catalytic Mn oxidation process.[27] Such sites are in addition to any possible anthracite carboxyl or hydroxyl coordination sites. Once the NGE process begins, the nature of the underlying mineral becomes secondary, as the outermost atomic surface (now $MnO_{x(s)}$) is active in adsorption and catalysis. In contrast, a media grain completely encapsulated with $MnO_{x(s)}$ may lose its catalytic properties if the oxide surface is covered by a thin layer of relatively non-sorptive mineral phase, such as calcite. Chemical extraction of this media would confirm the presence of an otherwise sufficient coating of $MnO_{x(s)}$ to support the NGE, but the media would show poor performance in removing Mn^{2+}.

Short bed absorber and reactor columns: Effluent profiles for the adsorption and catalytic removal tests at a hydraulic loading of 5 gpm ft^{-2} are shown in Figures 8 and 9, respectively. The effluent profiles are consistent with a sorptive capacity for Mn^{2+} increasing with pH. Additional tests (described in detail in Chapter 3) at different flow rates indicated that fluid to particle transport of Mn^{2+} is kinetically limiting, and the Freundlich isotherm describes adsorption equilibrium at levels typically encountered in practice, below $[Mn^{2+}] = 1$ mg L^{-1}. These results are consistent with prior work showing typical chromatographic behavior of Mn^{2+} in oxide-coated media filter columns.[28]

The oxidative removal tests used smaller quantities of coated media so that effluent $[Mn^{2+}]$ would remain quantifiable by flame atomic absorption. The goal of these tests was to establish a steady-state condition in the bed so that the rates of all kinetic processes (reactant transport and Mn^{2+} oxidation) would

be equal. The columns appear to have reached steady state after about 40 minutes (Figure 9); linear regressions through the last four data points of each test show no significant slope (Table 4).

The effluent [Mn^{2+}] of the final two samples (60 and 70 minutes) were averaged to obtain an estimate of the "steady state" global oxidation rate at each pH. The oxidation rates measured at the three pH conditions were significantly different ($p = 0.02$, single-factor ANOVA). The observed oxidation reaction stoichiometry and the evaluations of synthetic and natural OCM under different process conditions are discussed in detail in Chapter 3.

CONCLUSIONS

A rapid method for depositing synthetic manganese oxide coatings of onto anthracite and gravel filter media substrates was developed. These coatings show sorptive capacity for dissolved Mn^{2+} and can catalyze oxidative Mn^{2+} removal in presence of hypochlorite from pH 6.0 to 7.5. This technology may allow more controlled application of Mn^{2+} removal during rapid filtration. The ability of synthetic Mn oxides to sorb and coprecipitate with a wide variety of inorganic species such as Ra^{2+}, Zn^{2+}, Cd^{2+}, Cu^{2+}, Pb^{2+}, and Cr^{3+} suggests applications of this media coating technology for treatment of mine drainages and landfill leachates, and development of point-of-use absorption units for domestic water supply.[29, 30]

ACKNOWLEDGMENTS

This work was funded under a National Science Foundation grant to Dr. W. R. Knocke and Dr. D. L. Gallagher. The authors thank the Quantachrome

Corporation of Syosset, NY for donating B.E.T. analyses. Invaluable services were provided by Todd Solberg of the Department of Geological Sciences at Virginia Tech, who devised and performed the x-ray diffraction measurements and trained Merkle in analytical techniques. Dr. John Dillard, Dr. Mike Hochella, Dr. Jodi Junta and Udo Becker contributed through enthusiastic teaching and discussion. The assistance of Gerald Higgins and the staff of the Blacksburg-Christiansburg-VPI & SU Water Treatment Plant and the Electrical Department, City of Radford, is greatly appreciated.

LITERATURE CITED

1 - Knocke, W. R.; Occiano, S.; Hungate, R. Removal of Soluble Manganese from Water by Oxide-Coated Filter Media **1990**, AWWA Research Foundation, Denver, Colorado.

2 - Knocke, W. R.; Hamon, J.; Thompson, C. "Soluble Manganese Removal on Oxide-Coated Filter Media", J. AWWA **1988** (80:12), 65-69.

3 - Cleasby, J. L. "Iron and Manganese Removal - A Case Study", J. AWWA **1975**, 67:3:147 (March).

4 - Coffey, B. M.; Gallagher, D.L.; Knocke, W. R. "Modeling Soluble Manganese Removal by Oxide-Coated Filter Media", Journal of the Environmental Engineering Division - ASCE **1993** (119:4), 679.

5 - McGhee, T. J. Water Supply and Sewerage **1991**, McGraw-Hill, New York.

6 - *AWWA MainStream* **1994** (October), American Water Works Association, Denver, Colorado.

7 - Byerly, G. P. "Oxide-coated media aids in manganese control", *AWWA MainStream* **1994** (May), American Water Works Association, Denver, Colorado.

8 - Bailey, T. A. "Procedures for Conditioning Filters for Manganese Removal" (Appendix A), in: Knocke, W. R.; Occiano, S.; Hungate, R. Removal of Soluble Manganese from Water by Oxide-Coated Filter Media **1990**, AWWA Research Foundation.

9 - Coffey, B. M., and Knocke, W.R. "Removal of Soluble Iron and Manganese from Groundwater by Chemical Oxidation and Oxide-Coated Mixed-Media Filtration", in Proceedings of the ASCE - Environmental Engineering Division Conference **1990** (July), Washington, D.C.

10 - Nakanishi, H. "Kinetics of Continuous Removal of Manganese in a MnO_2-Coated Sand Bed", Kogyo Kagaku Zasshi **1967**, 70 (4), 407.

11 - Luther, G. "The Frontier-Molecular-Orbital Theory Approach in Geochemical Processes" in Aquatic Chemical Kinetics, **1990**, W. Stumm, Ed., John Wiley & Sons, Inc., U.S.A.

12 - Stone, A.; Morgan, J. "Kinetics of Chemical Transformations in the Environment" in Aquatic Chemical Kinetics, **1990,** W. Stumm, Ed., John Wiley & Sons, Inc., U.S.A.

13 - Wilson, D. "Surface and complexation effects on the rate of Mn(II) oxidation in natural waters", Geochim. Cosmochim. Acta **1980** (44),1311-1317.

14 - Davies, S. H. R. "Mn(II) Oxidation in the Presence of Metal Oxides", Ph.D. Dissertation, **1985** California Institute of Technology, U.S.A.

15 - Murray, J.; Balistrieri, L.; Paul, B. "The oxidation state of manganese in marine sediments and ferromanganese nodules", Geochim. Cosmochim. Acta **1984** (48), 1237-1247.

16 - Stone, A.T. and Morgan, J.J. "Reduction and Dissolution of Manganese (III) and Manganese (IV) Oxides by Organics", Environ. Sci. Technol. **1984** (18), 450-456.

17 - Junta, J. L. and Hochella, M. F. Jr. "Manganese (II) oxidation at mineral surfaces: A Microscopic and spectroscopic study", Geochim. Cosmochim. Acta **1994** (58), 4985-4999.

18 - Parkins, S., personal communication.

19 - Knocke, W. R.; Van Benschoten, J. E.; Kearney, M; Soborski, A.; Reckhow, D. A. "Alternative Oxidants for the Removal of Soluble Iron and Manganese" **1990**, AWWA Research Foundation, Denver, Colorado.

20 - American Water Works Association. Standard Methods for the Examination of Water and Waste Water **1992**, 18th ed., APHA, AWWA, WPCF, Washington, D.C.

21 - Greenwood, N. N. and Earnshaw, A. Chemistry of the Elements **1984**, Chapter 10, p. 442, Pergamon Press, Oxford, U.K.

22 - Chalker, C. P. "Characterization of coatings and interfaces" in Advanced Surface Coatings: a handbook of surface engineering **1991**, A. Matthews and D. Rickerby, Eds., Blackie & Son, Ltd, London.

23 - Smith, J. M. Chemical Engineering Kinetics **1981**, 3rd ed., McGraw-Hill, New York.

24 - Hochella, M. F., Jr. "Auger electron and x-ray photoelectron spectroscopies", in: Reviews in Mineralogy: Spectrosopic Methods in Mineralogy and Geology, **1988**, F. C. Hawthorne, Ed., Mineralogical Society of America, Washington, D.C.

25 - Murray, J.; Dillard, J.; Giovanoli, R.; Moers, H.; Stumm, W. "Oxidation of Mn(II): Initial mineralogy, oxidation state and aging", Geochim. Cosmochim. Acta **1985** (49) 463-470.

26 - Merkle, P. B.; Knocke, W. R.; Gallagher, D. L. "Filter Media Mineral Coatings: Filtration Theory and Practice", Proceedings of the Annual Conference of the American Water Works Association **1994** (June), New York.

27 - Davies, S. H. R. "Mn(II) Oxidation in the Presence of Lepidocrocite: The Influence of Other Ions", in Geochemical Processes at Mineral Surfaces **1986,** ACS Symposium Series No. 323, American Chemical Society, Washington, D.C.

28 - Occiano, S. "The Mechanisms for Free Chlorine Oxidation of Reduced Manganese in Mixed-Media Filters", M.S. Thesis, **1992** Dept. of Civil Engineering, Virginia Polytechnic Institute and State University, U.S.A.

29 - Valentine, R. L.; Kurt, A.; Meyer, J.; Walsh, D.; Mielke, W. Radium Removal Using Preformed Hydrous Manganese Oxides **1992**, AWWA Research Foundation, Denver, Colorado.

30 - Singh, S. K., and Subramanian, V. "Hydrous Fe and Mn Oxides - Scavengers of Heavy Metals in the Aquatic Environment", **CRC Critical Reviews in Environmental Controls 1984**, 14:1, 33-90.

TABLE 1

SUMMARY OF COATED MEDIA SYNTHESES

Sample	Stirring time (min)	Initial Volume (liters)	Media Conc. (g/L)	HOCl Addition (mg)†	Initial $[Mn^{2+}]$ (mg/L)	Initial $[HCO_3^-]$ (M)†	Mn (mg/g)
2	40	10	5	550	100	10^{-4}	2.8
3	90	10	50	2745	1000	10^{-3}	3.2
4*	40	10	5**	550	1000	10^{-4}	3.6
5*	60						4.4
6*	90						4.4
7	90	10	25	2745	1000	10^{-4}	4.2
10‡	120	10	50	550	370	4×10^{-3}	0.64
11	see text	6	480***	1375	1900	10^{-3}	2.0

† Oxidant (HOCl) and buffer solutions added discretely for some syntheses (see text for detailed descriptions)

* Samples 4, 5 and 6 were sequential samples during a single batch

** Starting material was sample 3

*** Starting material was sample 10

‡ Media rinsed with NaOCl solution at end of stage (see text)

TABLE 2

REACTION CONDITIONS FOR SAMPLES 8 AND 9

Sample 8: Batch tank coating

Step #1: Solution A: 0.84 g $NaHCO_3$ in 500 mL tap water
Solution B: 10 mL 5.5% NaOCl in 250 mL tap water
0 min. - To 10 L tap water, add 1 kg anthracite, 66 g $MnCl_2 \cdot H_2O$ stirring with paddle mixer at 60 rpm
5 min. - Add 75 mL solution B
12 min. - Add 150 mL solution A
20 min.- Add 75 mL solution B
25 min. - Add 100 mL solution A
30 min. - Add 100 mL solution B
55 min. - Add 10 mL 5.5% NaOCl solution
75 min. - Drain tank, rinse and air dry media.

Step #2: 0 min. - To 10 L tap water, add media from step #1, 27 g $MnCl_2 \cdot H_2O$, 0.84 g $NaHCO_3$ to stirred reactor, add oxidant solution (5 mL NaOCl in 250 mL tap water) at 25 mL min^{-1}.
15 min. - Stop stirring
60 min. - Drain tank, rinse and air dry media.

Step #3: Recoat media from step #2 by sample 2-4-A method (see text)

Step #4: Solution A: 3.36 g $NaHCO_3$ in 1 L tap water
Solution B: 5 mL NaOCl in 500 mL tap water
0 min. - To 10 L tap water, add 13 g $MnCl_2 \cdot H_2O$, stirring
5 min. - Add 150 mL each of solutions A and B
20 min. - Add 150 mL each of solutions A and B
40 min. - Add 170 mL solution B, 160 mL solution A
90 min. - Drain tank, rinse and air dry media.

Table 2: (continued) Reaction conditions for samples 8 and 9

Sample 9: Batch tank coating

Solution A: 3.36 g $NaHCO_3$ in 1 L tap water
Solution B: 10 mL NaOCl in 500 mL tap water
0 min. - To 10 L tap water, add 500 g 4-10 and
13 g $MnCl_2 \cdot H_2O$, and 150 mL each of solutions A and B, stirring
7 min. - Add 150 mL solution A
34 min. - Add 250 mL solution A
60 min. - Add 150 mL solution B, 250 mL solution A
90 min. - Add 150 mL solution B
110 min. - Add 50 mL solution B, 200 mL Solution A
130 min. - Drain tank, rinse and air dry media.

TABLE 3

MEDIA COATING LEVELS AND SURFACE AREAS

Sample	MnO_x, mg g^{-1} as Mn^{2+}	B.E.T surface area, m^2 g^{-1}	
		Single-point	Multi-point
Raw anthracite*	0.008	0.19	0.20
Raw anthracite	0.008	0.17, 0.18	0.16
Blacksburg	5.0	11.3	-
11	2.0	0.53, 0.59	0.51
8*	1.7	0.54	0.50
9*	1.9	0.90	0.87
12*	1.3	0.65	0.64
raw gravel	trace	1.60	-
coated gravel	0.36	1.35, 1.29	1.39

* - Surface area determinations performed by the Quantachrome Corporation

TABLE 4

REGRESSION ANALYSIS, Mn^{2+} OXIDATION STUDIES

Test	Significance, F statistic
pH 7.5	0.367
pH 6.75	0.200
pH 6.00	0.225

A

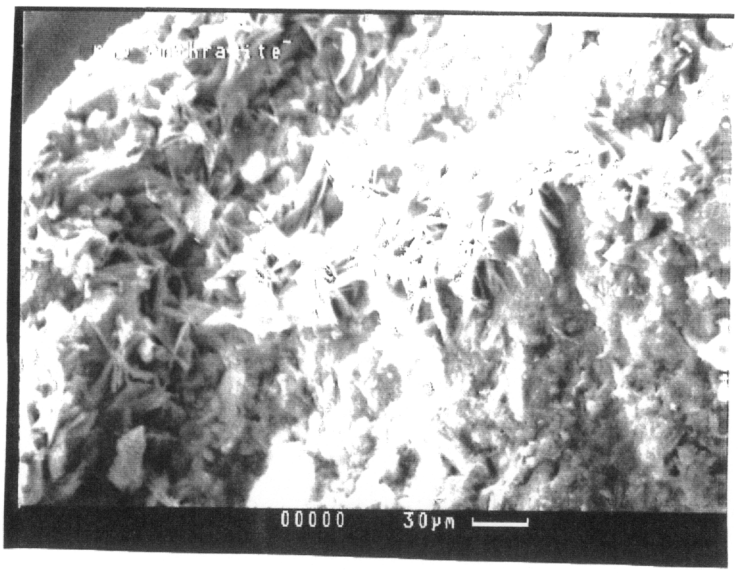

B

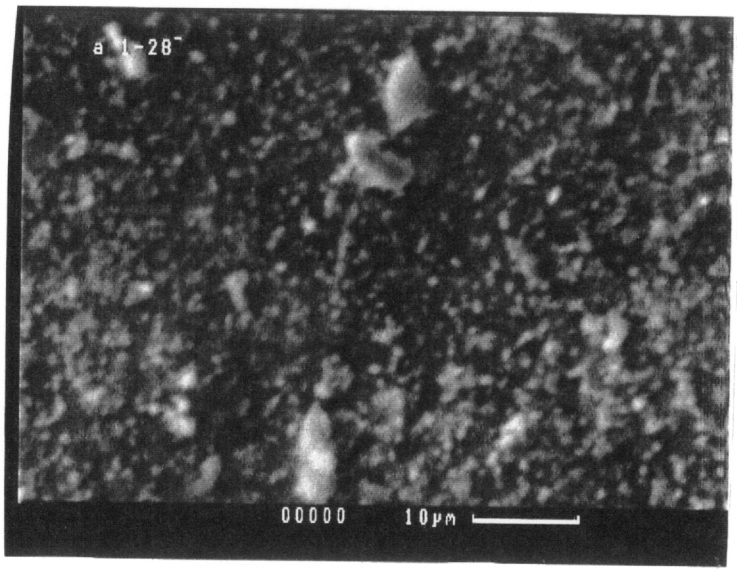

FIGURE 1 A) Native mineral deposit on uncoated anthracite (SEM). Fe and S identified by EDS as primary elemental constituents.

B) Particles embedded in uncoated anthracite surface (SEM). Qualitative energy dispersive x-ray spectral analysis (EDS) identified Al and Si as the primary cation constituents (excluding H^+).

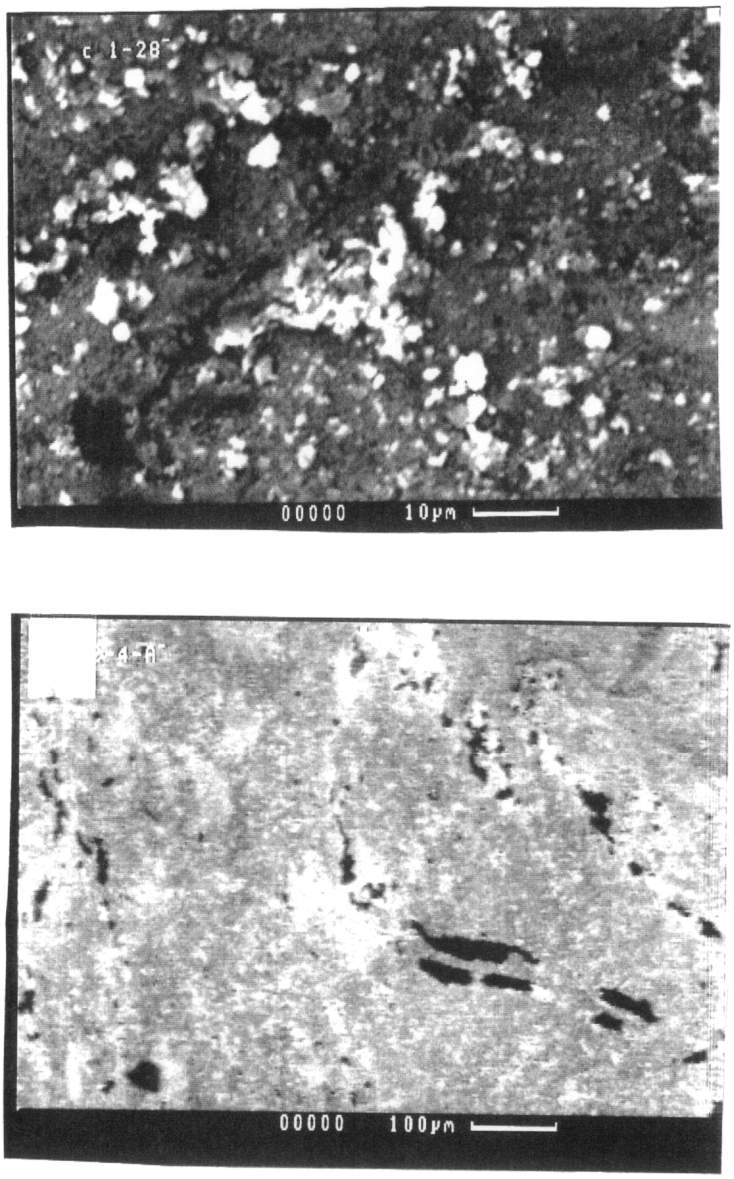

FIGURE 2 A) Initial stage of synthetic $MnO_{x(s)}$ deposition on anthracite media, sample 1, backscattered electron image (BSE). B) Sample 2, synthetic $MnO_{x(s)}$ coating on anthracite, BSE image showing anthracite surface as dark patches showing through bright $MnO_{x(s)}$ deposit.

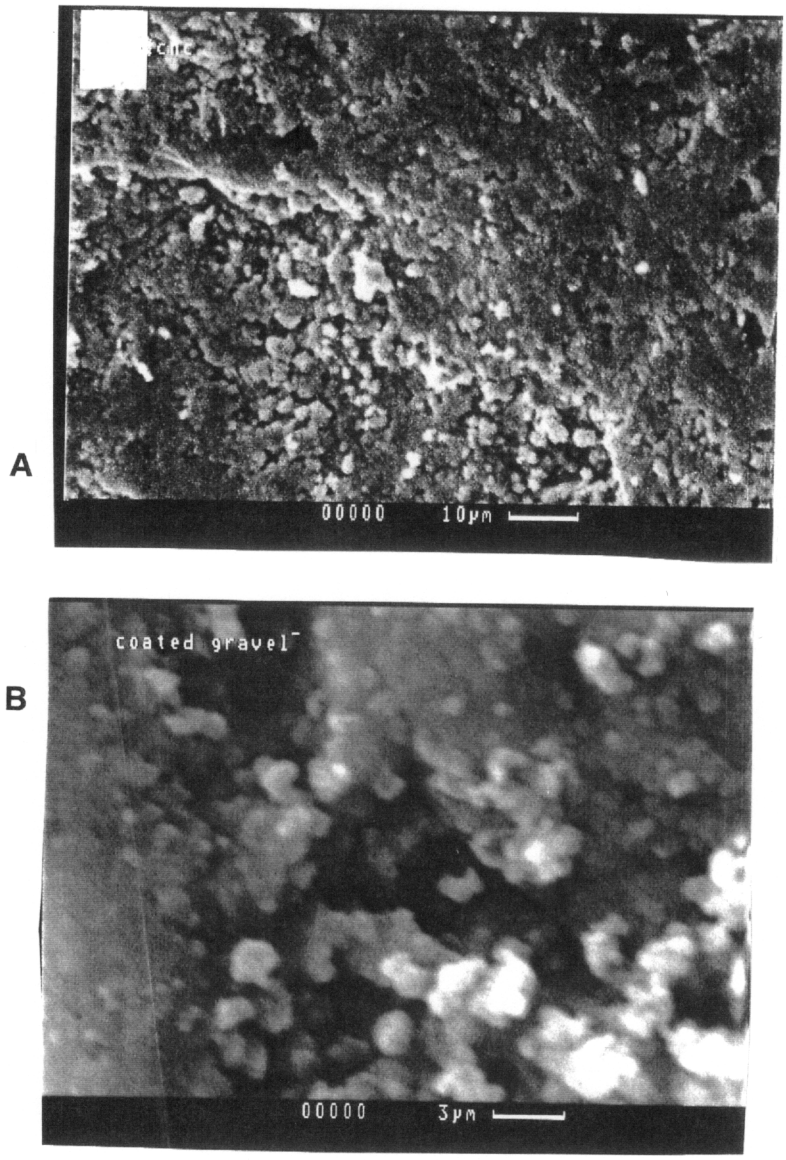

FIGURE 3 A) Sample 10, synthetic $MnO_{X(s)}$ coating on anthracite, SEM image of particles on consolidated coating.
B) Synthetic $MnO_{X(s)}$ coating on gravel media, SEM image of particles on consolidated coating.

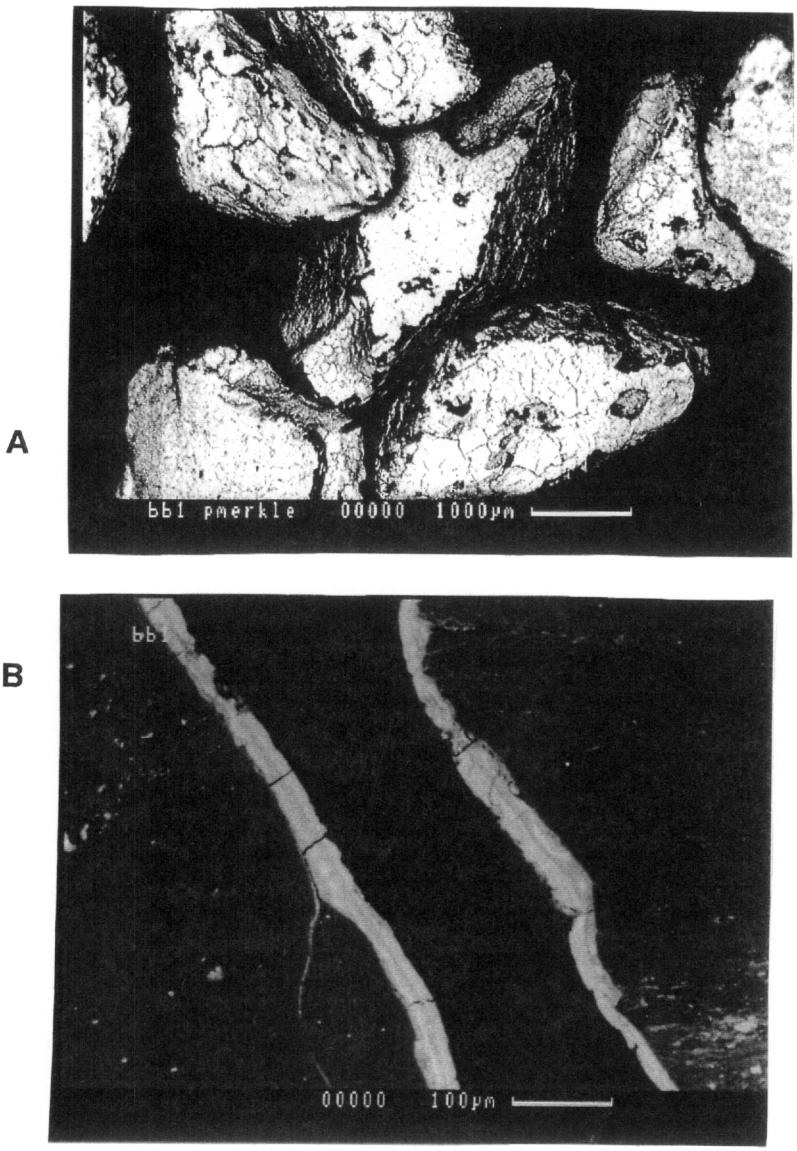

FIGURE 4 A) Blacksburg, VA oxide-coated anthracite media, BSE image of natural surface coating. Broken pavement appearance is probable artifact of sample preparation. Al, Mn, and Si identified by EDS as primary cation constituents.

B) Blacksburg, VA oxide-coated anthracite media, BSE image of polished cross section, showing banding features in exterior coating.

A

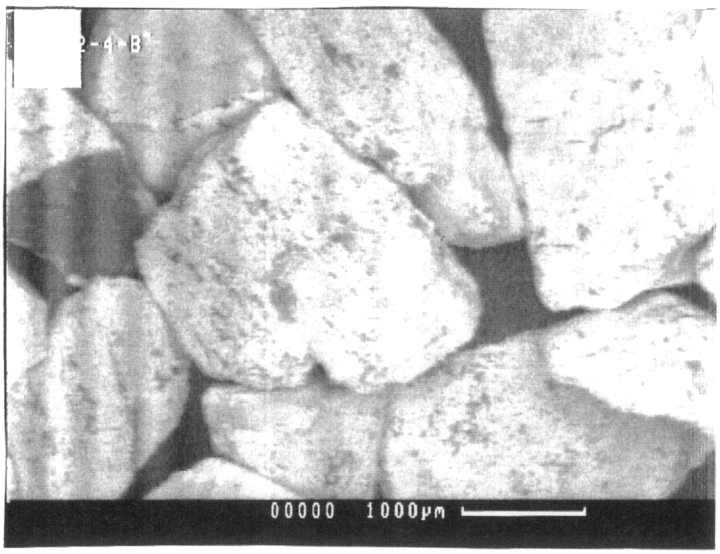

B

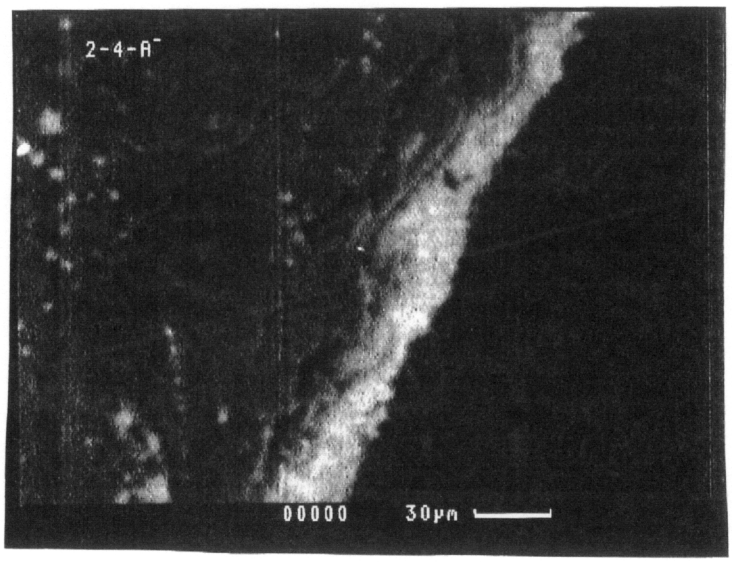

FIGURE 5: A) Sample 3, synthetic $MnO_{x(s)}$ coating on anthracite, BSE image, coating appears bright.
B) Sample 3, synthetic $MnO_{x(s)}$ coating on anthracite, BSE image of polished cross section.

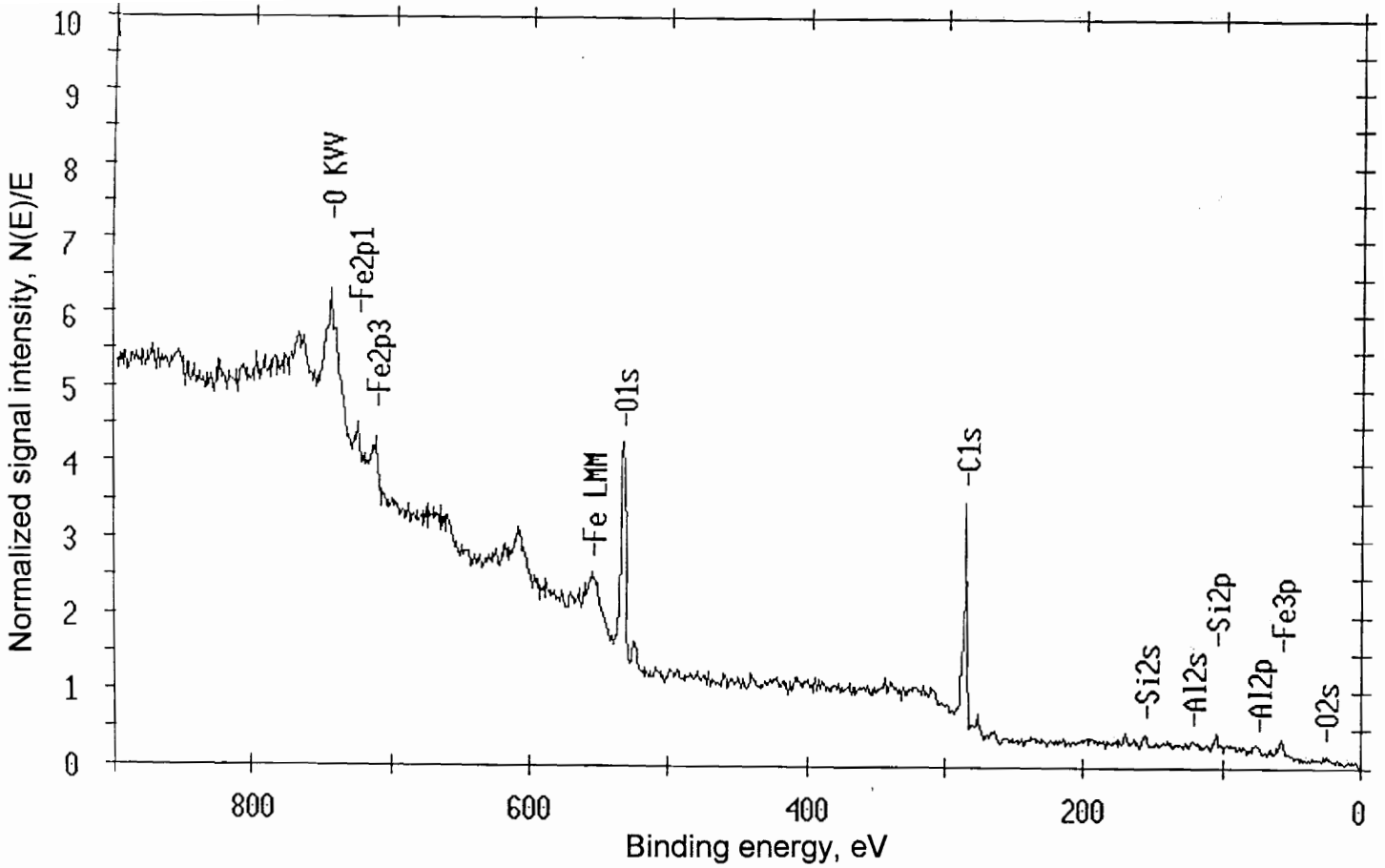

FIGURE 6 X-ray photoelectron spectrum of uncoated anthracite surface. Individual photoelectron peaks are labeled with the appropriate source orbital designation (e.g. C1s or Al2p). Characteristic Auger electron peaks are labeled by orbital transition (e.g. Fe LMM).

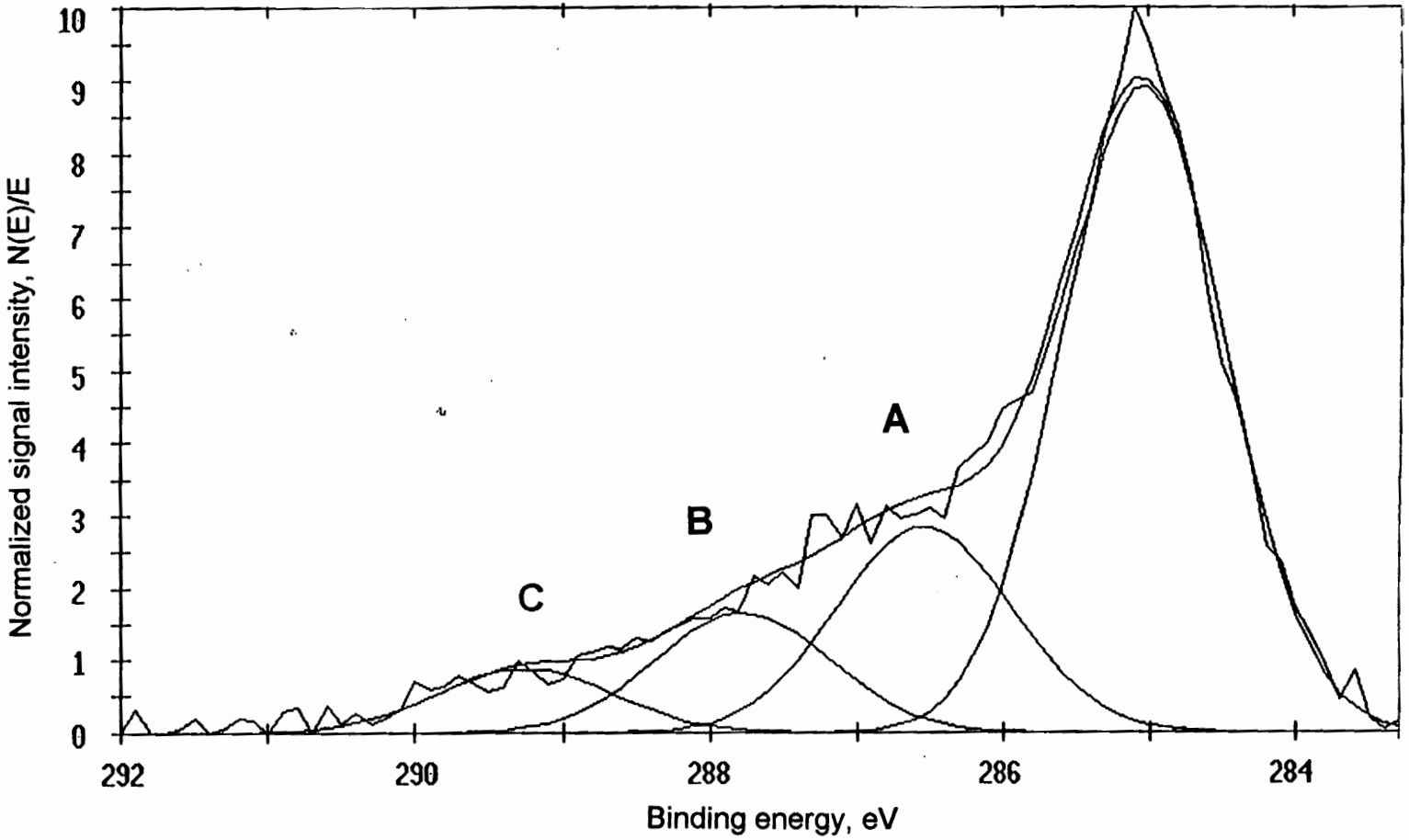

FIGURE 7 Scan of C1s peak region from X-ray photoelectron spectrum of uncoated anthracite. Smooth curves are fitted to the data (jagged line). Peaks identified: A) -OH (hydroxyl), B) -C=O (carbonyl), C) -COOH (carboxyl)

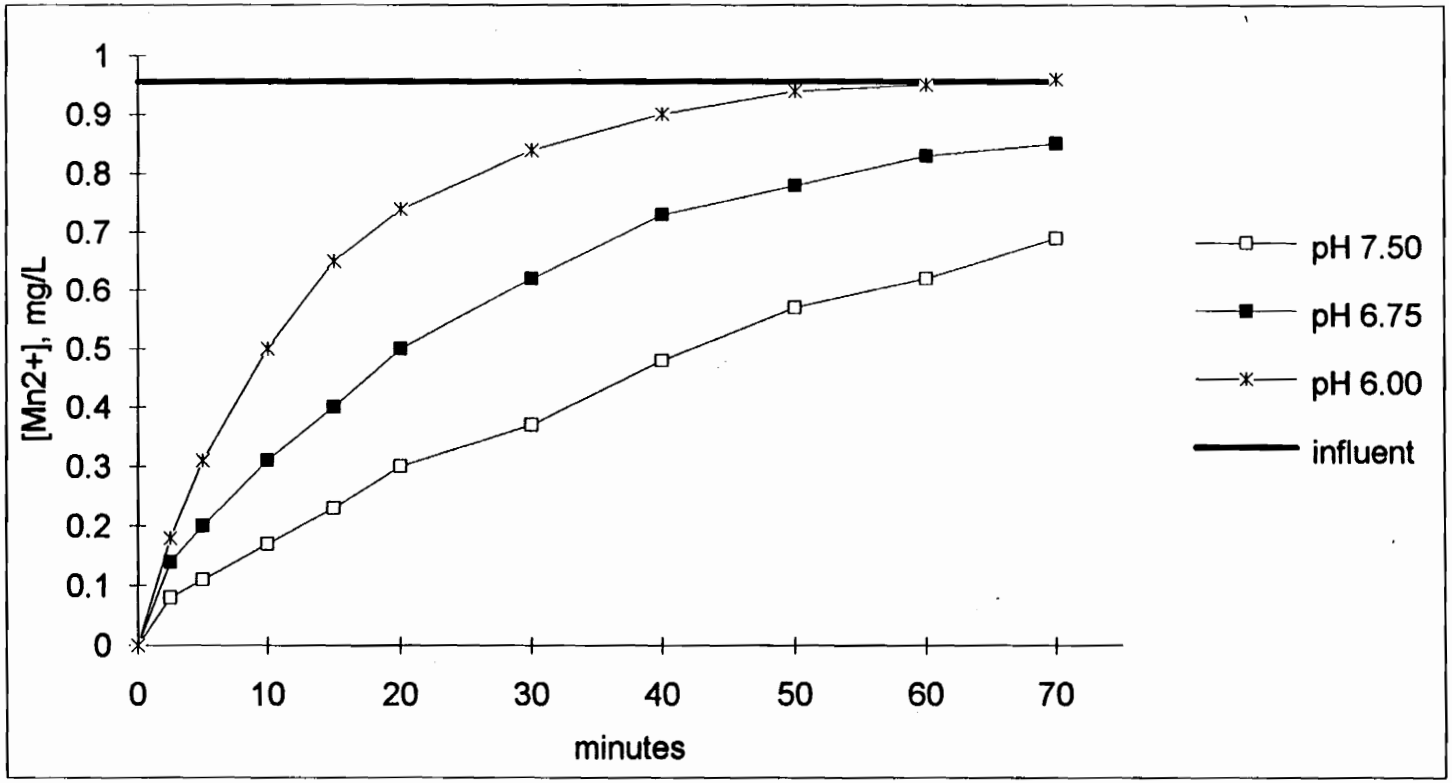

FIGURE 8 Sorption of Mn^{2+} on sample 11 (extractable Mn, 2 mg g^{-1} media), anthracite synthetically coated with $MnO_{x(s)}$. Column depth: 10 cm, column diameter: 4 cm, flow rate: 5 gpm ft^{-2}, mean influent $[Mn^{2+}]$: 0.96 mg L^{-1}, 10^{-3} M $HCO_3^=$ added to Milli-Q water, background [NaCl]: 0.26 g L^{-1}.

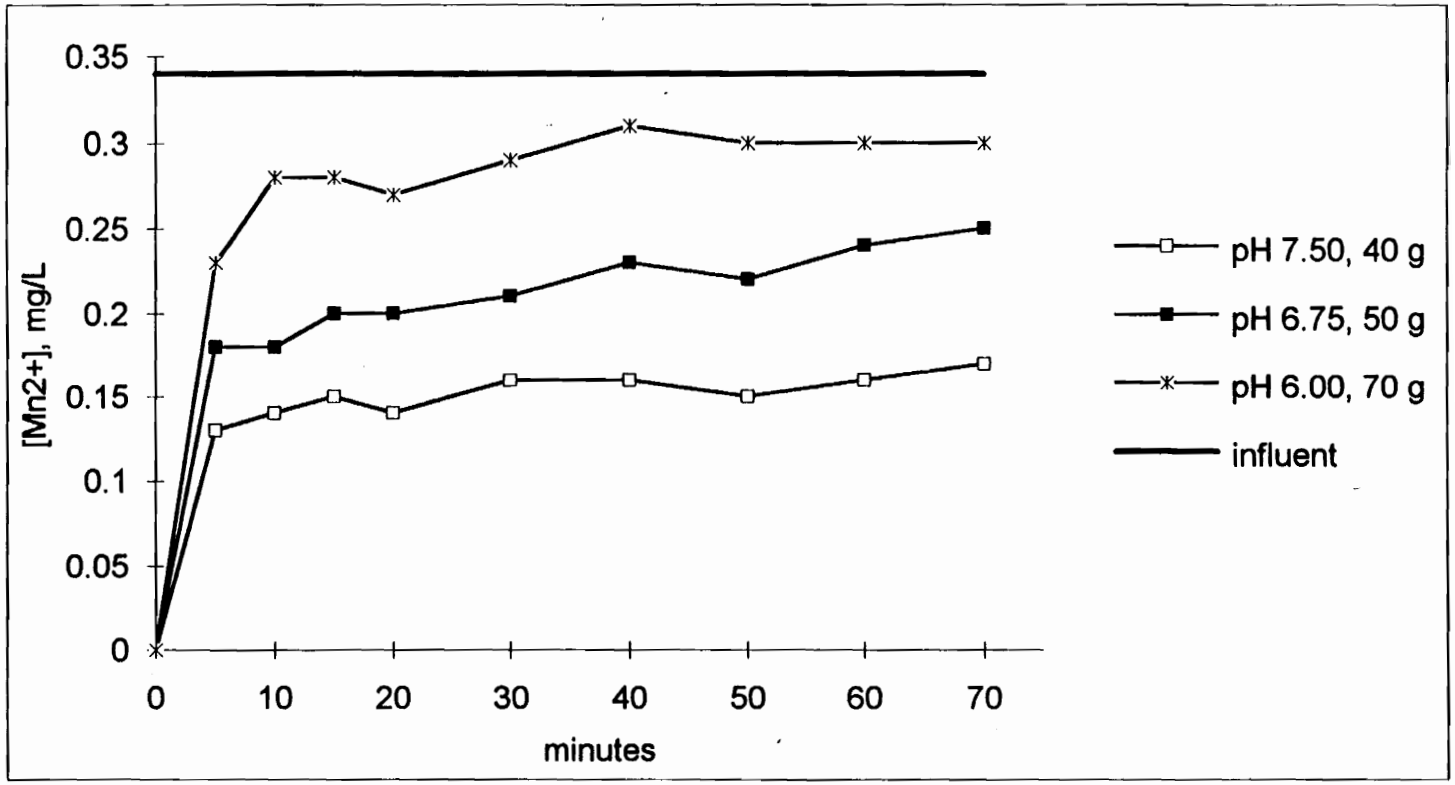

FIGURE 9 Sorption and oxidation of Mn^{2+} in the presence of free chlorine, sample 11 (extractable Mn, 2 mg g^{-1} media), anthracite synthetically coated with $MnO_{x(s)}$. Column depths: 1 cm per 10 g media, column diameter: 4 cm, flow rate: 5 gpm ft^{-2}, mean influent [Mn^{2+}]: 0.96 mg L^{-1}, mean free chlorine: 1 mg L^{-1}, 10^{-3} M $HCO_3^=$ added to Milli-Q water, background [NaCl]: 0.26 g L^{-1}.

CHAPTER 3

DYNAMIC PROCESS MODEL OF SOLUBLE MANGANESE REMOVAL BY OXIDE-COATED FILTER MEDIA

INTRODUCTION

The presence of dissolved Mn^{2+} in drinking water is undesirable for several reasons: it causes bad taste, stains on laundry and plumbing fixtures, and pipe-fouling deposits. In the U.S., the initial stages of the conventional process for treating most surface waters involves chlorination of the raw water, addition of aluminum sulfate or ferric chloride as coagulant, flocculation and settling of coagulated solids, and filtration. A common filter design, the dual-media filter, is a stratified bed of graded gravel and sand overlain with a layer of anthracite coal, for a total bed depth typically less than 1 meter.[1] If dissolved Mn^{2+} is present in the raw water, Mn-bearing mineral deposits or coatings may grow on the surface of the filter media. These deposits are known to absorb Mn^{2+}, and in the presence of free chlorine as oxidant, the coatings catalyze oxidation of sorbed Mn^{2+}, and the filters act as the treatment process for Mn removal.[2] This phenomenon is known as the "natural greensand effect" (NGE) process. Greensand is a glauconite mineral treated with $KMnO_4$ typically used in a fixed-bed contactor to remove soluble Mn^{2+}. Process options for Mn removal include addition of strong oxidants such potassium permanganate, ozone, or chlorine dioxide to produce $MnO_{x(s)}$, followed by solid-liquid separation processes such as coagulation, settling, and filtration. However,

these methods may produce colloidal $MnO_{x(s)}$ particulates which may not be efficiently removed by settling or filtration.

Oxide-coated media (OCM) perform a dual function in the NGE process, permitting two modes of operation for soluble Mn^{2+} removal. In the "intermittent regeneration" or "IR" mode, the OCM filter bed absorbs Mn^{2+} in the absence of a strong oxidant, with sorption capacity periodically regenerated by application of an oxidant such as free chlorine or potassium permanganate. In the "continuous regeneration" or "CR" mode, free chlorine is continuously supplied to oxidize the sorbed Mn^{2+} to insoluble $MnO_{x(s)}$ on the coated media surface, continuously regenerating sorption capacity and maintaining catalytic function.

While the NGE process is gaining acceptance for use in water treatment plants,[3] a predictive design model is needed for engineering control and process specification. In particular, a numerical process model which can account for dynamic changes in the process variables of flow rate, pH, and reactant levels is needed. The objective of this study was to produce such a model, based on fundamental process phenomena of mass transport, sorption, and surface-catalyzed Mn^{2+} oxidation.

BACKGROUND

A number of investigators have studied Mn removal by filter media over the past several decades, and the fundamental principles of sorption and surface oxidation have been established.[4-8] Analytical solutions for steady state process operation have been developed for both intermittent and continuous regeneration modes. Coffey *et al.*[9] modeled Mn oxidation in the presence of free chlorine at the oxide surface after the method of Nakanishi:[10]

$$Mn^{2+} + MnO(OH)_{2(s)} \Leftrightarrow MnO_2MnO_{(s)} + 2H^+ \quad \text{(sorption)} \quad (1)$$

$$MnO_2MnO_{(s)} + HOCl/OCl^- \Rightarrow 2MnO_{2(s)} + H^+ \quad \text{(oxidation)} \quad (2)$$

An implicit assumption in equations 1 and 2 is the regeneration of one surface site as $MnO(OH)_{2(s)}$ and incorporation of MnO_2 into the oxide phase. Keeping the regenerated sites in the accounting, the overall reaction is:

$$Mn^{2+} + MnO(OH)_{2(s)} + HOCl + H_2O \Rightarrow MnO_{2(s)} + MnO(OH)_{2(s)} + 3H^+ + Cl^- \quad (3)$$

The model developed in this work is based on a simplified version of equation 3. Since a detailed knowledge of the sorption site structure and Mn^{2+} oxidation product stoichiometry is lacking, equation 3 may be restated as:

$$Mn^{2+} + SITE + HOCl \Rightarrow MnO_{x(s)} + SITE \quad (4)$$

The reacting species of equation 4 are understood to pertain to the oxide surface region. In this scheme, Mn^{2+} is incorporated into the oxide surface as $MnO_{x(s)}$ replaces the sorption site originally utilized. The total number of sorption sites is independent of the amount of oxide deposited, an assumption which may not be valid over extended periods of filter operation. Also, any near-surface pH change (and corresponding localized change in pH-dependent site density) due to the sorption and oxidation reaction is neglected.

In this study, the simplified reaction of equation 4 was used as the basis for the dynamic numerical process model of the CR mode. The IR mode is a

special case of this model with no oxidant present, and the media bed performs as a filter-absorber unit. This NGE process model builds upon previous efforts by incorporating the Freundlich sorption isotherm for the process chemistry of interest, external and internal mass transport kinetics for Mn^{2+}, and the capability to apply dynamic boundary conditions for flow rate, pH, and reactant concentrations.

Several laboratory methods were adapted for use in characterizing the performance of OCM in the NGE process. The effect of $O_{2(aq)}$ concentration on Mn^{2+} uptake was examined by flow-through column study, and isotherms for OCM - Mn^{2+} systems were determined by a recycle sorber method. A differential reactor was used to assess the kinetics of Mn^{2+} oxidation by free chlorine for several different OCM as a function of flow rate, temperature, and process chemistry. The numerical models for both NGE process modes were developed after consideration of the physical and chemical nature of the oxide coating, characterized in a separate study (see Chapter 1 of this dissertation). The process models were calibrated with data from laboratory column tests on synthetically coated and naturally coated filter media for a range of pH, flow rate and Mn^{2+} and Ca^{2+} concentrations, and model validation studies were conducted at two filter plants to evaluate model predictive capabilities.

METHODS AND MATERIALS

I. Laboratory Studies

Sorption isotherms: A short-bed recycle absorber was used to determine sorption isotherms for Mn^{2+} on natural and synthetic OCM as a function of pH and $[Ca^{2+}]$. The absorber apparatus is depicted in Figure 1, and

the test protocol is summarized in Table 1. The flow-through bed technique was selected to facilitate mass transfer without agitating the media and detaching the coating, as might occur in a stirred-batch method. The 4 L volume of the recycle absorber reservoir was chosen to reduce errors caused by addition of acid or base solution to control pH. Any volume added to adjust the initial pH, typically 2-4 mL, was accounted for in the sorption capacity calculation. For acidic pH condition tests, acid was added to the volumetric flask during solution initial preparation. The typical amount of pH-control solution added during each test was less than 1 mL, or 0.025% of final reservoir solution volume, so this addition was neglected for purposes of sorption capacity calculation. The recirculation rate (10 gpm ft^{-2}) pumped 19 reservoir volumes through the media bed during the 150 minute test.

During method development, the reproducibility of the recycle technique was evaluated by replicate tests (n = 4) using a 1 L reservoir under the following solution conditions: time = 120 minutes, pH = 7.50, initial $[Mn^{2+}]$ = 5 mg L^{-1} (added as $MnCl_2 \cdot 4H_2O$), $[Ca^{2+}]$ = 10 mg L^{-1} (added as $CaSO_4 \cdot 2H_2O$), $[HCO_3^-]$ = 10^{-3} M (added as $NaHCO_3$), using 10 g of sample 1. The reservoir $[Mn^{2+}]$ time series for the four tests are shown in Figure 2a. The mean sorption capacity of this media calculated by the method of Table 1 was 0.0513 mg g^{-1}, with 95% confidence limits of 0.0471 and 0.0554 mg g^{-1}, approximately ±8% of the mean value. The time series of reservoir $[Mn^{2+}]$ during recycle absorber tests of synthetically coated anthracite sample 2 (2 mg g^{-1} extractable Mn) is shown in Figure 2b, with minimal (<2%) additional removal between 120 and 150 minutes at each pH condition.

Global rate study of Mn^{2+} oxidation by free chlorine: Global Mn^{2+} oxidation rates (mg Mn^{2+} g^{-1} min^{-1}) for oxide-coated media were determined with a differential reactor, a 4 cm diameter Pyrex column fitted with a perforated Teflon media support disk (see Figure 1). The feed solutions were prepared in a 20 L Pyrex reservoir from distilled deionized water with 10^{-3} M HCO_3^- (added as $NaHCO_3$) and background salt added ([NaCl] = 0.26 g L^{-1}). For the test with [Ca^{2+}] = 60 mg L^{-1} (added as $CaCl_2 \cdot 2H_2O$), NaCl was omitted to maintain constant ionic strength. Reservoir pH was adjusted with 0.5 M NaOH or HCl.

With the column stopcock open, the column and outlet tube were filled to hydrostatic equilibrium with this solution, then the stopcock was closed and the column completely filled. The support disk was allowed to settle down to the column base in order to avoid trapping air bubbles beneath it. Media was slowly poured into the column to settle on the disk, with gentle tapping on the side of the column to compact the bed. The stopcock was then opened and the overlying solution drained freely through the bed to re-establish hydrostatic equilibrium. Then, soluble Mn^{2+} was added to the reservoir by volumetric pipette from a 500 mg L^{-1} Mn^{2+} solution prepared from $MnCl_2 \cdot 2H_2O$ in Milli-Q water. Free chlorine was added by volumetric pipette from a 5.5% NaOCl solution, and reservoir pH was adjusted again to the desired level before solution was pumped onto the column. The media typically was in contact with the Mn^{2+}-free solution in the column for 5 minutes before application of the reservoir solution. Effluent samples were filtered through 0.45 μm syringe filters and immediately analyzed for Mn by flame atomic absorption, and effluent chlorine was determined by PAO titration method.[11]

The matrix of test conditions is summarized in Table 2. The flow rates and pH levels were chosen to span the range of filter-applied waters typically found in conventional treatment practice. The column effluent Mn^{2+} and free chlorine concentration results from this study were also employed for calibration of the process model for CR mode.

Sorption - desorption short bed absorber study: The procedure for the sorption-desorption column study is summarized in Table 3. The synthetically coated media sample 2 was used rather than a naturally coated media in order to avoid "site-specific" effects arising from coating characteristics that might be unique for any such sample. Column effluent samples were taken at regular intervals over the sorption and desorption stages, filtered through 0.45 μm syringe filters and analyzed by flame atomic absorption.

The effect of $[O_{2(aq)}]$ on Mn^{2+} sorption was investigated, with the detailed procedure and results summarized in Appendix I.

II. NGE Process Model

The model structure for both process modes incorporates the Freundlich isotherm to describe Mn^{2+} sorption, and is based on the "linear driving force approximation", or LDF model.[12] The simple LDF model assumes local sorption equilibrium at the surface, and transport through a film or boundary layer:

$$ds/dt = k_f a_V(C^* - C) \qquad (5)$$

where C is bulk solution concentration, C^* is the equilibrium solute concentration specified by the isotherm, and k_f is the fluid to particle mass transfer coefficient, with a_V the nominal geometric surface area per bed volume. An extension of the

simple LDF model is the LDF series model, which considers both external and internal mass transport resistances acting in series to govern solute uptake kinetics.

Intermittent Regeneration Mode: Initial evaluation of the short bed sorption-desorption results indicated that while the simple LDF model could predict the sorption leg of the breakthrough curve, under some conditions the desorption curve was over predicted. This indicated the possibility of a Mn^{2+} sorption hysteresis phenomena or hindered back-diffusion, as encountered in granular activated carbon (GAC) absorbers for organic compounds.[13] In a related study (Chapter 1, this dissertation), the $MnO_{x(s)}$ coatings were found to be similar in important respects to GAC media. Analysis of natural and synthetic OCM found high specific surface areas (0.56 to 135 $m^2\ g^{-1}$), with most surface area associated with micropores of diameter less than 70 Å.[14] This similarity suggested that internal transport kinetics could be a factor in Mn^{2+} sorption phenomena, as in GAC sorption of organics. The LDF series model was adopted, based on these considerations.

In the LDF series model for the IR mode (sorption only), both external film transport and internal transport are considered. The total equilibrium sorption capacity is apportioned into kinetically "available" and "unavailable" pools, corresponding to external/macropore sorption sites and internal/micropore sites:

$$Mn^{2+}_{(fluid)} + Site_{Av} \overset{k_1}{\leftrightarrow} Mn^{2+}(Ads_{Av}) + Site_{Un} \overset{k_2}{\leftrightarrow} Mn^{2+}(Ads_{Un}) + Site_{Av} \quad (6)$$

$$Sites_{total} = Site_{Av} + Site_{Un} = K\,[Mn^{2+}]^{1/n} \quad \text{(Freundlich isotherm)} \quad (7)$$

where:

$k1$ = fluid to surface transfer rate coefficient, cm min^{-1}

$k2$ = internal transport rate coefficient, cm min^{-1}

$Mn^{2+}_{(fluid)}$ = bulk fluid concentration

$Site_{Av}$ = sorption sites kinetically "available" by film transport

$Mn^{2+}(Ads_{Av})$ = Mn^{2+} sorbed to "available" sites

$Site_{Un}$ = sorption sites kinetically "unavailable"

$Mn^{2+}(Ads_{Un})$ = Mn^{2+} sorbed to "unavailable" sites

$Sites_{total}$ = total sorption sites specified by isotherm

This scheme involves considerable approximation, since all processes by which a soluble species may associate with an insoluble bulk mineral phase are not separately treated, such as lattice ion-exchange, surface diffusion, and pore diffusion. A schematic of several possible Mn^{2+} interactions with oxide-coated media is given in Figure 3. These processes are all "lumped" into the kinetic parameter k_2 and the division of equilibrium sorption capacity into available and unavailable pools by the model. Such a simplified structure of the internal transport processes operative in $MnO_{x(s)}$ coatings stops short of the complexity of state-of-the-art models developed for GAC systems, but was not elaborated further in this initial modeling effort because the characteristics of $MnO_{x(s)}$ coatings are likely site-specific and as yet not completely understood. This is in contrast with GAC media that are prepared to commercial and performance specifications, and in relative terms are physically and chemically well-characterized and amenable to a more explicit treatment of intraparticle sorption

and transport phenomena. Current models for GAC such as the HSDM (Homogeneous Surface Diffusion Model)[15] and PFPSDM (Plug-flow Pore Surface Diffusion Model)[13] consider radial concentration gradients in homogeneously porous GAC particles, multi-component adsorption equilibria, and phenomena such as hindered back-diffusion kinetics. An important difference between GAC and OCM is that the latter are completely porous particles of high surface area (200 -1000 m^2 g^{-1}), while a thin (5-125 μm) microporous shell of high surface area is active in Mn^{2+} sorption by OCM.[14] With these characteristics, surface diffusion of Mn^{2+} is likely to be the dominant internal transport mechanism. For the NGE process model developed here, it is the hypothesized transport mechanism.

For the IR model, values for the kinetic parameters k_1 and k_2 were derived from predictive correlations developed for GAC sorption, discussed in detail in subsequent sections. This leaves one parameter for NGE model calibration, "AFR", the kinetically available fraction of sorption capacity. When AFR = 1, the model reduces to the simple LDF model without intraparticle transport (k_2 = 0). The film transport parameter k_1 was estimated by the flow correlation of Gnielinski, modified to account for particle shape effects.[16] The internal transport parameter k_2 was estimated from the Keinath correlation,[17] with the surface diffusion coefficient D_S estimated from fundamental analysis. Longitudinal hydrodynamic dispersion is included in the model as a function of media diameter and flow rate. Predictive correlations used for mass transport parameters are discussed in subsequent sections.

Continuous regeneration: The intermittent regeneration model was modified to account for the surface oxidation reaction, which is assumed to be an irreversible process. The continuous regeneration model is:

$$Mn^{2+}_{(fluid)} + Site_{Av} \overset{k_1}{\leftrightarrow} Mn^{2+}(Ads_{Av}) + Site_{Un} \overset{k_2}{\leftrightarrow} Mn^{2+}(Ads_{Un}) + Site_{Av} \quad (8)$$

$$Mn^{2+}(Ads_{Av}) + HOCl_{(fluid)} \overset{k_3}{\rightarrow} MnO_{x(s)} + Site_{Av} \quad (9)$$

$$Sites_{total} = Site_{Av} + Site_{Un} = K\,[Mn^{2+}]^{1/n} \quad \text{(Freundlich isotherm)} \quad (10)$$

where:

k_3	=	apparent surface oxidation rate constant, $L^2\ mol^{-1}\ min^{-1}$
$HOCl_{(fluid)}$	=	bulk fluid oxidant concentration
$Site_{Av}$	=	sorption sites kinetically "available" by film transport
$Mn^{2+}(Ads_{Av})$	=	Mn^{2+} sorbed to "available" sites
$Site_{Un}$	=	sorption sites kinetically "unavailable"
$Mn^{2+}(Ads_{Un})$	=	Mn^{2+} sorbed to "unavailable" sites
$Sites_{total}$	=	total sorption sites specified by isotherm

In this model, further assumptions have been made in order to remain consistent with the IR model hypothesis that surface diffusion is the mechanism of Mn^{2+} internal transport . The surface which is active in the catalysis of Mn^{2+} oxidation is assumed limited to the external, kinetically available sites (see Figure 3a). The rationale for this assumption is that the oxidizing agents hypochlorous acid (HOCl) or hypochlorite (OCl^-) are presumably not species

which sorb to the $MnO_{x(s)}$ surface. They may reach the surface by turbulent and molecular diffusion processes, but once there, do not participate in surface diffusion to interior Mn^{2+} sorption sites. Essentially, the model assumes that once an oxidant molecule encounters a surface, it may encounter a sorbed Mn^{2+} and react. Thus, Mn^{2+} is free to diffuse into the interior of the coating to sites kinetically inaccessible to the oxidant, which reacts at the exterior available sites only. The observed coating structure is consistent with this reaction scheme, since coating micropore volume was found to vary linearly with coating amount (Chapter 1, this dissertation). If oxidant were able to reach interior sites, microporosity would be eliminated as $MnO_{x(s)}$ was deposited until all pores were filled. The apparent oxidation rate k_3, based on bulk fluid oxidant concentration, incorporates the intrinsic surface reaction rate and all pertinent oxidant film transport phenomena.

Fluid to surface (boundary layer) mass transfer: The mass transport rate constants (k_f or k_1) of Mn^{2+} from the bulk fluid to the particle surface as a function of particle diameter and flow rate were calculated by the correlation method of Roberts *et al.*[16] for irregularly-shaped media. They applied a simplified version of Gnielinski's relationship:

$$Sh \approx (2 + 0.644\, R^{1/2}\, Sc^{1/3})[1 + 1.5(1 - \phi) \qquad (11a)$$

Sh = Sherwood number, $k_f d_p D_L^{-1}$

R = Reynolds number, $u d_p \upsilon^{-1}$

Sc = Schmidt number, $\upsilon d_p D_L^{-1}$

ϕ = bed porosity

d_p = particle diameter

D_L = bulk liquid diffusivity

u = pore fluid velocity

υ = kinematic viscosity

Roberts *et al.* evaluated a particle shape correction factor Ψ, independent of R, to correct predicted k_f values to account for mass transport enhancement. They hypothesized that enhanced external transport resulted from boundary layer disruption and enhanced surface area of the rough, nonspherical GAC media used in their sorption experiments. In this study, the value of $\Psi = 2$ was used, which was the best-fit determined in their work for GAC media with surface roughness characteristics similar to those observed for OCM. Media grain diameter was estimated by sieve analysis for media of this study, using for d_p the d_{50} values determined from size distribution plots (Figure 4). Liquid diffusivity of Mn^{2+} was calculated by the Nernst equation:[18]

$$D_i^0 = l_i RT(Z_i F^2) \qquad (11b)$$

where:

D_i^0 = solute diffusivity, $cm^2\ s^{-1}$

l_i = solute dielectric parameter, $cm\ \Omega^{-1}\ mol^{-1}$

R = gas constant

F = Faraday constant, 96,500 C mol^{-1}

Z_i = solute charge

Surface diffusion: The surface diffusion kinetic term k_2 (or k_s) was estimated by the Keinath correlation[17] for k_s (cm min^{-1}), which is:

$$k_s A_v = 60\ D_s\ d_p^{-2} \qquad (12)$$

A_v = surface area, $cm^2\ cm^{-3}$ bed volume

D_s = surface diffusion coefficient, $cm^2\ s^{-1}$

d_p = particle diameter, cm

This correlation is typically applied to organic sorbents in GAC absorbers. The external surface area A_v is normally estimated by the spherical geometric area of the media based on d_p. However, for diffusion of Mn^{2+} on the oxide surfaces in this study, the exterior surface area in contact with the fluid (where surface diffusion initiates) is likely underestimated by this calculation, and corrected values were used.[19] Atomic force microscopy (AFM) measurements of surface roughness found a surface fractal dimension f_d of 2.16 for a synthetically coated media (Chapter 1, this dissertation). This corresponds to greater surface area per unit diameter vs. spherical geometry (f_d = 2.0). For a spherical particle of synthetically coated media (d_p = 0.12 cm, ρ_p = 1.59 g cm^{-3}, bed porosity ϕ = 0.49) the specific external surface areas estimated for geometric and fractal spheres S_g ($cm^2\ g^{-1}$) are:

Geometric spheres:

$$S_g = 6\ (\rho_p d_p)^{-1},\ cm^2\ g^{-1} \qquad (13)$$

A_v = 24,500 $cm^2\ cm^{-3}$ bed volume

Fractal spheres:

$$S_g = 6\ (\rho_p d_p^{1.16})^{-1} \qquad (14)$$

A_v = 34,400 $cm^2\ cm^{-3}$ bed volume

It should be emphasized here that the actual surface characteristics of oxide minerals in aqueous solution such as sorption site density, geometry and related surface diffusion phenomena are the subject of ongoing research. The *a priori* method presented here for estimation of D_S is an attempt to proceed from fundamental principles, to treat the oxide-coated media system in a manner consistent with the model hypothesis that surface diffusion is the mechanism of intraparticle Mn^{2+} transport. The surface diffusion coefficient D_S for Mn^{2+} on the oxide surface was estimated from consideration of the process as a random walk in which the adsorbed species "hops" from site to site. By the analysis given by Suzuki[20], for a sorbed Mn^{2+} at a sorption site with unit distance x between adjacent sites, D_S is:

$$D_S = 1/2\ (\Delta x)^2/\Delta t \qquad (15)$$

Δx = mean step size, Δt = step time

When the activation energy of hopping (E_S) is insignificant, the vibration frequency of the absorbed molecules υ_X provides an estimate of Δt and thus D_S:

$$\Delta t = (2\upsilon_X \exp(-E_S/RT))^{-1} \qquad (16)$$

$$\Delta t = (2\upsilon_X)^{-1}, \text{ for } E_S \cong 0 \qquad (17)$$

$$D_S = (\Delta x)^2 \upsilon_X \qquad (18)$$

$$\upsilon_X = 10^{11} - 10^{13}\ sec^{-1} \qquad (19)$$

For the Mn^{2+} - $MnO_{X(s)}$ system under consideration, υ_X is not known, but an estimate for D_S was derived from an estimate of the sorption site density of

cations on oxides. If we begin by assuming that D_S is 10^{-5} cm^2 sec^{-1}, on the order of 10 times the magnitude of the estimated solution diffusion coefficient for Mn^{2+} ($D_0 \cong 10^{-6}$ cm^2 sec^{-1}), evaluation in the likely range of values for υ_X results in these estimates for Δx by equation 18:

$$\Delta x \cong 3.1 \text{ Å} \quad (\upsilon_X = 10^{10} \text{ sec}^{-1})$$
$$\Delta x \cong 1 \text{ Å} \quad (\upsilon_X = 10^{11} \text{ sec}^{-1})$$
$$\Delta x \cong 0.31 \text{ Å} \quad (\upsilon_X = 10^{12} \text{ sec}^{-1})$$

With and Mn - O bond length of 1.9 Å, the estimate of $\Delta x \cong 3.1$ Å, appears reasonably consistent with a plausible geometry of the $MnO_{X(S)}$ surface site where Mn is the center of the surface-coordinated sorption complex. This result suggests that in this aqueous system, a lower value $\upsilon_X \cong 10^{10}$ sec^{-1} applies. As an independent check of this estimation method for Δx, the sorption site densities for α - $FeOOH_{(S)}$ (goethite) determined by several investigators[21] for a variety of solutes averaged 3.7 sites nm^{-2}. By analogy with $MnOOH_{(S)}$, one likely surface $MnO_{X(S)}$ phase, this implies that on the average, each site occupies 27 $Å^2$, for a radial site boundary separation distance Δx of 2.9 Å. Thus, D_S was estimated as 9×10^{-6} cm^2 sec^{-1}, using a mean $\Delta x = 3$ Å and $\upsilon_X = 10^{10}$ sec^{-1}. For the media considered above with $A_V = 34.4$ cm^2 cm^{-3} bed volume, k_S (k_2) = 1.1×10^{-3} cm min^{-1}.

Hydrodynamic dispersion: Longitudinal dispersion of Mn^{2+} and oxidant was estimated by the empirical correlation of Suzuki:[12]

$$Pe = 1.2\, d_p \qquad (20)$$

$$Pe = \text{Peclet number, } ud_p(E_z)^{-1} \qquad (21)$$

$$E_z = \text{longitudinal dispersion coefficient, } cm^2\ min^{-1}$$

This correlation was developed for R > 100 (turbulent regime). The range of R values encountered for the media employed in this study is 27 to 166, based on flow rate and particle diameter. The correlation for turbulent conditions was adopted for all flow rates for consistency with film transfer correlation assumptions, since enhanced turbulence is implicitly assumed for the non-spherical, rough media.

Model Numerical Implementation: The numerical model code was developed in the DYNAMO™ simulation language in single-precision arithmetic, using a variable step-size, third-order Runge-Kutta integration procedure employing backward differencing.[22] The method of lines was used to spatially extend in one dimension (bed depth) the model equations for mass transfer and reaction.[23] The method of lines approximates this set of partial differential equations in the time domain by finite difference approximation, and in the spatial domain by discretization of the bed depth. The resulting set of finite difference equations is solved sequentially in time for each spatial location, based on the boundary conditions imposed initially or dynamically during the course of the simulation. The maximum time step size allowed was 0.0375 seconds, with a spatial grid for model calibration of 0.2 cm (10 cm column

depth), and 0.5 cm for validation studies (32 cm column depth). The initial boundary conditions for flow rate and chemical species concentrations were specified, and the flow and influent reactant concentrations could be varied dynamically during the course of a simulation, as appropriate.

Model calibration and sensitivity analysis: The NGE process model was calibrated to laboratory column data using a multi-dimensional fitting algorithm based on least-squares error minimization, the downhill simplex method or "amoeba" technique.[24] The fitting algorithm was compiled in Microsoft FORTRAN, with the source code modified to provide the user with trial fitting parameter values to run the process model in batch mode. The tolerance for error minimization was 10^{-5}. The AFR (available fraction for sorption) parameter was varied for the IR case, with other kinetic parameters predicted by the correlation methods previously described. For the CR mode, AFR and the apparent oxidation rate k_3 were fitted simultaneously to column data at pH 7.50, 5 gpm ft^{-2}. This fitted value of k_3 was used to predict the remaining column data, with AFR being fitted. To evaluate the accuracy of the predictive correlation for film transfer, k_1 was fit to data from three flow rates (2.5, 5.0 and 10 gpm ft^{-2}) at pH 6.75, with AFR = 1.

A formal sensitivity analysis was performed for both intermittent and continuous regeneration model modes using results from pH 7.50, 5 gpm ft^{-2} conditions. The estimated model variances, parameter estimates, and sensitivity coefficients were determined by ordinary least squares analysis.[25] The assumptions of this method are: 1) the process model is appropriately specified, 2) the mean of random errors (ε) is zero, 3) model variance is constant and finite, 4) ε are not correlated with time, 5) the model is not over parameterized,

6) ε are independent and, for this nonlinear model case, asymptotically normally distributed. Under these assumptions, the model variance s^2 for N data points and p parameters is:

$$s^2 = \mathbf{e}^T\mathbf{e}\,(N-p)^{-1} \quad (22)$$

$\mathbf{e}$ = estimate of ε, i.e. observed - predicted value

$$\mathbf{e}^T\mathbf{e} = \Sigma e^2 = \text{sum of squared residuals, SSR} \quad (23)$$

The parameter estimate variances are given by:

$$\text{Var}(P) = s^2(\mathbf{X}^T\mathbf{X})^{-1} = s^2\Omega \quad (24)$$

$$\mathbf{X} = \text{Sensitivity coefficient matrix} \quad (25)$$

$$\mathbf{X} = d(C)_{x,t,}/d(P) \quad (26)$$

The diagonal elements of $s^2\Omega$ are the parameter variance estimates, with off-diagonal elements being the estimated parameter covariances.[26] The α-level confidence intervals for parameter estimates by Student's t distribution are estimated as:

$$\text{parameter C.I.} = P_i + t_{(1-\alpha/2,\ N-p)}\,(s^2\Omega_{ii})^{0.5} \quad (27)$$

P_i = best-fit parameter value

The correlations ($\mathbf{C}_{ij}$) of the model parameters are given by the off-diagonal elements of the correlation matrix:

$$\mathbf{C} = \Omega_{ij}(\Omega_{ii}\Omega_{ij})^{-0.5} \quad (28)$$

The "hat" matrix (**H**) diagonal gives the "leverage" of each data point in the fit:

$$H = \mathbf{X}(\Omega)\mathbf{X}^{T} \quad (29)$$

For a leverage > 2p/n, the data point is "influential" in the parameter estimate.[26]

Media analysis methods: Detailed procedures for the techniques for media extraction, surface area analysis, electron microscopy, and energy-dispersive x-ray analysis may be found in Chapter 1 of this dissertation, a study of OCM physical and chemical characteristics. The media used in model calibration and validation studies were examined by scanning electron microscopy (SEM) and standardless energy dispersive x-ray analysis (EDS). A discussion of the oxide coating characteristics as they may relate to model structure and performance follows presentation of the validation study results.

III. Validation Studies

Model validation studies were conducted in Fall, 1994, at the Blacksburg-Christiansburg-VPI and Durham, NC, Wade Brown water treatment facilities. Process water from each site was used to determine Mn^{2+} sorption isotherms. Bed porosities and media densities were determined from triplicate measurements of media packing in a volumetric cylinder. Oxide coating levels were determined by chemical extraction.[2] The validation column apparatus (dia. = 4.3 cm) is shown in Figure 5, with sample ports located at 8 cm intervals.

Blacksburg: Anthracite media was collected from the upper filter layer and rinsed in tap water. Media sorption capacity was regenerated by flow-

through application of a concentrated free chlorine solution in tap water (100 mg L^{-1} as HOCl). The media was rinsed thoroughly with distilled, deionized water and dried in air prior to isotherm determination and sieve analysis.

For both IR and CR validation studies at Blacksburg, untreated and filter-applied water were unavailable, although these process streams were the desired influents for validation. Finished water was used for all studies: prior to the IR studies, a 120 L reservoir was dechlorinated on site by stoichiometric addition of sodium hyposulfite with free chlorine determined by DPD tablet method,[11] and soluble Mn^{2+} added by volumetric pipette from a 25 mg L^{-1} $MnSO_4 \cdot H_2O$ stock solution. For CR mode, finished water and acidified Mn^{2+} solution was pumped into a 10L mixing tank (filled prior to start-up with finished water adjusted the desired [Mn^{2+}]), and the column was fed from the tank.

To place the media, the column was filled with a "packing solution" (distilled, deionized water adjusted to the pH of interest, with 0.26 g L^{-1} NaCl added). For each test, 472 g of media was poured into the filled column and allowed to settle with gentle tapping to a depth 8 cm above the first sample port. A slight cloudiness was seen in the column after packing, probably due to detached coating particles. The solution was drained to establish hydrostatic equilibrium, with approximately 5 cm water overlying the bed. During the column tests, reservoir and port samples were filtered by 0.45 μm syringe filter and analyzed within 1 hour of test completion by flame atomic absorption. A small amount of particulates were present on the filters, typically most visible in the first samples taken.

Durham: Anthracite media was collected from the indoor filter gallery at the Brown plant. The media was washed in tap water to remove loosely

attached solids, but the media coating was shed heavily, even under gentle rinsing. Plant personnel advised that the media from these filters would not rinse clean, but would continue to abrade. The rinsing was stopped, and the media was placed in a concentrated chlorine solution (800 mg L^{-1} as HOCl) for 8 hours, and rinsed again thoroughly in tap water prior to air and oven drying overnight at 90 °C. The Durham validation columns were packed as in the Blacksburg study, but the copious amount of coating detached from the media required rinsing with 10 L of packing solution for the effluent to clear. Coagulated, settled water (before chlorination) was retrieved for the IR study using the same reservoir method as in Blacksburg. This water appeared slightly turbid, and had a slight yellow color. Filter-applied water was used for the CR study, employing the mixing tank apparatus. Samples were filtered by 0.45 μm syringe filter and preserved for analysis within 12 hours by addition of 0.1 mL concentrated HCl. Particulates were more abundant on the filters than in the Blacksburg test.

RESULTS and DISCUSSION

I. Laboratory Studies

Sorption isotherms: The Freundlich isotherm equation is:

$$S = KC^{1/n} \tag{30}$$

$$\log (S) = n^{-1} \log (K) + \log C \tag{31}$$

S = amount of sorbed component, mg solute g^{-1} media

K = capacity factor, L g^{-1}

1/n = exponential factor

The Freundlich isotherm parameters determined by linear regression of the log-transformed data are summarized in Table 4, along with the regression statistics. The Freundlich isotherm was selected for use in the kinetic model since all isotherms determined were log-linear below $[Mn^{2+}]$ = 2 mg L^{-1}, which spans the range of process $[Mn^{2+}]$ likely to be encountered in treatment practice, as well as a recommended maximum $[Mn^{2+}]$ acceptable for NGE process application of 0.35 mg L^{-1} (see Chapter 4, this dissertation). The sorption capacity of naturally and synthetically-coated media increases with pH, and decreases with $[Ca^{2+}]$ = 60 mg L^{-1}, as shown in Table 4 for sample #2 and the Norfolk, NE sample.

The isotherms for synthetically coated media sample 2 as a function of pH are shown in Figure 6. The pH 6.00 isotherm exhibits saturation above $[Mn^{2+}]$ = 2 mg L^{-1}, suggesting that a Langmuir-type isotherm capable of accounting for media saturation may be appropriate under low pH or other chemical conditions which reduce sorption capacity. The Freundlich parameters determined at pH 6.00 for use in the model included the four lowest concentration points in the regression, in the linear portion of the plot.

Global rate study of Mn^{2+} oxidation by chlorine: The goal of these tests was to establish a steady-state condition in the bed so that the rates of all kinetic processes (reactant transport and Mn^{2+} oxidation) would be equal. The oxidative removal tests used 40 - 70 g of coated media (shallower bed depths) than the sorption-desorption tests so that effluent $[Mn^{2+}]$ would remain quantifiable by flame atomic absorption. The study results are summarized in Table 5. Columns at 5 gpm ft^{-2} appear to reach steady state after 40 minutes (Figure 7); linear regressions through the last four data points of all tests show no significant slope (Table 5). The effluent $[Mn^{2+}]$ of the final two samples of

each test were averaged to estimate the "steady state" global oxidation rate. Oxidation rates measured at the three pH conditions were significantly different ($p = 0.02$, single-factor ANOVA).

The differences in oxidation rate as a function of the physical and chemical media characteristics are of interest. The global Mn^{2+} oxidation rate (mg Mn^{2+} hr^{-1}) may be calculated on two different bases: per g media, or per mg extractable Mn. These rates for synthetic and natural media plotted against extractable Mn (Figure 8) show that additional Mn coating above several mg g^{-1} does not greatly increase the oxidation rate. On the basis of oxidation rate per mg extractable Mn, the rate declines with increasing coating amount. Plotted against surface area, the global oxidation rates per mg Mn show the same pattern (Figure 9). This suggests that the measured surface area (and presumably all sorption capacity) is not actively participating in the oxidation process. Oxidation rate per mg Mn also decreases with increasing coating micropore volume (Figure 10), consistent with the surface area result.

If the test columns reached steady state, the observed rate differences between the various flow, pH and influent [Mn^{2+}] conditions should be accounted for by mass transfer and sorption capacity characteristics. The global oxidation rates determined as a function of flow rate are shown in Figure 11, and are plotted with the predicted film transfer coefficient. The observed variation in oxidation rate is consistent with the effect of enhanced mass transfer at higher flow rates. Global oxidation rates also increase with influent pH (Figure 12) and [Mn^{2+}] (Figure 13), consistent with the predicted increase in Mn^{2+} sorption capacity from the isotherm (capacity plotted for the influent [Mn^{2+}] of each test).

Oxidation of Mn^{2+} to Mn^{3+} is indicated by the stoichiometry measured under these conditions where oxidant is supplied in 200% excess to the Mn^{2+} feed rate. The mean (95% confidence interval) for reaction stoichiometry was 0.59 (0.381 - 0.790) mg HOCl per mg Mn^{2+}, compared with the theoretical oxidant demand of 0.65 mg HOCl per mg Mn^{2+} for oxidation to Mn^{+3}. In plant practice, oxidant may be in even greater excess, and a higher average Mn oxidation state may result, consistent with the prior studies of Knocke *et al.*[2]

Intermittent regeneration calibration: The results of model fitting for intermittent regeneration process mode are given in Table 6, with special fitting cases summarized in Table 7. The best-fit value of the parameter AFR (available fraction for sorption) is listed along with the fitting statistic root mean squared error (rms error) for each model fit. Selected plots of model fit vs. test data are discussed here, with the remaining plots included in Appendix II. Best-fit values of AFR less than 1 correspond to the LDF series model. The simple LDF model with no internal mass transport corresponds to AFR = 1, and the rms error for this model is given if the simple LDF model is not the best fit .

For 7 out of 16 conditions in the sorption-desorption tests, the simple LDF model (AFR = 1) provided a better fit than the LDF series model. The LDF series model (AFR < 1) worked best when media sorption capacity was highest, generally at higher pH; at pH 7.50, it provided an average 30% reduction in rms error as compared to AFR = 1, and an average 9% reduction at pH 6.75. The pattern of model fits are shown in Figure 14a, a plot of best-fit AFR against calculated equilibrium sorption capacity for the influent [Mn^{2+}] of each test. The test conditions for the four points indicated as outliers from this pattern are interesting: points a, c, and d had influent [Mn^{2+}] of approximately 0.34 mg L^{-1},

and point b was the Blacksburg media. For the latter case, the better fit of the LDF series model may be due to differences in coating-specific characteristics (such as composition or structure) affecting Mn^{2+} sorption and internal mass transport, such as coating thickness, site distribution within the coating, and coating porosity. For the former three cases, a concentration-dependent effect on internal mass transport is suggested, since the AFR parameter implicitly accounts for any such effects. A concentration dependence of surface diffusion coefficient not accounted for by the model is one such effect. In figure 14b, a trend of increasing rms error with decreasing pH is apparent (adj. R^2 =0.69, F significance 7e-5), corresponding with a lower absolute sorption capacity. No trend was found for rms error against flow rate (Figure 14c).

In general, the model could satisfactorily reproduce the IR column effluent profiles for the lower flow (2.5 and 5 gpm ft^{-2}) and higher pH (6.75 and 7.50) conditions, suggesting that fluid to particle mass transport and isotherm behavior is adequately accounted for in model structure. Figures 15 to 17 depict the best-fit model results for pH 7.50 at the three flow rates tested. As an evaluation of the applicability of the modified Gnielinski correlation, the model was fit to results at pH 6.75 for each of the three flow rates by varying k_1, the film transfer coefficient (Table 7). The AFR was set to 1 for these fits for internal consistency, since the LDF series model provided only slight improvements in fit for 2.5 and 5 gpm ft^{-2} flow rates. The best-fit k_1 values were close to the predicted values, with the greatest error at 10 gpm ft^{-2}.

The model fit for the elevated Ca^{2+} test at lower influent $[Mn^{2+}]$ is also good (Figure 18), also indicating that the isotherm is reliably implemented by the model. The prediction for pH 6.75 at 10 gpm ft^{-2} shows over prediction during

desorption (Figure 19), although the sorption fit is good. The model fits at 2.5 gpm ft^{-2} for pH 6.75 and 6.00 are satisfactory (Figures 20 and 21). However, at pH 6.00 the model demonstrates over prediction during the early phase of sorption. This error worsens at 10 gpm ft^{-2} at pH 6.00 (Figure 22).

This and other cases of poor model fit using AFR were evaluated further by trial fitting, allowing additional model parameters to vary (such as k_1 and k_2). Based on the multi-parameter fitting, the model failure can be attributed to either inaccuracies in parameter estimation or inappropriate structure. If the best-fit parameters values thus determined are consistent with a reasonable physical or chemical process pertaining to the conditions of model failure, then this new process may be incorporated in to the model for predictive use. Such an analysis excludes gross experimental and model implementation error as a cause of model inconsistency.

The model boundary conditions were examined as a possible cause of model error by including a mixing zone in the model, treated as a continuous stirred tank reactor (CSTR) prior to the media bed. This corresponds to the small amount (50 mL) of Mn^{2+}-free packing solution overlying the bed, which initially mixed with the column influent. This could have produced an initial gradual increase in $[Mn^{2+}]$ rather than a step increase as simulated. However, the addition of the CSTR produced no marked improvement in the model prediction. The model was then fit by varying k_1, k_2, and AFR simultaneously (Figure 23, Table 7), which produced a more realistic fit. The fitted value for k_1 was 7 times the predicted value, and AFR was 0.485. This is not consistent with the best-fit pattern from the other tests, that the k_1 correlation is satisfactory and that AFR = 1 for this low pH. Another fit was conducted, allowing the k_1 and

Freundlich K parameters to vary, with AFR = 1. An improved fit resulted, but again the fitted values were in disagreement with the predicted values (k_1 = 10 times predicted, K = 42% of measured value). Based on this failure analysis, the current model does not have predictive ability at this particular high flow rate, low sorption capacity condition. The model for intermittent regeneration mode in general tends to be less accurate in combined conditions of high flow and low absolute sorption capacity (which typically but not exclusively occurs at low pH).

The model fit for the Blacksburg media #1 was surprisingly good for both sorption and desorption, considering the extreme conditions of the test (Figure 24). This media had a low sorption capacity in comparison to its oxide-coating amount (Table 4), so the effluent showed Mn^{2+} breakthrough almost immediately. The fitted AFR of 0.63 for the LDF series model indicates that this media had a significant amount of sorption capacity in interior sorption sites.

Continuous regeneration calibration: Model calibration results for the CR mode are summarized in Table 8. The model was first calibrated to one of the triplicate pH 7.50, 5 gpm ft^{-2} tests, allowing both AFR and k_3, the apparent oxidation rate constant, to vary simultaneously. The fitted value of k_3 was used to predicted all other results, fitting only AFR. This rationale is based on the assumption that surface oxidation deposits new $MnO_{x(s)}$ on kinetically available reactive sites during the test, and the intrinsic surface oxidation rate in controlled laboratory conditions should not vary greatly.

An implication of the model assumption that only available reactive sites are significant in Mn^{2+} oxidation is that the best-fit AFR values for CR mode should not be greater than the AFR values for the corresponding conditions of the sorption-desorption test. The optimized two-parameter fit is shown in Figure

25, with k_3 = 9.48 x 10^3 L^2 mol^{-1} min^{-1}, and AFR = 0.555 for the 3 cm bed depth. The best-fit AFR for sorption-desorption was 0.775, so the lower AFR value is consistent. Two replicate columns were predicted with these values, with depths of 3 and 4 cm (Figures 26 and 27, respectively). The replicate pure predictions are good, considering the likely differences in actual boundary conditions between replicates from any day-to-day process and analytical equipment variability.

The model predictions for pH 7.50 at flows of 2.5 and 10 gpm ft^{-2} are excellent (Figure 28 and 29); note the differences in column depth for these and subsequent tests which were required to obtain similar, quantifiable effluent [Mn^{2+}]. The best-fit AFR values of 0.565 and 0.562, respectively, are close to the best-fit AFR of 0.555 from the pH 7.50, 5 gpm ft^{-2} flow condition. This is consistent with the assumption that AFR is independent of flow, and accounts primarily for unknown surface phenomena which may be more related to pH and solution chemistry effects rather than a pure flow effect. The predictions for pH 6.75 and 6.00 at 5 gpm ft^{-2} support this argument, with best-fit AFR values of 0.71 and 0.915, respectively. For the high [Ca^{2+}] condition at pH 7.50 and 5 gpm ft^{-2} (Figure 30), the best-fit AFR is 0.71, again less than the sorption-desorption value under the same conditions (AFR = 0.87).

The Blacksburg #1 media test was predicted using the best-fit AFR and k_3 values from the fit to synthetic sample #2 (Figure 31, Table 8). The fit was slightly higher for these values, and rms error was reduced by 50% for the best-fit AFR = 0.876. However, this AFR is higher than the best-fit for sorption (0.63), which is inconsistent with the pattern seen for the synthetic media. The Swift Run media test showed a similar pattern of over prediction by the synthetic

media best-fit AFR (Figure 32), with a best-fit AFR of 1. The differences in best-fit AFR between synthetic, Blacksburg and Swift Creek media may result from real differences in the initial coating characteristics that govern kinetic availability or type of reactive sites. A primary difference may be coating composition: for example, the synthetic media surface is nearly pure $MnO_{x(s)}$, while the outer layer of the Blacksburg coating (5 mg g^{-1} extractable Mn) actually contains more Al than Mn, as determined by EDS analysis. (Al:Mn, 3:1 atomic ratio). The deposition of fresh $MnO_{x(s)}$ may result in a net production of sites on the original $(Al,Mn)O_{x(s)}$ surface, (rather than simple site replacement, as assumed by the model), so the available sorption capacity may actually increase during the test. Also, a higher concentration of sites at the new exterior coating surface would result in more kinetically available sites, different from the initial available site distribution in the coating. Alternatively, the pore structure of the coating and surface roughness may affect mass transfer kinetics somehow not accounted for by the lumped parameter approach.

Model sensitivity analysis: A partial model sensitivity analysis was conducted on single short-bed column studies of both NGE process modes. Results of model variance and parameter estimation are summarized in Table 9 for 1% changes in parameters from the best-fit values. Note that this sensitivity analysis is based on model response to small changes in parameter values for these specific conditions of media type, chemical condition, bed depth, and test duration. Under different conditions, both qualitative and quantitative differences in the analysis should result. The estimated confidence intervals for AFR are $\pm$ 2.4% for IR, and $\pm$ 6.7% for CR. The AFR and k_3 parameters are not

highly correlated (r = -0.67), but the confidence interval for k_3 is ± 48% of the best-fit value.

The AFR sensitivity coefficient (s) for effluent [Mn^{2+}] is shown in Figure 33 for the IR mode. The units of s are mg L^{-1} per change in AFR. For the sorption leg (t < 75 minutes), effluent [Mn^{2+}] is initially most sensitive to changes in AFR, with |s| (absolute value) declining with time. During desorption, s is relatively constant. The point leverages from the **H** matrix indicate that the first five sample times of Figure 16 are influential in the parameter estimation, consistent with sorptive uptake dominating the early breakthrough curve.

In CR mode, s for AFR shows the same pattern of |s| declining with time (Figure 34). The s for the oxidation rate constant k_3 shows |s| increasing with time from near zero initially (Figure 35). The first two and last two times are influential points for this analysis (Figure 25). This is consistent with the early curve dominated by sorption, and the latter portion governed by oxidation at steady state. For a longer time series, the confidence interval for k_3 would likely narrow, as more points in the oxidation-controlled regime would be included. The sensitivity coefficients may be directly compared on a relative dimensionless basis by parameter elasticities, τ, defined as:

$$\tau = (\%\Delta C) / (\%\Delta P) \qquad (32)$$

The elasticities are plotted in Figure 36, showing that during the early phase of the test, effluent [Mn^{2+}] is more sensitive to changes in AFR than k_3. The oxidation rate constant k_3 becomes relatively more influential as the column reaches a steady state condition.

II. Validation Studies

Blacksburg: The first intermittent regeneration validation test at Blacksburg was for steady state conditions of pH (7.4), flow (5 gpm ft^{-2}), and influent [Mn^{2+}] (0.45 mg L^{-1}). The model prediction for this condition is shown in Figure 37, using the best-fit k_3 (9.48 x 10^3 L^2 mol^{-1} min^{-1}) and AFR of 0.63 from the Blacksburg sorption-desorption study. The model prediction is unsatisfactory, particularly in the last half of the test (rms error = 0.105). Since the media used for validation (Blacksburg #2, Table 4) was different from the calibration media, the model was fit by varying AFR (Figure 38). The best-fit value was 1, and the improvement in prediction at longer times is slight (rms error = 0.085). On qualitative analysis, the column data resemble a continuous regeneration test, in that the 8 cm samples do not reach the influent level, and appear to reach a steady state below this concentration. Since the column feed was prepared from dechlorinated finished water, a small amount of free chlorine may have remained. The DPD colorimetric method was used to verify dechlorination, with the minimum scale calibration of 0.2 mg L^{-1}. Using a free chlorine level of 0.1 mg L^{-1} and AFR of 0.876 from the lab calibration, the prediction improves somewhat (Figure 39, rms error = 0.060).

The first validation test for steady state CR mode was conducted at pH 7.4, 9.4 gpm ft^{-2}, with influent [Mn^{2+}] = 0.23 mg L^{-1} (Figure 40). The test was predicted using the AFR = 0.876 from the differential reactor study of Blacksburg media #1 (collected in May, 1994). The media used in the test (Blacksburg #2) was collected in September, 1994. Effluent [Mn^{2+}] was below the flame AA method quantification limit[27] (0.04 mg L^{-1}) for all sample depths past 8 cm. The model prediction is qualitatively accurate in that a steady state is achieved, but

Mn^{2+} removal is underestimated. The flow rate of the test is high, so the model tendency for poorer fit at high flow and low sorption capacity could be responsible for this lack of fit. As discussed later, oxide surface conditions changed between the media sampling dates, and this might account for the poor model performance. However, the column data confirms under controlled conditions the efficiency of NGE process performance; even at this high flow rate, effluent [Mn^{2+}] removal at 32 cm is over 90% of the influent.

The second steady-state CR mode validation test used Blacksburg media #2 at pH 6.6 and 9.35 gpm ft^{-2}. With AFR = 0.876 from the best-fit to Blacksburg media #1, the model prediction is extremely poor (Figure 41), and even by increasing AFR to 1, the model greatly over estimates effluent [Mn^{2+}] (Figure 42). Again, the model failed in calibration to this regime of high flow and low sorption capacity, one explanation of poor correspondence. Another explanation is that the isotherm determined in the lab on the dechlorinated feed was inaccurate (Table 4), which may have resulted from addition of excess hyposulfite. The confidence intervals for the Blacksburg validation isotherms are less precise than those determined with laboratory-prepared solutions. This suggests some experimental error associated with the dechlorination process, possibly excess hyposulfite addition. A systematic underestimation of media sorption capacity for the Blackburg validation is consistent with the result of the CR mode test at pH 7.4 (Figure 40), where [Mn^{2+}] removal was also underestimated when predicted with the mean isotherm parameters. The reversal of the AFR pattern for the Blacksburg media #2 (a higher AFR in CR mode than for IR mode) may be an artifact of isotherm uncertainty (a higher AFR

compensating for underestimation of sorption capacity), or this may reflect some characteristic of the coating different from the Blacksburg #1 media.

Durham: The IR mode validation at Durham was conducted at pH 6.0 and 5 gpm ft^{-2}. No prior laboratory work tests were done on the media, so no AFR values were available for prediction. The model greatly over predicts $[Mn^{2+}]$ removal for this test with AFR = 0.5 (Figure 43). If the laboratory isotherm was determined accurately, one reason for the poor fit may have been that the media sorption capacity was not completely regenerated by the immersion in concentrated free chlorine solution (see discussion of continuous regeneration test). This implies a different initial condition for the model in which some fraction of sorption capacity is already utilized. To account for incomplete regeneration, the model boundary conditions were set to an initial 25% regeneration of the sorption capacity, as determined by the isotherm at the influent $[Mn^{2+}]$. The AFR was set to 0.5, with all unavailable sites utilized. This greatly improved the qualitative model result, with much earlier breakthrough predicted (Figure 44). Further adjustment of the initial condition improves the prediction (Figure 45), with AFR = 0.25 and a 12.5% regeneration level. These hypothetical initial conditions may not reflect the actual regeneration status of the media. Given the unusual structure of the coating (see following discussion), the batch regeneration method used may not have provided sufficient time for complete regeneration. Another explanation of the observed early breakthrough is that submicron particulates passed through the syringe filters that subsequently dissolved upon sample preservation by acid addition.

The CR mode test at Durham was conducted at pH 6.0 and 3.9 gpm ft^{-2}, under dynamic influent $[Mn^{2+}]$. Because the Durham media was suspected to

be partially regenerated, the media for this test was regenerated again in the column. Free chlorine solution (1000 mg L^{-1}) was fed at 1 gpm ft^{-2} until influent and effluent free chlorine concentrations were equal, followed by rinsing with distilled water at pH 6.0 until no free chlorine was detected in the effluent. The AFR parameter was used to fit the model to the test data. (Only the top sample port (4 cm) remained above the flame AA quantification limit.) The model shows good agreement with the data for AFR = 0.185 (Figure 46). This is a relatively low value in comparison to the range of AFR values fit to synthetic and Blackburg media laboratory column tests of CR mode.

Media Analysis: Chapter 1 of this dissertation summarizes a comprehensive survey of oxide-coated media characteristics. The media used for the validation studies show marked differences in extractable Mn (Table 4), and as will be shown, corresponding differences in coating thickness and structure that could affect processes related to model parameters. The characteristics of the synthetically coated media (2 mg extractable Mn g^{-1}) are distinct from the validation media, with $MnO_{x(s)}$ coating thickness of 30 - 40 μm, and a surface oxidation state of Mn(IV) (see Chapter 2 for detailed description of the synthetically coated media). In contrast, the naturally coated media from Blacksburg and Durham consist of Mn, Al, and trace amounts of Fe and Si.

The Blacksburg #1 media (collected May 1994) used in the sorption-desorption test is shown in Figure 47a, an SEM view of the media surface. The coating appears relatively smooth on the scale of 100 μm (the surface cracking may be an artifact of sample drying). The cross-section backscattered electron (BSE) image (Figure 47b) shows the coating as thin bright rings surrounding the dark anthracite grains. (In SEM/BSE mode, brightness corresponds to higher

nuclear density). The Blacksburg #2 validation media (collected September 1994) shows a similar surface (Figure 48a), and a similar appearance by cross section BSE (Figure 48b). In terms of physical structure, the coatings do not appear markedly different.

The BSE images of media cross sections indicate compositional variation as brightness "rings" within the 20 - 30 μm thick coatings (Figure 49a and b). This variation was evaluated by standardless EDS analysis of the ring features, summarized in Table 10. Between May and September 1994, the media experienced many backwash cycles, with potential for removal of the original coating, and deposition of new $MnO_{x(s)}$. The inner dark band of Blacksburg #1 is richer in Mn than the inner band of Blacksburg #2, while the outer bands are similar in composition. In terms of media sorption capacity, if $MnO_{x(s)}$ provides sorption sites, there are relatively more sorption sites in the external, kinetically available region of Blacksburg #2. The model parameter AFR for this media should be higher than for #1, in which sites are distributed more evenly with coating depth.

The Durham media coating is markedly different in roughness and thickness from the synthetic and Blacksburg coatings. The outer surface (Figure 50a) is porous, with pillar-shaped features appearing to grow outward in a surface depression. At higher magnification, these show micron-scale growths at the pillar ends indicating that the coating is actively growing at the tips (Figure 50b), a feature consistent with mass-transfer limitation in this surface depression. This feature suggests that the AFR model parameter reflects a real phenomenon, wherein a small fraction of the outermost available sites are being continuously regenerated. Recall that the best-fit AFR for this media in CR

mode was 0.185, the lowest of any media evaluated. The cross section BSE images show the coating as thick, irregularly distributed deposits (Figure 51), with internal variation in composition. The internal macroporosity and dendritic surface features of this coating (and others studied, see Chapter 1) supports the hypothesis that internal sites are not participating in $MnO_{x(s)}$ deposition.

A mass-balance study by Crowe[28] of the NGE process provided an example of the effect of near-surface coating alteration on aspects of NGE process performance. In this related study, Blacksburg # 1 media was used in May, 1994 to begin a long-term evaluation of filter backwash performance in continuous regeneration mode. Media columns were fed with finished water with Mn^{2+} added, and were periodically backwashed. At the Blacksburg plant, zinc orthophosphate (Zn:P, 2:1) was routinely added to finished water to control distribution system corrosion. In November 1994, the chemical feed composition was changed to Zn:P of 1:1, increasing the amount of phosphate added. After this change, the Mn recovery from column backwash water decreased, with an apparent reduction in the amount of $MnO_{x(s)}$ deposits removed by the backwashing procedure. A post-backwash sample was taken of this media, shown in cross section in Figures 52a and b. The deposit is thicker than the other Blacksburg coatings (40 - 50 μm), and consists of three distinct regions: an inner dark band, an outer bright band, and bright particulates on the outer surface. The composition of the inner dark band does not resemble that of the corresponding features in Blacksburg media #1 or #2, but the outer bright band composition closely matches the outer bright band of Blacksburg #1. The outer bright particles are rich in Mn, and relatively poorer in Al and Si than the underlying coating, probably the most recent deposits. The Al content of this

pre-backwash coating suggest sorption of Al in some form, since the column feed was post-filter finished water in which soluble Al species would presumably constitute the major fraction of Al entering these columns. This also suggests a major role for OCM in control of soluble Al levels in filtered water. If incorporation of soluble Al species into the oxide coating is taking place, this represents a significant surface phenomenon not accounted for in the NGE process model. The model calibration studies using distilled, deionized water would thus have lacked an important component of solution chemistry which could have indicated any model error resulting from this omission.

CONCLUSIONS

This initial attempt at characterization and predictive modeling of the NGE process determined that:

1) The Freundlich isotherm and modified Gnielinski mass transfer formulation incorporated in the LDF/LDF series model structure consistently accounts for system behavior, with model failure evident for extreme conditions of low sorption capacity and high flow.

2) The dynamic NGE process model for the intermittent regeneration mode (Mn^{2+} sorption) can be calibrated by one adjustable parameter (AFR) to account for Mn^{2+} removal by synthetically coated and naturally coated media under controlled laboratory conditions. For the continuous regeneration mode (Mn^{2+} oxidation), the simplifying model assumptions of Mn^{2+} oxidation at available sites provide satisfactory fits to laboratory data under a variety of boundary conditions. The physical structure of naturally coated media provides evidence to support the model assumptions concerning both process modes.

3) The validation study indicated that the model was not useful for prediction of field process application, probably due to variation in composition and structure between the lab and field media evaluated. This indicates that initial coating conditions play an important role in parameter estimation and model predictive capability. The Durham study was hampered by experimental difficulties with media preparation, but the data demonstrate efficient NGE continuous regeneration performance under extreme conditions of low sorption capacity (a function of pH and coating type) and high flow rate. In both the Blacksburg and Durham validation studies, the model could explain observed poor model predictions by incorporation of initial and boundary conditions (such as insufficient regeneration) that may have pertained to the actual system.

This initial effort at modeling of the NGE process demonstrates the applicability of simple chromatographic models to the problem, and that incorporation of the oxidation reaction can explain many aspects of system behavior, despite evident variation in coating structure and composition. Understanding the effect of recent coating history may be critical in accurately incorporating boundary conditions that predict process performance in full-scale filter installations. There are similarities between GAC sorption and the NGE intermittent regeneration process in this regard related to sorption capacity: a major problem in GAC systems is the effect of pre-absorbed organic compounds which reduce capacity. Since Mn oxides can absorb and incorporate other inorganic species, the NGE process may be considered as "GAC for inorganics". Additional modeling research drawing on advances in GAC modeling may prove fruitful, if the advantages of having one or two uncorrelated adjustable parameters are retained in the effort.

LITERATURE CITED

1 - McGhee, T. J. Water Supply and Sewerage **1991**, McGraw-Hill, New York.

2 - Knocke, W. R.; Occiano, S.; Hungate, R. Removal of Soluble Manganese from Water by Oxide-Coated Filter Media **1990**, AWWA Research Foundation, Denver, Colorado.

3 - *AWWA MainStream* **1994** (October), American Water Works Association, Denver, Colorado.

4 - Zapffe, C. "The History of Manganese in Water Supplies and Methods for Its Removal", J. AWWA **1933** (25:5), 655.

5 - Edwards, S. E.; McCall, G. B. "Manganese Removal by Breakpoint Chlorination", Water & Sewage Works **1946**, 93, 303.

6 - Griffin, A. E. "Significance and Removal of Manganese in Water Supplies", J. AWWA **1960**, (52), 1326.

7 - Cleasby, J. L. "Iron and Manganese Removal - A Case Study", J. AWWA **1975**, (67:3), 147 (March).

8 - Knocke, W. R.; Hamon, J.; Thompson, C. "Soluble Manganese Removal on Oxide-Coated Filter Media", J. AWWA **1988** (80:12), 65-69.

9 - Coffey, B. M.; Gallagher, D. L.; Knocke, W. R. "Modeling Soluble Manganese Removal by Oxide-Coated Filter Media", Journal of the Environmental Engineering Division - ASCE **1993** (119:4), 679.

10 - Nakanishi, H. "Kinetics of Continuous Removal of Manganese in a MnO_2-Coated Sand Bed", Kogyo Kagaku Zasshi **1967**, 70 (4), 407.

11 - American Water Works Association. Standard Methods for the Examination of Water and Waste Water **1992**, 18th ed., APHA, AWWA, WPCF, Washington, D.C.

12 - Suzuki, M. Adsorption Engineering, Chapter 7, Chemical Engineering Monographs No. 25, **1990**, Kodansha Ltd., Tokyo, and Elsevier Science Publishers, Amsterdam

13 - Hong, S.; Summers, R. S. "Impact of Backwashing and Desorption on GAC Breakthrough of Natural Organic Matter", Proceedings of the Annual Conference of the American Water Works Association **1994** (June), New York.

14 - Merkle, P. B.; Knocke, W. R.; Gallagher, D. L. "Filter Media Mineral Coatings: Filtration Theory and Practice", Proceedings of the Annual Conference of the American Water Works Association **1994** (June), New York.

15 - Crittenden, J. C.; Weber, W. J., Jr. "Predictive Model for Design of Fixed-Bed Absorbers: Parameter Estimation and Model Development", Journal of the Environmental Engineering Division - ASCE **1978**, (104:EE2), 185.

16 - Roberts, P. V.; Cornel, P.; Summers, R. S. "External Mass-Transfer Rate in Fixed-Bed Adsorption", Journal of the Environmental Engineering Division - ASCE **1985**, (11:6), 891.

17 - Keinath, T. M. "Modeling and Simulation of the Performances of Adsorption Contactors", in: Mathematical Modeling in Environmental Engineering, Proceedings of the **1972** Eighth Annual Workshop, AEEP, Nassau, Bahamas.

18 - Horvath, A. L. Handbook of Aqueous Electrolyte Solutions, **1985**, Ellis Horwood Ltd., Chichester, England.

19 - Merkle, P. B. "A Weather-Driven Model of the Atmospheric Deposition of Semivolatile Organic Compounds to Near-Shore Aquatic Environments", M.S. Thesis, **1991**, Marine Sciences Research Center, State University of New York at Stony Brook, U.S.A.

20 - Suzuki, M. Adsorption Engineering, Chapter 4, Chemical Engineering Monographs No. 25, **1990**, Kodansha Ltd., Tokyo, and Elsevier Science Publishers, Amsterdam.

21 - Davis, J. A.; Kent, D. B. "Surface Complexation Modeling in Aqueous Geochemistry", in: Reviews in Mineralogy: Mineral-Water Interface Geochemistry, **1990**, M. F. Hochella, Jr. and Art F. White, Eds.

22 - Pugh-Roberts Associates, Inc. "Professional DYNAMO Plus™", **1986**, Cambridge, Massachusetts, U.S.A.

23 - Davis, M. E. Numerical Methods and Modeling for Chemical Engineers, **1984**, J. Wiley & Sons, New York.

24 - Press, W. H., Teukolsky, S. A., Vetterling, W. T., Flannery, B. P. Numerical Recipes in Fortran: The Art of Scientific Computing, **1992**, Cambridge University Press.

25 - Judge, G. G., Griffiths, W. E., Hill, R. C., Lee, T.S. The Theory and Practice of Econometrics, **1980**, J. Wiley & Sons, New York.

26 - Troutman, B. M. "Errors and Parameter Estimation in Precipitation-Runoff Modeling: 1. Theory", **1985**, Water Resources Research, (21:8), 1195.

27 - Dewhirst, S., personal communication.

28 - Crowe, A., personal communication.

TABLE 1

PROTOCOL FOR RECYCLE ABSORBER ISOTHERM DETERMINATION

Reagents: (solutions prepared with Milli-Q water)

Solution A: 25 mg L^{-1} $[Mn^{2+}]$ (using $MnSO_4 \cdot H_2O$)

Solution B: 7 g L^{-1} NaCl

solutions for pH adjustment: 0.5 M HCl, 0.5 M NaOH

336 mg $NaHCO_3$, 880.4 mg $CaCl_2 \cdot 2H_2O$

1. To 2 L volumetric flask, add 150 mL of NaCl solution B and the $NaHCO_3$. Fill to volume and drain into reservoir. (For tests with $[Ca^{2+}]$, omit solution B, add the $CaCl_2 \cdot 2H_2O$ and dissolve by swirling the flask before filling).

2. To 2 L volumetric flask, add solution A to obtain the desired initial $[Mn^{2+}]$ of the recycle solution, and fill. Drain into reservoir, and insert pH probe and thermometer.

3. Begin pumping solution through apparatus at 10 gpm ft^{-2}, wetting all surfaces. Drop Teflon support disk into filled column to avoid air trapping. Adjust pH of recirculating solution to desired value by dropwise addition of acid or base to reservoir. Place tubing loop from pump in ice water bath. When pH is stabilized, circulate solution for 5 minutes, then take a 10 mL sample (initial $[Mn^{2+}]$) and filter through 0.45 micron syringe filter.

5. Add 20 - 60 g of media to column and close system (time = 0 minutes). Be careful to equilibrate pressures by loosening the sample plug and column stopper as appropriate. There is a hazard of the Pyrex vessels breaking, as well as stoppers and glass tubes being ejected with force.

6. Sample the reservoir at 30, 60, 90, 120, and 150 minutes, taking a 10 mL sample and filtering as for the initial sample. During the recirculation period, monitor pH and adjust by dropwise addition of acid or base to the reservoir (most pH change occurs during the initial 30 minute period).

7. For the 150 minute final sample, drain all the solution back into the reservoir before sampling. Analyze samples by flame AA immediately.

Calculation of sorption capacity (correcting for sample removal):

$$Mn^{2+} \text{ uptake (mg)}: (CV)_{initial} - (CV)_{final} - (V_S \times \Sigma (C_t))$$

C = reservoir $[Mn^{2+}]$

V = reservoir volume (assume 3.990 L initial, 3.950 L final)*

V_S = sample volume (10 mL)

C_t = sample $[Mn^{2+}]$ for time = 30, 60, 90, 120 min

TABLE 2

TEST CONDITIONS FOR GLOBAL Mn^{2+} OXIDATION RATE STUDY

Variable	**Levels**			
pH:	6.00	6.75	7.50	
flow:	2.5	5.0	10.0	gpm ft^{-2}
temperature:	16°C	25°C		
media:	Sample #2 (synthetically coated anthracite, 2 mg g^{-1} extractable Mn) Naturally-coated anthracite media: Blacksburg VA, Norfolk NE, Swift Run VA, Durham NC (2), Portsmouth VA coated gravel Mn greensand			
$[Mn^{2+}]$	0.15	0.35	0.70 mg/L	
[HOCl]	1.0 mg L^{-1}			
$[Ca^{2+}]$	0	60 mg L^{-1}		

Test conditions:

Flow = 5 gpm ft^{-2}, $[Mn^{2+}]$ = 0.35 mg L^{-1}, $[Ca^{2+}]$ = 0 mg L^{-1} unless indicated:

1. Sample 2:
   a. (flow) x (pH = 7.50)*
   b. (pH)
   c. ($[Ca^{2+}]$ = 60)
   d. ($[Mn^{2+}]$) x (pH = 7.50)
   e. (temp) x (pH = 7.50)

2. Naturally coated media & greensand
   a. (natural & greensand) x pH = 7.5
   b. Swift Run x (pH = 7.50, 6.75)
   c. Blacksburg #1 x (pH = 7.50)

* - Triplicate test at pH = 7.50

TABLE 3

PROTOCOL FOR SHORT BED SORPTION - DESORPTION TEST

1. Calibrate peristaltic pump to desired flow rate by pumping into 2 L graduated cylinder for five minutes. For the 4 cm diameter column, 1 gpm ft^{-2} = 51.2 mL min^{-1}. Place tubing loop in ice water bath after pump head to control solution temperature.

2. Fill 20 L and 10 L Pyrex reservoirs with distilled deionized water, add NaCl (0.26 g L^{-1}) and $NaHCO_3$ (10^{-3} M) and stir to dissolve. For columns with $[Ca^{2+}]$ = 60 mg L^{-1}, omit NaCl to maintain constant ionic strength I = 0.005 M. Adjust pH of 10 L reservoir to desired level and fill column, then add Teflon support disk as in isotherm test.

3. Add 100 g of synthetic media to filled column, gently tapping on side to pack to a depth of 10 cm. Drain solution, leaving approximately 5 cm overlying the bed to prevent media disruption when feed begins.

4. To 20 L reservoir, add Mn^{2+} from $MnSO_4 \cdot H_2O$ stock solution by volumetric pipette to obtain desired concentration. Stir and adjust pH to desired level. Recirculate feed solution through pump and tubing for five minutes to equilibrate surfaces. Sample reservoir for influent $[Mn^{2+}]$.

5. Begin sorption feed, take effluent samples at regular intervals, filter and store in clean, Teflon-capped glass vials. Take reservoir sample during sorption stage.

6. At end of sorption stage, remove intake tube from 20 L reservoir, quickly rinse with desorption feed solution (discarding rinsate), then place intake tube in 10 L reservoir of Mn^{2+} - free solution. Take sample of 10 L reservoir.

7. Take effluent samples at regular intervals, filter and store in clean, Teflon-capped glass vials. Take reservoir sample during desorption stage.

8. Analyze samples by flame AA immediately after test. Rinse tubing and column with tap water, rinse in 0.5% HCl acid bath, rinse copiously with distilled deionized water and dry in oven.

TABLE 4

FREUNDLICH ISOTHERM PARAMETERS FOR OXIDE COATED MEDIA

Media	Mn, mg g^{-1}		K (95% C.I.), L g^{-1}	1/n (95% C.I.)	Adjusted R^2 (n pts.)	Significance, F statistic
Sample 2	2	7.5	0.186 (0.180, 0.193)	0.249 (0.220, 0.277)	0.988 (7)	3.4e-6
Sample 2	2	6.75	0.127 (0.098, 0.165)	0.484 (0.288, 0.680)	0.974 (5)	8.8e-3
Sample 2	2	6.0	0.057 (0.036, 0.088)	0.956 (0.494, 1.420)	0.963 (4)	0.012
Sample 2	2	7.5*	0.081 (0.072, 0.092)	0.447 (0.369, 0.526)	0.995 (4)	1.7e-3
Sample 2	2	6.75*	0.037 (0.027, 0.051)	0.655 (0.366, 0.974)	0.997 (3)	0.024
Blacksburg #1	5	7.5	0.060 (0.052, 0.069)	0.626 (0.494, 0.759)	0.999 (3)	0.011
Blacksburg #2	8.3	7.4†	0.073 (0.033, 0.161)	0.387 (-0.086, 0.859)	0.981 (3)	0.061
Blacksburg #2	8.3	6.6†	0.04 (0.003, 0.557)	1.21 (-1.13, 3.55)	0.954 (3)	0.096
Durham, NC	51	6.0†	0.833 (0.023, 30.2)	0.376 (-0.957,1.71)	0.855 (3)	0.173
Swift Run, VA	20	7.5	0.201 (0.155, 0.261)	0.668 (0.394, 0.942)	0.988 (3)	0.021
Norfolk, NE	13.8	7.5*	0.229 (0.126, 0.415)	0.459 (0.153, 0.765)	0.931 (4)	0.023
Norfolk, NE	13.8	6.75*	0.116 (0.091, 0.147)	0.399 (0.240, 0.559)	0.974 (4)	0.085

* - $[Ca^{2+}] = 60$ mg L^{-1}

† - For model validation, using dechlorinated site water (see text for details)

TABLE 5

GLOBAL Mn^{2+} OXIDATION RATE STUDY RESULTS

Media (mg/g extracted Mn)	Oxidation rate, mg Mn^{2+} g^{-1} hr^{-1}	Regression* F statistic significance	Condition
synthetic (2) (n=3)	**0.0584 (0.0472 - 0.0696)†**	**0.20, 0.225, 0.367**	**pH 7.5, 5 gpm ft^{-2}**
NB3 (14)	0.062	0.487	" "
Swift Run (20)	**0.074**	0.225	" "
Portsmouth (32)	0.063	1	" "
Durham #1 (75)	**0.097**	0.684	" "
Durham #2 (8)	**0.084**	0.553	" "
Blacksburg #1 (5)	**0.023**	0.106	" "
gravel (0.7)	**0.008**	1	" "
Mn greensand	**0.11**	0.865	" "
Swift Run (20)	0.055	0.225	pH 6.75
syn. (2)	**0.029**	0.225	$[Mn^{2+}]$ = 0.15 mg L^{-1}
syn. (2)	**0.078**	0.053	$[Mn^{2+}]$ = 0.7 mg L^{-1}
syn. (2)	**0.041**	0.225	Ca^{2+} = 60 mg/L
syn. (2)	**0.030**	0.2	pH = 6.75
syn. (2)	**0.010**	0.225	pH = 6.00
syn. (2)	0.053	0.326	16 °C
syn. (2)	**0.044**	0.741	2.5 gpm ft^{-2}
syn. (2)	**0.077**	0.51	10 gpm ft^{-2}

† - Mean and 95% confidence interval (three replicates), with **bold** values outside the estimation interval.

TABLE 6

MODEL FITTING RESULTS: SORPTION - DESORPTION, SYNTHETIC MEDIA #2

pH	Flow rate, gpm ft^{-2}	Influent $[Mn^{2+}]$, mg L^{-1}	Influent $[Ca^{2+}]$, mg L^{-1}	Available fraction for sorption, AFR (fitted)	RMS error, mg L^{-1} (fitted)	RMS error, mg L^{-1} (AFR = 1)
6.00	2.5	1.01		1	0.122	
	5.0	0.95		1	0.178	
	10.0	0.94		1	0.185	
6.75	2.5	0.97		0.915	0.067	0.072
	5.0	0.95		0.920	0.117	0.120
	10.0	0.94		1	0.100	
	5.0	0.325		0.49	0.089	0.121
	5.0	1.01	60	1	0.156	
	5.0	0.38	60	1	0.092	
7.50	2.5	0.98		0.865	0.061	0.075
	5.0	0.97		0.775	0.052	0.109
	10.0	0.96		0.875	0.060	0.080
	5.0	0.315		0.32	0.044	0.084
	5.0	1.0	60	1	0.089	
	5.0	0.38	60	0.87	0.024	0.029

TABLE 7

MODEL FITTING RESULTS: SPECIAL CASES, SORPTION - DESORPTION

pH	Flow rate, gpm ft^{-2}	Media	$[Mn^{2+}]$, mg L^{-1}	Fitted parameter(s)	Parameter value fitted (predicted)	RMS, mg L^{-1}
6.75	2.5	Synthetic #2	0.97	k_1, (AFR = 1)	0.52 (0.56) cm min^{-1}	0.070
	5.0	" "	0.95	" "	0.80 (0.78) cm min^{-1}	0.120
	10.0	" "	0.94	" "	1.24 (1.10) cm min^{-1}	0.096
6.00	10.0	" "	0.94	k_1	10.8 (1.1) cm min^{-1}	
				Freundlich K	0.024 (0.057) L g^{-1}	
				(AFR = 1)		0.088
	10.0	" "	0.94	k_1	7.82 (1.1) cm min^{-1}	
				k_2†	0.0087 (0.0011) cm min^{-1}	
				AFR	0.485	0.131
7.50	5	Blacksburg #1	0.95	AFR	0.63	0.047
				AFR	1	0.091

TABLE 8

MODEL FITTING RESULTS: CONTINUOUS REGENERATION, STEADY STATE CONDITIONS

pH	Flow rate, gpm ft^{-2}	Media	$[Mn^{2+}]$, mg L^{-1}	Fitted parameter(s)	Fitted parameter value(s)	RMS, mg L^{-1}
7.50	5	Synthetic #2	0.34	AFR	0.555	0.0063
				k_3	9.48×10^3 L^2 mol^{-1} min^{-1} (values for "predicted")	
7.50	5	" "	0.33	predicted		0.010
7.50	5	" "	0.33	predicted		0.017
7.50	2.5	" "	0.33	AFR	0.565	0.0073
					1	0.086
7.50	10	" "	0.32	AFR	0.562	0.0024
					1	0.091
7.50†	5	" "	0.38	k_3 predicted, AFR =1		0.027
6.75	5	" "	0.34	AFR	0.71	0.0084
				k_3 predicted, AFR =1		0.042
6.00	5	" "	0.35	AFR	0.915	0.016
				k_3 predicted, AFR =1		0.017
7.50	5	Blacksburg #1	0.35	AFR	0.876	0.012
				predicted		0.024
7.50	5	Swift Run	0.35	AFR	1	0.032
				predicted		0.098

† - $[Ca^{2+}]$ = 60 mg L^{-1}

TABLE 9

MODEL SENSITIVITY ANALYSIS AND PARAMETER ESTIMATION

Process mode	Conditions	Fitted parameter	95% C.I.	Model variance, $(mg\ L^{-1})^2$	Parameter correlation
Intermittent regeneration	10 cm bed, pH 7.50, 5 gpm ft^{-2}	AFR = 0.775	0.7564 - 0.7936	2.69×10^{-3}	
Continuous regeneration	3 cm bed, pH 7.50, 5 gpm ft^{-2}	AFR = 0.555 $k_3 = 9.48 \times 10^3$ $L^2\ mol^{-1}\ min^{-1}$	0.517 - 0.593 $4.96 - 14.0 \times 10^3$	4.27×10^{-5}	-0.67

TABLE 10

SUMMARY OF ENERGY-DISPERSIVE X-RAY ANALYSES

Sample	Figure	Coating region	Atomic ratios		Atomic percentage†		
			Al : Mn	Si : Mn	Al	Mn	Si
Blacksburg #1	49a	inner dark band	5.9	1.6	25.4	4.3	6.9
		outer bright band	3	0.5	24.4	8.2	4
Blacksburg #2	49b	inner dark band	64	20	25.6	0.4	8.1
		outer bright band	2.6	0.4	23.7	9.3	3.3
Pre-backwash		inner dark band	3.7	1.9	23.6	6.4	6.4
		outer bright band	2.9	0.6	23.5	8.2	4.6
		outer bright particle	0.31	0.04	9.69	30.9	1.2

† - Standardless analysis; cation (Z) percentage on basis of Al, Mn, Na, Mg, Si, P, K, Ca, Ti, Fe; assumed Z:O = 1

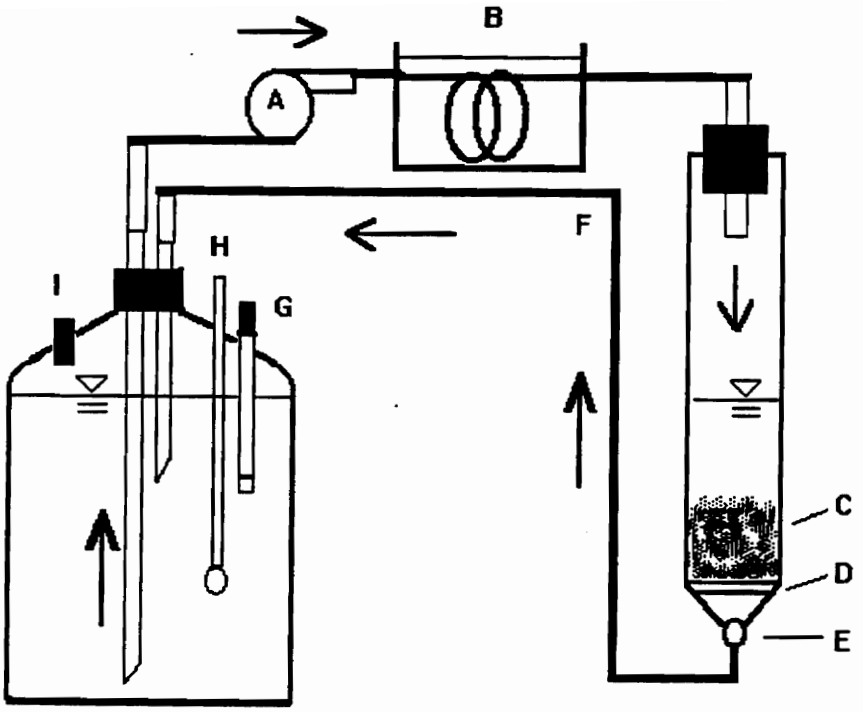

FIGURE 1: Recycle absorber apparatus for isotherm determination

A: peristaltic pump
B: cooling bath
C: oxide-coated media bed
D: perforated Teflon support disk
E: Teflon stopcock
F: recycle line
G: pH probe
H: thermometer
I : sampling port

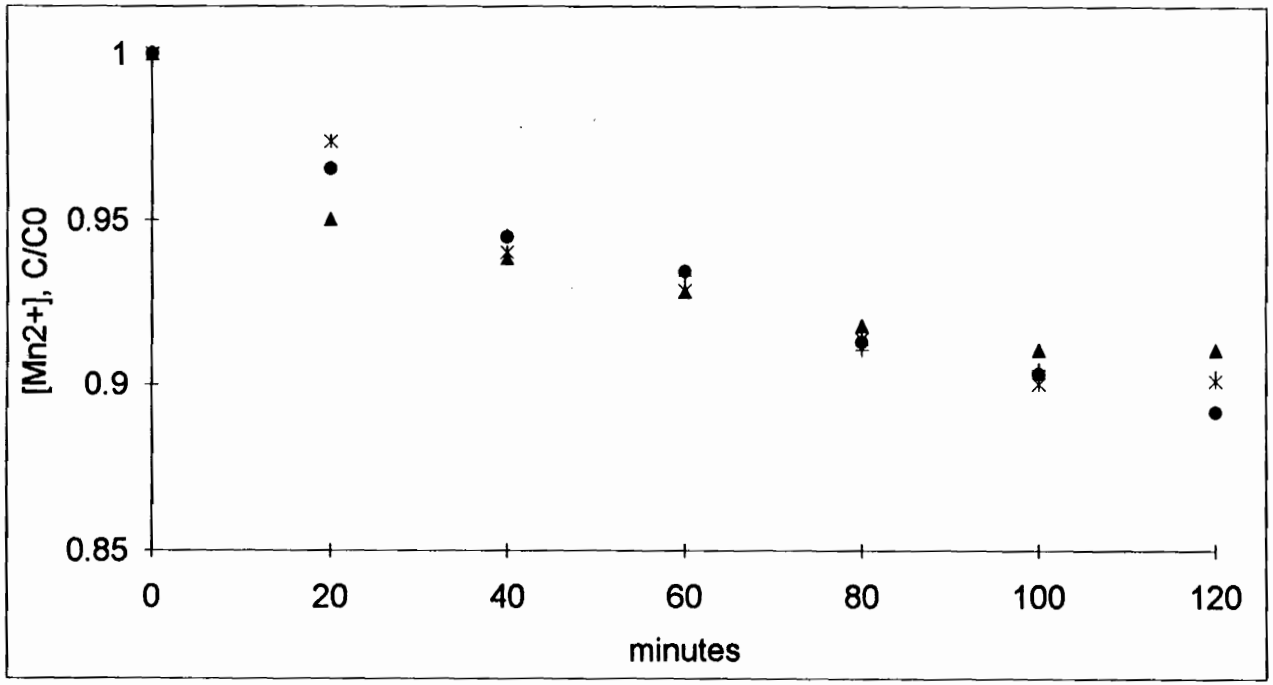

FIGURE 2A: Time series of 1 L recycle absorber reservoir [Mn^{2+}] during isotherm determinations: pH 7.50, initial [Mn^{2+}] = 5 mg L^{-1}, [Ca^{2+}] = 10 mg L^{-1}, synthetically coated media #1, (four replicates).

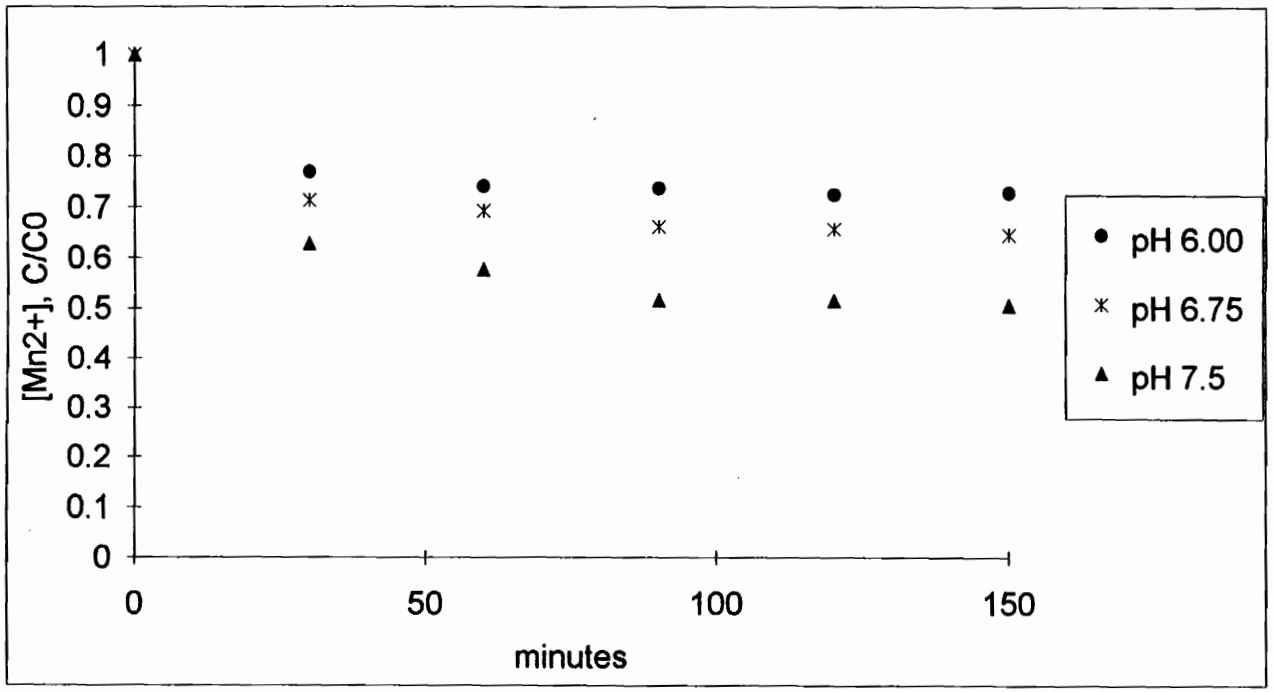

FIGURE 2B: Time series of 4 L recycle absorber reservoir [Mn^{2+}] during isotherm determinations for three pH conditions, synthetically coated media #2.

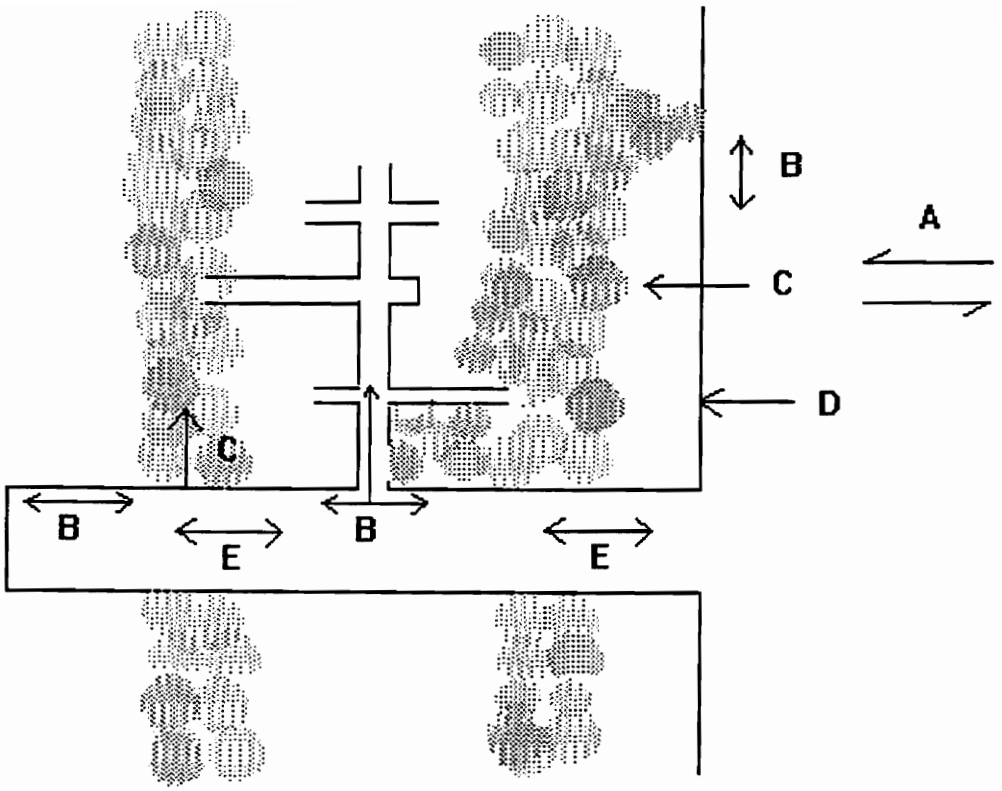

FIGURE 3: Diagram of hypothetical mass transport and surface interactions of $Mn^{2+}_{(aq)}$ with media oxide coating. Shaded bands represent compositional variation within the coating.

A. fluid to surface mass transfer (reversible)
B. surface diffusion (exterior and interior surfaces)
C. lattice ion exchange (irreversible)
D. oxidation (irreversible)
E. diffusion in pore fluid

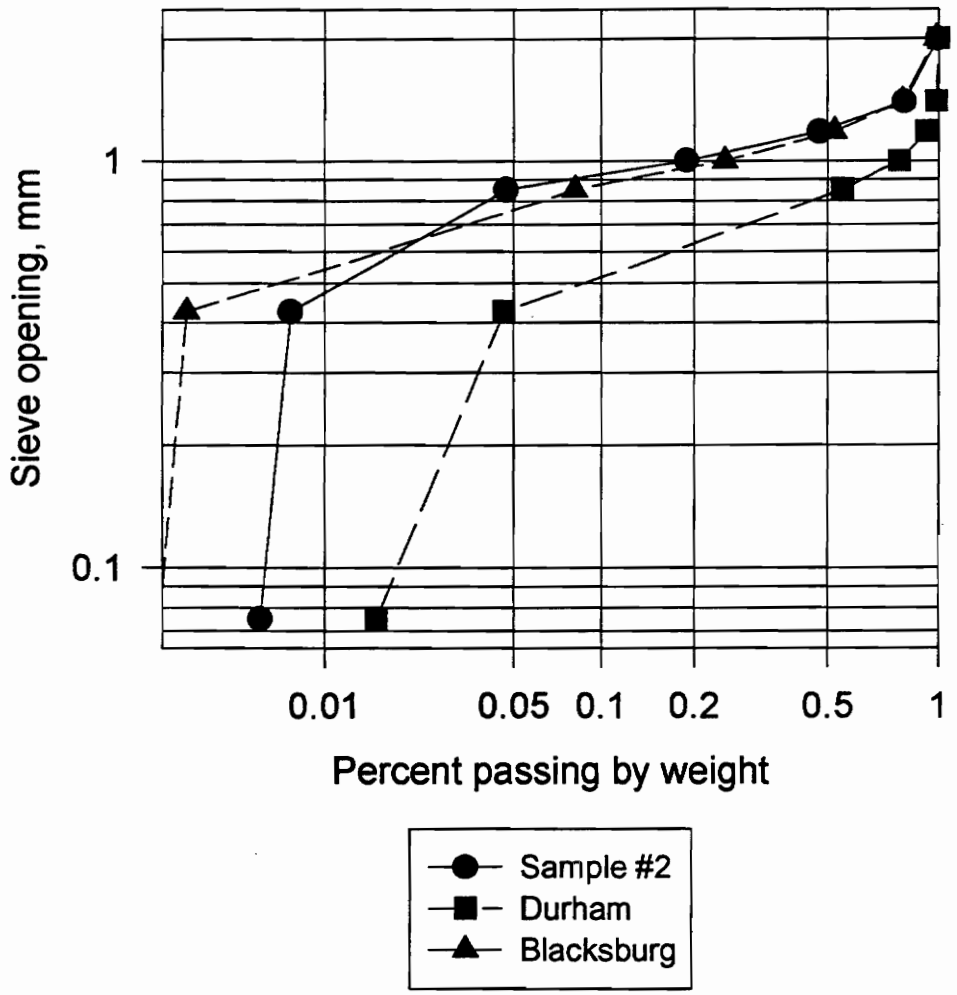

FIGURE 4: Size distributions of media used in model calibration and validation studies. Extractable Mn contents: Sample #2, 2 mg g^{-1}; Durham, 51 mg g^{-1}; Blacksburg #2, 8.3 mg g^{-1}.

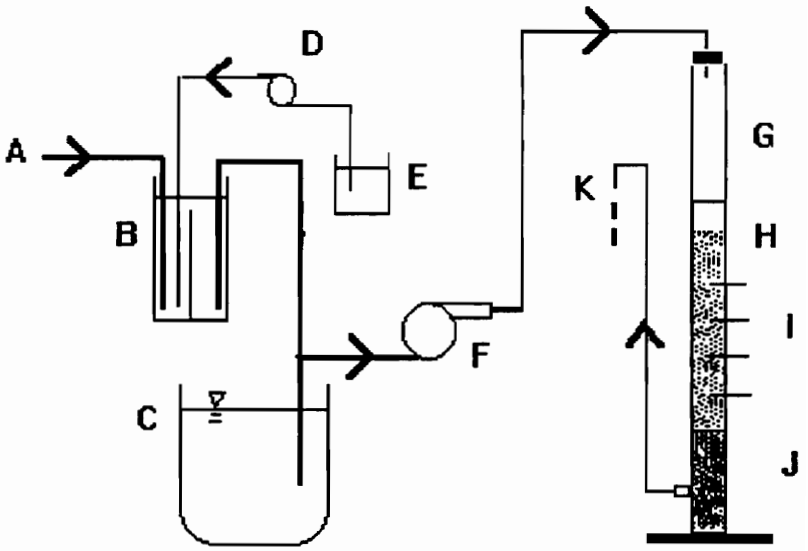

FIGURE 5: Apparatus for model validation studies.

Continuous regeneration mode:

A. feed water containing free chlorine
B. 10 L mixing tank with baffle
D. peristaltic pump for Mn^{2+} feed
E. Mn^{2+} solution reservoir

Intermittent regeneration mode:

C. 120 L reservoir containing Mn^{2+}

Both modes:

F. peristaltic pump for column feed
G. column, 4.3 cm diameter
H. media bed with overlying solution
I. sample ports
J. gravel support
K. outflow

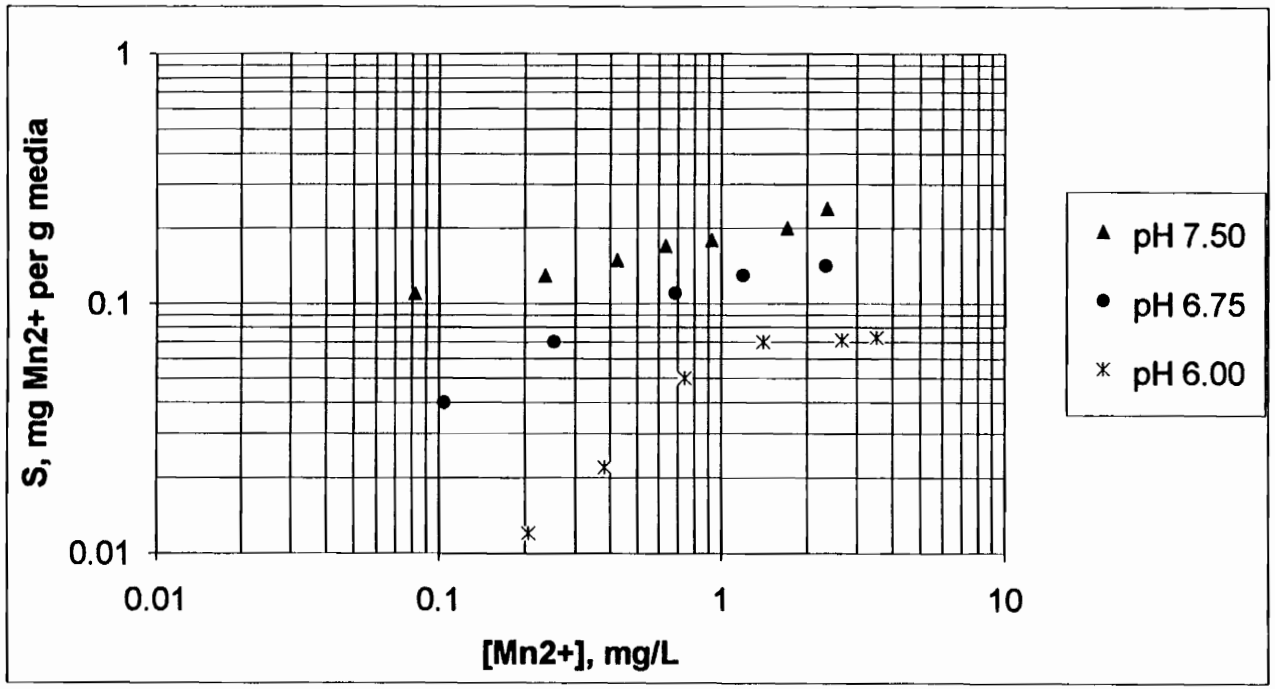

FIGURE 6: Isotherms for $Mn^{2+}_{(aq)}$ uptake by synthetically coated media #2 (2 mg g^{-1} Mn) determined by recycle absorber method.

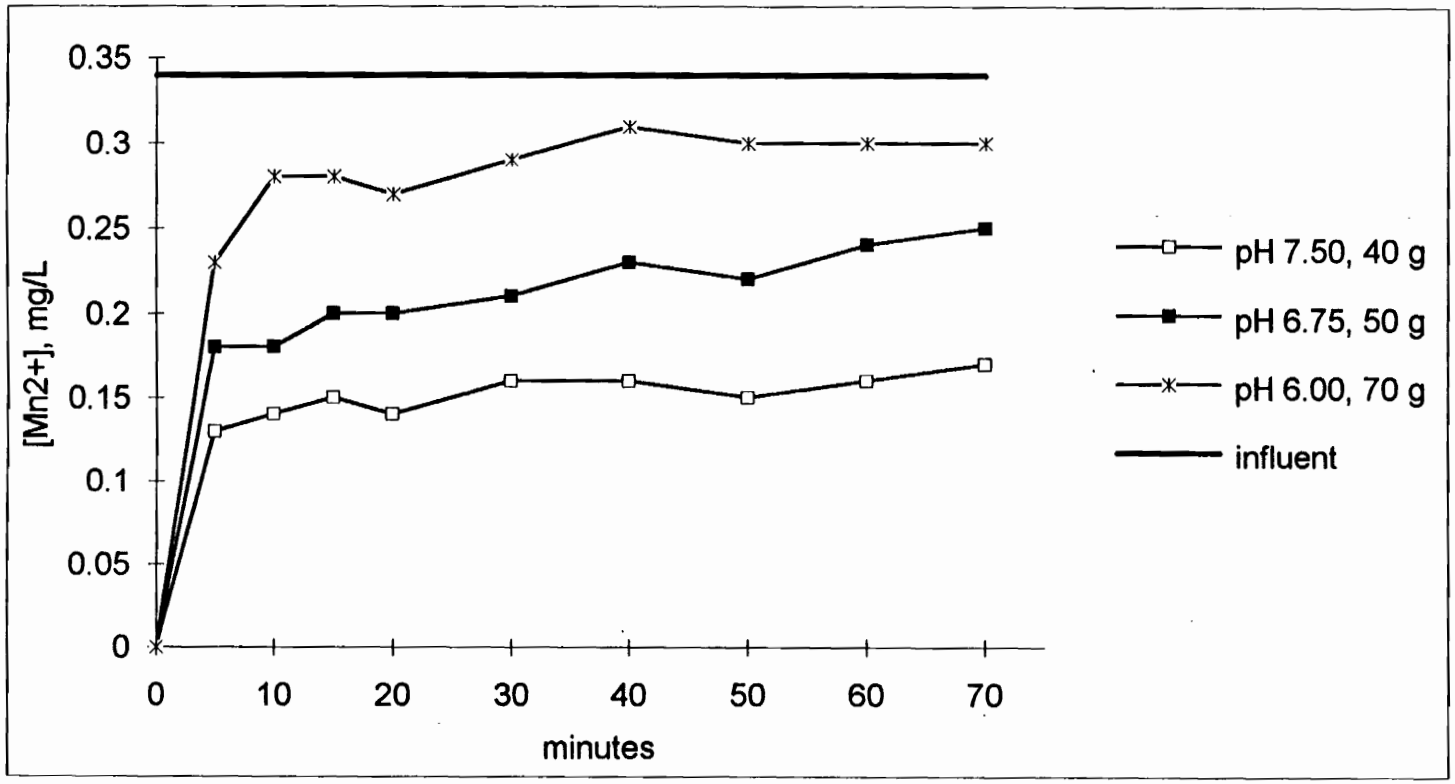

FIGURE 7: Effluent [Mn^{2+}] profiles of differential reactor tests: continuous regeneration mode for three pH conditions, synthetically coated media #2 (2 mg g^{-1} Mn), 10 g media = 1 cm bed depth.

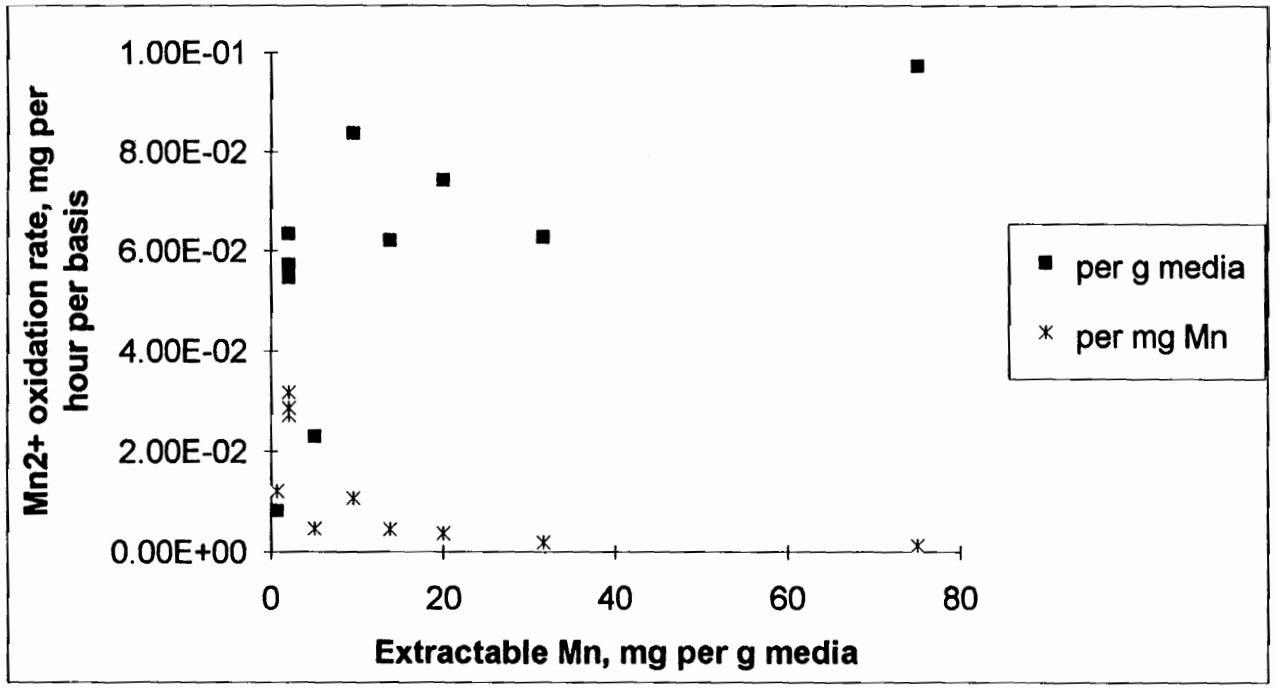

FIGURE 8: Global Mn^{2+} oxidation rates vs. extractable Mn^{2+}, estimated by differential reactor tests of synthetic and natural oxide-coated media, pH 7.50, 5 gpm ft^{-2}. Rates calculated on the basis: 1) per gram of coated media, and 2) per mg extractable Mn.

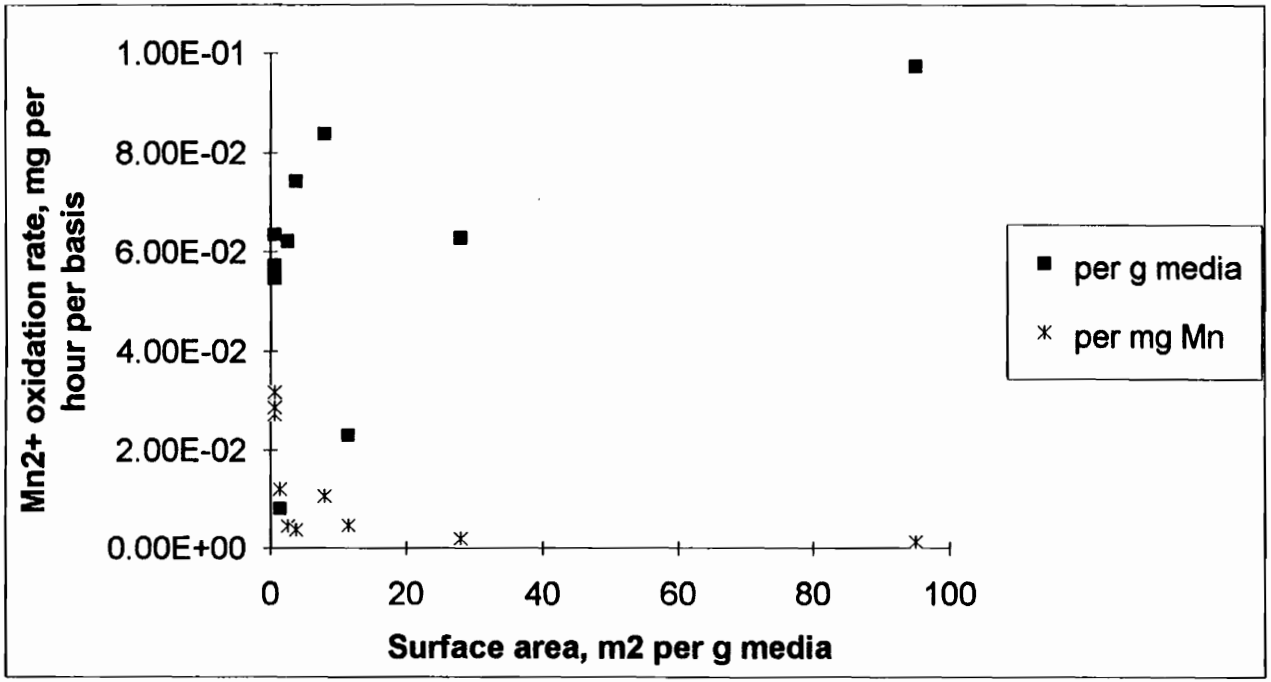

FIGURE 9: Global Mn^{2+} oxidation rates vs. media surface area, estimated by differential reactor tests of synthetic and natural oxide-coated media, pH 7.50, 5 gpm ft^{-2}. Rates are given by: 1) per gram of coated media, and 2) per mg extractable Mn.

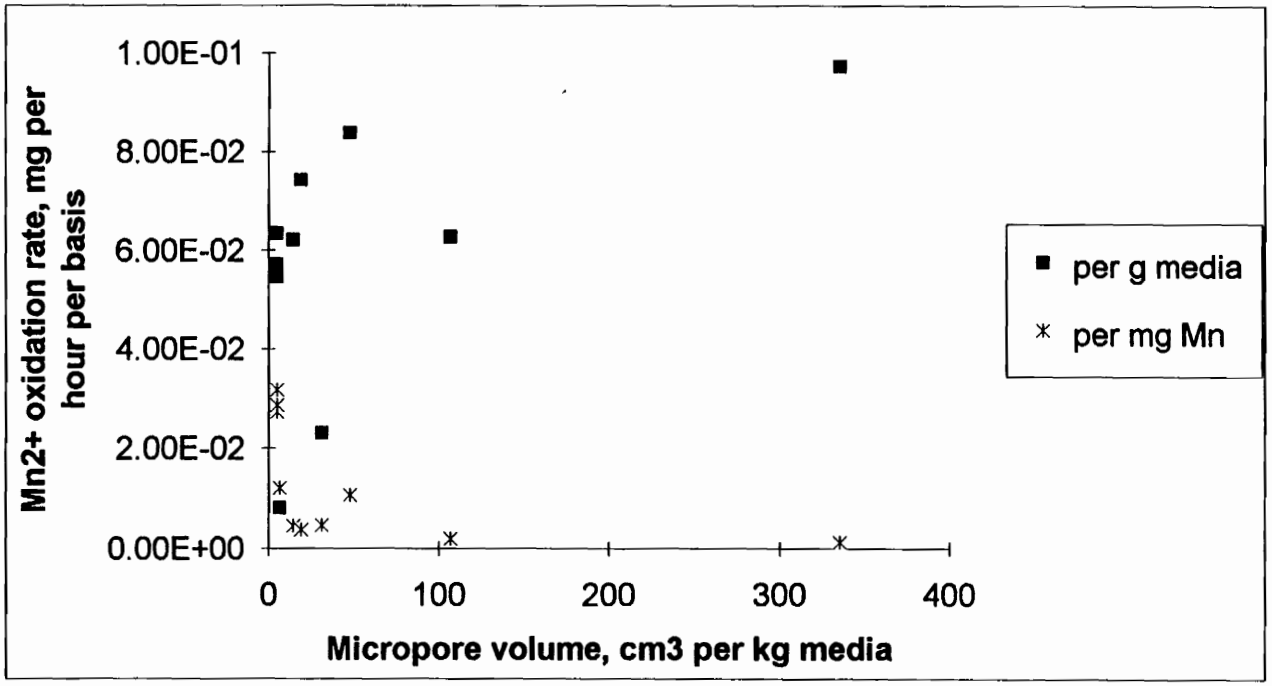

FIGURE 10: Global Mn^{2+} oxidation rates vs. media micropore volume, estimated by differential reactor tests of synthetic and natural oxide-coated media, pH 7.50, 5 gpm ft^{-2}. Rates calculated on the basis 1) per gram of coated media, and 2) per mg extractable Mn.

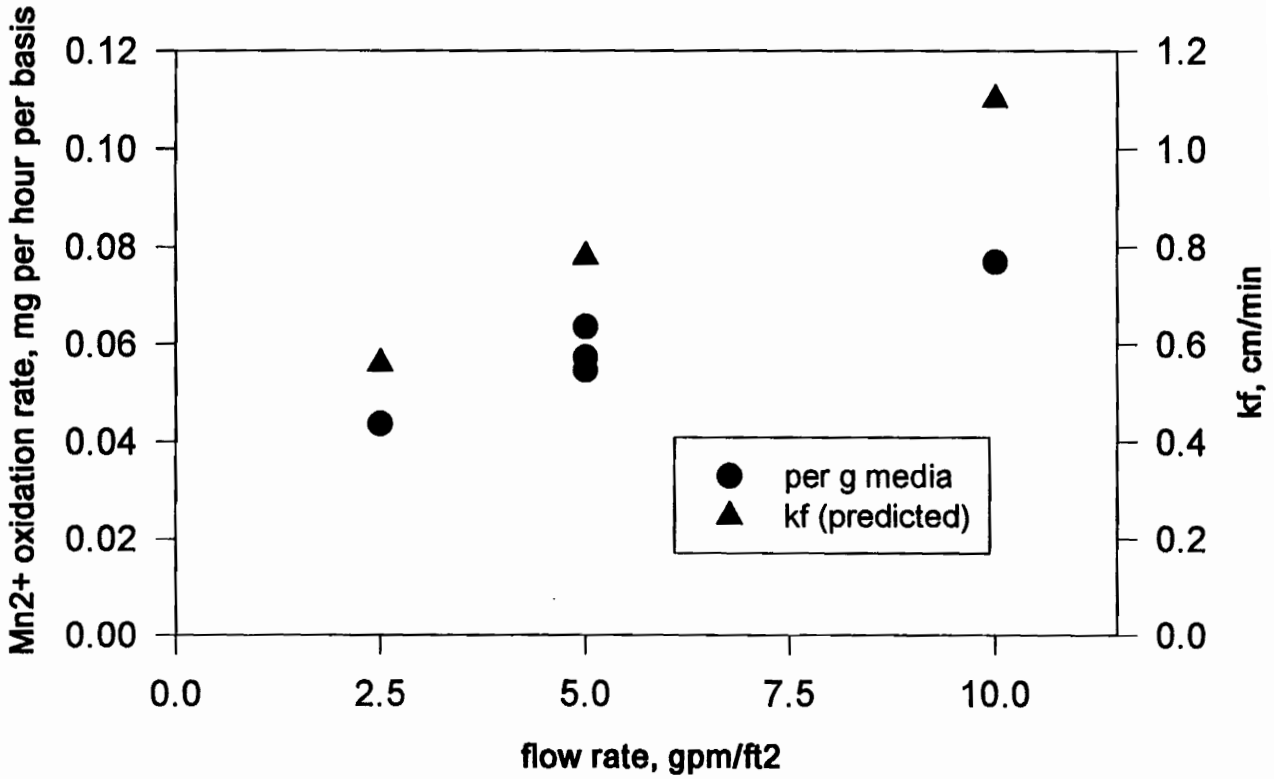

FIGURE 11: Global Mn^{2+} oxidation rates for three flow rates at pH 7.50, synthetic media #2, plotted with mass transfer coefficient k_f predicted by modified Gnielinski correlation.

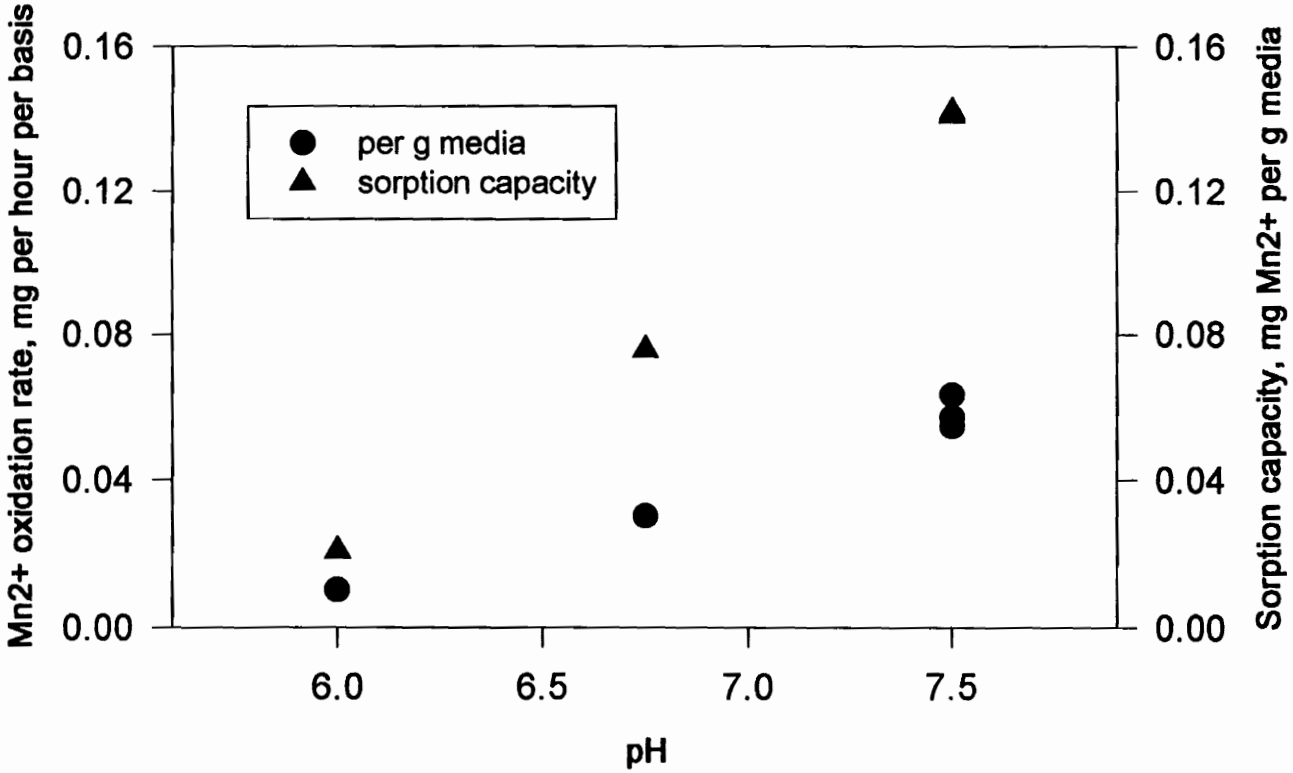

FIGURE 12: Global Mn^{2+} oxidation rates for three pH conditions at 5 gpm ft^{-2}, synthetic media #2, plotted with media sorption capacity estimated by the isotherm at the test influent [Mn^{2+}].

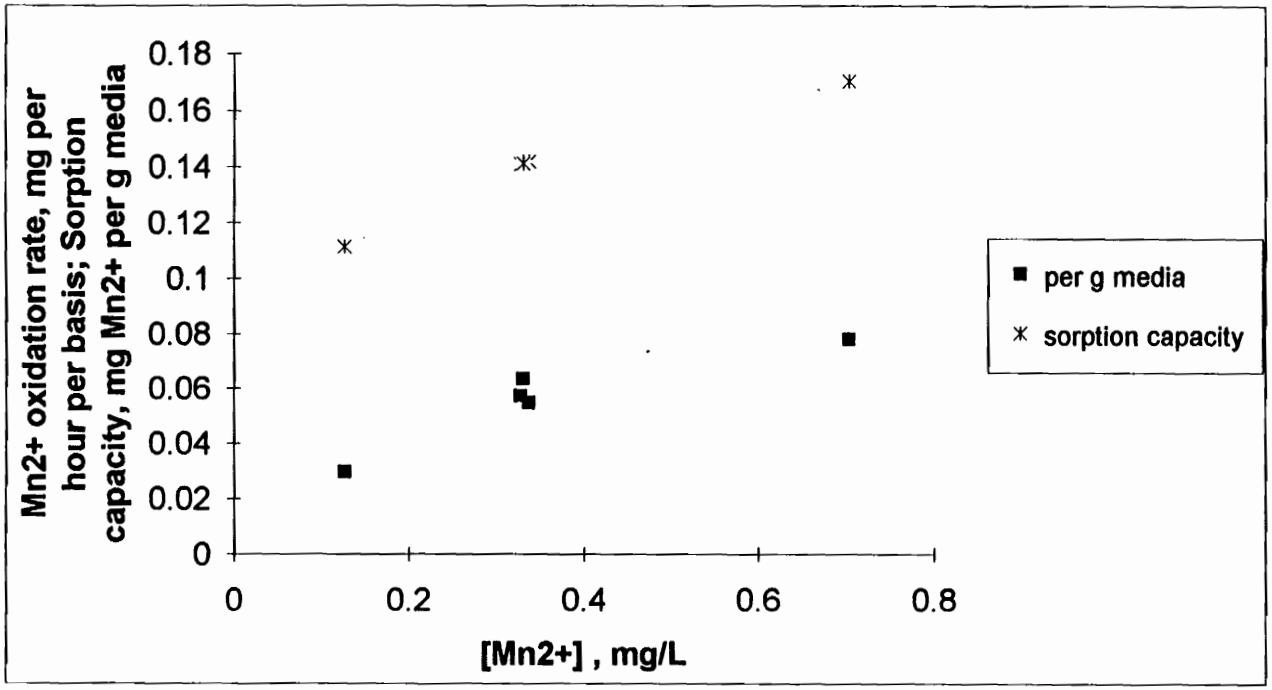

FIGURE 13: Global Mn^{2+} oxidation rates for three influent [Mn^{2+}] conditions at 5 gpm ft^{-2}, synthetic media #2, plotted with media sorption capacity estimated by the isotherm at the test influent [Mn^{2+}].

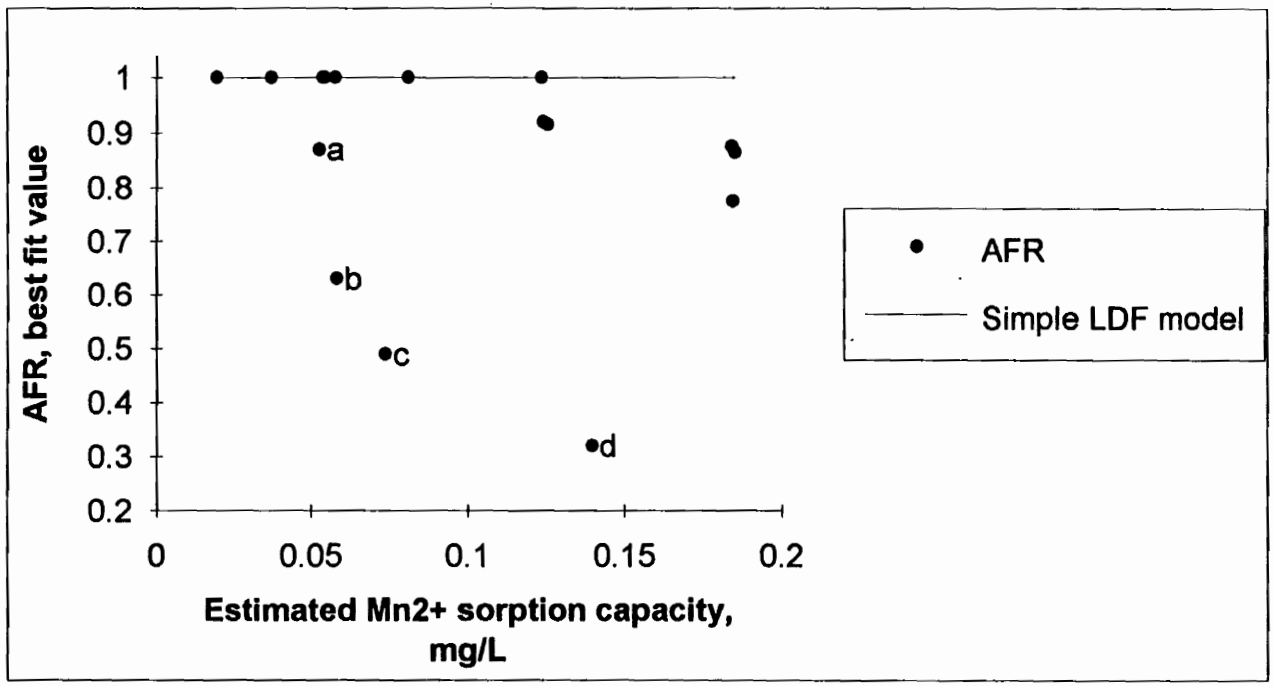

FIGURE 14A: Intermittent regeneration model calibration, synthetic media #2: fitted parameter AFR (available fraction for sorption) as a function of estimated media sorption capacity. Indicated points a,c, d: influent $[Mn^{2+}] \cong 0.34$ mg L^{-1}; b = Blacksburg #1 media.

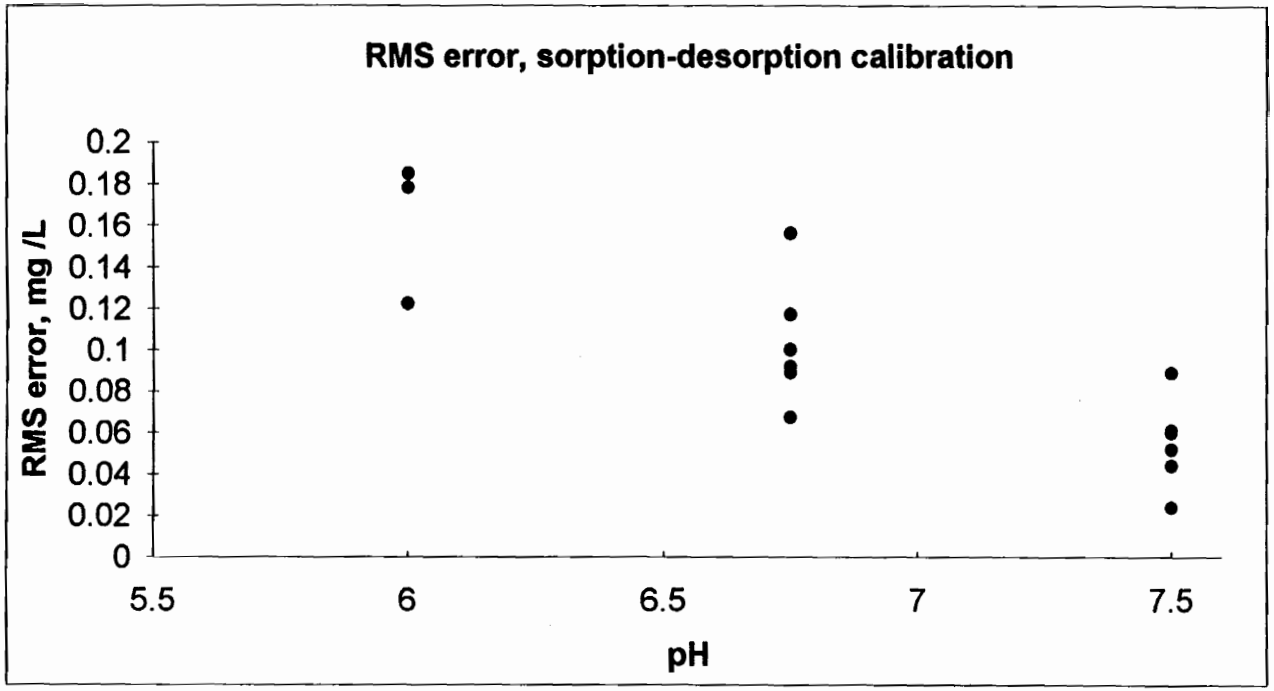

FIGURE 14B: Intermittent regeneration model calibration, synthetic media #2: root mean square error (RMS) vs. pH. The trend of increasing error at lower pH is significant (adj. R^2 = 0.69, F significance = 7e-5).

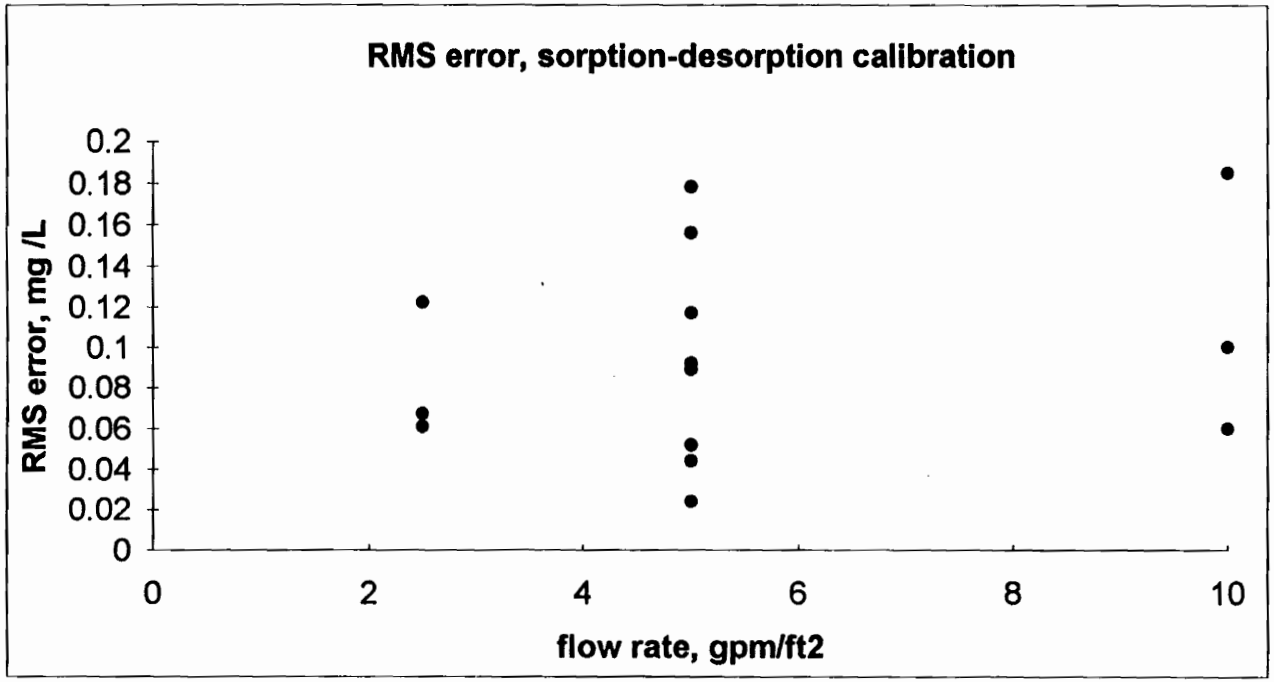

FIGURE 14C: Intermittent regeneration model calibration, synthetic media #2: root mean square error (RMS) vs. flow rate. No significant trend of RMS with flow rate.

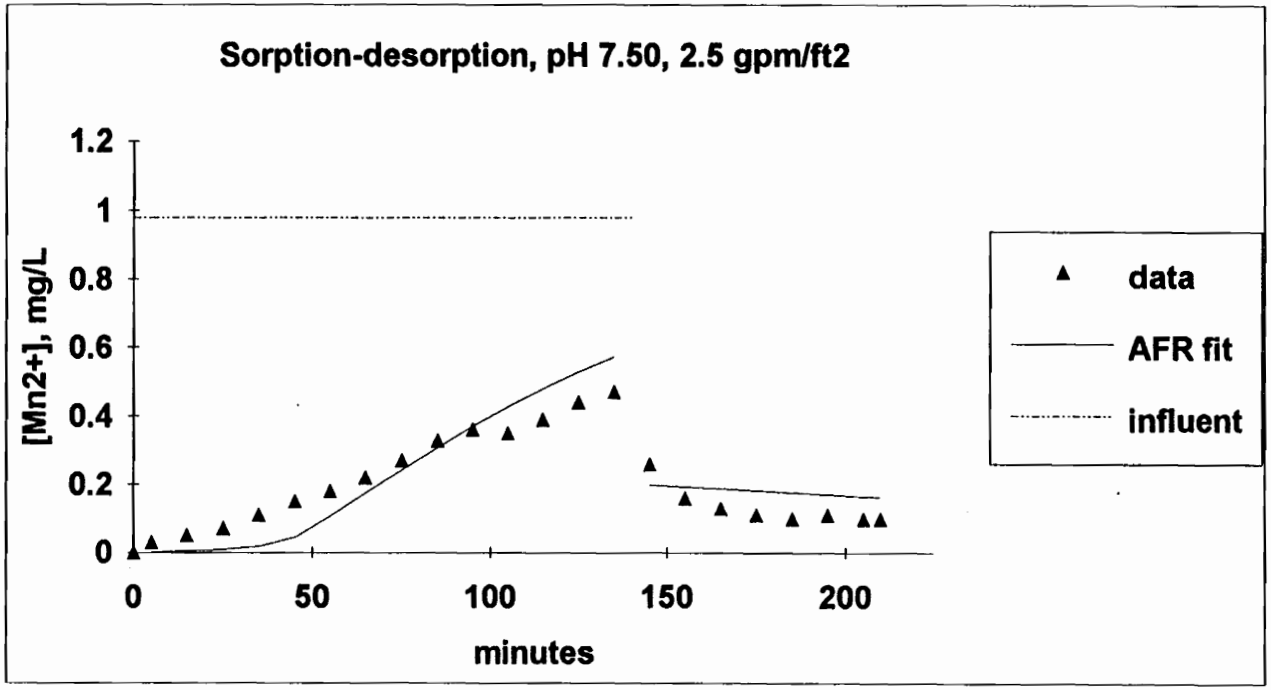

FIGURE 15: Intermittent regeneration model calibration, dynamic influent $[Mn^{2+}]$, pH 7.50, 2.5 gpm ft^{-2}, synthetic media #2, model prediction using best-fit AFR (see Table 6).

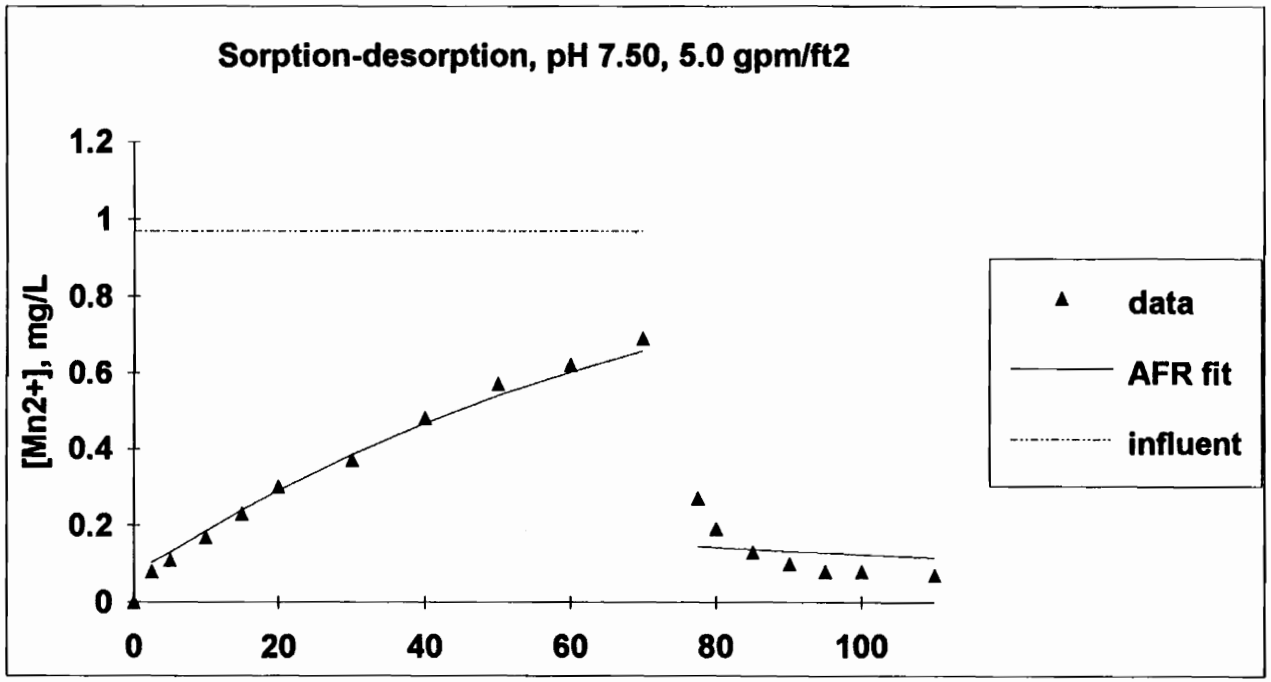

FIGURE 16: Intermittent regeneration model calibration, dynamic influent $[Mn^{2+}]$, pH 7.50, 5 gpm ft^{-2}, synthetic media #2, model prediction using best-fit AFR (see Table 6).

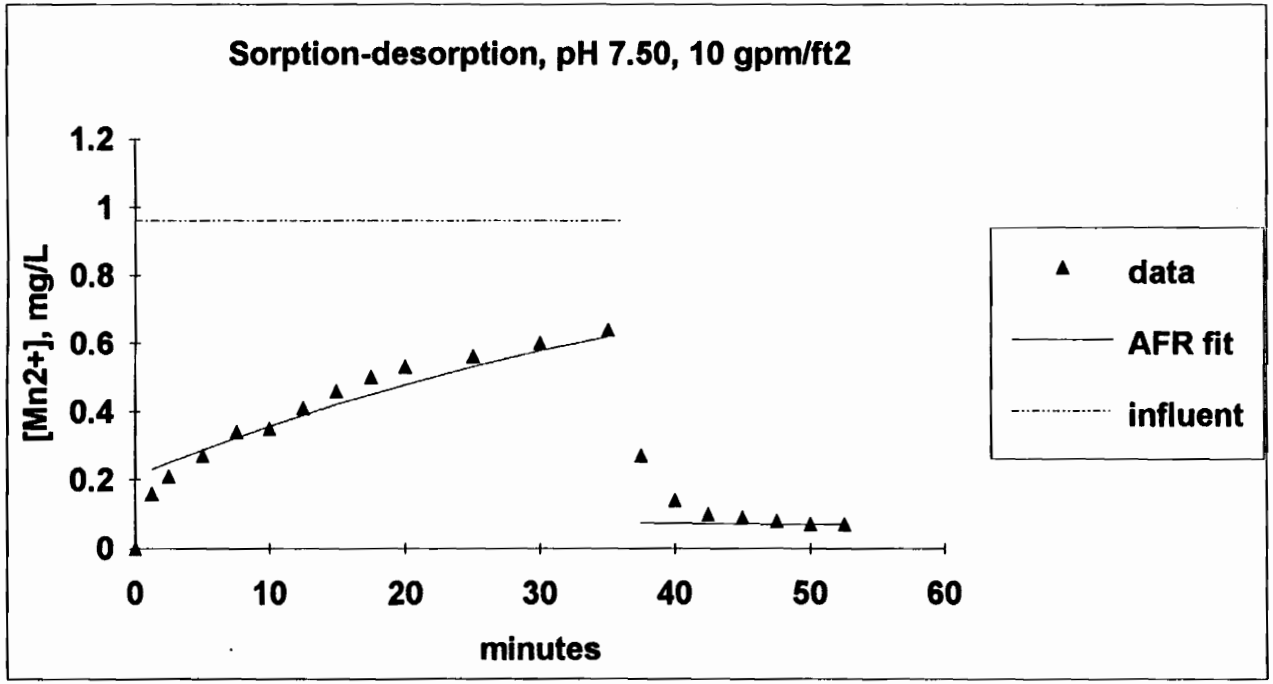

FIGURE 17: Intermittent regeneration model calibration, dynamic influe
$[Mn^{2+}]$, pH 7.50, 10 gpm ft^{-2}, synthetic media #2, model prediction usir
best-fit AFR (see Table 6).

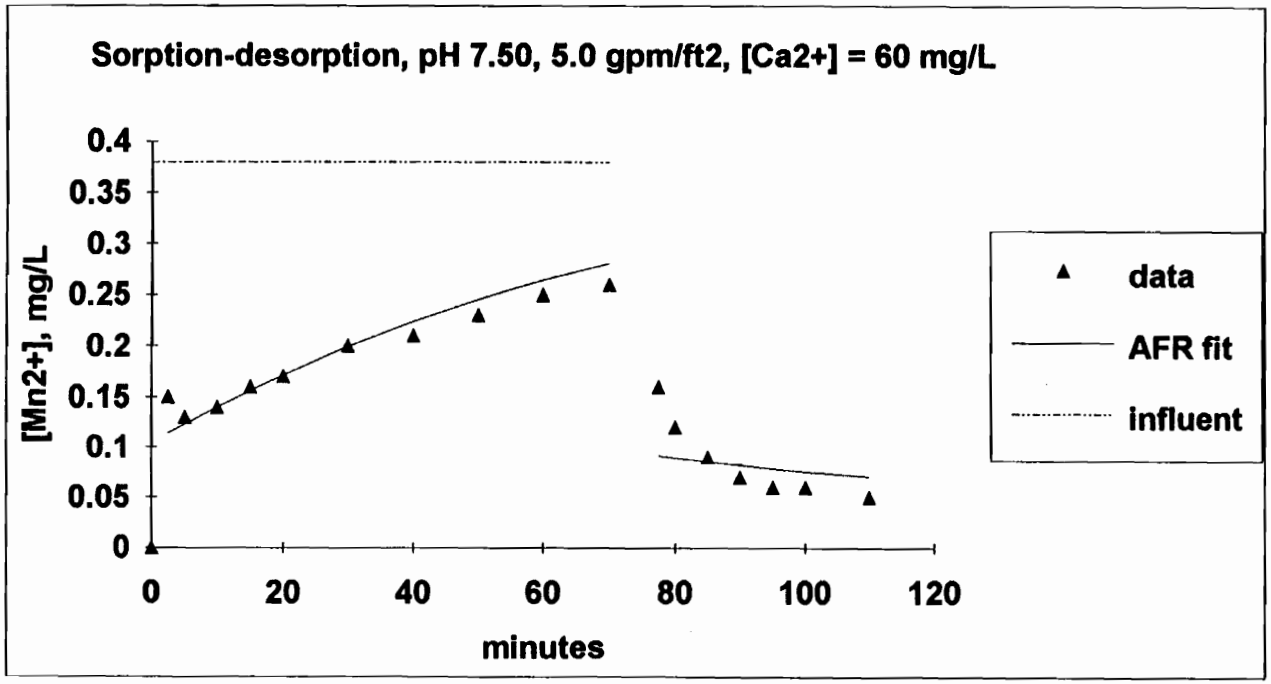

FIGURE 18: Intermittent regeneration model calibration, dynamic influent $[Mn^{2+}]$, $[Ca^{2+}]$ = 60 mg L^{-1}, pH 7.50, 5 gpm ft^{-2}, synthetic media #2, model prediction using best-fit AFR (see Table 6).

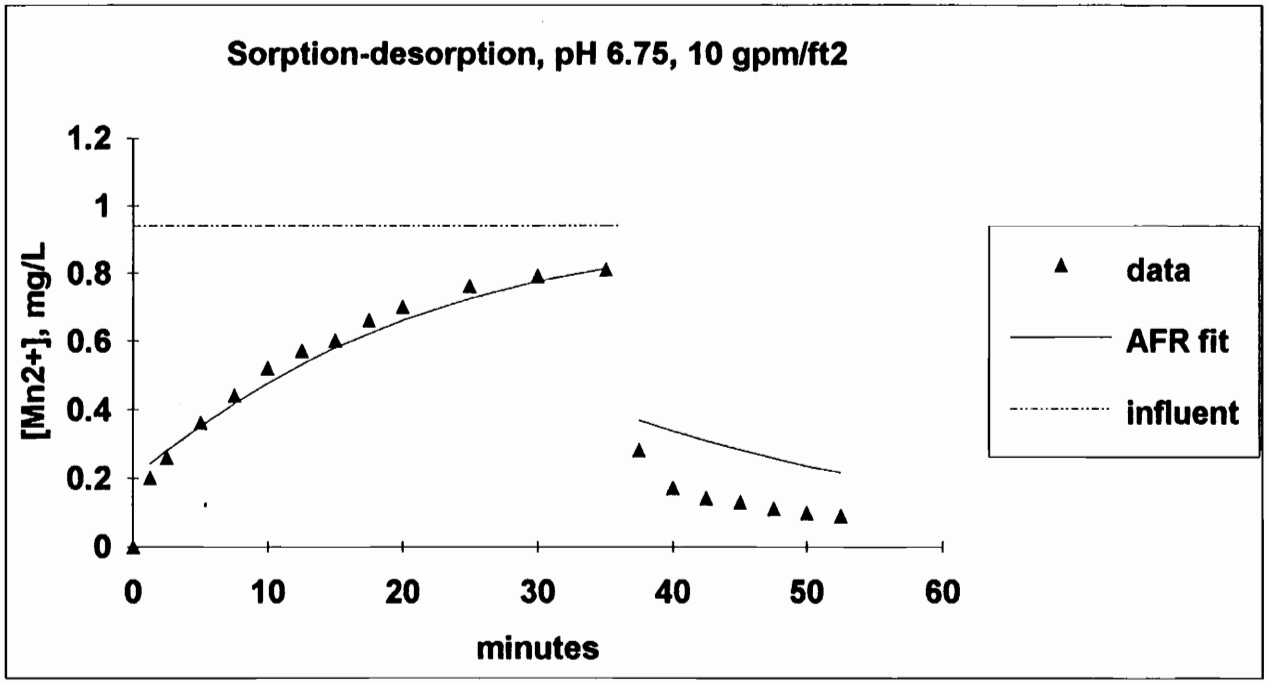

FIGURE 19: Intermittent regeneration model calibration, dynamic influent [Mn^{2+}], pH 6.75, 10 gpm ft^{-2}, synthetic media #2, model prediction using best-fit AFR (see Table 6).

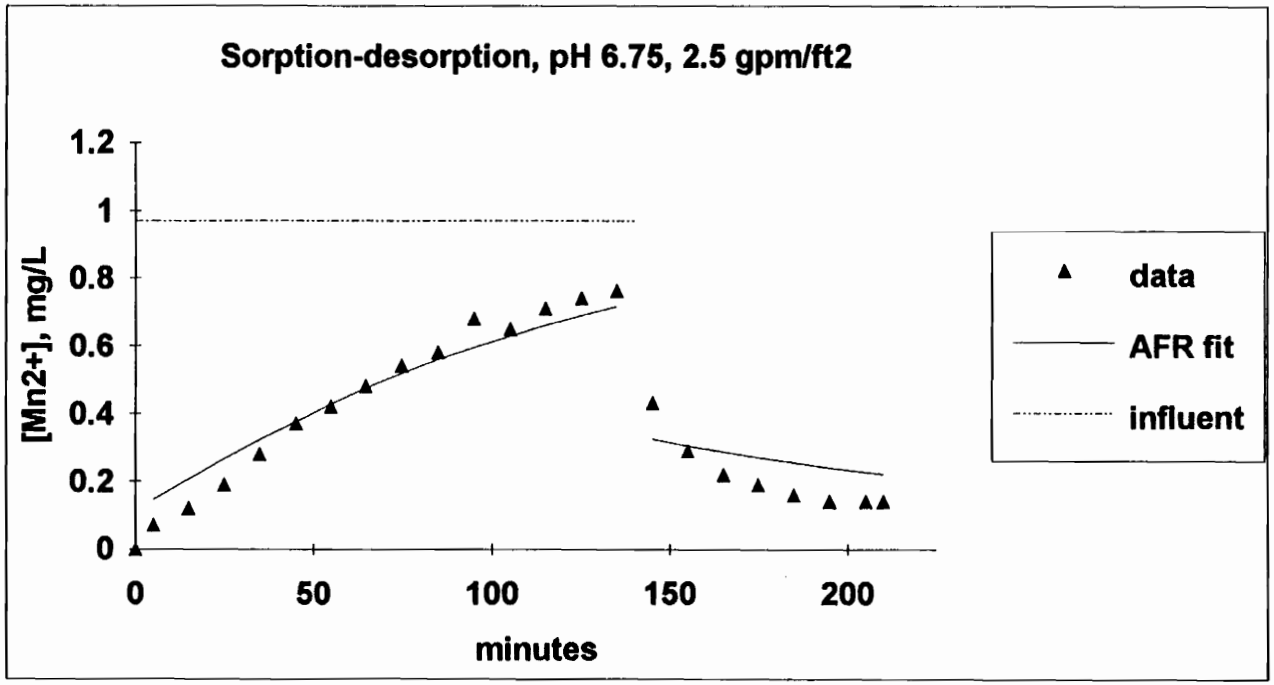

FIGURE 20: Intermittent regeneration model calibration, dynamic influent $[Mn^{2+}]$, pH 6.75, 2.5 gpm ft^{-2}, synthetic media #2, model prediction using best-fit AFR (see Table 6).

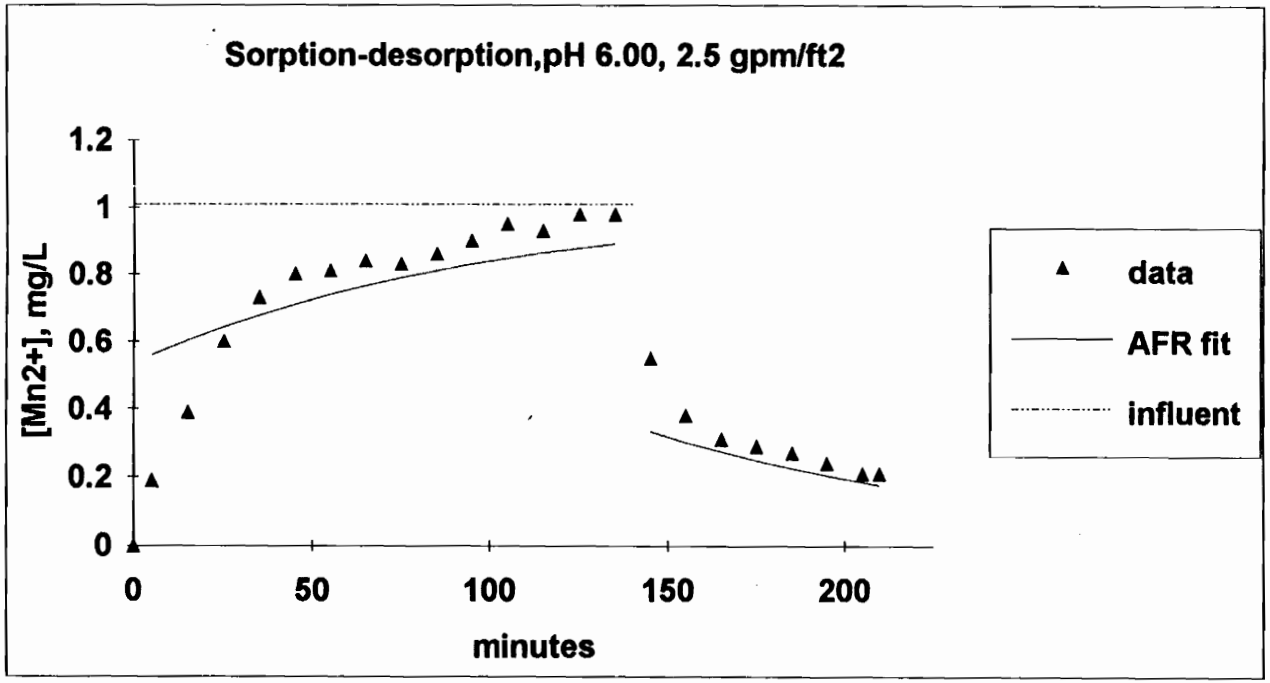

FIGURE 21: Intermittent regeneration model calibration, dynamic influent $[Mn^{2+}]$, pH 6.00, 2.5 gpm ft^{-2}, synthetic media #2, model prediction using best-fit AFR (see Table 6).

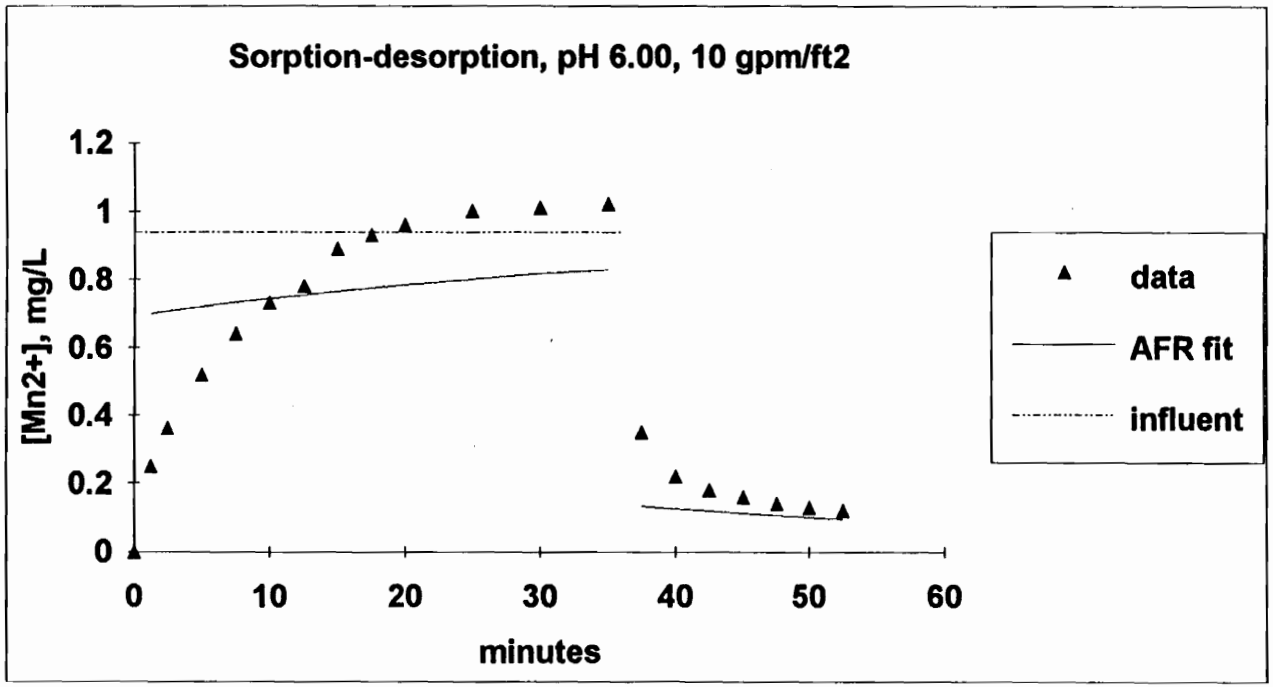

FIGURE 22: Intermittent regeneration model calibration, dynamic influent $[Mn^{2+}]$, pH 6.00, 10 gpm ft^{-2}, synthetic media #2, model prediction using best-fit AFR (see Table 6).

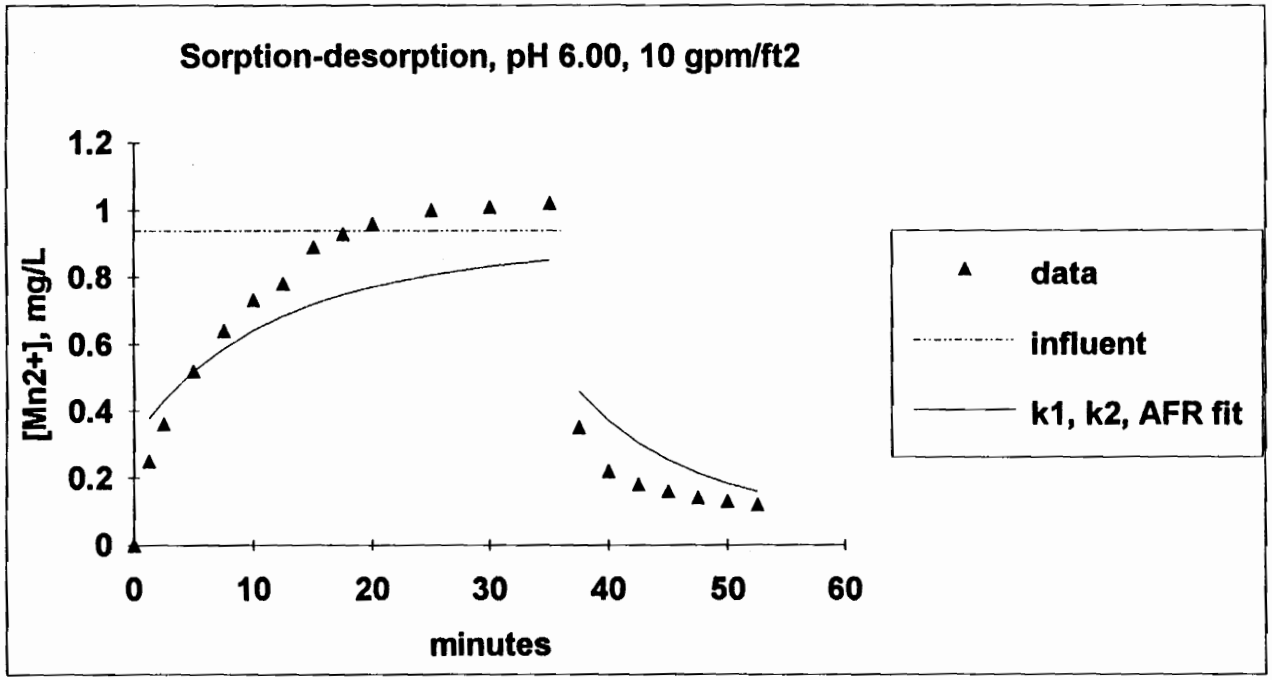

FIGURE 23: Intermittent regeneration model fitted by varying three model parameters simultaneously: k_1 (fluid to surface mass transfer), k_2 (surface diffusion), and AFR (available fraction for sorption).

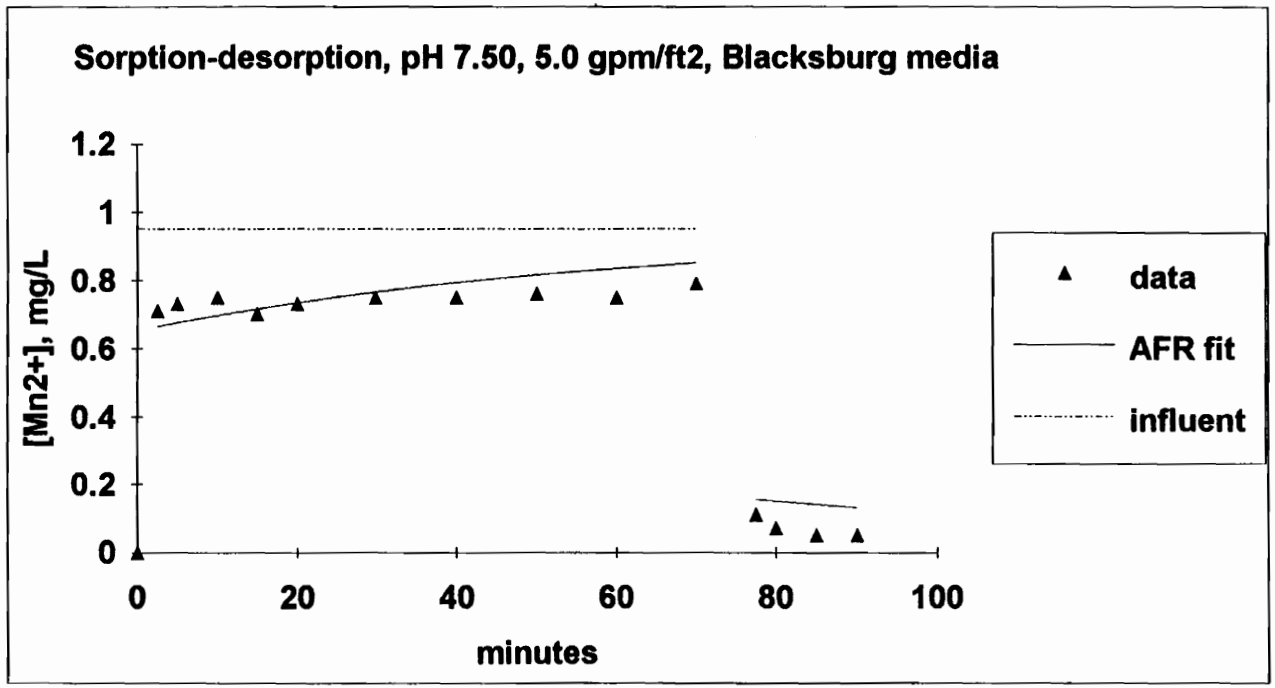

FIGURE 24: Intermittent regeneration model calibration, dynamic influent [Mn^{2+}], pH 7.50, 5 gpm ft^{-2}, Blacksburg media #1, model prediction using best-fit AFR (see Table 7).

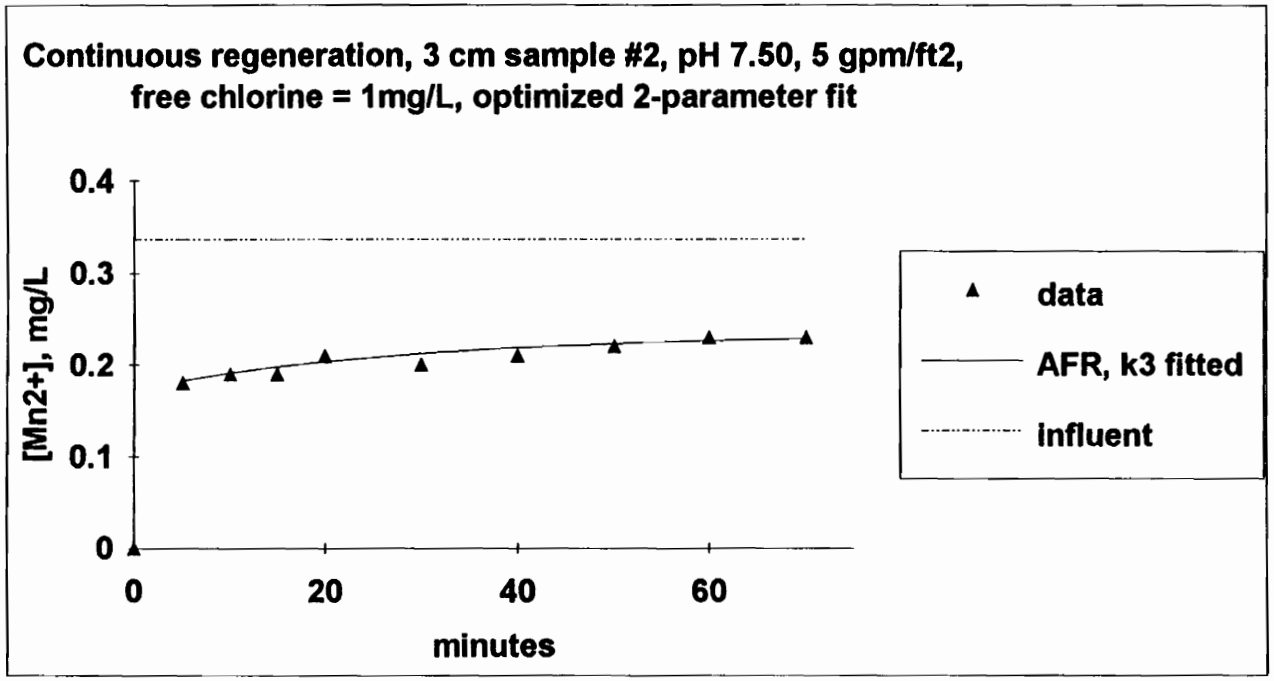

FIGURE 25: Continuous regeneration model calibration at pH 7.50, 5.0 gpm ft^{-2}, fitting AFR and k_3 (apparent oxidation rate constant).

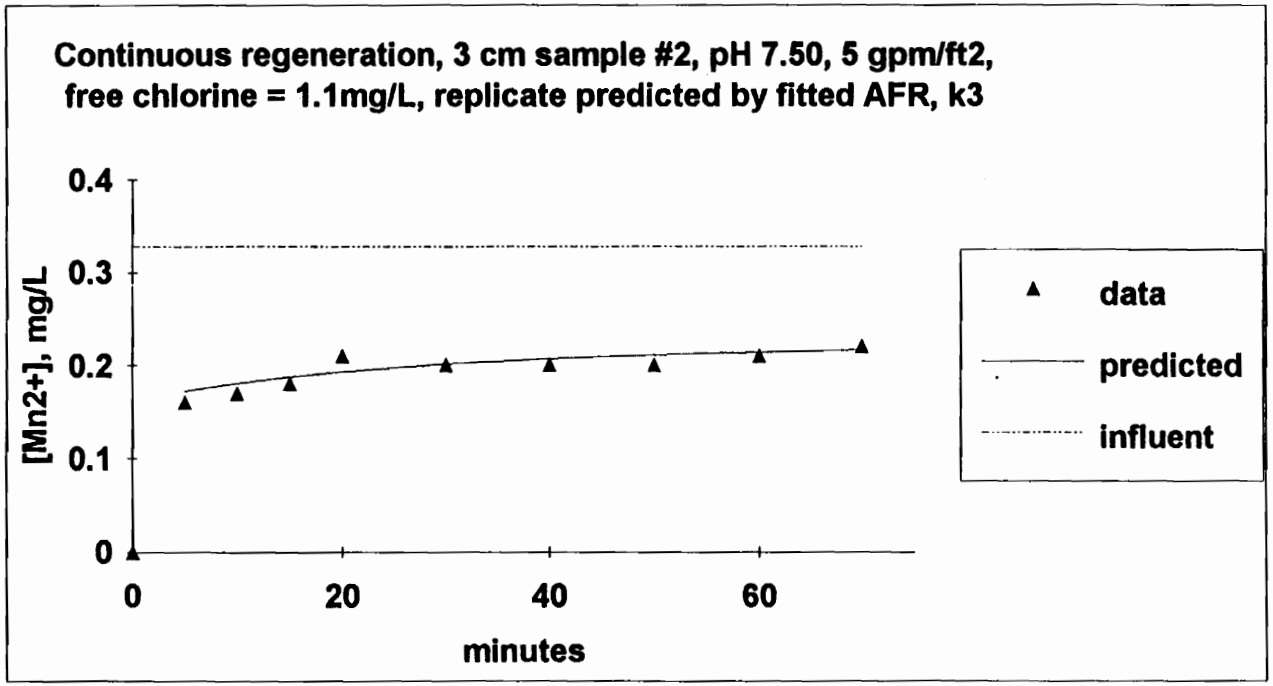

FIGURE 26: Model prediction for replicate test #1 using best-fit k_3 and AFR from calibration of Figure 25.

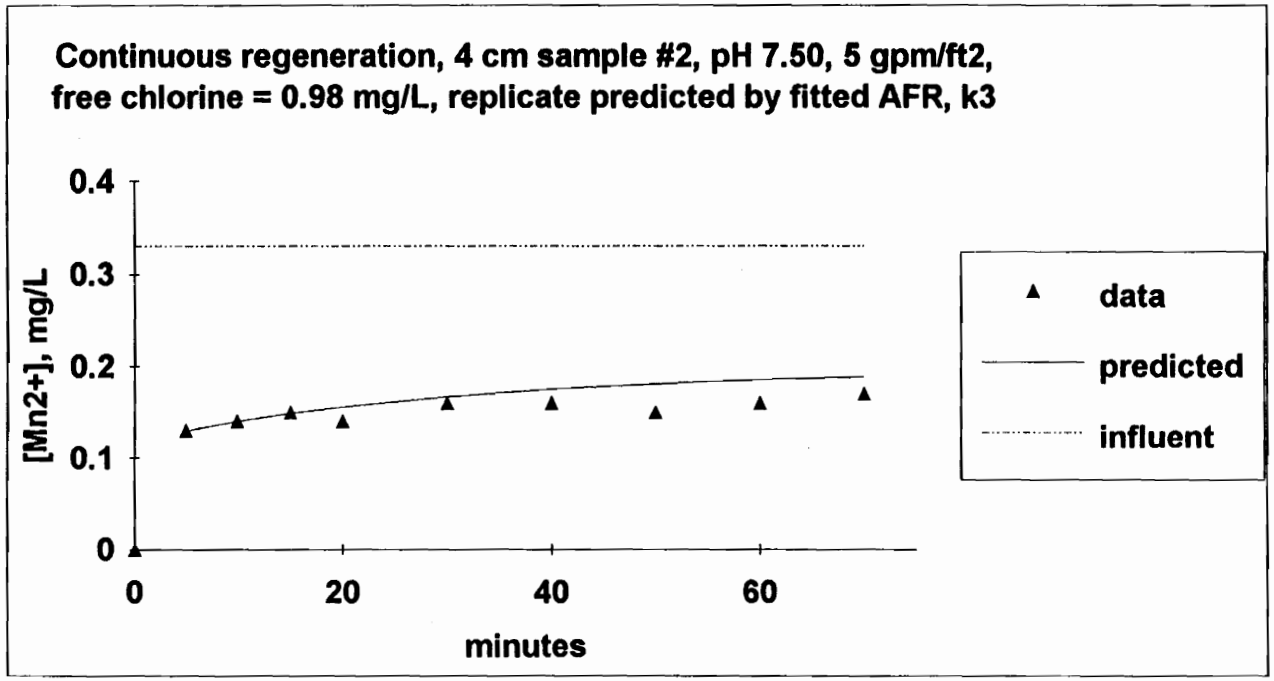

FIGURE 27: Model prediction for replicate test #2 using best-fit k_3 and AFR from calibration of Figure 25.

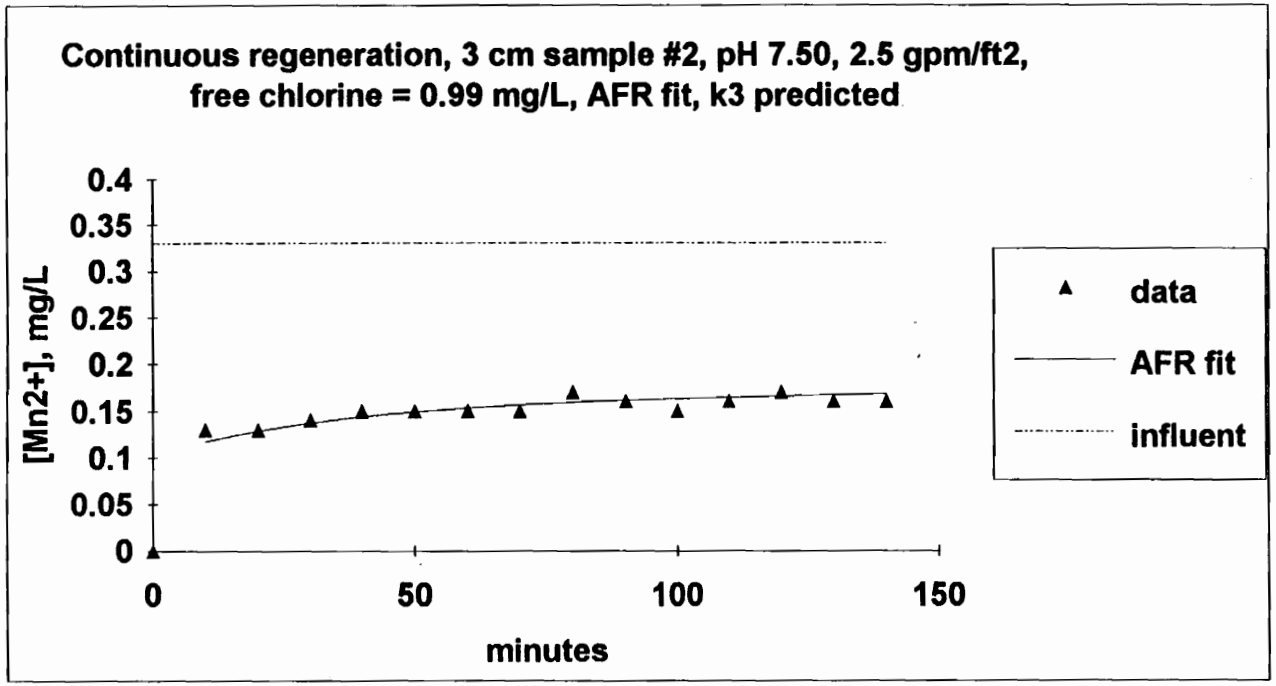

FIGURE 28: Continuous regeneration model calibration at pH 7.50, 2.5 gpm ft^{-2}, fitting AFR with k_3 predicted by fit of Figure 25.

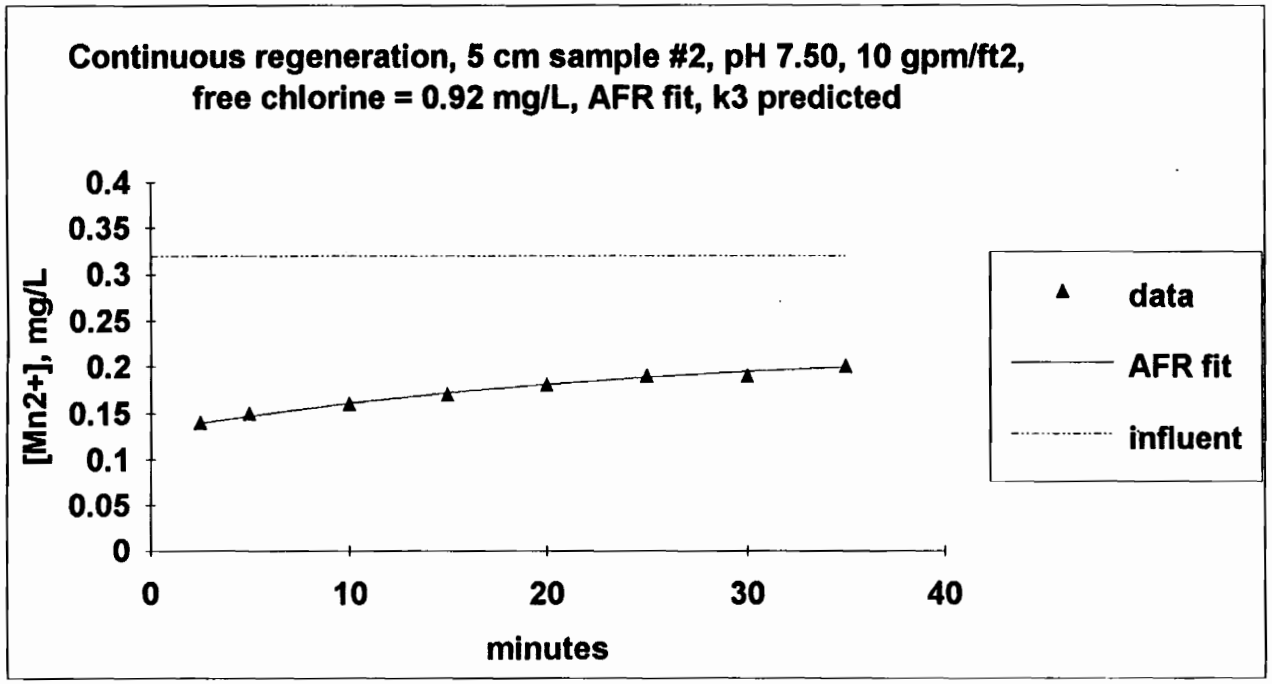

FIGURE 29: Continuous regeneration model calibration at pH 7.50, 10 gpm ft^{-2}, fitting AFR with k_3 predicted by fit of Figure 25.

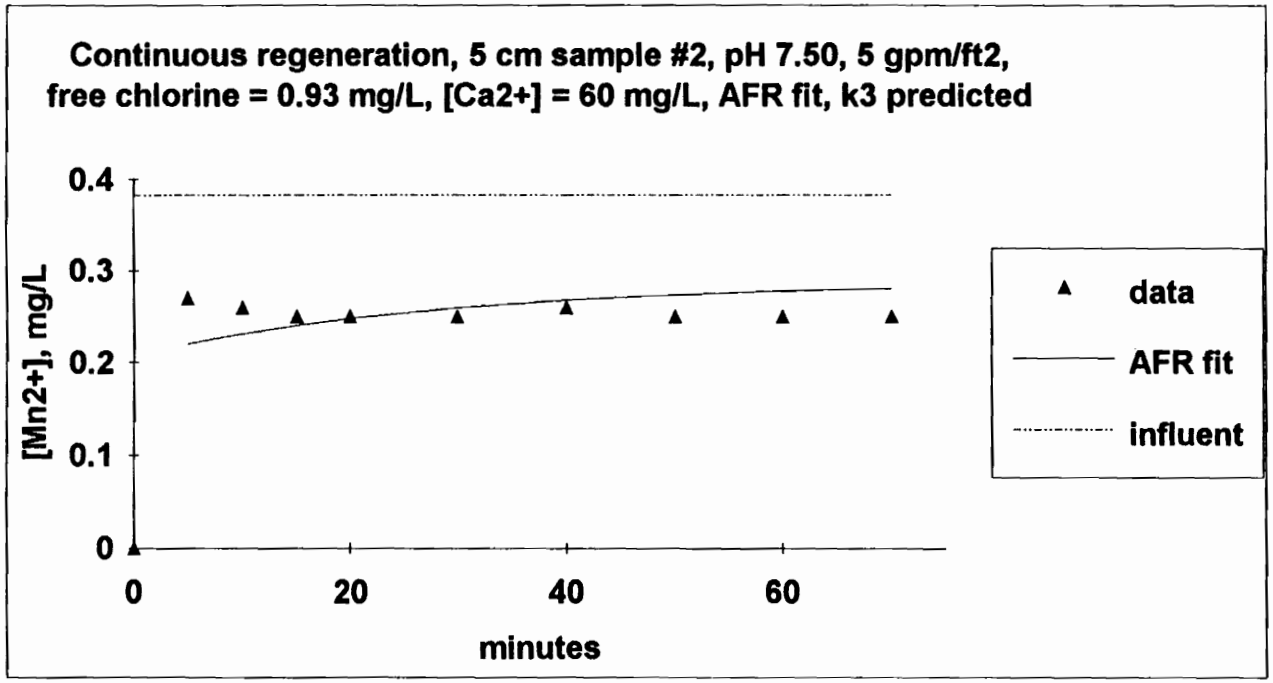

FIGURE 30: Continuous regeneration model calibration at pH 7.50, 5 gpm ft^{-2}, $[Ca^{2+}]$ = 60 mg L^{-1}, fitting AFR, k_3 predicted by fit of Figure 25.

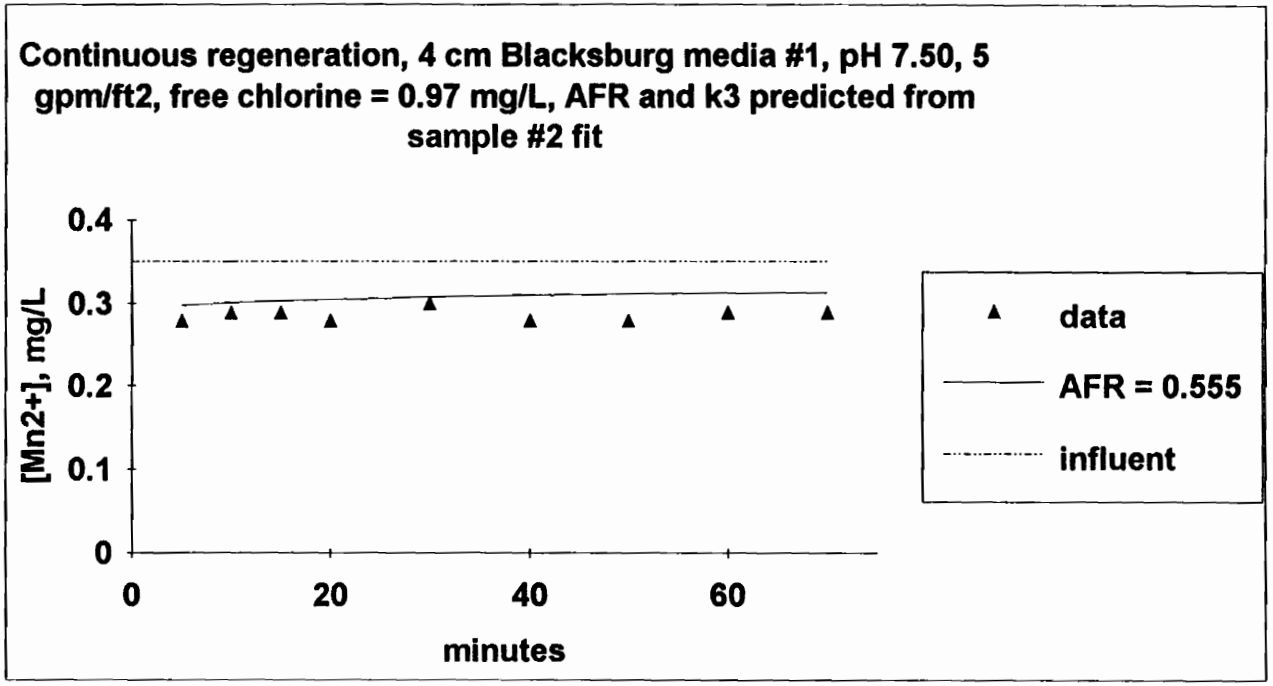

FIGURE 31: Continuous regeneration, Blacksburg media #1, with AFR and k3 predicted by Figure 25 fit for synthetic media #2.

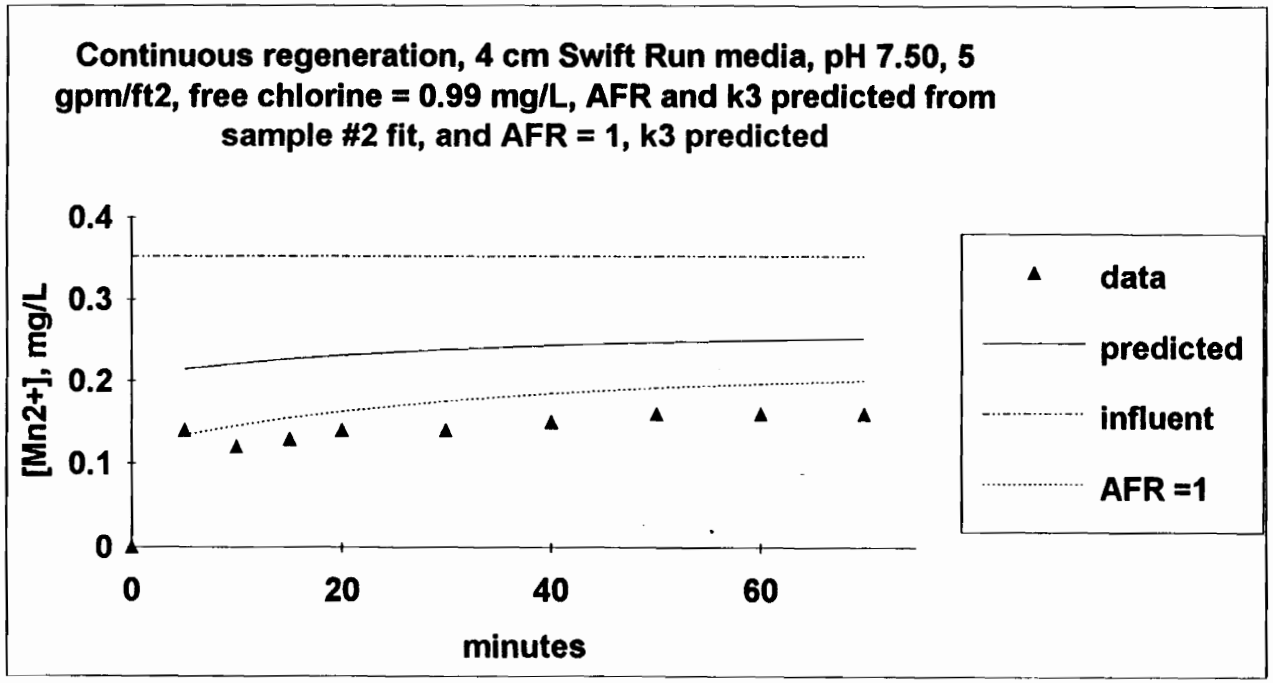

FIGURE 32: Continuous regeneration, Swift Run media, with AFR and k3 predicted by Figure 25 fit for synthetic media #2; also showing best-fit AFR = 1 with k3 predicted.

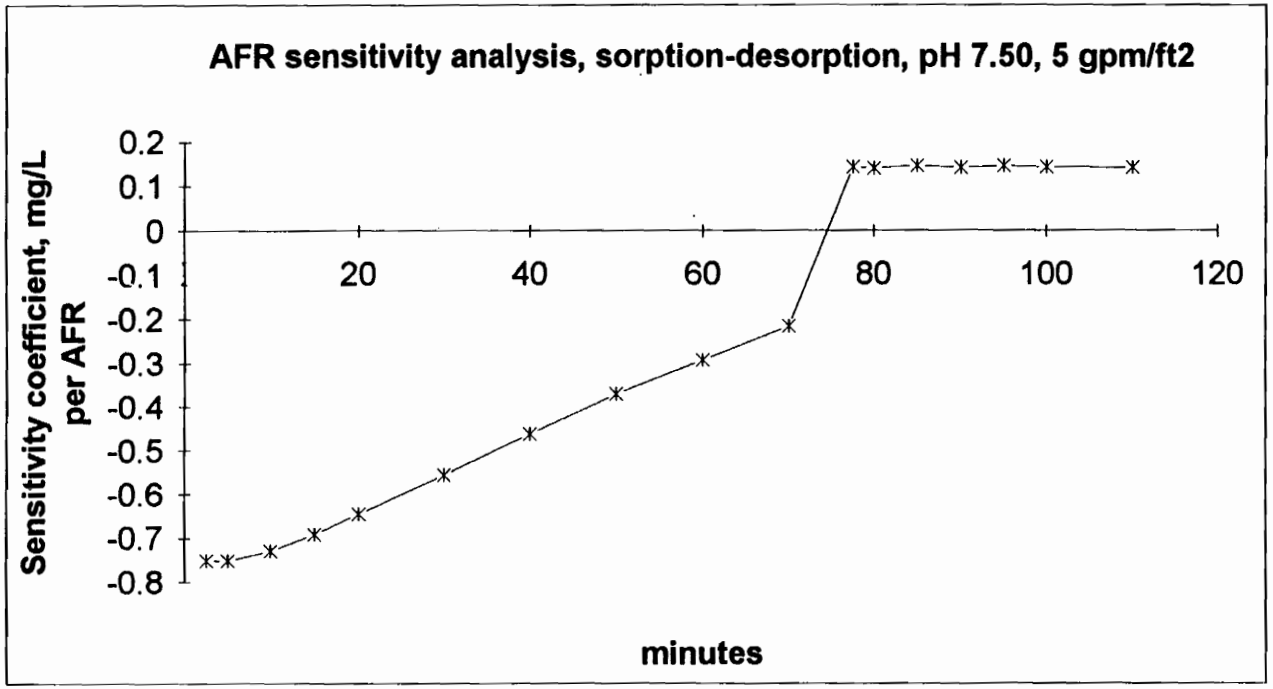

FIGURE 33: Intermittent regeneration model sensitivity analysis for AFR parameter.

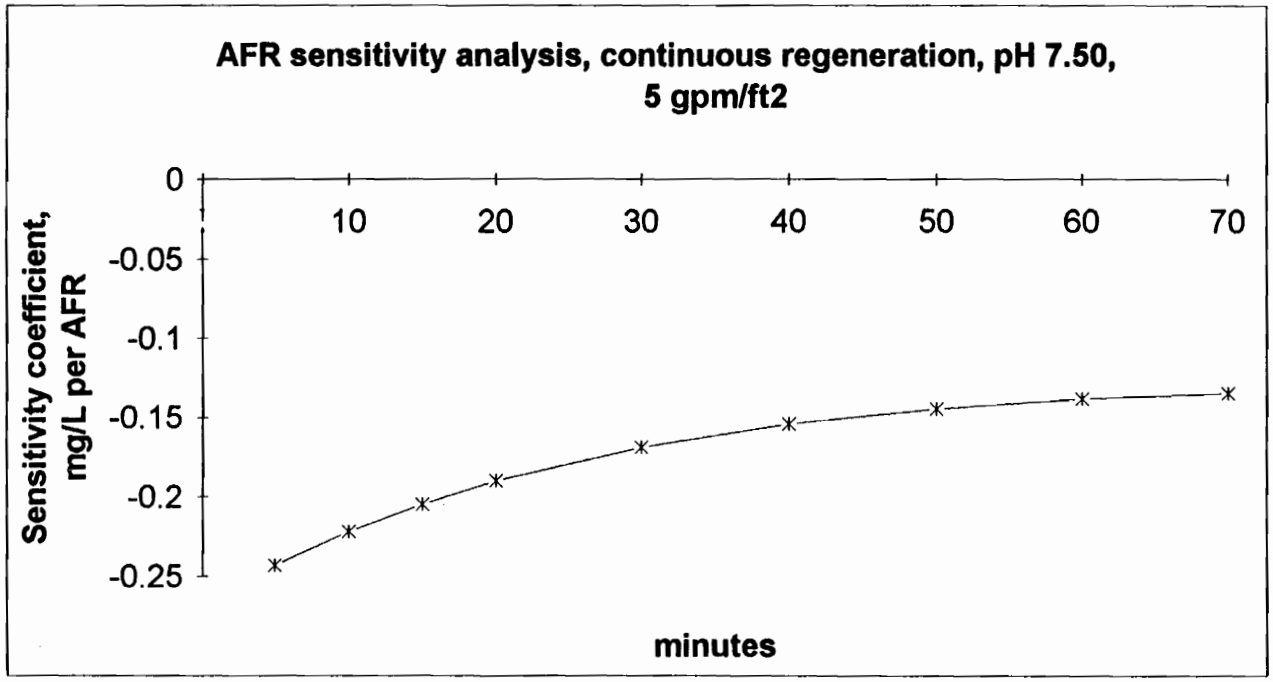

FIGURE 34: Continuous regeneration model sensitivity analysis for AFR parameter.

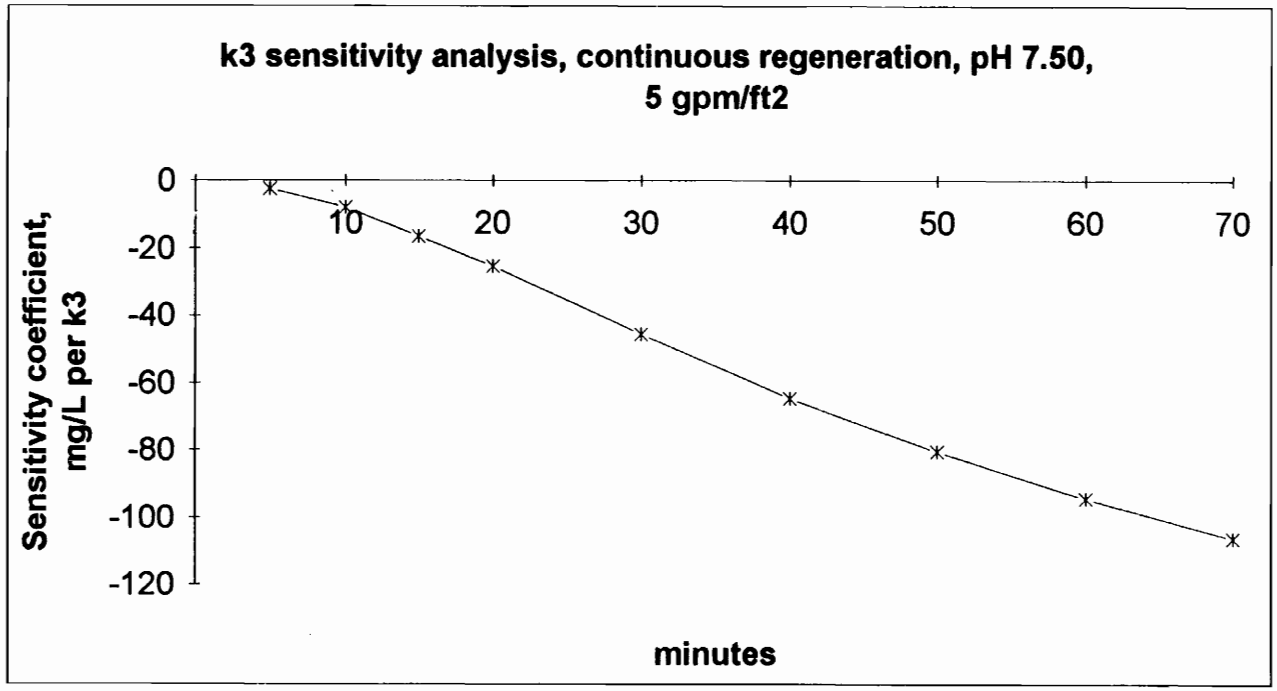

FIGURE 35: Continuous regeneration model sensitivity analysis for k_3 (apparent oxidation rate) parameter.

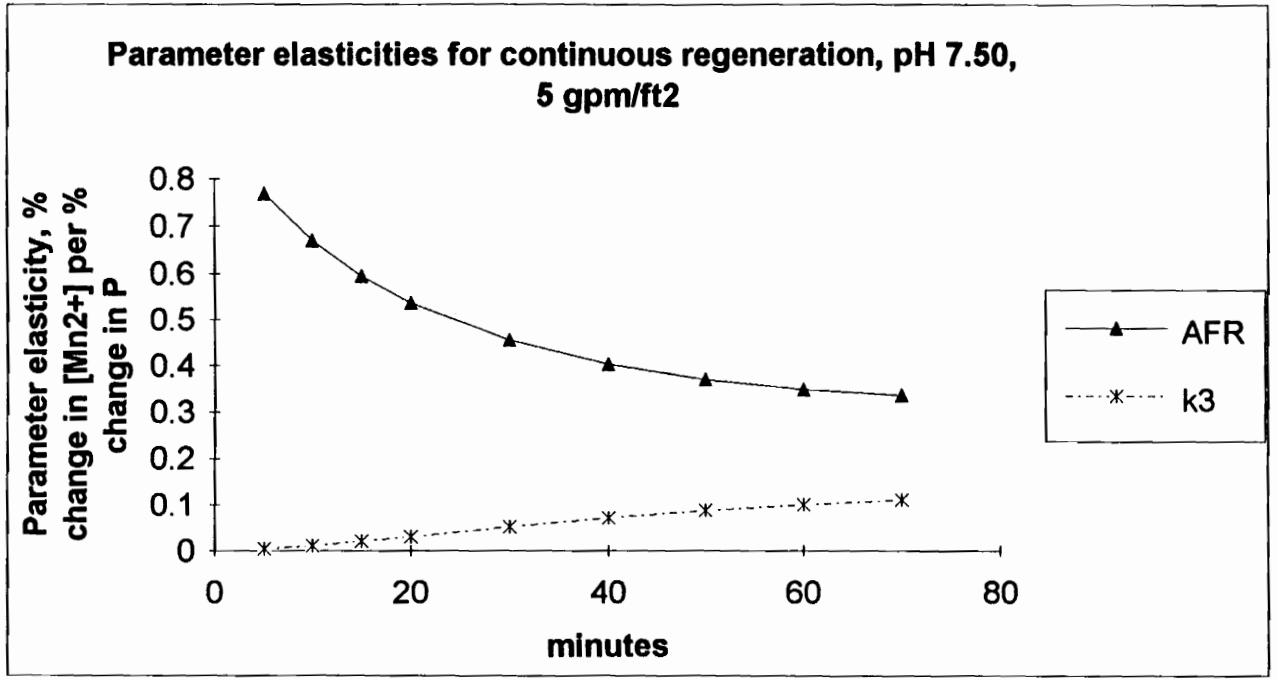

FIGURE 36: Continuous regeneration model parameter elasticities.

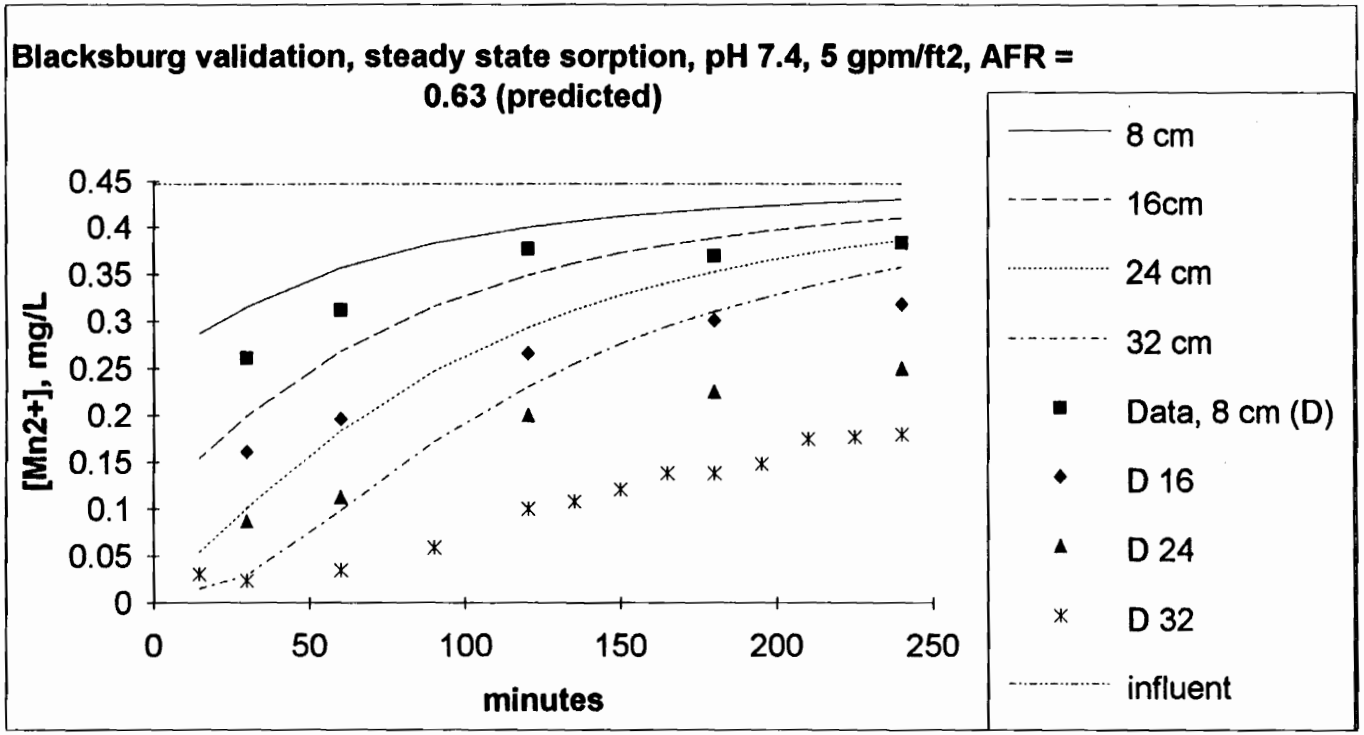

FIGURE 37: Validation study, intermittent regeneration, Blacksburg media #2, predicted by best-fit AFR from lab calibration to Blacksburg media #1.

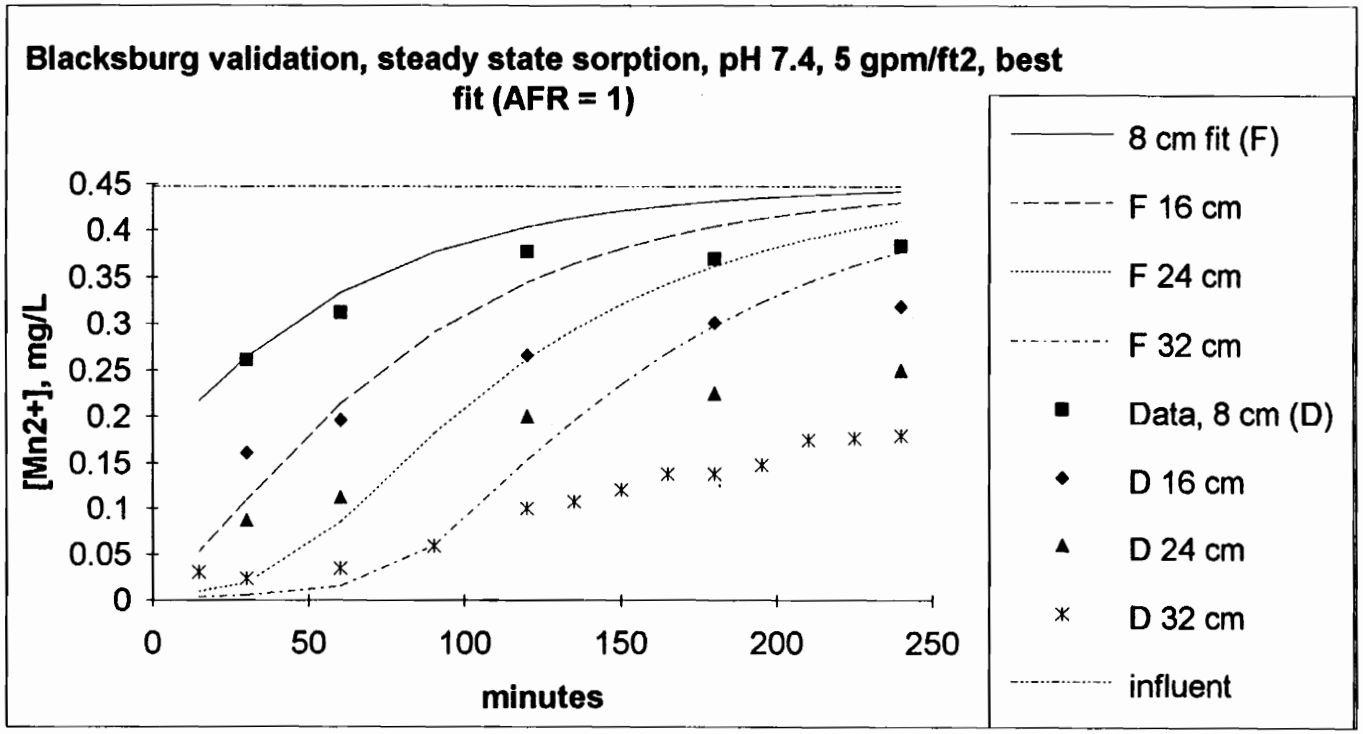

FIGURE 38: Validation study, intermittent regeneration, Blacksburg media #2, best-fit AFR = 1.

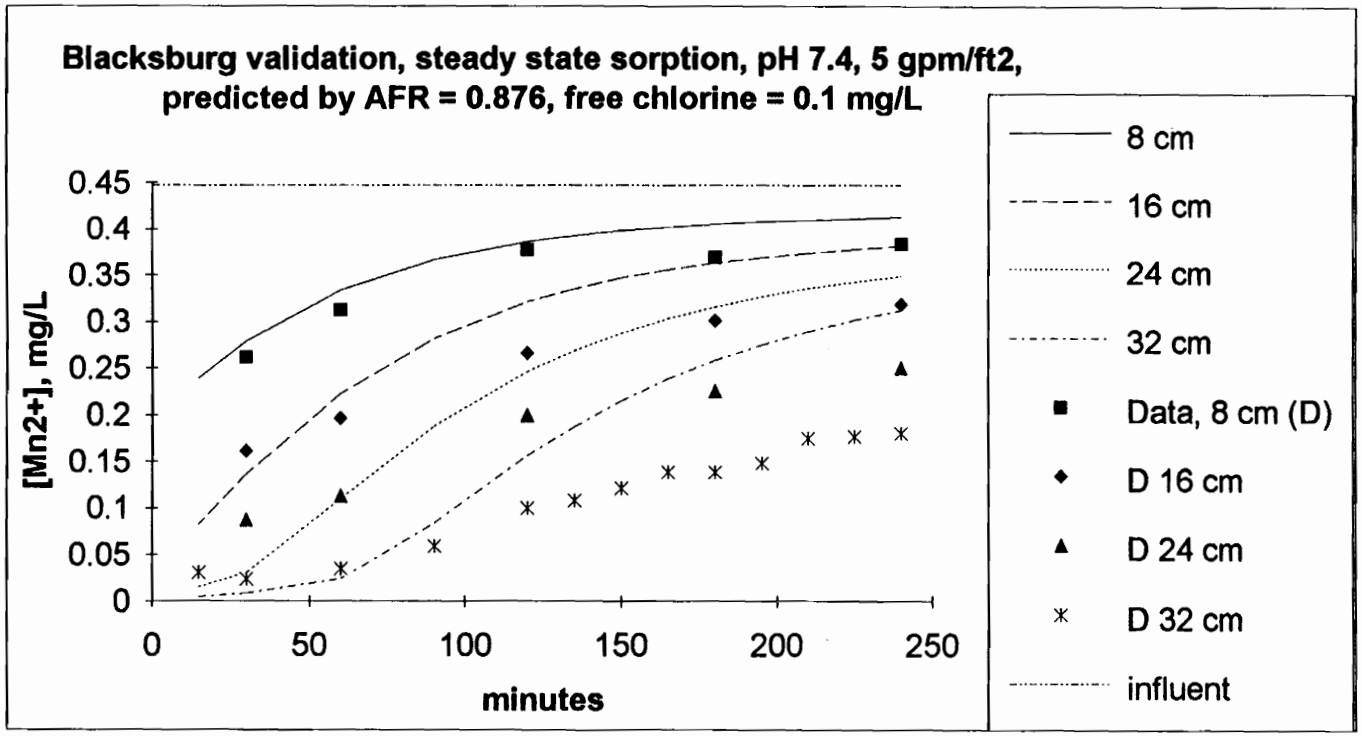

FIGURE 39: Evaluation of possible experimental condition error for the Blacksburg intermittent regeneration validation study.

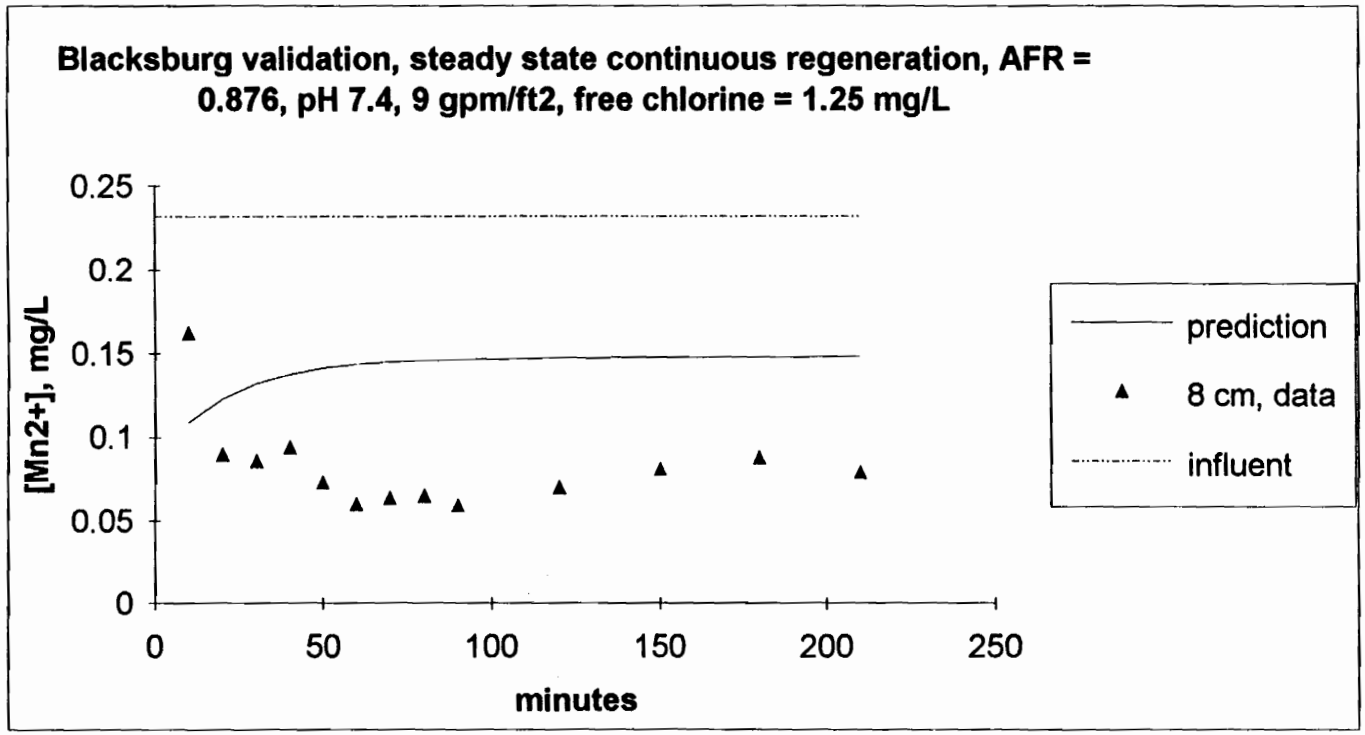

FIGURE 40: Validation study, continuous regeneration pH 7.4, Blacksburg media #2, predicted by AFR from Blacksburg #1 calibration.

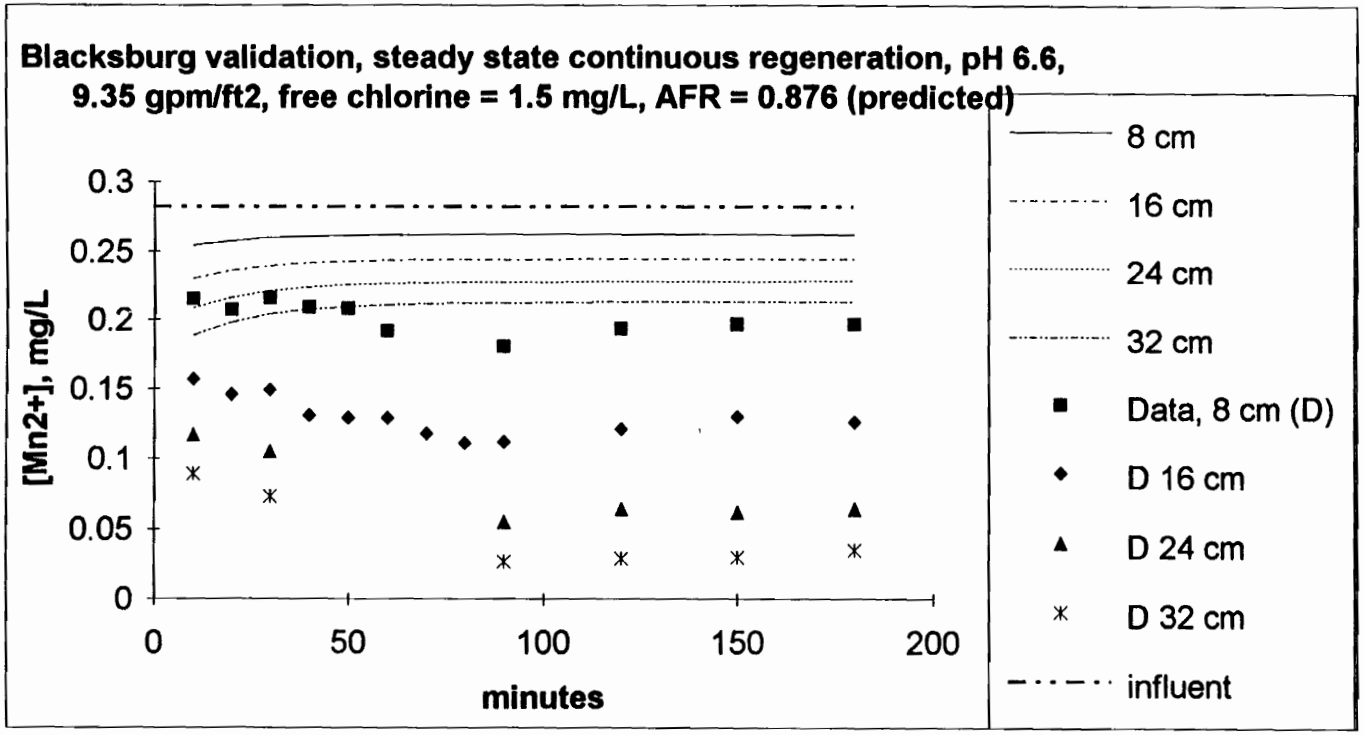

FIGURE 41: Validation study, continuous regeneration pH 6.6, Blacksburg media #2, predicted by AFR from Blacksburg #1 calibration.

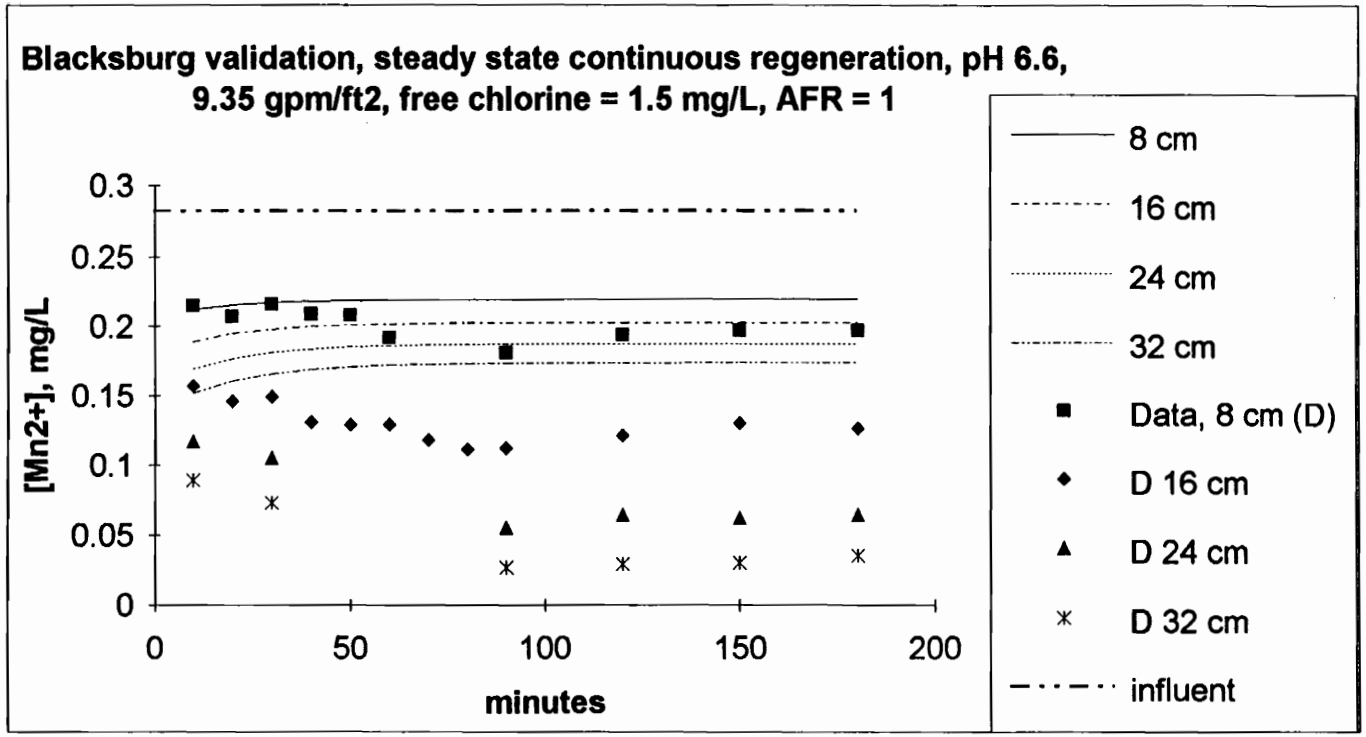

FIGURE 42: Validation study, continuous regeneration pH 6.6, Blacksburg media #2, predicted by AFR =1.

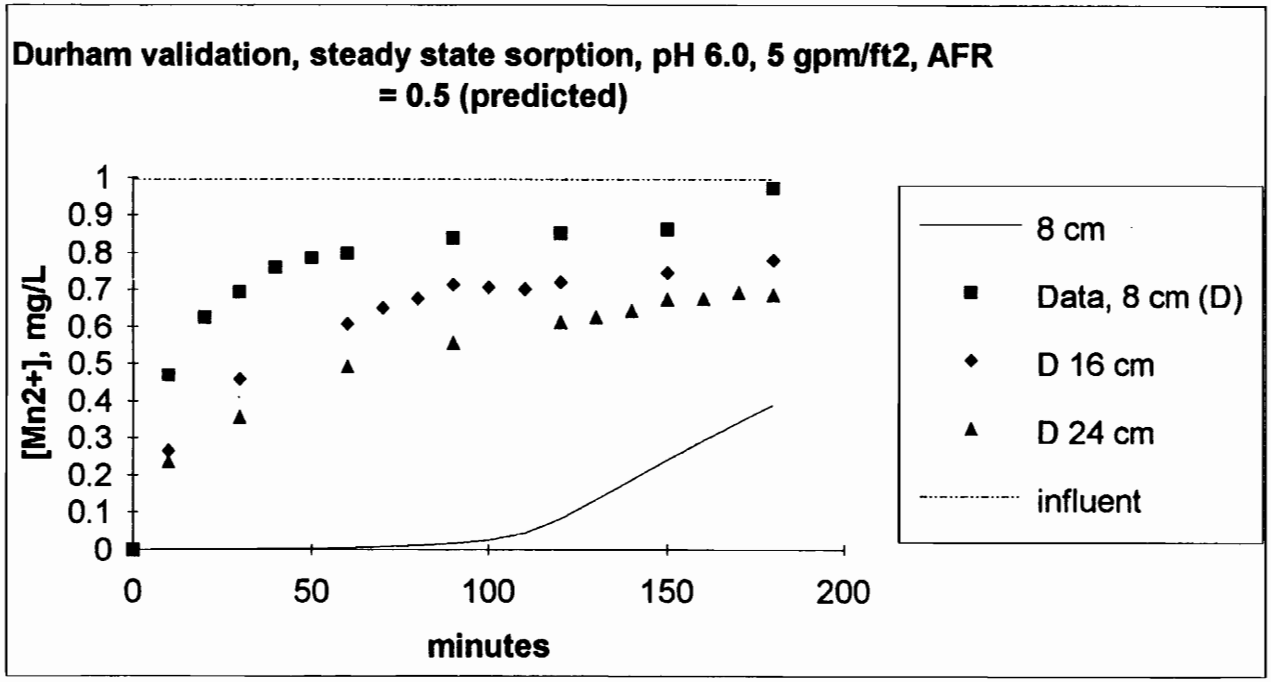

FIGURE 43: Validation study, intermittent regeneration pH 6.0, Durham, predicted by AFR = 0.5.

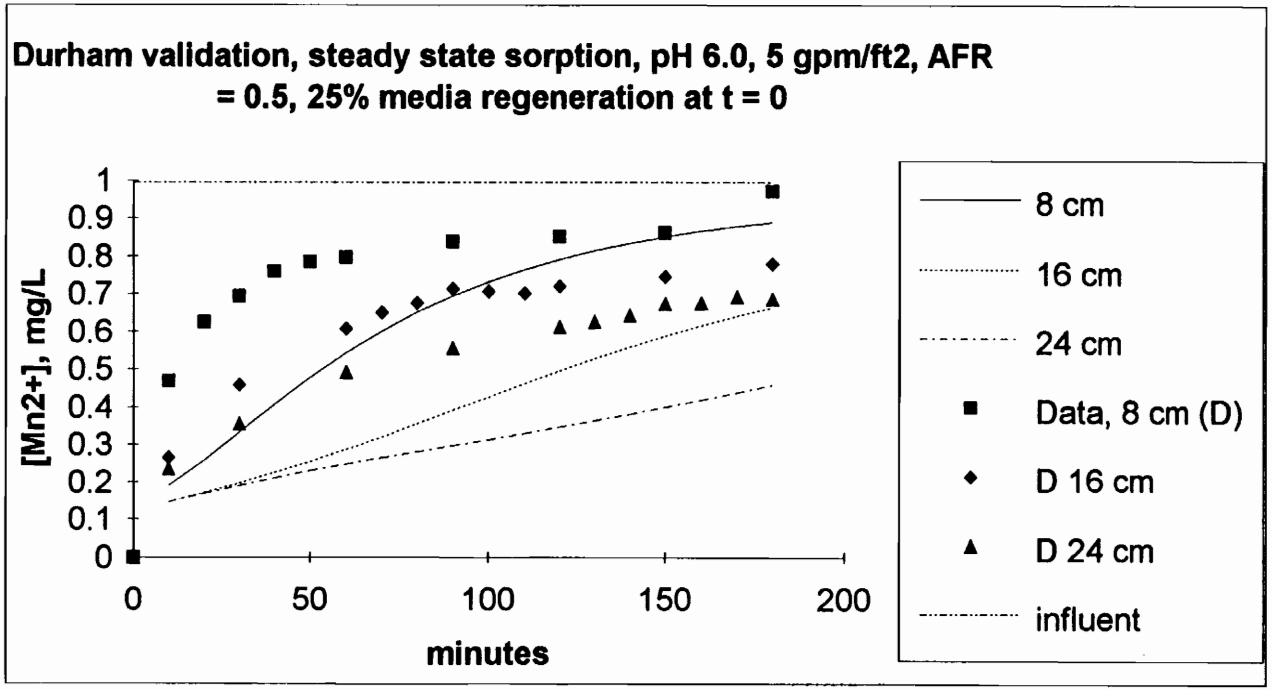

FIGURE 44: Evaluation of possible experimental condition error for the Durham intermittent regeneration validation study, AFR = 0.5, 25% media regeneration.

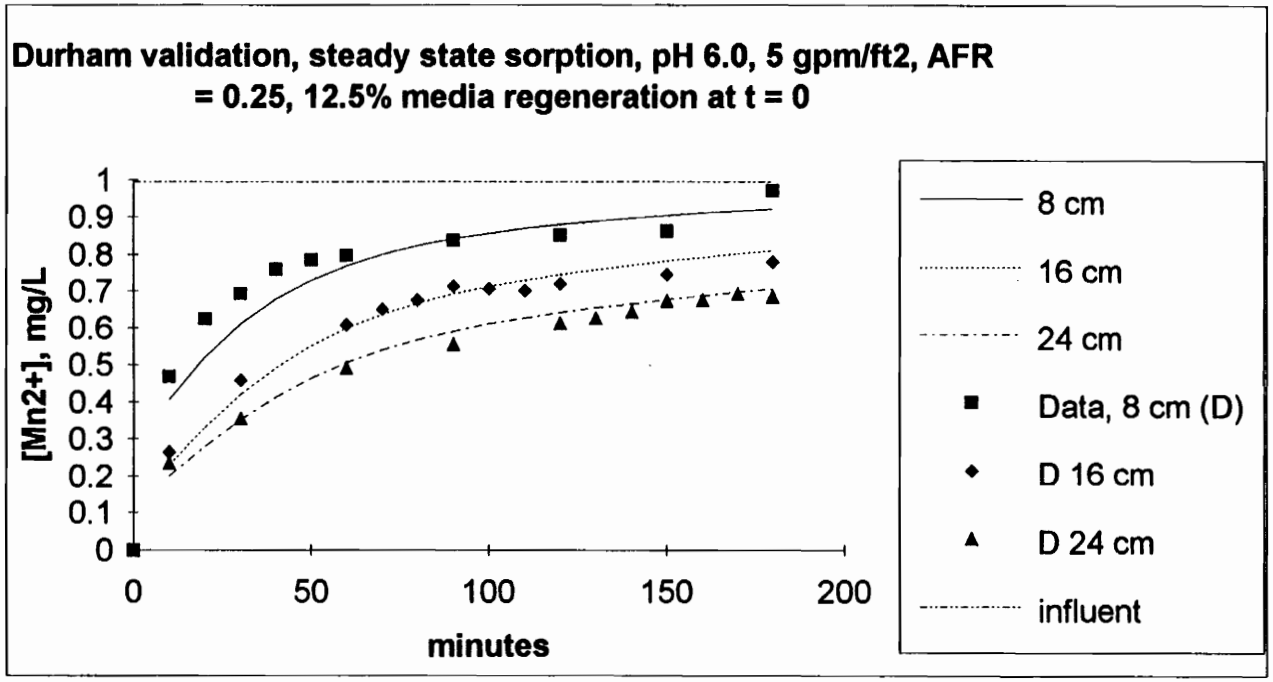

FIGURE 45: Evaluation of possible experimental condition error for the Durham intermittent regeneration validation study, AFR = 0.25, 12.5% media regeneration.

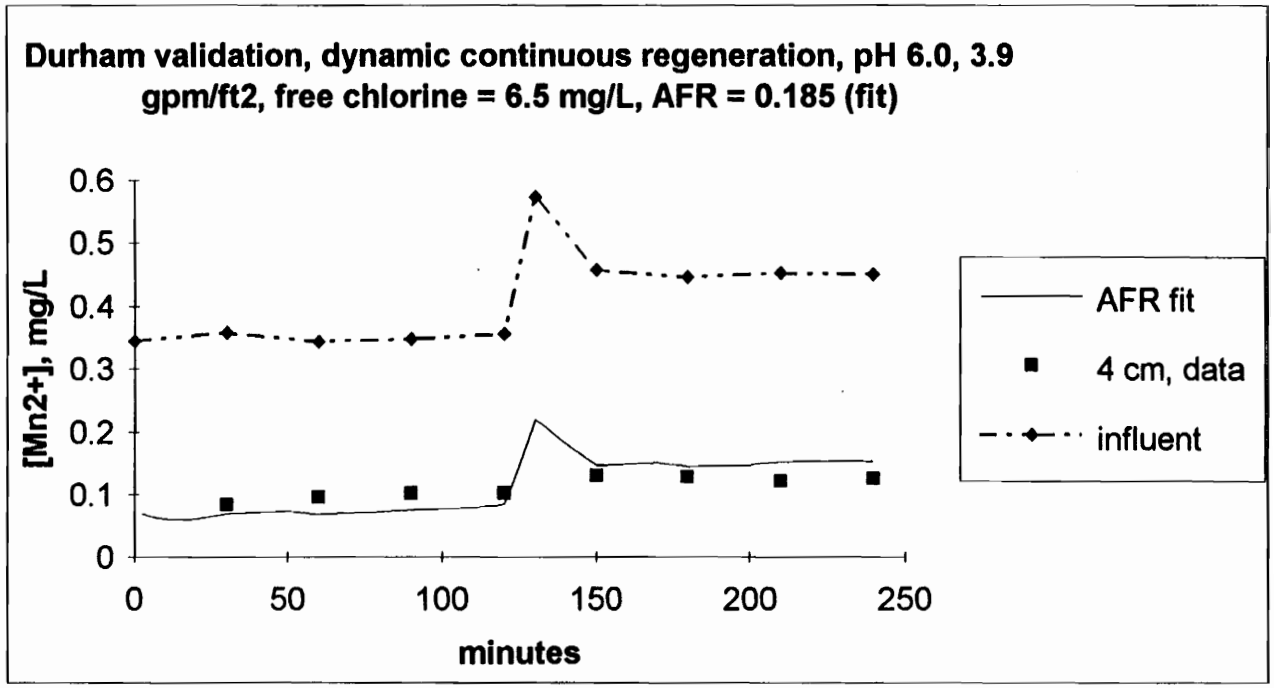

FIGURE 46: Validation study, dynamic continuous regeneration, Durham, best-fit AFR = 0.185.

A

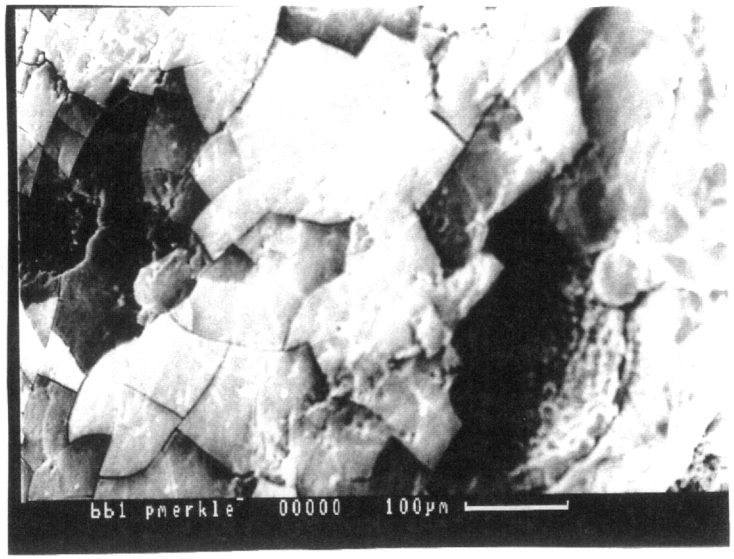

B

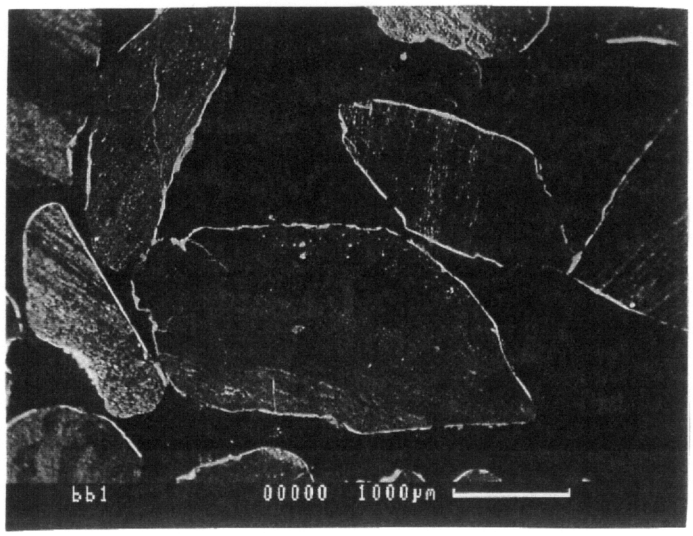

FIGURE 47: A) SEM of Blacksburg #1 coating surface. Cracking is a probable artifact of sample preparation.
B) Cross-section SEM/BSE of Blacksburg #1 media. Coating appears as thin, bright lines surrounding anthracite grains.

A

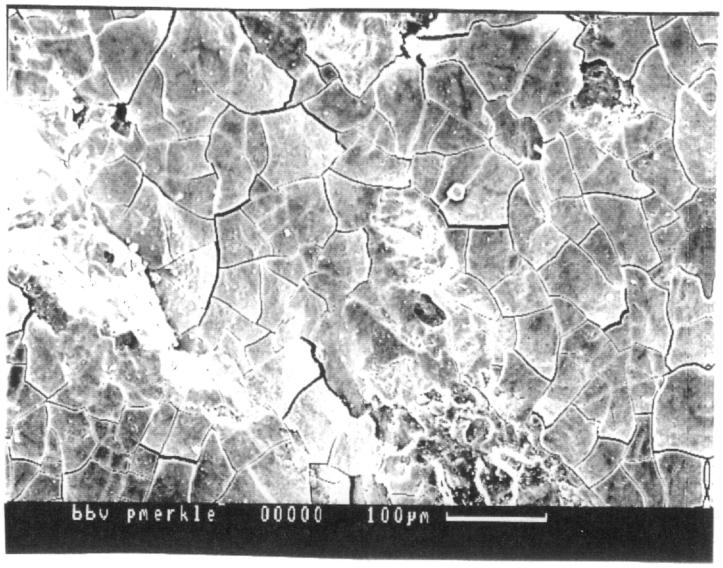

B

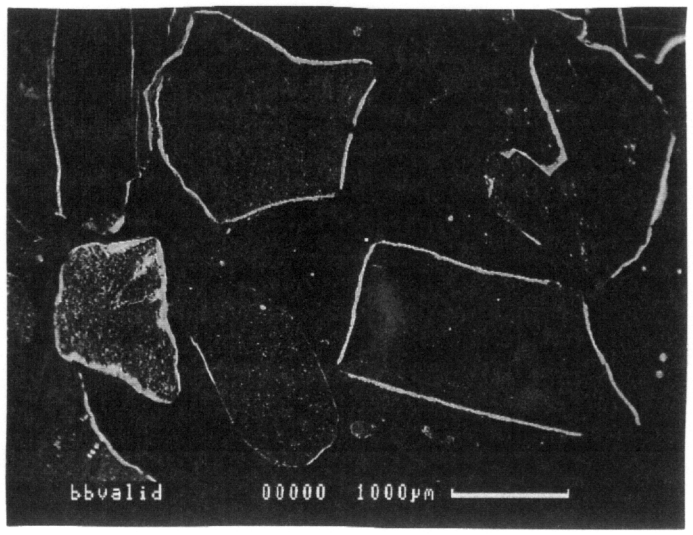

FIGURE 48: A) SEM of Blacksburg #2 coating surface. Cracking is a probable artifact of sample preparation.

B) Cross-section SEM/BSE of Blacksburg #2 media. Coating appears as thin, bright lines surrounding anthracite grains.

A

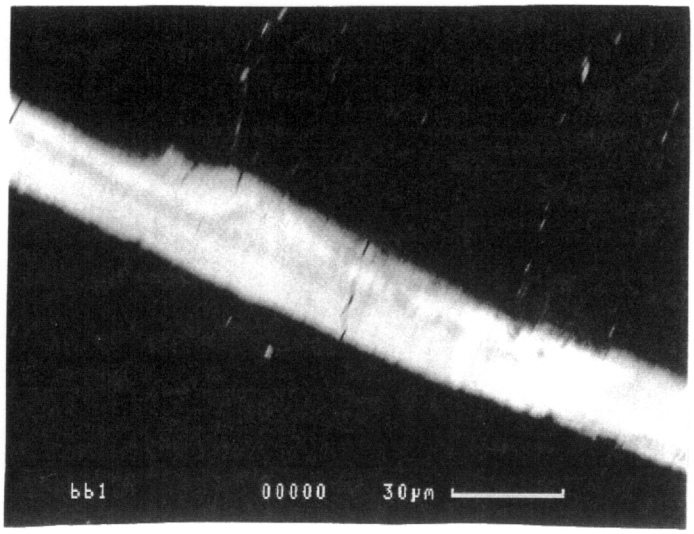

B

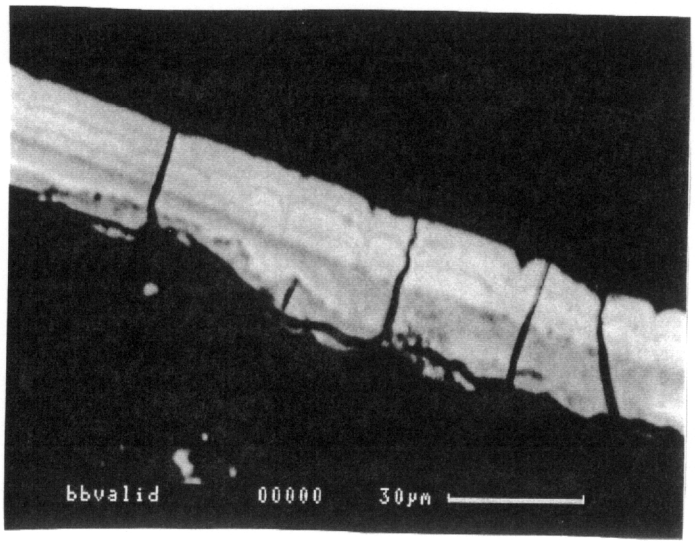

FIGURE 49: A) Cross-section SEM/BSE of Blacksburg #1 media, showing layering features corresponding to variation in composition. Media grain at upper right.

B) Cross-section SEM/BSE of Blacksburg #2 validation media, showing layering features corresponding to variation in composition. Media grain at lower left.

A

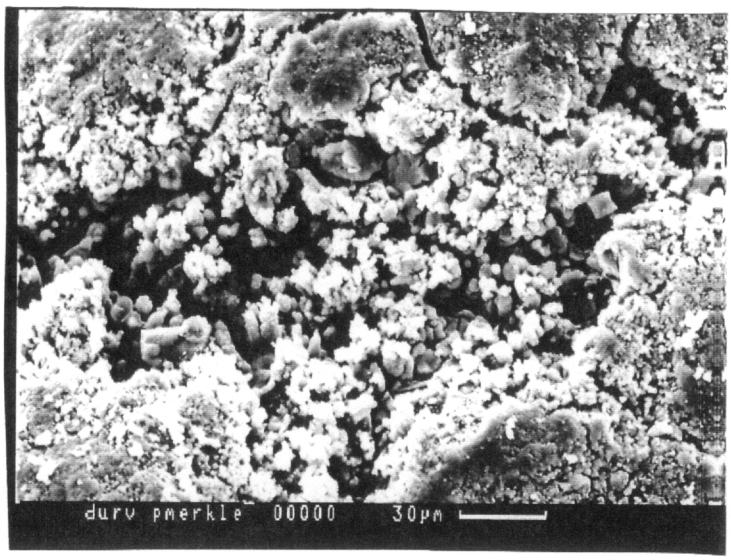

B

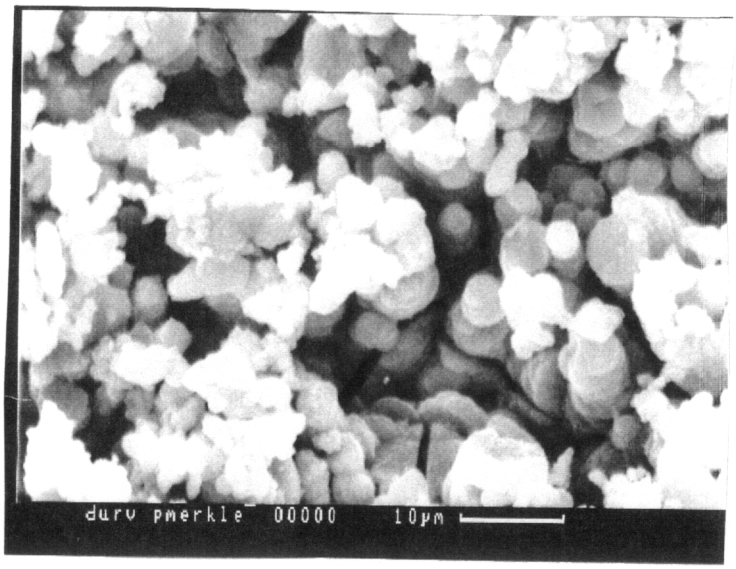

FIGURE 50: A) SEM of Durham validation media, showing surface porosity and roughness.

B) SEM of central region of Fig. 50A, showing columnar features suggesting active growth at the exterior tips.

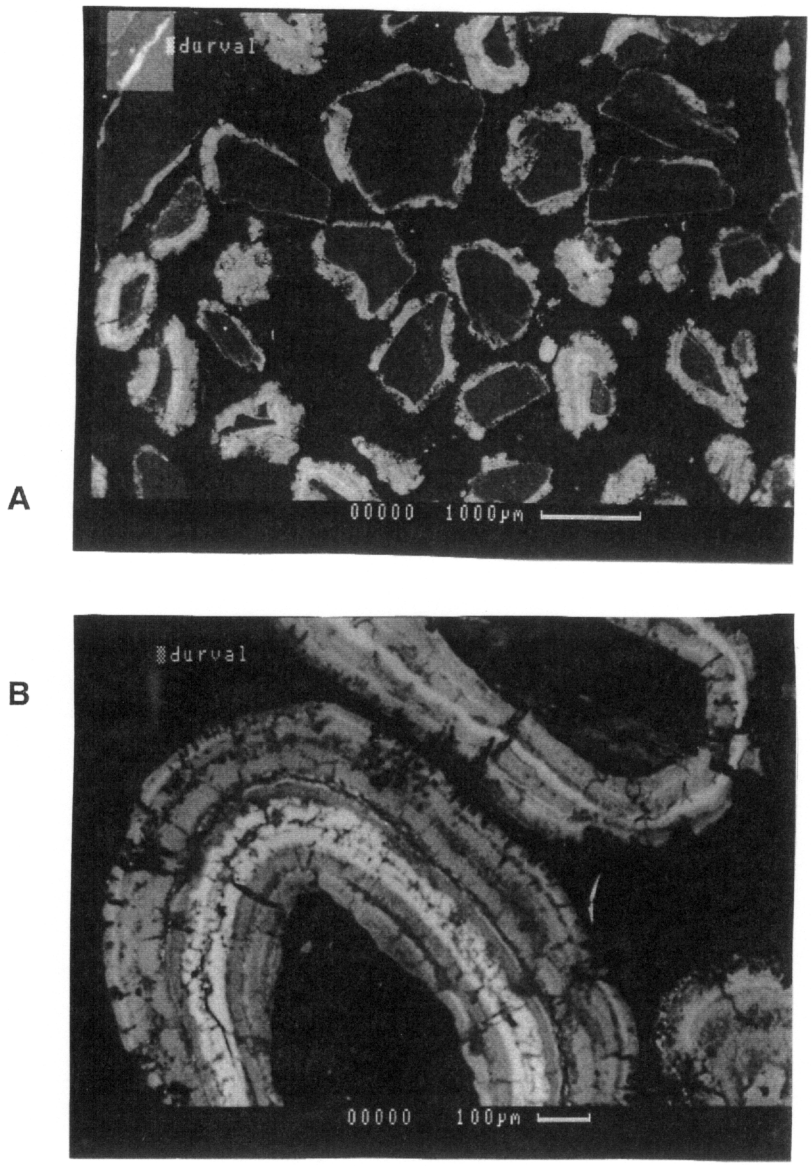

FIGURE 51: A) Cross-section SEM/BSE of Durham validation media.
B) Detail of cross-section SEM/BSE of Durham coating, with variation in composition and internal porosity features evident.

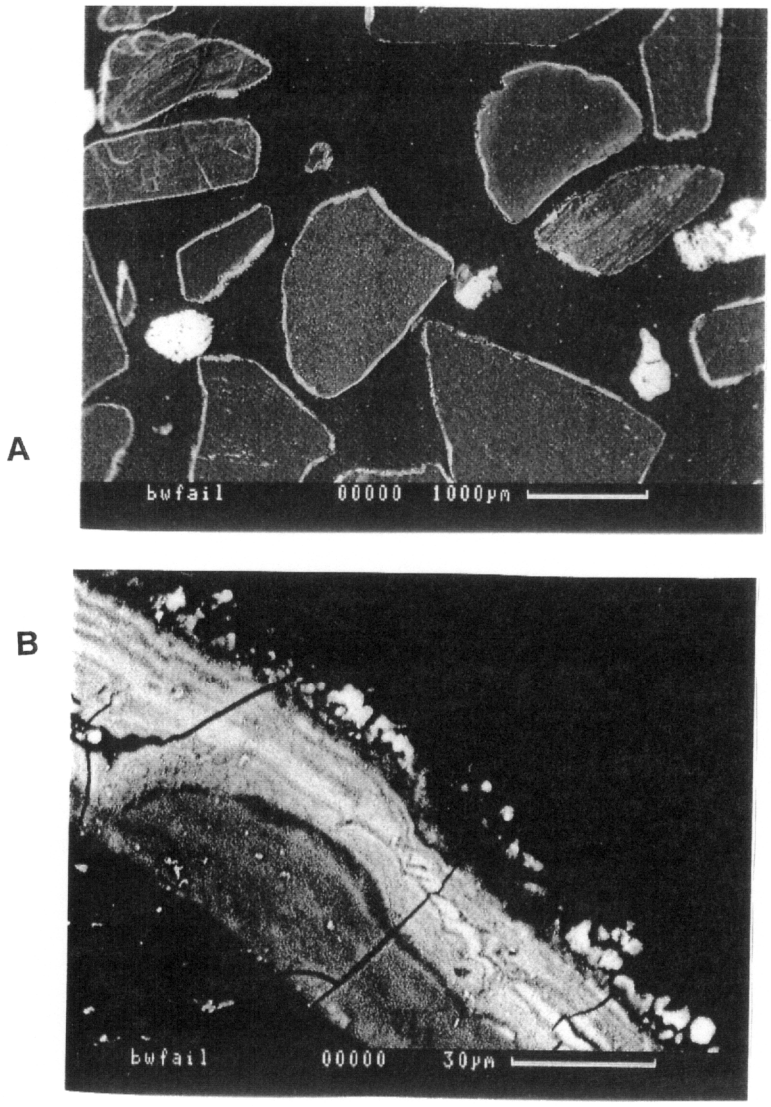

FIGURE 52: A) Cross-section SEM/BSE of post-backwash media from long-term pilot study of Crowe.

B) Detail of cross-section SEM/BSE of post-backwash media. Three regions are evident: inner, dark band; middle band; exterior bright particles (media grain at lower left).

CHAPTER 4

PRACTICAL GUIDE FOR APPLICATION OF THE NATURAL GREENSAND EFFECT PROCESS

INTRODUCTION

In this chapter, some practical guidelines for process implementation and control of the "natural greensand effect" (NGE) are discussed. The process model for Mn^{2+} removal that has been developed is primarily intended for use by a water treatment engineer in the design of pilot studies. It may also be used to predict the suitability of the process for a raw water or process chemistry of interest. The initial stage in implementing the NGE in a filter or absorption plant requires a simple evaluation protocol of media analysis and laboratory-scale filter column tests. Maintaining process performance during elevated raw water Mn^{2+} conditions may be best accomplished through control of the process variables of flow, pH, background ion and oxidant concentrations. Restarting the process in a filter after an idle period, or after a period of operation where Mn^{2+} was not present in the filter-applied water may often necessitate additional steps to maintain finished water quality. The practical engineering aspects of process implementation, maintenance, and reinitiation discussed here are not intended as exhaustive or rigorously technical treatments of pertinent issues or all possible conditions that might be encountered, but rather as a guide for start-up and troubleshooting of full-scale NGE filter/absorber operation.

Prior to NGE implementation, water source management techniques to minimize Mn^{2+} in filter-applied water should be investigated. Hypolimnetic aeration of reservoirs, terminal reservoir maintenance, and watershed control practices to reduce reservoir eutrophication are proven means of reducing Mn^{2+} levels in raw water. It is important to characterize the speciation of Mn causing elevated finished water [Mn^{2+}], and to understand that the NGE process removes dissolved Mn^{2+}, and not particulate $MnO_{x(s)}$ species. In some cases, Mn-rich particulates may result from pre-oxidation of raw source water with O_3 or $KMnO_4$, and these may pass through a dual-media filter to impair finished water quality. Also, certain treatment process configurations may recycle particulate $MnO_{x(s)}$ from pre-oxidation or filter backwash, resulting in the unintentional release of Mn^{2+} in sludge blanket clarifiers or settling basins where reducing conditions may occur.

To implement the NGE process for the first time in an existing filter, a simple laboratory-scale assessment protocol may be followed. This protocol is outlined below, with explanatory comments. Chapters 1 to 3 may be consulted for procedural details of the techniques specified, such as media extraction, media regeneration, and short bed absorber tests.

NGE LAB ASSESSMENT PROTOCOL

a) Evaluate process chemistry of filter-applied water and desired mode of filter operation (continuous or intermittent NGE)

For effective operation of NGE in the intermittent mode (sorption only), the pH of filter-applied water must be maintained in a range favorable for sorption, typically between pH 6.0 and 8.0 (given that an adequate level of

sorptive oxide coating is present). Below this range, sorption capacity may be inadequate for typical filter bed depths and oxide coating levels, and short absorber runs can result. Above this pH range, solution phase oxidation or precipitation of Mn^{2+} may occur, and the risk of particulate Mn formation increases, with concomitant risk of filter breakthrough of these particulate species. Within the target pH range, sorption capacity may be decreased by the presence of competing solutes, such as Ca^{2+}. For influent [Mn^{2+}] above 0.35 mg L^{-1}, the NGE process should be considered with caution, given the high risks to customer satisfaction resulting from inadvertent process failure. The impact of Mn-rich filter-backwash recycle streams on residuals disposal and process chemistry should also be considered.[1] Release of soluble Mn^{2+} from clarifier and terminal reservoir sludges may increase the filter-applied Mn^{2+} concentration above the level of the raw water source, increasing free chlorine demand across the filter.

For operation in continuous NGE mode, the specific impacts of influent [Mn^{2+}], pH, and [Ca^{2+}] must be evaluated. However, the presence of free chlorine allows the process to perform well at the low end of the pH range, or in the presence of Ca^{2+} since sorption capacity is constantly regenerated. The competitive oxidant demand of dissolved organic carbon must be accounted for in calculating the filter-applied chlorine dose, which should be sufficient to maintain a free chlorine residual in the filter effluent of 1 mg L^{-1}. Process chemistry favorable for good continuous NGE performance is compatible with slightly acidic pH conditions typical of enhanced coagulation for removal of disinfection by-product precursors.

b) Analyze the filter media currently in place by extraction

Since the sorption and oxidation steps of the NGE occur on the media surface, a sufficient quantity of $MnO_{x(s)}$-coated surface is required. For filters operating in continuous regeneration mode, a synthetic coating amount of 0.3 - 2 mg g^{-1} appears sufficient to implement the process in a dual-media filter, given the appropriate process chemistry, as demonstrated by laboratory and operating filter plant studies.[2] The 0.3 mg g^{-1} coating amount was adequate for good performance in Bridgeport, Connecticut filter plant. Since the media sorption capacity and catalytic removal ability is a strong function of pH, a coating amount that provides adequate Mn^{2+} removal at pH 7.5 may not be satisfactory at pH 6.0. However, even an abundant $MnO_{x(s)}$ coating (5 - 100 mg/g) may be covered with a relatively non-sorptive mineral deposit, and will not perform well even under favorable pH conditions. This situation could arise in a filter plant practicing conventional treatment with seasonally-elevated [Mn^{2+}] in a reservoir source. The prior season's Mn-rich deposit remains on the filter media throughout the intervening period of low filter-applied [Mn^{2+}], and a poorly-sorptive Al-rich layer is deposited. When the next elevated [Mn^{2+}] event begins, NGE process performance may initially be poor if the underlying Mn-rich deposit is obscured and unavailable for sorption. The sorptive properties of existing media should be evaluated with the short-bed absorber test protocol described in subsection d) below.

c) If sufficient MnO_x is present, regenerate a media sample to determine the oxidant demand

The sorptive capacity of an existing media may be saturated with Mn^{2+}. If such a media is used to initiate the NGE in either intermittent or continuous mode, poor performance is likely. For intermittent operation, the media's capacity for absorption is already depleted, so it will require regeneration before use. For start-up of continuous NGE, Mn^{2+} removal may be initially poor, although the amount of free chlorine supplied is sufficient for oxidation of the filter-applied [Mn^{2+}]. Satisfactory effluent levels may not be attainable due to the pre-existing oxidant demand. This demand may be estimated by the column method described in Chapter 2. If an existing NGE process has failed, determining the media oxidant demand is a useful initial troubleshooting step. Free chlorine supplied to the failed filter may have been insufficient, and regeneration is required to restore sorption capacity. A sample of regenerated media can then be used for a short-bed absorber test.

Illustrating this trouble-shooting method, the oxidant demand of an anthracite filter media from a plant (Norfolk, NE) practicing the continuous NGE process was evaluated after process failure. Over several months, the filters were supplied with less than the stoichiometric requirement of free chlorine for Mn^{2+} oxidation. The free chlorine demand was 2.4 g kg^{-1}, or about 1.9 kg m^{-3} on a filter bed volume basis. The process performance was restored after the repeated dosing of the existing filter media with a high free chlorine concentration (> 300 mg L^{-1}), and an increase in filter-applied free chorine concentration.

d) Conduct a short-bed absorber test with the regenerated media to assess Mn^{2+} uptake.

The short-bed absorber test method described in Chapter 3 may be used by a process engineer to perform a bench-scale evaluation of the applicability of the NGE process for the physical and chemical conditions of interest. A bed depth of 10 cm of regenerated natural or synthetically-coated media should be sufficient for an initial evaluation of both intermittent and continuous regeneration modes. A full-depth column test is also appropriate, since a design based on the short-bed test alone may underestimate full-scale Mn^{2+} removal. The influent solution chemistry and hydraulic loading for the test should match that of the filter-applied water. Several tests spanning the likely range of variations in pH, $[Mn^{2+}]$, free chlorine, temperature and other chemical and physical parameters of interest may be appropriate. The short-bed absorber tests will also provide calibration data for process modeling if needed.

e) Determine the sorption isotherm of the regenerated filter media at process chemical conditions of pH, $[Mn^{2+}]$, $[Ca^{2+}]$ in the absence of free chlorine

This step is required for rigorous application of the kinetic process model, and requires construction of a recycle sorber unit similar to that described in Chapter 3. Based on this work, three or four points on the isotherm below the expected maximum $[Mn^{2+}]$ expected in the process conditions of interest should be adequate to determine Freundlich isotherm parameters, including one or more isotherm determinations near the desired effluent $[Mn^{2+}]$ in order to avoid extrapolation errors. All isotherms determined in this study were log-linear

below 0.35 mg L^{-1}, in the desired "safe" range of influent [Mn^{2+}]. For any significant variations in the filter-applied water chemistry such as pH and [Ca^{2+}], an isotherm should be determined. After construction of the recycle sorber unit, determination of a four-point isotherm requires about two 8-hour work days.

f) Predict process performance using the kinetic model

After the isotherm determination, the kinetic model may be used to simulate NGE process performance under the conditions of interest. With an estimate of the media d_{50}, the flow correlations may be used to estimate the external and internal transport parameters. The model may then be rigorously calibrated to short-bed absorber data, as done in Chapter 3. For intermittent regeneration, the available sorption capacity parameter (AFR) may be used for fitting the model, and both AFR and the oxidation rate parameter (k3) may be fitted for continuous regeneration. This process can be time-consuming; a less labor-intensive alternative to the rigorous calibration would be trial-and-error fitting to short-bed absorber data, starting with values for AFR and k3 determined in this study. With parameter estimates from fitting, a pilot-scale filter run may be simulated, with the model set for the appropriate filter depth and run duration, as done in Chapter 3.

In conventional dual media filters the NGE process is essentially employing the filter bed as a filter-sorber for Mn^{2+}. Care must be taken that the process pH and background ion levels will enable satisfactory performance with the type and amount of $MnO_{x(s)}$ present on the media surface. For continuous regeneration mode, the full-scale simulation will indicate whether effluent [Mn^{2+}]

approaches unacceptable levels during the filter run, which would indicate that further pilot studies are needed.

g) Use the model to evaluate impact of non-steady state process variables

As demonstrated in Chapter 3, the model may be used to simulate dynamic process conditions, including changes in flow rate, influent $[Mn^{2+}]$, free chlorine, and pH. Before proceeding with a dynamic numerical analysis, an appreciation for qualitative process heuristics may be beneficial in deciding what level of effort in this direction is needed. Table 1 summarizes the general effects on effluent $[Mn^{2+}]$ of changes in various process parameters. For example, decreasing the pH will tend to increase effluent $[Mn^{2+}]$ in continuous regeneration mode, all other conditions equal. If the expected process variation is an increase in pH, dynamic modeling is not required since the expected effect is an improvement in an already satisfactory process. However, care must be exercised if the anticipated pH is much higher than 8, since under this condition undesirable particulate $MnO_{x(s)}$ species may be formed. In continuous regeneration mode, even a decrease in pH may not cause any detectable increase in effluent $[Mn^{2+}]$ over a 0.6 to 0.9 m bed depth. Some process effects are counter-intuitive, especially for intermittent regeneration. A marked decrease in influent $[Mn^{2+}]$ during a filter run may in some cases cause a desorption "spike", resulting from sorptive equilibrium being re-established at the lower $[Mn^{2+}]$ concentration. The same result applies for an increase in $[Ca^{2+}]$ or any other solute that may decrease sorption capacity.

The dynamic capability of the model may be most useful for the case where several simultaneous changes may occur during continuous regeneration

mode. Such changes could be driven by the need for alternate or additional water sources during high demand periods, as when surface water withdrawals are limited by stream flow maintenance requirements. For example, if a plant implemented a periodic blending of a groundwater source with a river source, this could result in a decrease in filter-applied pH and a concurrent increase in Mn^{2+} and Ca^{2+} concentrations to levels which adversely affect continuous NGE process performance. Without careful monitoring of effluent $[Mn^{2+}]$ and appropriate adjustments to process conditions, it is possible that the effluent $[Mn^{2+}]$ could suddenly exceed the desired level. Based on qualitative analysis, an increase in filter-applied free chlorine, pH and/or a decrease in flow rate might be indicated to recover from a process failure, if one is encountered. In anticipation of the new sourcing strategy, the model could be used to simulate alternative control strategies, and indicate whether pilot studies are needed in case marginal performance is predicted.

CASE STUDY: Implementation of the Continuous NGE Process

Mr. Ken Carlson conducted a full-scale trial of the continuous NGE process at the Fort Collins, CO Water Utility in 1994. This plant draws some of its raw water from a reservoir (depth = 50 m) supplied by snow runoff. The plant experiences seasonal elevation in dissolved Mn^{2+} during the summer when the reservoir stratifies and hypolimnetic hypoxia results from bacterially-mediated biogeochemical processes.[3] The plant treats the raw water with $KMnO_4$, followed by upflow sludge blanket clarification, chlorination and dual-media filtration. The filter-applied water pH typically ranges from 6.8 to 7.0, with a natural hardness of 28 - 40 mg L^{-1} as $CaCO_3$. The trial was performed to

evaluate Mn^{2+} removal in the filters as a final "polishing" step, since 0.05 - 0.08 mg L^{-1} total Mn (approximately 50% dissolved, 50% colloidal particulates) is sometimes found in the filter feed from the sludge blanket clarifiers during the seasonal Mn^{2+} event.

Prior to the beginning of the seasonal Mn^{2+} increase, the test filter was prepared by regeneration with free chlorine, and a core sample of the bed was taken and sectioned for analysis at Virginia Tech. The filter was continuously run with excess free chlorine supplied in the influent, and no backwashing was performed. Additional core samples were taken and sectioned into five depth intervals for analysis at approximately 7 and 16 weeks after the beginning of the elevated Mn^{2+} levels. Upon receipt at Virginia Tech, the media were air dried, analyzed by SEM and EPMA techniques (see Chapter 1 for detailed description), and extracted for analysis of Mn content. The media characteristics with depth, and the core Mn contents are summarized in Table 2. The initial core sample had less than 1 mg g^{-1} extractable Mn throughout its depth. The Mn was highest in the anthracite-rich core sections, and the sand grains appeared uncoated. It is likely that the extractable Mn found in the sand-rich core sections resulted from the trace anthracite present.

The depth profiles of extractable Mn^{2+} are shown in Figure 1. The marked increase in Mn in the upper layers of this unbackwashed filter is consistent with efficient Mn^{2+} removal by the autocatalytic continuous NGE process. The filter effluent [Mn^{2+}] was below the goal of 0.02 mg L^{-1} throughout the study. The sand fraction of the week 7 and week 16 cores had a brownish discoloration not present in the initial core samples, suggesting that $MnO_{x(s)}$

growth initiated there in this long-term study. The free chlorine demand of core #2 was 0.004 mg g^{-1}, indicating that sufficient oxidant was supplied to the filters.

SUMMARY and CONCLUSIONS

The practical guidelines and test procedures given here should enable an engineer to evaluate the feasibility of the NGE process for a new filter installation, as well as implement and maintain its operation in an existing plant. Developing a familiarity with the qualitative effects on effluent [Mn^{2+}] of process variable dynamics will assist the engineer in anticipating and correcting problems when rapid response is required. For process design and modification studies, the kinetic process model can be used to optimize Mn^{2+} removal for a given set of conditions, or explore how expected process dynamics will affect finished water quality.

The NGE process has the proven potential for reducing production costs and increasing customer satisfaction where Mn^{2+} is a concern. It may be argued that the fundamental principles of full-scale NGE process operation and maintenance are understood to a degree comparable with the widely-practiced activated carbon absorption process. The engineered application of oxide-coated media should be considered as an option for routine treatment process design. As demand for drinking water continues to increase with population growth, the need for exploitation of lower-quality water sources will grow. The NGE process is an example of a technology which provides substantial economic and product quality benefits, making possible the utilization of such marginal water sources without additional major capital requirements.

LITERATURE CITED

1 - Cornwell, D. A.; Lee, R.G. "Waste stream recycling: its effect on water quality", J. AWWA **1994** (86:11), 50-63.

2 - Byerly, G. P. "Oxide-coated media aids in manganese control", *AWWA MainStream* **1994** (May), American Water Works Association, Denver, Colorado.

3 - Carlson, K.; Knocke, W. R.; Gertig, K. "Modeling Manganese Oxidation with Potassium Permanganate", Proceedings of the Annual Conference of the American Water Works Association **1994** (June), New York.

TABLE 1

LIKELY QUALITATIVE EFFECTS OF DYNAMIC CONDITIONS ON FILTER EFFLUENT [Mn^{2+}]†

Process mode	Process condition	Change during filter run (+ or -)	Effluent [Mn^{2+}] (+ or -)
Continuous regeneration	pH	+	-
	[Mn^{2+}]	+	+
	free chlorine	-	+
	[Ca^{2+}]	+	-
	flow rate	+	+
Intermittent regeneration	pH	-	+ (initial desorption)
	[Mn^{2+}]	-	+ (desorption)
	[Ca^{2+}]	+	+ (desorption)
	flow rate	+	+

† - Not all of these changes may result in a measurable change in effluent [Mn^{2+}] from a full-scale filter. For example, in continuous NGE operation a decrease in pH may result in a deeper penetration of soluble Mn^{2+} into the upper layer of the filter bed, while effluent [Mn^{2+}] remains below analytical detection limit. The directions of change indicated are the likely tendencies which may be considered in process evaluations.

TABLE 2

FILTER CORE ANALYSES: FT. COLLINS, CO NGE PROCESS STUDY

Core depth	Media	Extractable Mn, mg g^{-1} Initial	Week 7	Week 16
2" - 4"	anthracite, trace sand	0.83	2.1	2.04
6.5" - 8"	anthracite, trace sand	0.59	1.4	1.51
10.5" - 12"	anthracite & sand mix	0.55	1.15	0.69
14.5" - 16"	primarily sand	0.10	0.27	0.17
18.5" - 20"	sand, trace anthracite	0.04	0.09	0.14

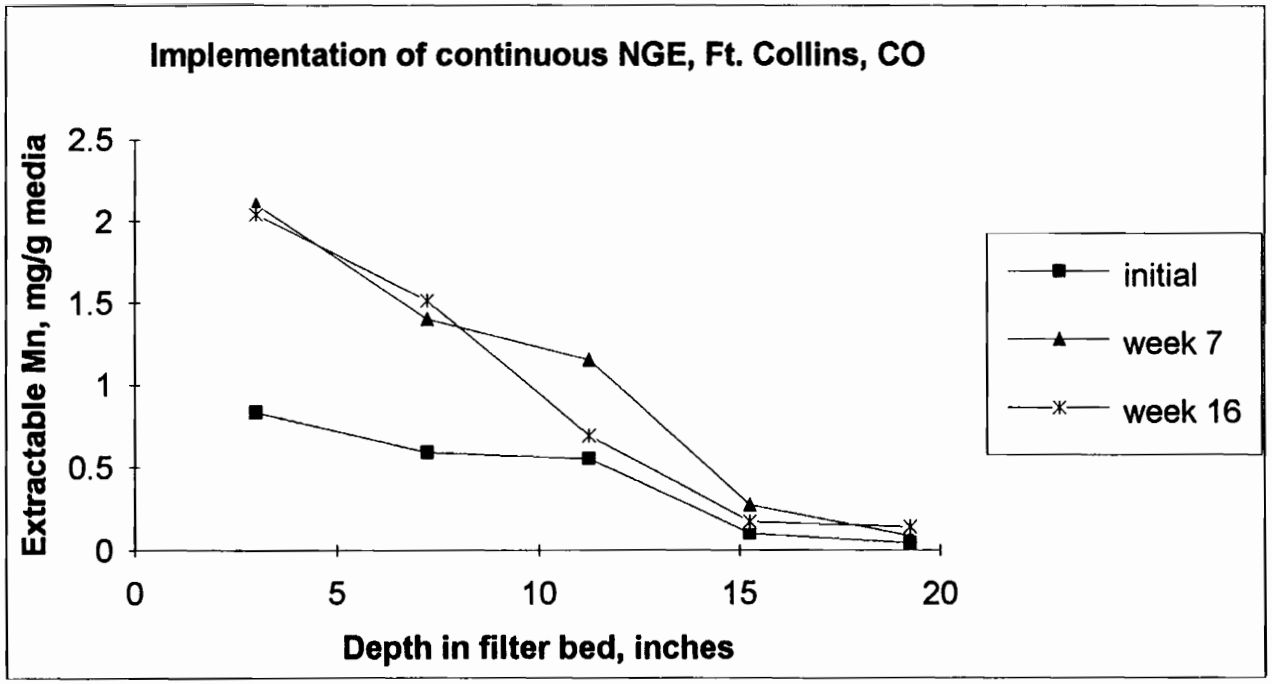

FIGURE 1: Profile of extractable Mn from core samples of a dual-media filter run in NGE continuous regeneration mode without backwash at the Ft. Collins, CO, Water Utility, August - November, 1994. Approximate process conditions: pH 6.8 - 7.0, hardness 28 - 40 mg L^{-1} as $CaCO_3$, total [Mn] = 0.05 - 0.08 mg L^{-1} (50% dissolved Mn^{2+}, 50% colloidal particulates).

CHAPTER 5

SUMMARY

In this work, oxide-coated filter media have been shown to be physically and chemically complex to a degree not previously considered or anticipated by workers in the field of water treatment. It is arguable that further understanding of media coating characteristics as described by geological science techniques may be needed to advance filtration theory, and this effort has only produced an outline of topics of interest for further research. The primary goal of this research was a predictive model of the NGE process based on fundamental chemical reactions at the media surface. In retrospect, if the nature and complexity of coating variation had been known, it is doubtful that this goal would have been contemplated in its original scope. However, this work has shown that accepted model structures for sorption processes may provide predictive capability for the NGE process under well-defined conditions. The documentation of the isotherm behavior of coated media and the applicability of flow correlations for estimation of mass transport kinetics are key findings which should prove useful to subsequent investigators.

A practical component of the research program was the development of a media coating method, which was satisfactorily accomplished. The media characterization studies enabled a greater understanding of both mass transport and reaction phenomena, a perspective not apparent from characterization by chemical extraction alone. The process model that resulted was an initial attempt at describing and simplifying obviously complex phenomena so that a

practical engineering tool was obtained, even though the Mn^{2+} - $MnO_{x(s)}$ system is not well understood from the viewpoint of fundamental reactions.

While the model validation was not completely satisfactory (partially due to experimental difficulties), model failure was typically conservative, meaning that the model tended to over-predict effluent [Mn^{2+}] when the actual process was performing well, especially under conditions of low sorption capacity and high flow. In a practical sense, for a high influent [Mn^{2+}] (> 0.10 mg L^{-1}) such conditions are not particularly suitable for sorption of Mn^{2+} using coated media in IR mode, since the media are essentially performing as a weak, low-capacity ion-exchange resin. The media bed depth required to maintain satisfactory effluent [Mn^{2+}] for a reasonable filter run duration is probably not realistic, considering the associated hydraulic head loss. For influent [Mn^{2+}] below 0.10 mg L^{-1}, the IR mode may be a feasible treatment option which should be evaluated with pilot studies.

It is hoped that this work will enable engineers to consider with greater confidence the NGE process as a viable treatment option for soluble Mn^{2+} removal. Adaptation of this process for removal of other inorganic contaminants from both drinking water and wastes is a promising avenue for further research.

APPENDIX I

EFFECT OF OXYGEN ON Mn^{2+} UPTAKE BY OXIDE-COATED MEDIA

Laboratory filter columns were used to evaluate the effect of $O_{2(aq)}$ on Mn^{2+} uptake by synthetically coated media at pH 7.00. Although surface-catalyzed oxidation of Mn^{2+} by $O_{2(aq)}$ has been shown to be extremely slow below pH 8.5,(refs), this study was performed to support the process modeling assumptions that sorption rather than oxidation by $O_{2(aq)}$ is the primary mechanism of Mn^{2+} removal in the absence of free chlorine for pH values in the range of 6.0 to 7.50. In a Pyrex column (dia. = 4 cm), 50 g of synthetically coated anthracite media sample 1 (1.3 mg g^{-1} extractable Mn) were supported on a perforated Teflon disk. The bed depth was 4.75 cm, and porosity was 0.47, calculated from triplicate measurements of packing in a volumetric cylinder. The hydraulic loading rate was 2.5 gpm ft^{-2}.

The solution conditions were as follows: in 20 L distilled deionized water, influent [Mn^{2+}] was approximately 0.5 mg L^{-1} (added as $MnSO_4 \cdot H_2O$), [$HCO_3^=$] = 10^{-3} M over atmospheric contribution (added as $NaHCO_3$), and 68 mg L^{-1} NaCl was added for background ions. A YSI Model 54 oxygen meter was used to monitor reservoir [$O_{2(aq)}$] during the tests. For the deoxygenated columns, reagents were added to the reservoir, which was then bubbled with nitrogen until [$O_{2(aq)}$] was at a minimum. The pH was then adjusted to 7.00 by addition of 0.5 N NaOH. The minimum [$O_{2(aq)}$] achievable by this technique was 0.55 mg L^{-1}. Note that this is still near the stoichiometric requirement for Mn oxidation to $MnO_{2(s)}$, so the experiment tests a saturated (5.5 mg/L [$O_{2(aq)}$]) vs. a depleted

[$O_{2(aq)}$] condition. Column effluent samples were filtered through 0.45 μm syringe filters and analyzed immediately by flame atomic absorption. Replicate columns of each condition were tested.

The results of the column tests are given in Figure I-A, shown as dimensionless effluent concentration vs. time. There is no difference between oxygenated and deoxygenated treatments at 105 minutes (two sample t-test assuming unequal variances, $\alpha = 0.05$). This finding is consistent with the model assumption that depletion of soluble Mn^{2+} in the presence of this synthetically-coated anthracite is due to sorption rather than Mn^{2+} oxidation by O_2 over the time scale of the column studies. This also implies that surface-catalyzed Mn^{2+} oxidation by O_2 is negligible compared to any observed oxidation by free chlorine at pH 7.50, and presumably at lower pH.

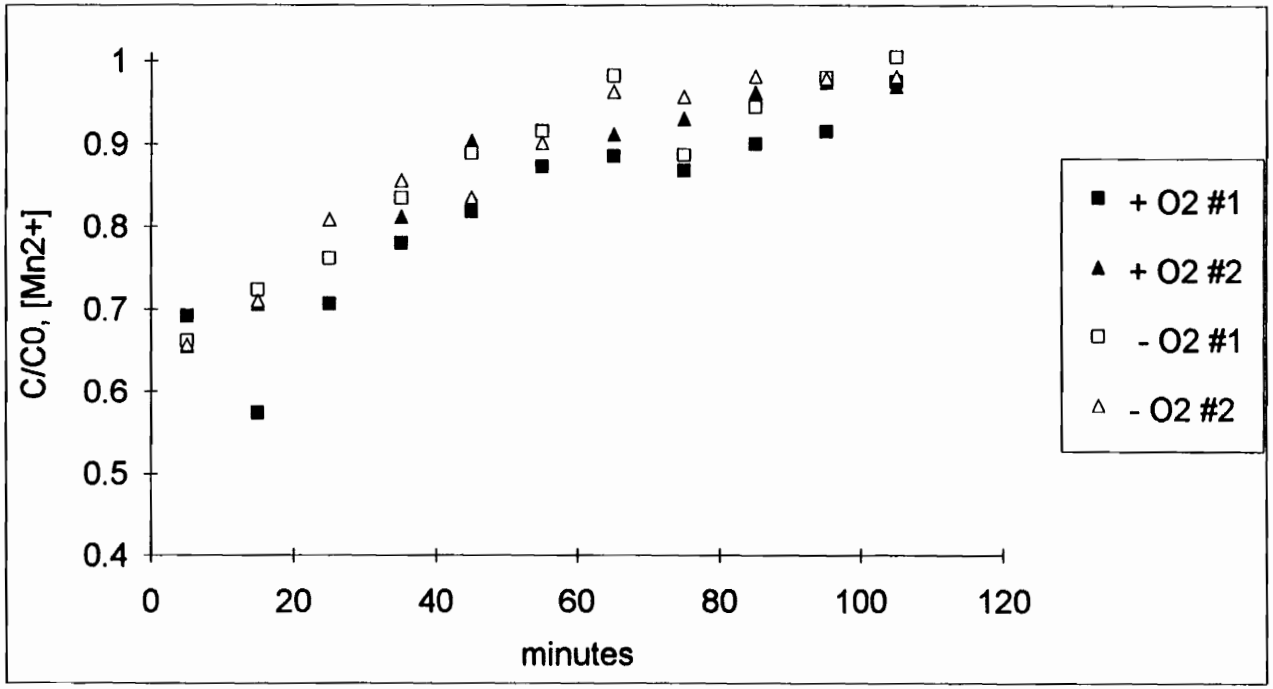

FIGURE I - A: Effluent [Mn^{2+}] profiles, Mn^{2+} sorption in oxygenated and deoxygenated conditions. Influent [Mn^{2+}] = 0.5 mg L^{-1}, pH = 7.00, synthetically coated media #1 (1.3 mg g^{-1} extractable Mn). Oxygenated conditions (+O_2), [$O_{2(aq)}$] = 5.5 mg L^{-1}, deoxygenated conditions (-O_2), [$O_{2(aq)}$] = 0.55 mg L^{-1}.

APPENDIX II

MODEL CALIBRATION RESULTS

This Appendix consists of figures depicting results of the laboratory model calibration which are not discussed in Chapter 3. Please consult Chapter 3 for additional details.

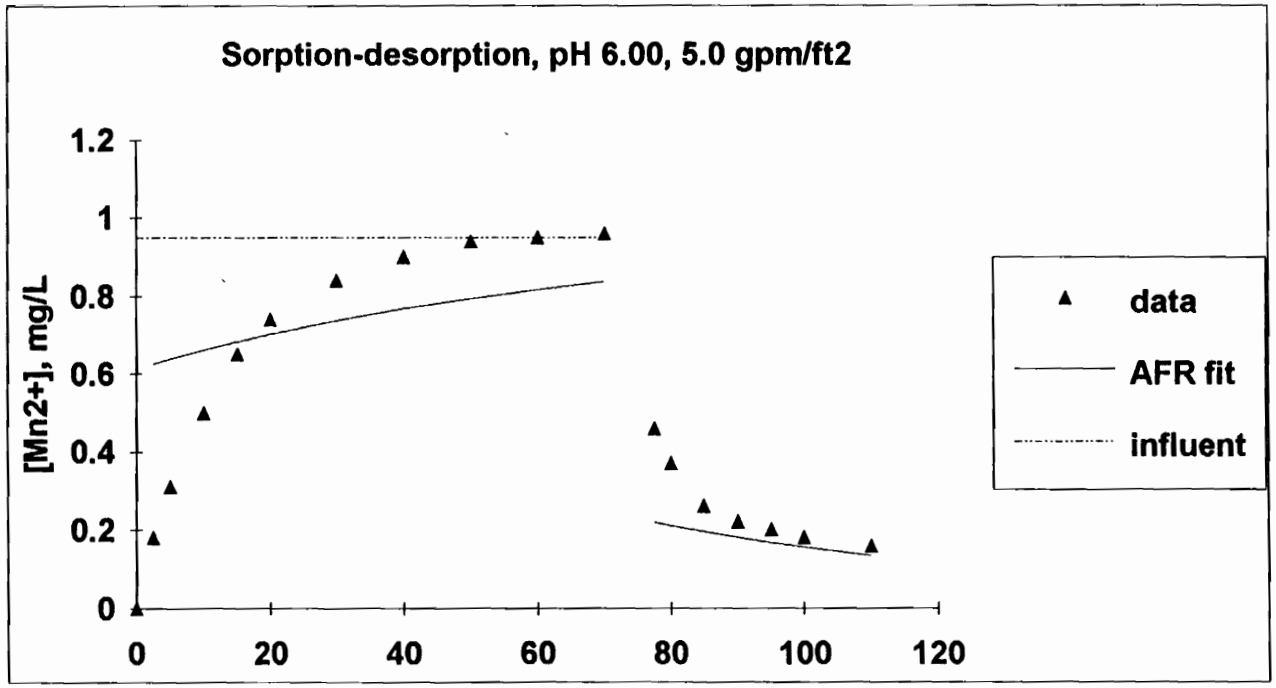

FIGURE II - A: Intermittent regeneration model calibration, synthetic media #2.

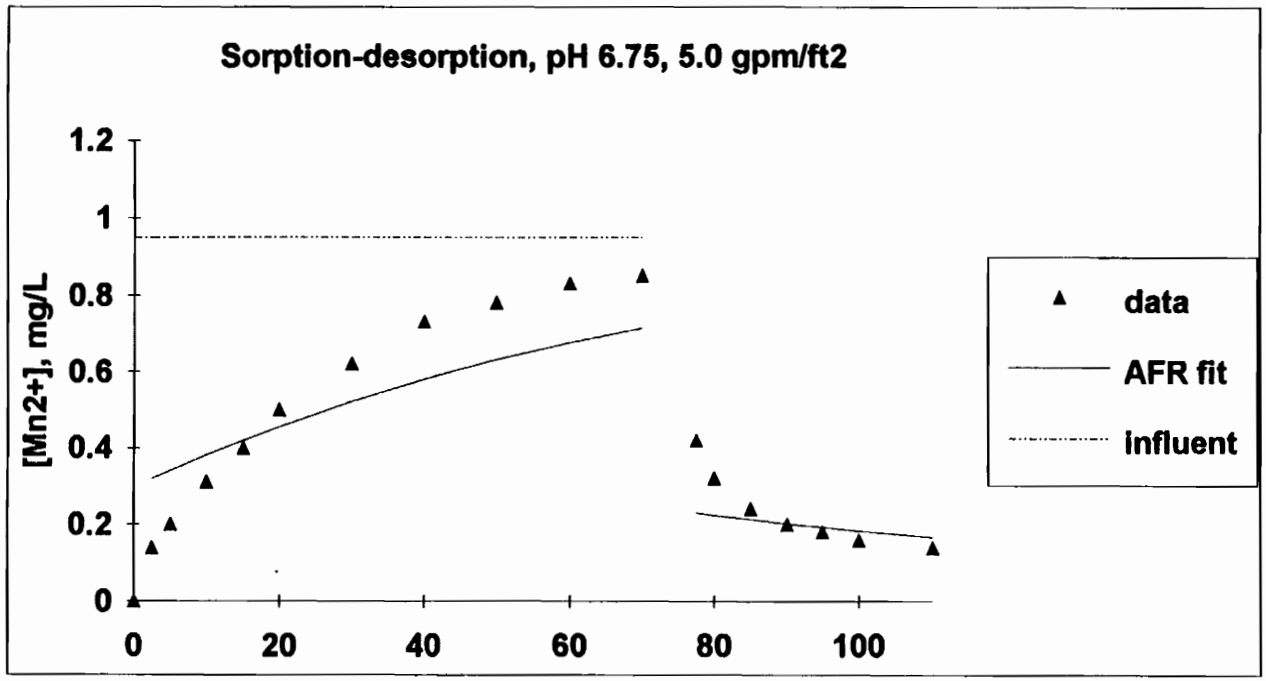

FIGURE II - B: Intermittent regeneration model calibration, synthetic media #2.

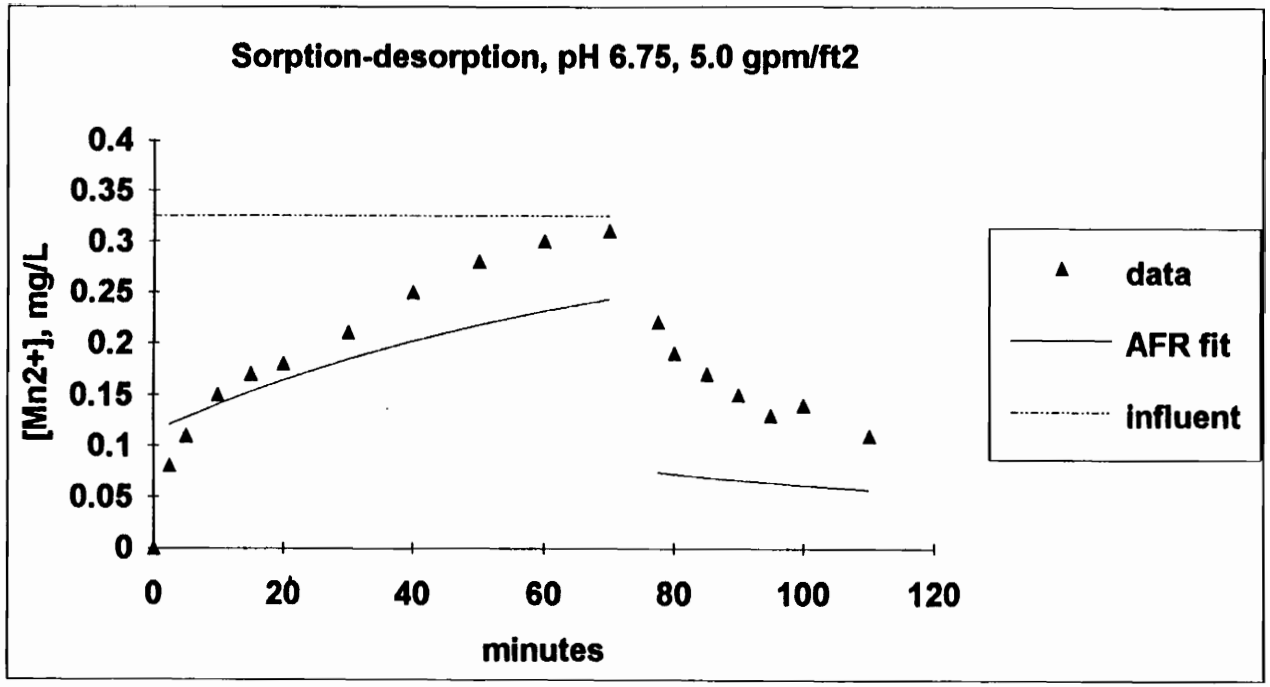

FIGURE II - C: Intermittent regeneration model calibration, synthetic media #2.

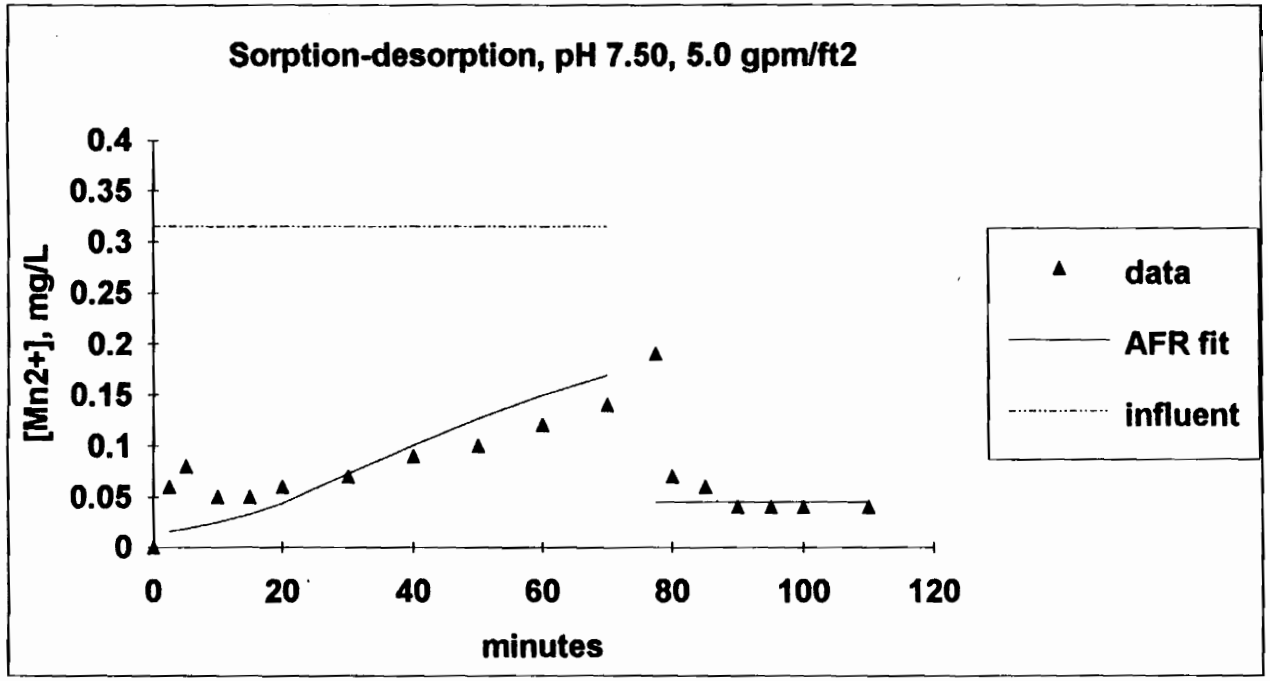

FIGURE II - D: Intermittent regeneration model calibration, synthetic media #2.

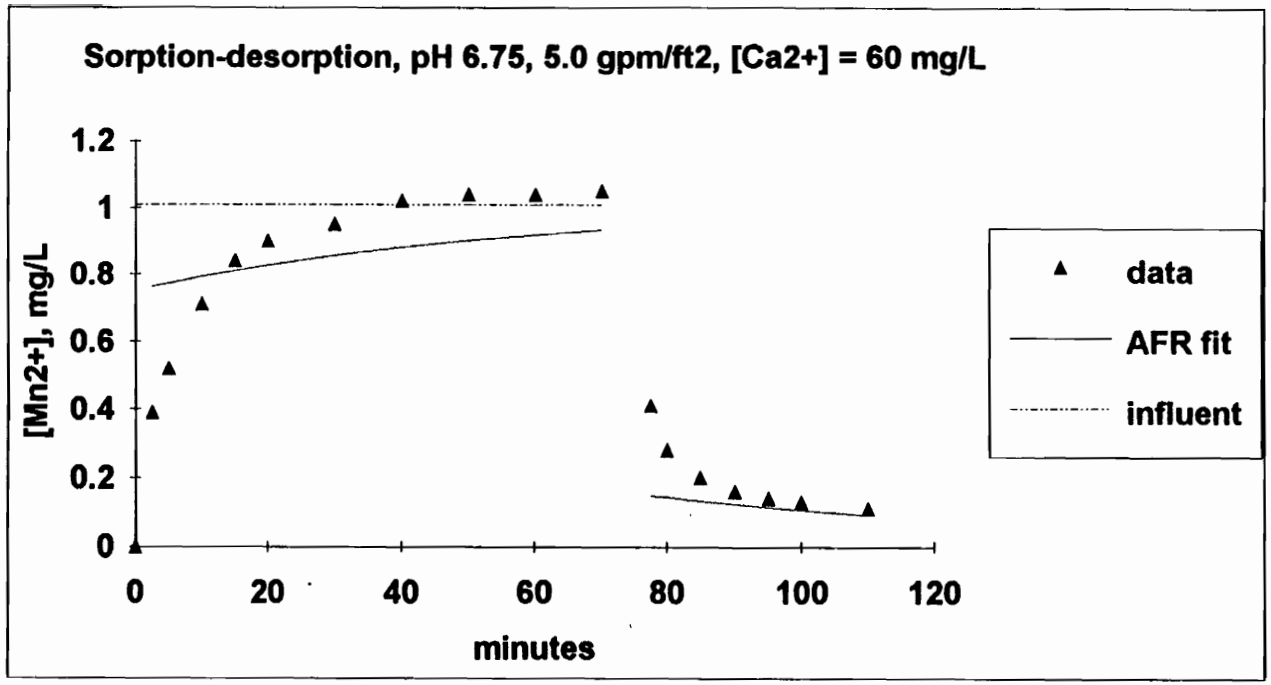

FIGURE II - E: Intermittent regeneration model calibration, synthetic media #2.

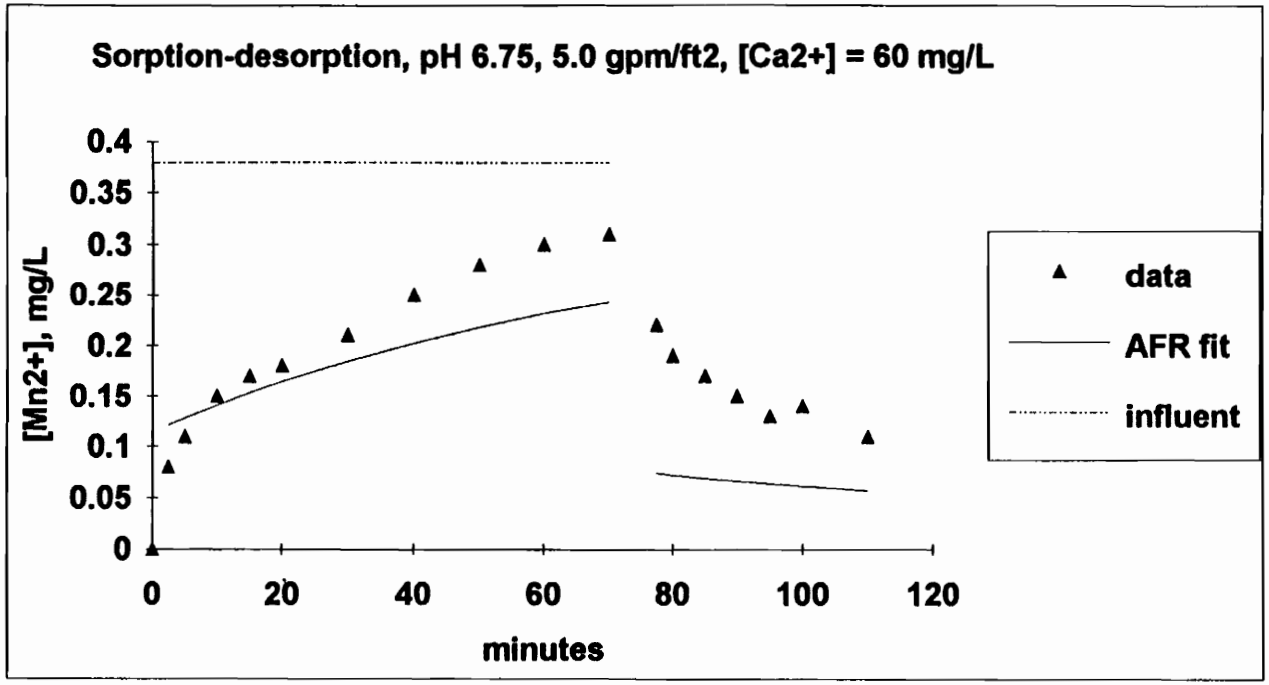

FIGURE II - F: Intermittent regeneration model calibration, synthetic media #2.

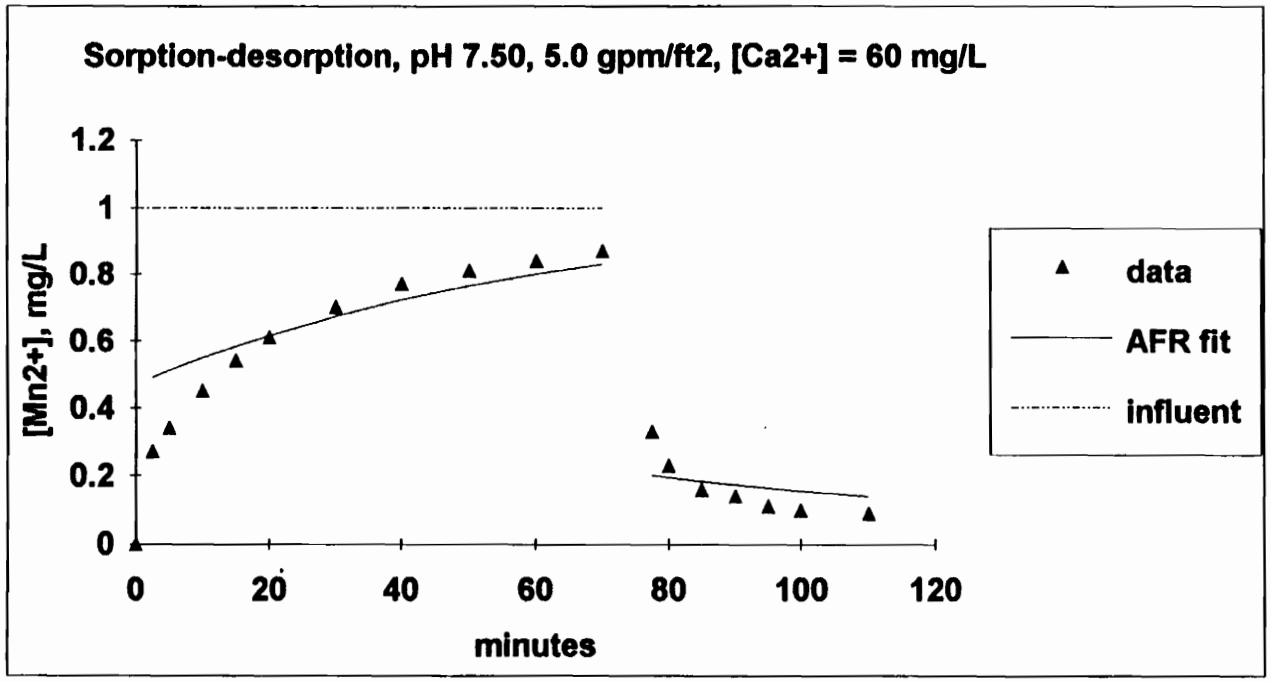

FIGURE II - G: Intermittent regeneration model calibration, synthetic media #2.

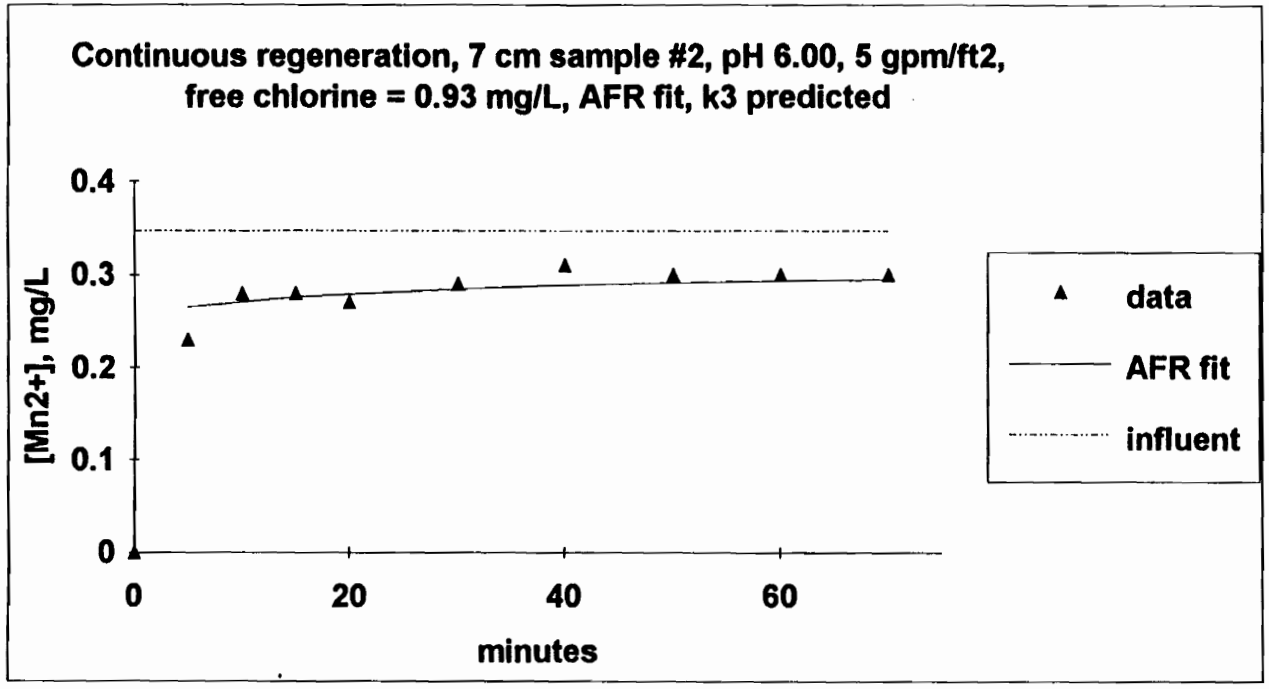

FIGURE II - H: Continuous regeneration model calibration, synthetic media #2.

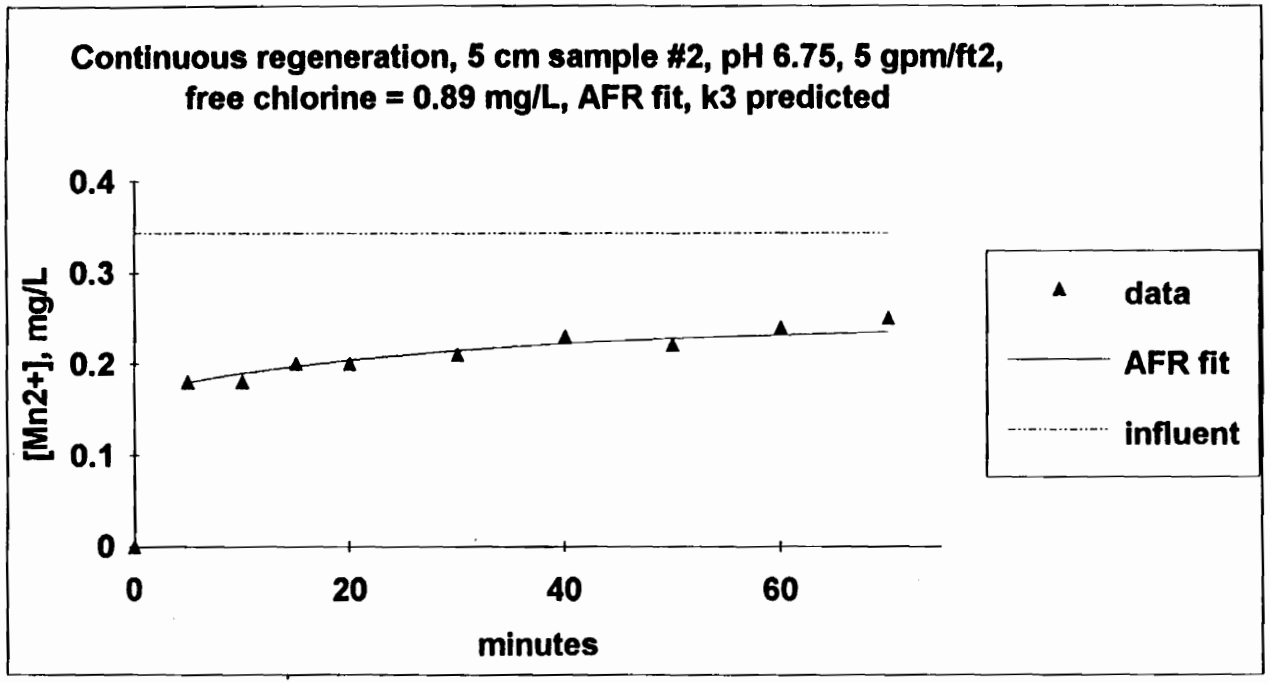

FIGURE II - I: Continuous regeneration model calibration, synthetic media #2.

VITA

Peter Benedict Merkle was born in Greenville, South Carolina, a son of Robert and Mary Merkle. He attended primary and secondary school in Southern Maryland, graduating from Ryken High School. He received two Bachelor of Science degrees from the Massachusetts Institute of Technology (Management and Chemical Engineering), with an engineering research internship at the Cabot Corporation, Billerica, MA.

In 1984, he joined Dow Chemical U.S.A Coatings and Resins in sales and technical service for aerospace, electronic and structural composite polymers. In 1986, he joined CIBA-GEIGY Plastics as corporate and distributor account sales manager for the western U.S. In 1988, he visited archaeological sites in Mexico and the British Isles, and hiked the Appalachian Trail from Georgia to Maine. He completed studies in 1991 for the Master's degree in Marine Environmental Science (Chemical Oceanography) at the Marine Sciences Research Center Waste Management Institute, State University of New York at Stony Brook. He was awarded a Charles E. Via, Jr. Doctoral Fellowship by the Virginia Tech Department of Civil Engineering, Environmental Division. Upon completion of doctoral studies, he accepted a position as Senior Member of Technical Staff in the Energy and Environment Division nuclear waste storage assessment and remediation group of the Sandia National Laboratories, Albuquerque, NM.

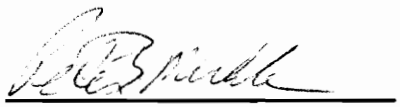

(Peter B. Merkle)